Campus Bio-Medico University of Rome

Doctoral Thesis

Emergent Dynamics of Electrically Coupled β-cells: Implications for Physiopathology of the Endocrine Pancreas

Author:
Alessandro Loppini

Supervisor:
Prof. Simonetta Filippi

A thesis submitted in fulfilment of the requirements
for the degree of Doctor of Philosophy

in

Biomedical Engineering
Campus Bio-Medico University of Rome

XXVIII ciclo

March 2016

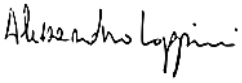

Acknowledgements

The work presented in this dissertation has been possible thanks to several persons who supported me from both a scientific and a human point of view, and who deserve special acknowledgements.

First of all, thanks to my supervisor Prof. Simonetta Filippi, who first trusted me and gave me the opportunity to expand my skills in her wonderful team, driving my work with great knowledge and interest. Special thanks go to Prof. Christian Cherubini, who has been, and still is, both a wonderful professor and a master of life who constantly inspired me with pleasant and fruitful discussions. I really acknowledge Dr. Alessio Gizzi, who always treated me as a friend, taught me as a brother and has been a wonderful guide in the good scientific practice.

Particular thanks to Prof. Morten Gram Pedersen with whom I've had the pleasure to work and who shared his huge knowledge and rigorous attitude to research with me. I'm very much indebted to Prof. H. Eugene Stanley, who kindly hosted me in his laboratory during my research project, enlightening me with his wisdom.

Last but not least, very special thanks to my family and my friends who constantly supported me, trusted me and loved me.

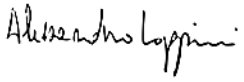

Contents

Alessandro Loppini

Alessandro Loppini

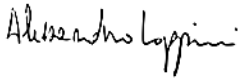

List of Figures

Alessandro Loppini

Alessandro Loppini

List of Tables

Alessandro Loppini

Chapter 1

Introduction

More than 40 years of research studies on the endocrine β-cells have enlightened most of the fundamental mechanisms involved in insulin secretion in rodents, with a vast published literature that confirms our knowledge of the electrophysiology of these cells, based on both experiments and mathematical models. Although, much more remains to be understood, with particular regards to the loss of β-cell functionality in pathologies such as diabetes.

Among the mechanisms involved in the normal regulation of insulin secretion in mouse islets, gap junction electrical coupling was shown to be an essential aspect in β-cell endocrine function. Intercellular communications induced by such coupling represent in fact an efficient way through which cells can synchronise their intrinsically heterogeneous activity, homogenising pancreatic islets response to glucose stimuli, improving glucose responsiveness, and giving rise to a global pulsatile insulin release, which is more effective than a constant insulin supply. Therefore in this scenario, the pancreatic islet is a complex structure where β-cells explicate their function through communication. It is also proven that the loss of direct electrical coupling in rodents leads to an altered β-cells function, characterised by impaired glucose tolerance and insulin secretion. Interestingly, in this case, the resulting pattern of hormone release resembles those observed in diabetic patients, thus suggesting that the beneficial effect of electrical coupling may be compromised or lost in diabetic islets. In confirmation of that, recently published studies show altered expressions of the protein forming junctional channels in in-vitro environments resembling diabetic inflammatory condition, and an increase resistance to cytotoxic compounds in the case of electrically coupled β-cells. Moreover such metabolic disorders can have dramatic effects on the islet architecture itself and alter intercellular communication by topological modification of the islet, which are very likely to occur

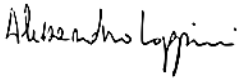

especially in autoimmune forms of diabetes, where β-cells are progressively killed by an intra-islet infiltrate of immune cells.

Such evidence requires investigating deeply gap junction properties between β-cells, extending the knowledge accumulated on rodents to the less studied human case. Concerning this, published literature have shown interesting aspects regarding the human islet. In fact, in common with rodents, also in humans are expressed proteins forming gap junctional channels, and moreover, functional tight junctions have been observed by histological studies. Furthermore, an even more intriguing fact is that human islet architecture is completely different compared to the mouse islet. Therefore, it is reasonable to think that gap junction channels not only have a role in homogenising and synchronising the response of human β-cells, but it can also be hypothesised that such a different topology of the islet have a considerable effect on cells emergent activity and could imply significant functional differences respect to the rodent case. Unfortunately, the human β-cell electrophysiology has been analysed only recently, and electrical coupling between human β-cells remains a largely unexplored topic.

Therefore, in this dissertation a mathematical modelling approach is adopted to investigate gap junction coupling effect on the emergent dynamics of β-cell populations, trying to analyse the collective behaviour of coupled cell clusters in-silico. Different electrophysiological models are used in this framework to reproduce the dynamics of both mouse and human β-cells. Specifically, based on a mouse electrophysiological model, two studies here presented are focused on the analysis of the emergent electrical activity of coupled cell populations, and its robustness upon operating conditions, such as the cluster topology, the stimulatory glucose concentration, and the intrinsic biological noise. Finally, a third study based on a mathematical model fine-tuned on human electrophysiology attempts to estimate and analyse gap junction coupling between human β-cells, validating obtained results against the few available experimental studies.

This dissertation contains new results outlined in the following. At first, a study of compact β-cell clusters shows that a coherent dynamics characterises β-cells in mouse islets. This robust dynamical state ensures a long-range correlated cellular activity, and it is strictly dependent on both glucose stimulation level and cluster size. The β-cell cluster is able to switch from coherent to uncorrelated dynamics resembling phase transition and critical phenomena observed in other physical systems. It is worth noting that a similar regulation of the dynamics around a critical point is a feature of other biological networks, such as neuronal networks. At second, a study concerning the topological effects on the emergent dynamics shows that the β-cells in mouse islets can be viewed as a fully coupled functional unit while the human islet seems to be characterised by functionally distinct modules of β-cells. This substantial difference is mainly due to

Alessandro Loppini

the percolated network architecture underlying β-cells arrangement in human islets, which induces a complex pattern of intercellular synchronisations. It is important to note that such pattern shows scale-free similarity features characteristic of the percolated cluster resembling the human β-cell arrangement, not observed in the compact mouse architectures. Finally, the third study represents to the best of our knowledge the first attempt to estimate gap junction conductance between human β-cells. Results obtained are surprisingly in agreement with the reported values of the junctional conductance between mouse β-cells. The analyses of small coupled populations of human β-cells show moreover that the estimated strength of coupling can substantially alter the emergent dynamics, and consequently the insulin release.

A brief description of the content of the Chapters is given in the following. In Chapter 2 the basic notions about the anatomy and physiology of the Pancreas are introduced. The structure of the exocrine and endocrine tissues forming the pancreatic gland is explained, with particular regards to the endocrine cells and their role in glucose homeostasis. The pancreatic endocrine pathologies, such as islet tumors and diabetes, and their deleterious effect on blood glucose regulation are also discussed. Chapter 3 describes the mathematical framework of the Hodgkin-Huxley type electrophysiological models, used in the following to reproduce the electrophysiological response of the β-cells. In this context, both the deterministic formulation and the stochastic generalisation of the Hodgkin-Huxley type model are explained. Electrophysiology of the mouse β-cell, and the gap junction channels properties are discussed in Chapter 4. In Chapter 5 the Sherman-Rinzel-Keizer model of mouse β-cell electrical activity is introduced, discussed and generalised. Finally, the model generalisation is used to analyse the coherent activity of β-cell compact clusters. In Chapter 6 the differences in islet architecture between mouse and human are discussed, and the generalised Sherman-Rinzel-Keizer model is further used to analyse synchronisation phenomena on β-cell clusters by varying cluster topology and operating conditions. Both the electrophysiology and the mathematical modelling of human β-cells are described in Chapter 7. In Chapter 8 such model is generalised to the case of coupled β-cells and is used to estimate and investigate gap junction coupling in the human case. Finally, in Chapter 9 the obtained results are summarised and the novelty aspects are discussed, suggesting possible future directions.

In the following the list of the publications on which this dissertation is based:

- Alessandro Loppini, Antonio Capolupo, Christian Cherubini, Alessio Gizzi, Marta Bertolaso, Simonetta Filippi, and Giuseppe Vitiello. On the coherent behavior of pancreatic beta cell clusters. *Physics Letters A*, 378(44):3210-3217, 2014.

Alessandro Loppini

- Christian Cherubini, Simonetta Filippi, Alessio Gizzi, and Alessandro Loppini. Role of topology in complex functional networks of beta cells. *Physical Review E*, 92(4):042702, 2015.

- Alessandro Loppini, Matthias Braun, Simonetta Filippi, and Morten Gram Pedersen. Mathematical modeling of gap junction coupling and electrical activity in human β-cells. *Physical Biology*, 12(6):066002, 2015.

- Marta Bertolaso, Antonio Capolupo, Christian Cherubini, Simonetta Filippi, Alessio Gizzi, Alessandro Loppini, and Giuseppe Vitiello. The role of coherence in emergent behavior of biological systems. *Electromagnetic biology and medicine*, 34(2):138-140, 2015.

- Alessandro Loppini, Matthias Braun, Simonetta Filippi, and Morten Gram Pedersen. Modeling gap junction coupling and electrical activity in human β-cells. *Islet Study Group Meeting 2014*, Lausanne, Switzerland.

Alessandro Loppini

Chapter 2

The Pancreas: anatomy and physiopathology

In this section, the basic concepts of the anatomy and physiology of the pancreas are given. In particular, exocrine and endocrine pancreatic functions are explained with particular regards to the endocrine islets cells, which regulate blood glucose homeostasis. The activity of endocrine cells is crucial to maintain glycemic conditions in a physiological range, and their altered function can lead to pathological conditions. Concerning this, endocrine pancreas pathologies are also discussed in the following, specifically describing the pathogenesis of the most common diabetic conditions.

2.1 Structure of the Pancreas

The pancreas is an organ (gland) composed of both exocrine and endocrine tissues. It is located in the retroperitoneal space and presents an elongated conical form (see Fig. 2.1). On average it is $\simeq 17 - 20\,cm$ in length, and $70 - 80\,g$ in weight, and its structure is formed by four macroscopic different regions: head, neck, body, and tail. The head is located in the right extremity and it is attached to the duodenum, in which is secreted the exocrine product. The neck instead, i.e. the pancreatic isthmus located at the level of the superior mesenteric artery and vein, connects the head with the body, which in turn is in contact with the omental bursa anteriorly (posterior to the stomach), and with the superior mesenteric artery, the left suprarenal gland, and the left kidney posteriorly. The tail of the pancreas is located at the left extremity of the organ and is in contact with the splenic flexure, the left kidney, and with the hilum of the spleen in the apical region.

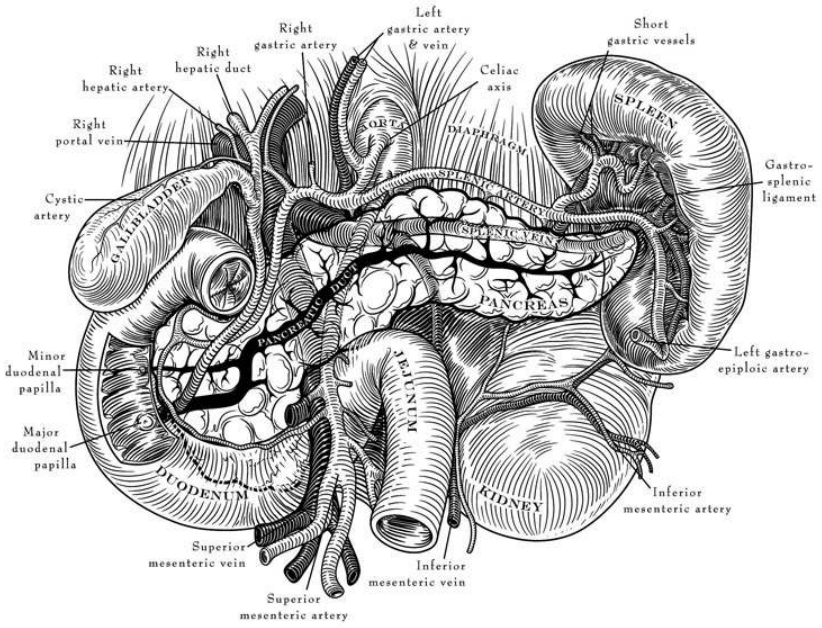

FIGURE 2.1: Qualitative representation of the pancreas, showing main ductal structures and blood vessels.

The pancreas is rich of excretory ducts, blood vessels and nerve fibers. The exocrine product flows in the duodenal tract via two main ducts: the major pancreatic duct (Wirsung duct), and the accessory pancreatic duct (Sontorini duct). The major pancreatic duct extends along the principal axis of the organ, and the accessory duct originates from it at the neck level. Their role is thus to collect exocrine secretory products from the other dutcules and ducts, and convey it in the duodenum. Such ducts secrete a large amount of sodium bicarbonate that mixes with the secretory product of the exocrine tissue to form pancreatic juice. In addition, the major pancreatic duct joints with the hepatic bile duct at the level of the ampulla of Vater, where is connected to the duodenum. Concerning blood vessels, from the common hepatic artery originate the gastroduodenal, and the posterior and anterior pancreaticoduodenal arteries, which supply blood to the head of the pancreas. Instead, from the splenic and the superior mesenteric arteries originate vessel tracts that reach body and tail of the pancreas. Then, the splenic, mesenteric, and portal veins collect the blood outflow from the pancreas. Finally, the organ is innervated by both sympathetic, parasympathetic and afferent fibers, which are distributed along ducts, vessels, and in the exocrine and endocrine compartments. Both gabaergic, cholinergic, adrenergic fibers and peptide-containing neurons have been shown to contribute to such rich innervation. [1, 2]

2.1.1 Exocrine matrix

The exocrine matrix represents about the $\simeq 80\%$ of the volume of the pancreas. It is characterised by a tubuloalveolar structure, and it is mainly formed by functional units called "acini" (represented in Fig. 2.2(a)). Each acinus is composed by several acinar cells ($\simeq 6-8$) surrounding a central lumen that connects to progressively larger pancreatic ducts. These cells have a pyramidal shape, with a basal area that contains endoplasmic reticulum and basophilic elements, and an apical zone which contains acidophilic zymogen granules and where the cytoplasmic membrane project a multitude of microvilli in the central lumen. As mentioned above, the secretory product of the combined activity of acini and ductal cells is the pancreatic juice, which serves to regulate digestion processes of the nutrients in the intestinal tract, and to protect the gastrointestinal environment. It is mainly formed by water, electrolytes, and by proteolytic, lipolytic, lysosomal and nucleolytic enzymes. Exocrine secretion is regulated by both humoral mechanisms and neural signalling. The main hormone regulators are the secretin, which stimulates the release of a juice rich in bicarbonate and with low concentrations of enzymes, and the cholecystokinin (CCK), which contrarily is a stimulant of enzyme secretion more than bicarbonate secretion. Gastrin is another stimulant with comparable effects respect to CCK, despite being less powerful. In addition, the vagus nerve and adrenergic nerves regulate exocrine secretion by enhancing enzymes concentration and modulating pancreatic blood flow respectively. Also hormones secreted by the endocrine pancreas can modulate exocrine activity, mainly by the inhibitory effects of glucagon, pancreatic polypeptide, and somatostatin. [1, 2]

2.1.2 Endocrine tissue

The endocrine pancreas is formed by ellipsoidal clusters of cells scattered throughout the exocrine matrix, which take the name of "islets of Langerhans". All the endocrine cells contribute to only the 2% of the whole wet weight of the organ in an adult. Pancreatic islets are highly variable in size and composition: they contain about $2000-6000$ endocrine cells and are characterised by a radius in the range $20-300\,\mu M$ (see Fig. 2.2(b)). The resulting structure is highly vascularised and innervated, thanks to the blood vessels a nerve fibers projecting within the pancreas and described above. At least 5 different types of cells can be recognised within the islet: α, β, γ (PP-cells), δ, and ϵ-cells. Several studies have pointed out that the endocrine cells fraction and their spatial organisation within the islet is highly heterogeneous both in the single pancreas and between different species [4–6]. For instance, functional differences have been found in the adult rat pancreas between islets from the head and the body/tail regions, while

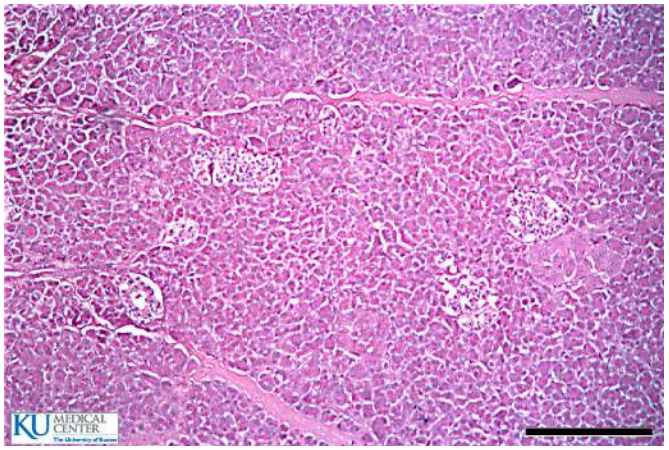

(a)

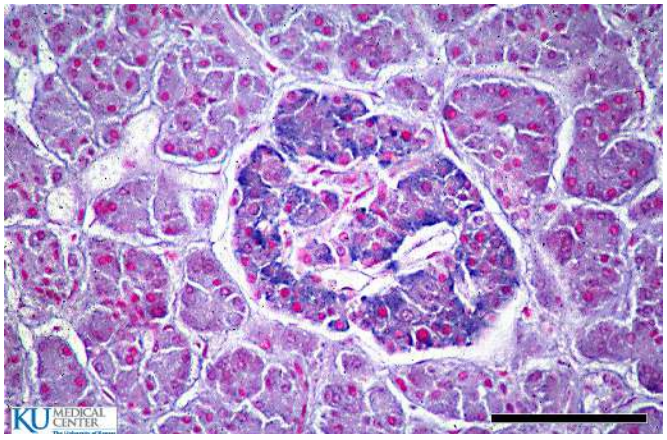

(b)

FIGURE 2.2: Pancreatic slices showing the exocrine matrix (a) and the endocrine islets (b). Bars length is equal to $250\,\mu m$ (a), and $30\,\mu m$ (b). Images from the University of Kansas Medical Center database [3].

in humans a 2-fold increase in the total endocrine mass was observed in the tail compared to the head and body of the pancreas. Considering this heterogeneity, the average composition of the islet in rodents is: $60-80\%$ β-cells, $15-20\%$ α-cells, $<10\%$ δ-cells, and $<1\%$ γ and ϵ-cells. [1, 7]

α-cells. These cells secrete glucagon, i.e. a 29 amino acid peptide derived from proglucagon. Other products that can be obtained from this precursor are glicentin, GLP-1, and GLP-2. Secretion from α-cells is crucial for the control of blood glucose level. Contrarily to insulin secretion, glucagon is released in hypoglycemic conditions and it is able to increase glycemic blood level by the promotion of hepatic gluconeogenesis and glycogenolysis, and by inhibition of glycolysis and glycogenesis. Instead, hyperglycaemia suppresses glucagon secretion. Although it is proven that the characteristic electrical activity of the α-cells drives the hormone release by a calcium-dependent exocytosis, the exact mechanism regulating such activity are still debated. A direct

suppression of electrical activity regulated by glucose is hypothesised, but also paracrine interaction and neural signalling seem to have a role in secretion. [7, 8]

β-cells. β-cells have a key role in glucose homeostasis, together with α-cells. They release insulin in response to high glucose concentrations. Insulin is a 51 amino acid peptide formed by an A and a B chain, and is derived from the precursor proinsulin. It is stored in secretory vesicles together with zinc in hexameric crystalline structures, and it is co-secreted with the C-peptide (the C chain connecting the A and B chains in the proinsulin form) and the islet amyloid polypeptide (IAPP). As in the α-cells, calcium-dependent exocytosis of insulin from β-cells is driven by a characteristic electrical activity triggered from glucose uptake. In addition, several sub-cellular mechanisms, and autocrine and paracrine signals regulate electrical activity and insulin release. The effect of insulin is to lower blood glucose level, mainly by controlling nutrients absorption and by increasing glycogenesis and suppressing gluconeogenesis. Instead, the IAPP function is not fully understood, although experimental evidence suggests that it can inhibit glucose uptake and glycogenesis stimulated by insulin in rat skeletal muscle, and it is able to stimulate basal insulin secretion and to inhibit secretion under stimulatory conditions. In addition, it can inhibit gastric emptying with a similar effect compared to CCK. [7, 8]

γ-cells. These cells are also called pancreatic polypeptide (PP) cells, from the 36 amino acid peptide that is released from them. In human, γ-cells are mainly located within islets in the posterior area of the head of the pancreas, and, in general, are smaller compared to the other islet cells. The pancreatic polypeptide is stored in secretory granules whose release is mainly regulated by the autonomic nervous system. In addition, also paracrine interaction and glucose can have a stimulatory or inhibitory effect on the release. The main effects of PP are to inhibit insulin and somatostatin secretion from β and δ-cells respectively, to affect exocrine secretion, to reduce gastrointestinal motility, to inhibit gastric acid secretion and, in general, to slow down digestion. Furthermore, it is also hypothesised that PP is involved in the regulation of satiety. [7, 8]

δ-cells. δ-cells release somatostatin, that is a cyclic tetradecapeptide synthesised from the precursor prosomatostatin. The hormone is stored in membrane-limited vesicles and its exocytosis is regulated by intracellular calcium and cyclic AMP. Agents that promote somatostatin secretion are the same that stimulate insulin secretion. Thus, δ-cells respond to glucose in a similar way respect to β-cell. Somatostatin is able to inhibit both insulin and glucagon secretion, and to inhibit functions of the gastrointestinal tract leading to a decrease in nutrients entry rate into the portal circulation. [7, 8]

ϵ-cells. These cells release ghrelin, a 28 amino acid peptide derived from the precursor proghrelin. This hormone can affect β-cell activity via the GSH-R receptor, inhibiting

Alessandro Loppini

insulin secretion, although some controversial evidence of a stimulatory effect of insulin release was also reported. In addition, published studies showed a stimulatory effect of ghrelin on PP, somatostatin and glucagon secretion. [7–9]

2.2 Glucose homeostasis

Endocrine islets have a central role in the regulation of glucose homeostasis, and their function is to maintain nutrients concentration in the blood within an appropriate range respect to metabolic needs. To achieve this fine control, secretion from islet cells varies based on metabolites and hormone concentrations, and in response to neural signalling. In particular, insulin and glucagon secreted from β and α-cells are crucial regulators of metabolites flux into tissues, such as liver, muscle, and adipose tissue, and modulate glucose absorption and production in both postprandial and fasting times.

The ingestion and the absorption of a balanced meal stimulate insulin, PP, and somatostatin secretion, and inhibit glucagon secretion. Somatostatin may control in this condition the nutrient entry rate into the circulation while insulin regulates nutrient removal from the blood into liver, muscle and adipose tissues. A protein-based meal results instead in the secretion of insulin, glucagon, somatostatin and PP, and in enhanced levels of amino acids in the blood. In this scenario somatostatin and PP could control amino acids entry rate in the circulation while insulin controls their absorption in peripheral tissues. Generally, insulin blood concentration evoked by amino acids ingestion is too low to promote glucose uptake from peripheral tissues; therefore, blood glucose levels are mainly regulated by hepatic glucose production. This production is inhibited by secreted insulin, and stimulated by glucagon, thus resulting in an overall maintenance of glucose concentration.

In fasting and starvation conditions nutrient levels are regulated by a balance between utilisation and production rates. These rates depend on the concentrations of insulin and glucagon in the blood. For instance, during overnight fast the gradual decrease in blood glucose concentration leads to an increased glucagon secretion and a reduced insulin release. In turn, decreased insulin/glucagon ratio promotes glycogenolysis and gluconeogenesis in the liver, thus forming glucose via degradation of glycogen and elaboration of lactate, glycerol, and amino acids. Moreover, in this condition fatty acids and glycerol are released from adipose tissue. Fatty acids can be used by other tissues instead of glucose, and glycerol has a positive feedback on the hepatic gluconeogenesis. In long starvation periods, the major stores of nutrients in the body used to supply metabolic needs are adipose tissue and muscle proteins, which release fatty acids and glycerol, and amino acids respectively. In addition, in such situation glucose disposal is restricted

Alessandro Loppini

to the sole tissues totally dependent on glucose. To note that starvation also activates ketogenesis in liver cells, by which fatty acids are degraded to form ketone bodies, that can be used by the brain as an alternative to glucose for some of its functions.

Similar metabolic adaptations take place during exercise lasting several minutes, where muscle cells gradually switch from glycogen and glucose consumption to fatty acids metabolism. In parallel, insulin concentration decreases and glucagon level increases progressively. In pregnancy instead, maternal metabolism is regulated on longer time scales. The first six months are characterised by an increased intake of nutrients that are stored in adipose tissue. However, the increase of placental hormones concentrations during pregnancy causes a reduction of the peripheral tissue sensitivity to insulin, in order to limit the nutrients storage and make them available to the fetus. In normal conditions this event is balanced by a progressive increase of β-cells sensitivity to glucose stimulation (or β-cell mass increase), thus glycemic control is fulfilled by an increased insulin secretion. [7]

2.3 Endocrine cells pathologies

Damage of the endocrine islets has dramatic effects on glucose homeostasis. Specifically, underproduction or overproduction of islet hormones leads to a loss of control in glucose uptake and release, from the liver and the peripheral tissues. Usually, islet hormones overproduction, or production of hormones normally secreted in other areas, is observed in some types of endocrine tumors. These endocrine pathologies are rare, with a prevalence of less than 1 per 100,000. Between them, insulinoma syndrome is characterised by hyperinsulinism, i.e. excessive production of insulin, and hypoglycemia; similar hypoglycemic conditions are also found in proinsulinoma syndrome, which is associated with high levels of proinsulin. Instead, in glucagonoma tumor an overproduction of glucagon leads to hyperglycemic conditions. In addition, there are also reported cases of PPoma and somatostinoma syndromes, characterised respectively by an overproduction of pancreatic polypeptide and somatostatin. Other tumors express hormones not usually observed in pancreatic islets, such as VIPoma and gastrinoma. In these conditions vasoactive intestinal polypeptide (VIP) and gastrin are secreted respectively. [1, 7]

Besides these rare pathologies, a more relevant clinical problem is related to the underproduction, or loss of efficacy, of insulin secreted by β-cells, that leads to hyperglycemia. Such metabolic disorders are commonly known as Diabetes mellitus. Chronic hyperglycemia in these pathological states may be associated with several and severe complications, affecting organs like hearth, kidneys, eyes, blood vessels, and nerves [10]. In the year 2000, the reported prevalence of diabetes from the World Health Organization

(WHO) was 2.8%, with the projection of 4.4% by 2030 [11]. More recent data highlight an even more dramatic picture, with 1.5 million of deaths directly caused by diabetes in 2012 (WHO) [12], and a reported prevalence of 9% in 2014 (WHO) [13]. Data reported in 2015 from the International Diabetes Federation show moreover that diabetes contributes to the 12% of the global health cost, and projections suggest increasing trends [14]. The American Diabetes Association classifies diabetes into four groups: Type 1 diabetes, Type 2 diabetes, gestational diabetes mellitus and others [10]. Type 1 and Type 2 diabetes represent about $5-10\%$ and 90% of all cases of diabetes respectively.

2.3.1 Type 1 Diabetes

Type 1 Diabetes (T1D), also called insulin-dependent or juvenile-onset diabetes, is a polygenic disease characterised by an autoimmune destruction of β-cells. About the 50% of genetic susceptibility is explained by the HLA-DRB1 and HLA-DQB1 class II loci, on chromosome 6p21, coding for surface proteins of the antigen-presenting cells (APCs) [15–17]. It is likely that in T1D such proteins lead to an efficient presentation of β-cell autoantigens to T-helper cells, thus stimulating the activation of cytotoxic T cells [16]. Other susceptibility genes are represented by the insulin gene (INS), on chromosome 11p15, and by the CTLA4 (coding for T cells surface proteins) on chromosome 2q33 [18, 19]. In these cases, altered expressions of INS or CTLA4 could affect insulin tolerance and T cells self-reactivity respectively. Several infiltrating cells have been observed in T1D human islets, such as APCs, macrophages, helper and cytotoxic T cells, B lymphocytes (not present in some cases) and natural killer cells. Destruction of β-cells is thus mediated by both cytotoxic T cells, via the Fas/Fas ligand pathway, and secreted cytokines, such as interleukin IL-1β, interferon IFN-γ, and tumor necrosis factor TNF-α [16]. Usually, the β-cell mass loss is a slow process, occurring over years, and leading to a $70-80\%$ reduction of β-cells [20]. Such loss leads to low insulin levels in the blood, to a not balanced effect of the glucagon-induced glucose production in the liver, and to fasting hyperglycaemia. In these conditions, there is also an increase in the degradation rate of triglycerides and muscle proteins, with activation of ketogenesis in liver cells [7]. T1D is therapeutically treated with insulin administration and diet.

2.3.2 Type 2 Diabetes

Type 2 Diabetes (T2D) is the most prevalent form of diabetes. Both genetic and environmental factors are involved in the pathogenesis of T2D. For instance, a T2D family history causes a 2/4-fold increased risk to develop glucose intolerance or diabetes [21]. T2D and glucose intolerance are moreover observed in the 88% of monozygotic twins. In

Alessandro Loppini

addition, the PPARγ transcriptor factor, regulating adipogenesis and insulin sensitivity, and genes coding for SUR1 and Kir6.2, subunits involved in β-cell glucose sensing, can affect T2D susceptibility [21]. Also lifestyle and diet habits play a role in T2D insurgence. In this scenario, over nutrition and physical inactivity lead to free fatty acids and triglycerides induced insulin resistance, which in selected individuals is combined to a long-term defection in insulin secretion. This impairment is mainly due to a progressive loss of β-cell mass and functionality, thus leading to hyperglycaemia. Inflammatory conditions of the islet are observed in the process, characterised by mechanisms such as lipotoxicity, glucotoxicity, oxidative stress, endoplasmic reticulum stress, and islet amyloid oligomers formation. Usually, T2D onset is after the age of 40 years, although increasing cases have been observed recently in young people [22]. In some cases, T2D can be controlled with a correct diet and physical exercise, and with drugs such as sulphonylureas, biguanides and insulin therapies otherwise. [7, 16, 21]

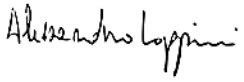

Chapter 3

Mathematical modeling of excitable cells

Cells in living organisms usually present electrical potentials across their cytoplasmic membrane. This occurs mainly because of the different ions concentrations of extracellular and intracellular solutions, due to passive and active properties of the cell membrane. In addition, a specific class of cells, named "excitable cells", are able to modify their membrane potential in response to external stimuli in order to accomplish specific functions, like hormone release, signals transmission, muscle contraction etc. Usually, several thousands of ion channels, regulating charges flows across the membrane, in combination with other sub-cellular mechanisms are involved in such phenomena. Hodgkin and Huxley were well aware of this biological evidence when they were studying the propagation of electrical signals in the squid giant axon, and they focused their work on building a mathematical model able to describe cell excitation and electrical signal propagation in nerve fibers. Since this mathematical framework takes into account common properties of excitable cells, a very similar formulation can be adopted to build electrophysiological models of β-cells activity. The aim of this chapter is then to describe the Hodgkin-Huxley formalism, both in the classical deterministic case and when random fluctuation of charges flows due to stochastic gating of ion channels are taken into account.

3.1 Hodgkin-Huxley formalism

A living cell can be viewed as a complex system continuously interacting with the external environment and with other cells. Intracellular and extracellular spaces are filled with aqueous solutions of salts, that dissociate into anions and cations. The ions more

commonly found in this environment are Na^+, K^+, Ca^{2+}, Cl^-. The cytoplasmic membrane is the sole biological complex that provides a barrier between the intracellular space and the outer world, blocking free inflow and outflow of materials and water. It is formed by a phospholipid (water-insoluble) bilayer with a thickness of about $7.5\,nm$ that is selectively permeable to ions and molecules. Water-filled pores with diameters of about $0.8\,nm$, protein lined pores, and transmembrane proteins are dispersed on and across the membrane. Active and passive mechanisms regulate materials flows through the lipid bilayer. Active transport processes are characterised by an energy cost while passive ones are usually driven by favorable electrochemical gradients. Osmosis, simple diffusion of lipid-soluble molecules, carrier-mediated diffusion of large molecules, as well as ions flow through specific channels are an example of passive transport, while exchange pumps are an example of active transport. In the following a mathematical formulation of the electro-diffusion process is given in order to obtain a useful relation quantifying the electrical potential across the membrane due to different ions concentrations. Finally, the equivalent electrical circuit of the cell membrane, and the Hodgkin-Huxley type modelling of ion currents are shown.

3.1.1 Diffusion across the membrane: the Goldman-Hodgkin-Katz equation

A mathematical description of diffusion can be obtained from a mass balance of the diffusing chemical both with a local or with a global formulation. Using a global formulation, and considering a macroscopic region Ω, the mass balance equation can be written as:

$$\frac{d}{dt}\int_\Omega c\,dV = \int_\Omega f\,dV - \int_{\delta\Omega} \mathbf{J}\cdot\mathbf{n}\,dA\,,$$

where c is the concentration of the diffusing chemical, f is the production rate per unit volume of the chemical (consumption terms could be taken into account as well), $\delta\Omega$ is the surface boundary of Ω, $\mathbf{J}$ is the flux per unit area across the boundary, and $\mathbf{n}$ is the outward unit normal to the boundary $\delta\Omega$. Thanks to the divergence theorem, the flux term can be rewritten as:

$$\int_{\delta\Omega} \mathbf{J}\cdot\mathbf{n}\,dA = \int_\Omega \nabla\cdot\mathbf{J}\,dV\,;$$

thus, considering a fixed volume, it is possible to write the mass balance equation in a local form:

$$\frac{\partial c}{\partial t} = f - \nabla\cdot\mathbf{J}\,.$$

By considering the well-known Fick's Law, the flux of the diffusing chemical is:

$$\mathrm{J} = -D\,\nabla c\,,$$

Alessandro Loppini

where D is the diffusion coefficient. In the case of a spherical solute molecule large compared to the solvent molecules, D is directly proportional to the temperature and inversely proportional to the radius of the solute molecule and to the coefficient of viscosity of the solute. The substitution of this constitutive law into the mass balance equation, leads to the classic reaction-diffusion equation:

$$\frac{\partial c}{\partial t} = f + \nabla \cdot (D \nabla c) \,.$$

Usually, both concentration gradients and electrical potential gradients (i.e. electrical fields) contribute to the chemical flux. To embed this evidence in the mass balance, the Nernst-Planck equation can be used, thus defining the total flow of a chemical as:

$$\mathrm{J} = -D \left(\nabla c + \frac{zF}{RT} c \nabla \phi\right) ,$$

where z is the valence of the ion, F is the Faraday constant, R is the universal gas constant, and T is the absolute temperature. In the one-dimensional case, and by imposing the condition of zero flux, the previous equation can be written as:

$$\frac{dc}{dx} + \frac{zF}{RT} c \frac{d\phi}{dx} = 0 \,;$$

bringing the second term on the right hand side of the equation and dividing by c:

$$\frac{1}{c}\frac{dc}{dx} = -\frac{zF}{RT}\frac{d\phi}{dx} \,.$$

It can be assumed that this condition holds across the cell membrane when there is no flux of the chemical. Integrating this equation between the position of the interior side of the membrane x_i and the position of the external side x_e leads to:

$$\int_{x_i}^{x_e} \frac{1}{c}\frac{dc}{dx}\, dx = -\int_{x_i}^{x_e} \frac{zF}{RT}\frac{d\phi}{dx}\, dx \,,$$

that is

$$\int_{c_i}^{c_e} \frac{dc}{c} = \int_{\phi_e}^{\phi_i} \frac{zF}{RT} d\phi \,.$$

The solution can be easily obtained:

$$\ln\left(\frac{c_e}{c_i}\right) = \frac{zF}{RT}(\phi_i - \phi_e) \,.$$

Therefore, considering that $V = \phi_i - \phi_e$ is the potential difference across the membrane, the famous Nernst equation can be recovered:

$$V = \frac{RT}{zF} \ln\left(\frac{c_e}{c_i}\right) .$$

Alessandro Loppini

In general, the electric field depends on the local charge density and is not constant across the membrane. Although, in a first approximation a constant field through the thickness L of the membrane can be supposed, obtaining $\frac{d\phi}{dx} = -\frac{V}{L}$. Considering the steady state and substituting this relation into the Nernst-Plank equation, a single ODE for the chemical concentration is obtained:

$$\frac{dc}{dx} - \frac{zFV}{RTL}c + \frac{J}{D} = 0\,.$$

Integrating this equation between 0 and L, i.e. along the spatial thickness of the membrane, considering the boundary conditions $c(0) = c_i$ and $c(L) = c_e$, leads to:

$$J = P\frac{zFV}{RT}\frac{c_i - c_e\exp(-\frac{zFV}{RT})}{1-\exp(-\frac{zFV}{RT})}\,;$$

where $P = D/L$ is the permeability of the membrane to the chemical. Multiplying the flux by zF, the Glodman-Hodgkin-Katz (GHK) current equation can be obtained. When the diffusive and the electrical terms of the flow are balanced, the total flux is zero, and the expression of the Nernst potential can be recovered. When dealing with several ion species, it is useful to define the potential at which the total electrical current is zero, that is called the GHK potential. Taking into account ions with valence $z = \pm 1$, and a zero net current, it is possible to write

$$\sum_{j,z=1} P_j\frac{c_i^j - c_e^j\exp(-\frac{FV}{RT})}{1-\exp(-\frac{FV}{RT})} + \sum_{j,z=-1} P_j\frac{c_i^j - c_e^j\exp(\frac{FV}{RT})}{1-\exp(\frac{FV}{RT})} = 0\,,$$

whose solution leads to an expression for the GHK potential:

$$V = -\frac{RT}{F}\ln\left(\frac{\sum_{j,z=1} P_j c_i^j + \sum_{j,z=-1} P_j c_e^j}{\sum_{j,z=1} P_j c_e^j + \sum_{j,z=-1} P_j c_i^j}\right)\,,$$

this physical quantity is commonly known as cell membrane resting potential. [23]

3.1.2 Cell membrane equivalent circuit

Cell membrane bilayer causes a charges separation since it is not fully permeable to ions. Ion channels within the membrane instead provide specific pathways through which ions can flow. Such evidence can be used to build an equivalent electrical circuit that grasps cell membrane behaviour. Specifically, charges separation property can be easily modelled with a capacitor, current flow through channels can be modelled by resistive currents, and electrochemical gradients driving the ion fluxes can be viewed as voltage generators. In general, ion currents can be both linear and nonlinear functions

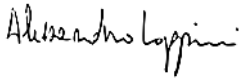

of the transmembrane potential, and could also depend on the concentration of some other chemical. As a first step, it's useful to consider the membrane model taking into account only its passive properties, i.e. passive channels, as it is represented in Fig. 3.1(a).

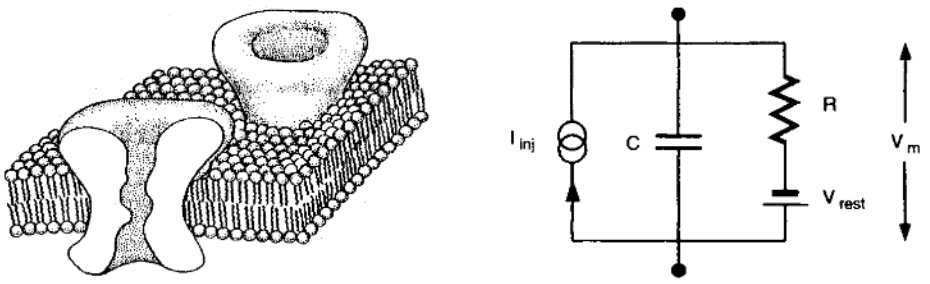

(a) (b)

FIGURE 3.1: (a) Passive ion channels spanning cell membrane bilayer. (b) Equivalent membrane circuit considering passive channels and an applied external current, where R is channels resistance, V_{rest} the resting cell potential, V_m the transmembrane voltage and I_{inj} is the injected external current. From ref. [24].

In this case, the equivalent circuit of the cell membrane (Fig. 3.1(b)) is the standard RC passive parallel circuit, where I_{inj} is an applied external current (called I_e in the following), and V_{rest} (V_r in the following) is the cell resting potential, i.e. the transmembrane potential value at which the net current is zero, considering no applied external stimuli.

An equation that describes the dynamics of this circuit can be easily derived by applying Kirchhoff's law to one node:

$$C_m \frac{dV}{dt} + \frac{V - V_r}{R_m} = I_e \,.$$

Multiplying by R_m and substituting $\tau = R_m C_m$ leads to

$$\tau \frac{dV}{dt} = -V + V_r + R_m I_e \,,$$

which, by considering the initial condition $V(0) = V_r$, has the solution:

$$V(t) = V_r + R_m I_e (1 - e^{-t/\tau}) \,.$$

To note that as $t \to \infty$, $V(t) \to V_\infty = V_r + R_m I_e$. As it can be seen, this is the standard time course of the voltage during the capacitor charging. If the applied current is switched off at time $t = t_o$, and by assuming $V(t_o) = V_\infty$, the standard discharge time course is recovered:

$$V(t) = V_r + R_m I_e \, e^{-(t-t_o)/\tau}$$

Alessandro Loppini

These two expressions summarise the response of a passive membrane to an applied current step. It's also useful to recall that the *RC* parallel circuit acts as a low-pass filter for time-varying inputs with a certain frequency, and it is possible to figure out this aspect easily in the Fourier space. Some cortical cells show exactly this kind of behaviour and exert a filtering effect at the high frequencies. [24]

Usually, cell's membrane does not contain only passive elements but is rich in active ion channels that show a variable resistance depending on environmental conditions. By taking this into account, the membrane circuit has to be modified considering active ion currents, as it is shown in Fig. 3.2.

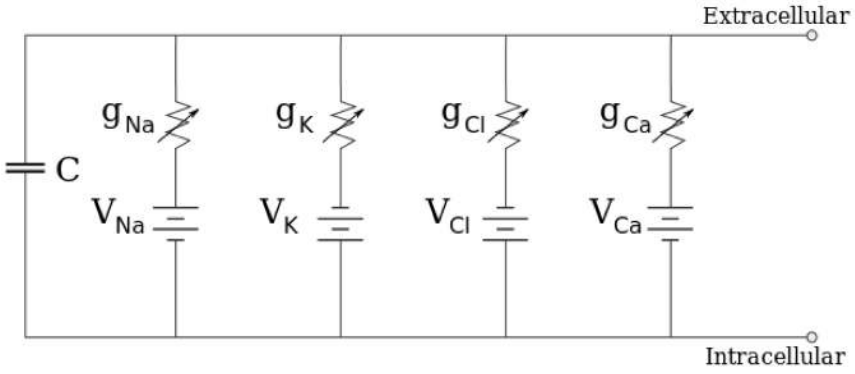

FIGURE 3.2: Equivalent membrane circuit considering active ion channels, where C is the membrane capacitance, and V_x and g_x are respectively the Nernst potential and the variable conductance for the ion x.

The arrow over the resistor symbolises a variable conductance that usually is a function of transmembrane potential and time. In this case it is not considered the applied external current. Applying Kirchhoff's law to one node of the circuit, and considering no net buildup of charges inside and outside the cell, it is possible to write:

$$C_m \frac{dV}{dt} + I_{ion} = 0\,,$$

where C_m is the capacitance of the membrane, and I_{ion} is the sum of all the ionic currents. Different models can be used to specify the ion current form, such as the linear model and the GHK nonlinear model. In the classic membrane circuit formulation, each single ionic current (as it can be deducted from the circuit), is expressed as the product of the ion channel conductance and the difference between the transmembrane voltage and the ion Nernst potential, i.e. $I_x = g_x(V - V_x)$.

As anticipated before, usually the conductance is a function of the voltage, whose macroscopic value is the result of the opening and closing events of an entire population of independent channels. Instead, constant conductance values are usually adopted to

model leakage passive factors. To note that considering this expression for the ion currents, and the steady state condition in membrane circuit equation, it is possible to derive a formulation of the membrane potential for the linear model analogous to the GHK potential:

$$V = \frac{\sum_x g_x V_x}{\sum_x g_x} .$$

[23, 25]

3.1.3 Membrane channel conductances

Taking into account the previous section, a quite general formulation of the membrane channel conductance is $g = G(V(t), t)$. In their fundamental work Hodgkin and Huxley, with the use of voltage clamp experiments, focused on the modelling of the sodium and potassium conductances involved in the signal propagation taking place in the squid giant axon [26]. They experimentally observed the time course of ion conductances and their variations respect to the applied voltage stimuli. In summary, conductances follow a general dynamics

$$\frac{dg}{dt} = f(v, t) ,$$

where v is the difference between the transmembrane and the resting potentials $v = V - V_r$. Experimental measures showed that the K^+ conductance followed a sigmoidal increase in response to an applied constant voltage and an exponential decrease when the stimulus was switched off.

Moreover, time constants and steady state plateau values were strictly dependent on the applied voltage amplitude (see Fig. 3.3(a)). Focusing on these observations, such time course can be well represented by the power of a variable n, i.e. gating variable, following a first order kinetics. Thus, they rewrote the potassium conductance as $g_K = \bar{g}_K n^4$, where $\bar{g}_K$ is the whole potassium conductance, and n takes values in the range $[0, 1]$ and obeys the following dynamics:

$$\frac{dn}{dt} = \frac{n_\infty(v) - n}{\tau_n(v)} .$$

Solutions of this equation, after the switching-on and switching-off of the stimulus, are respectively

$$n(t) = n_\infty(v) \left[1 - e^{(-t/\tau_n(v))}\right] , \quad n(t) = n_\infty(v) e^{(-t/\tau_n(v))} ,$$

whose fourth power leads to the desired sigmoidal increase and exponential decrease. Experimental measures of the Na^+ conductance instead showed a more complex behaviour in response to applied voltage steps, with an initial increase followed by a decay.

Alessandro Loppini

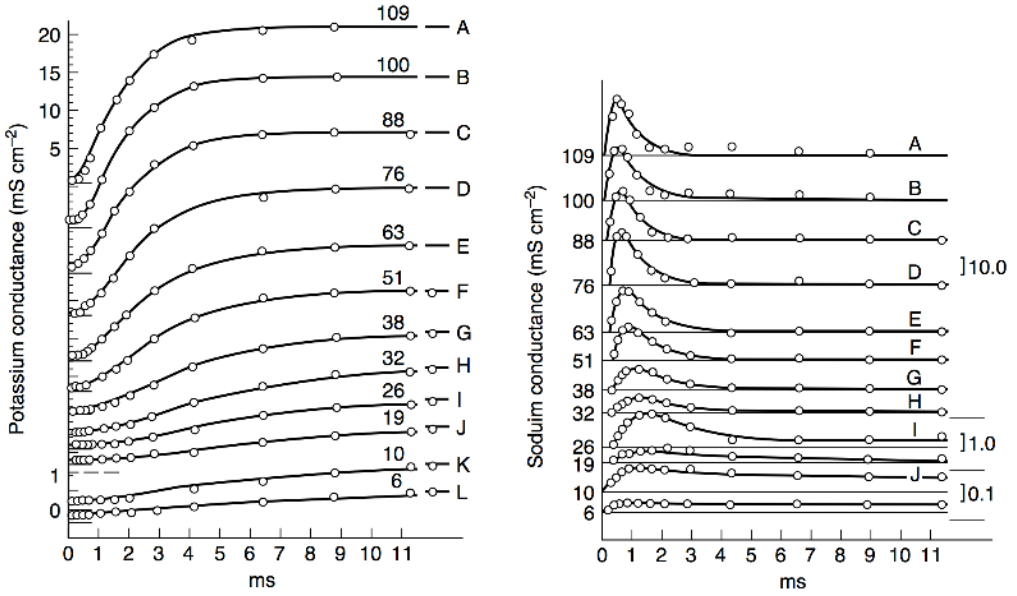

FIGURE 3.3: (a) Potassium conductance time course in response of increasing voltage steps. (b) Sodium conductance time course in response of increasing voltage steps. From ref. [26].

Peak value, steady state value, and time constants of the initial activation and the following inactivation showed a dependence on the stimuli amplitude also in this case, as it can be seen in Fig. 3.3(b). Hodgkin and Huxley modelled this type of behaviour with the use of two gating variables m (activation process) an h (inactivation process), both obeying a first order kinetics like the one used for the potassium activation variable n:

$$\frac{dm}{dt} = \frac{m_\infty(v) - m}{\tau_m(v)}, \quad \frac{dh}{dt} = \frac{h_\infty(v) - h}{\tau_h(v)}.$$

On this basis, sodium conductance was rewritten as $g_{Na} = \bar{g}_{Na} m^3 h$, where the third power was set for a data fitting purpose.

Steady-state activation and inactivation curves $n_\infty(v), m_\infty(v), h_\infty(v)$, and time constants $\tau_n(v), \tau_m(v), \tau_h(v)$ were calculated from the experimental data. In Fig. 3.4 the computed functions are reported.

Steady-state activation is a sigmoidal increasing function of the potential while steady-state inactivation is a decreasing sigmoidal function, and in general, this is valid for most of the Hodgkin-Huxley type electrophysiological models.

Alessandro Loppini

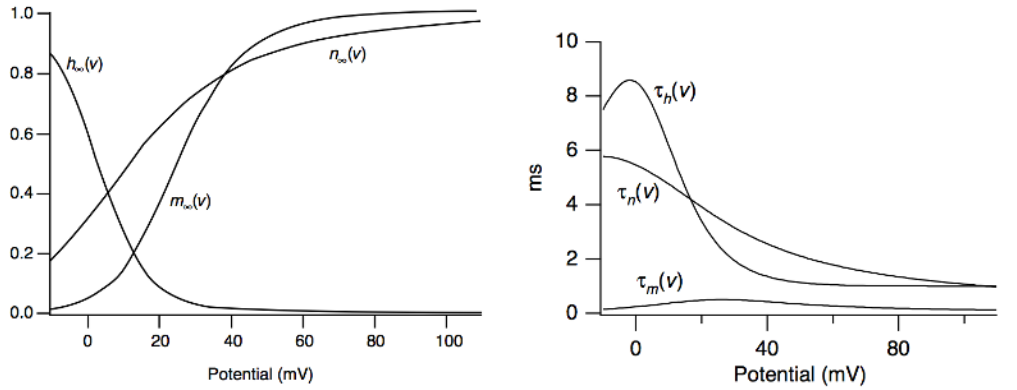

FIGURE 3.4: (a) Steady-state activation and inactivation curves as functions of the voltage. (b) Time constants as functions of the voltage. From ref. [23].

Another formulation of the gating variable dynamics is usually derived by considering a trivial reaction scheme, i.e. taking into account the variable m:

$$(1-m) \underset{\beta_m}{\overset{\alpha_m}{\rightleftharpoons}} m \ ,$$

where $(1-m)$ and m are the proportions of particles in a "closed" and in an "open" state respectively, and the transition probabilities between states are functions of the voltage. Such scheme can be mathematically described by a first order differential equation:

$$\frac{dm}{dt} = \alpha_m(v)(1-m) - \beta_m(v)m \, .$$

This description is equivalent to the one shown before by considering:

$$m_\infty(v) = \frac{\alpha_m(v)}{\alpha_m(v)+\beta_m(v)} \, , \quad \tau_m(v) = \frac{1}{\alpha_m(v)+\beta_m(v)}$$

[23, 25]

Most of the text books report the Hodgkin-Huxley model specifying the α and β functions instead of the steady-state and time constant functions. About the values of the powers taken into account for the activation and inactivation variables, it's interesting to note that there is also another physical reason to the specific choices, which is the number of activating or inactivating domains that form a single ion channel. In conclusion, the membrane potential dynamical equation coupled with the gating variables dynamics form a closed system of ODE, defining the final Hodgkin-Huxley model of the squid giant axon. Such framework can be used to model several types of excitable

cells, like cardiac cells, neurons and β-cells. Generally, in such Hodgkin-Huxley based models of excitable cells, cell membrane conductance for the ion channel x is usually expressed as $g_x = \bar{g}_x m_x^p h_x^q$. There can be no inactivation, or instantaneous activation or inactivation, or independence of time constants upon the voltage; such experimental evidence is taken into account to fine-tune model parameters. To note that most of the times, steady-state activation and inactivation, and time constant sigmoidal functions are expressed via the use of Boltzmann or hyperbolic tangent functions.

3.2 Channel gating as a stochastic process

The development of the patch clamp techniques in the second half of the 20th century led to new insights on ion currents dynamics. Such techniques allow monitoring current flow in small pools or even single ion channels, analysing small patch of the cell membrane. Experimental studies based on this approach pointed out a stochastic behaviour of the single channel dynamics, characterised by a random sequence of opening and closing events. The analysis of the average behaviour of a large number of single channel recordings showed however that a deterministic macroscopic dynamics emerges from an ensemble of such a microscopic stochastic process. In Fig. 3.5 a representation of such behaviour is given.

Because of this, a deterministic representation of ion currents like the one used by Hodgkin and Huxley is most of the times in agreement with the recorded whole cell data, i.e. when large pools of ion channels are taken into account. However, it fails to give a good representation of the phenomena when noise effects are not well averaged and when they can substantially alter the emergent macroscopic behaviour. In these cases, the intrinsic stochastic nature of single channels dynamics has to be considered. There are several methods to model this biological noise, among which the Markov approach and the Langevin formulation, both discussed in the following.

3.2.1 Markov approach

A Markov process is a very important class of stochastic processes, in which the state of the system at time t it's a stochastic variable that depends only on the state of the system at time $t-1$, and can be probabilistically predicted from that. Such a process is usually called "memoryless" process. In this context channel gating can be viewed as a continuous-time Markov process where the system's state takes values on a discrete set (open states, closed states, or inactivated states). It's useful to show this approach for an ion channel that obeys a first order kinetic, like the one used to describe the

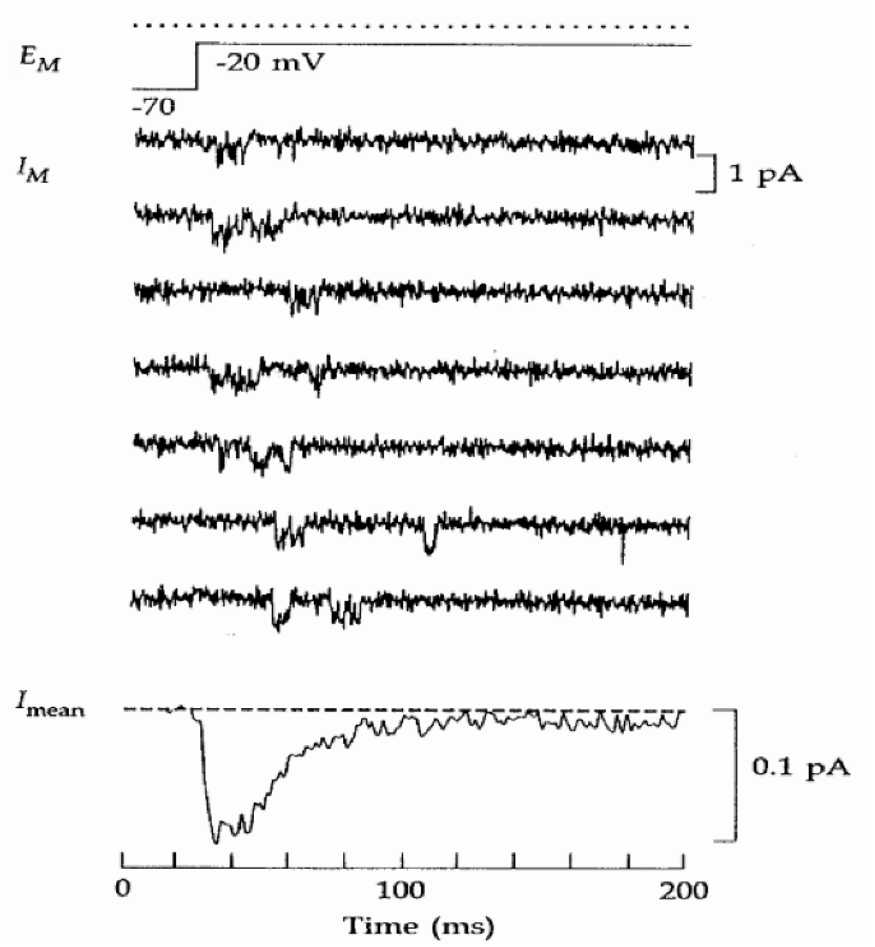

FIGURE 3.5: Single channel currents from patch clamp recordings (top), and average current from several hundreds of channels (bottom). From ref. [25].

activating and inactivating particles in the previous section. The channel can be in an open or closed state, i.e. $S \in \{C, O\}$, and can "jump" from one state to the other with probabilities $k^{+/-}$:

$$C \underset{k^-}{\overset{k^+}{\rightleftharpoons}} O \ .$$

Since it's a stochastic process, the interest is to know the probability that the channel is in a certain state at the time t, that is $P_i(t) = \text{Prob}(S = i, t)$. Assuming that the channel is in the closed state, the probability to make a transition to the open state during a time interval Δt is equal to $k^+\Delta t$, while the probability that an open channel makes a transition to the closed state is $k^-\Delta t$. Multiplying these quantities by $P_c(t)$ and $P_o(t)$ respectively, an expression for the actual transition probabilities it's obtained. Taking this into account, is possible to express the probability that the channel is in an open (or closed) state at times $t + \Delta t$, given the probability that is actually open (or

closed) at time t:

$$P_o(t+\Delta t) = P_o(t) + P_c(t)k^+\Delta t - P_o(t)k^-\Delta t\,,.$$

Moreover, since the total probability must be conserved:

$$P_c(t) + P_o(t) = 1\ .$$

Substituting and taking the limit $\Delta t \to \infty$:

$$\frac{dP_o(t)}{dt} = k^+(1-P_o(t)) - k^-P_o(t)\,.$$

This equation has the same form of the one adopted for the description of large ensembles of activating and inactivating particles in the Hodgkin-Huxley formulation, and can be used to compute the open probability dynamics of the channel.

Alternatively, it is possible to calculate the evolution of the probabilities based on a matrix formulation. Specifically, given the two-state channel and the transition probabilities between states described above, it's possible to define a "transition probability matrix" where the element ij is the transition probability from state j to state i:

$$\begin{aligned} Q &= \begin{bmatrix} \text{Prob}(S=C, t+\Delta t|S=C,t) & \text{Prob}(S=C,t+\Delta t|S=O,t) \\ \text{Prob}(S=O,t+\Delta t|S=C,t) & \text{Prob}(S=O,t+\Delta t|S=O,t) \end{bmatrix} \\ &= \begin{bmatrix} 1-k^+\Delta t & k^-\Delta t \\ k^+\Delta t & 1-k^-\Delta t \end{bmatrix}. \end{aligned}$$

All columns of Q sum to 1 because of probability conservation. Introducing a vectorial form for the channel state, $\vec{P}(t) = [P_c(t)\,P_o(t)]^T$, the channel state probability at time $t+\Delta t$ is computed via matrix multiplication:

$$\vec{P}(t+\Delta t) = Q\vec{P}(t)\,.$$

Applying iteratively the previous equation leads to an expression for the evolution of the probabilities generalised on an arbitrary number m of steps:

$$\vec{P}(t+m\Delta t) = Q^m\vec{P}(t)\,.$$

Alessandro Loppini

A useful measure that can be calculated for such a stochastic process is the dwell time, that is the average time spent by the channel in a closed or open state. For instance, considering a closed channel at time t, the probability that it remains closed at time $t + \Delta t$ is $1 - k^+\Delta t$. From this, the probability that the channel is still close after a number m of steps is:

$$\text{Prob}(C, t + m\Delta t|C, t) = (1 - k^+\Delta t)^m \,.$$

Substituting $\tau = m\Delta t$ in the previous, and taking the simultaneous limits $\Delta t \to 0$, $n \to \infty$:

$$\text{Prob}(C, [t, t + \tau]|C, t) = \lim_{m\to\infty} \left(1 - \frac{k^+\tau}{m}\right)^m = e^{-k^+\tau} \,.$$

In order to calculate the dwell time for the closed state, a transition to the open state during interval $[t + \tau, t + \tau + d\tau]$ needs to be considered. Since $k^+d\tau$ is the probability for the latter transition, the probability distribution function of the closed time is:

$$\begin{aligned} \text{Prob}(\tau < \tau_c \leq \tau + d\tau) &= \text{Prob}(C, [t, t + \tau]|C, t)\text{Prob}(O, t + \tau + d\tau|C, t + \tau) \\ &= e^{-k^+\tau}k^+d\tau \,. \end{aligned}$$

The average closed time, i.e. the closed dwell time, can thus be easily obtained as

$$\langle\tau_c\rangle = \int_0^\infty \tau e^{-k^+\tau}k^+d\tau = \frac{1}{k^+} \,.$$

A similar expression can be deduced also for the open dwell time:

$$\langle\tau_o\rangle = \frac{1}{k^-} \,,$$

Hence, in a channel with two states i and j, the dwell time for the state i is the inverse of the transition rate from state i to state j. These considerations can be extended to multiple state channels, and analysing experimental dwell times is possible to infer the underlying kinetic scheme of the ion channel.

Since macroscopic currents are the result of the opening and closing of an ensemble of such channels, it is of interest to analyse the behaviour of a large number of Markov

processes like the one described above. Specifically, the interest is to study the statistics of the number of open channels, strictly linked to the observed whole-cell current. The first step is to consider a number N of channels. The probability to find n channels in an open state at time t is $P_o(n,t)$, and since the channels can be only in two states, n open channels imply $N-n$ closed channels:

$$P_o(n,t) = P_c(N-n,t)\,.$$

In a time interval Δt four different events can affect the probability to have n open channels: 1) $n-1$ channels are open, and one closed channel jumps to the open state; 2) $n+1$ channels are open, and one channel closes; 3) n channels are open, and one channel closes; 4) n channels are open, and one closed channel jumps to the open state. Considering that each of the open or closed channel can make the transitions described above, the gain and loss terms are respectively:

i) $k^+(N-n+1)P_o(n-1,t)\Delta t$,

ii) $k^-(n+1)P_o(n+1,t)\Delta t$,

iii) $k^- n P_o(n,t)\Delta t$,

iv) $k^+(N-n)P_o(n,t)\Delta t$.

Such terms can be used to write an equation for the probability to find n open channels at time $t+\Delta t$:

$$\begin{aligned} P_o(n,t+\Delta t) \;=\; & P_o(n,t) + k^+(N-n+1)P_o(n-1,t)\Delta t + k^-(n+1)P_o(n+1,t)\Delta t \\ & -k^- n P_o(n,t)\Delta t - k^+(N-n)P_o(n,t)\Delta t\,. \end{aligned}$$

Taking the limit $\Delta t \to 0$, an ordinary differential equation for $P_o(n,t)$ can be obtained:

$$\frac{dP_o(n,t)}{dt} = K_1 P_o(n-1,t) - K_2 P_o(n,t) + K_3 P_o(n+1,t)\,,$$

with $K_1 = k^+(N-n+1)$, $K_2 = k^+(N-n) + k^- n$, and $K_3 = k^-(n+1)$. Such set of $N+1$ equations, one for each n with $0 \le n \le N$, is called "master equation", and its equilibrium solution, i.e the stationary probabilities for each n, is given by the binomial distribution,

$$P_o^\infty(n) = \binom{N}{n} p^n (1-p)^{N-n}\,,$$

Alessandro Loppini

where $p = k^+/(k^+ + k^-)$. Such distribution has a mean value Np, that is the equilibrium value of the number of open channels that can be deduced from the kinetic scheme shown before. In order to study the dynamics of the average number of open channels, both sides of the master equation have to be multiplied by n, summing over the all possible values of open channels:

$$\begin{aligned}\frac{d\left(\sum_{n=0}^{N} nP_o(n,t)\right)}{dt} &= k^+\sum_{n=0}^{N} n(N-n+1)P_o(n-1,t) - k^+\sum_{n=0}^{N} n(N-n)P_o(n,t) \\ &\quad + k^-\sum_{n=0}^{N} n(n+1)P_o(n+1,t) - k^-\sum_{n=0}^{N} n^2 P_o(n,t)\,,\end{aligned}$$

To write this equation in terms of average open and closed channels is convenient to analyse separately the right-hand side (rhs). Considering the first two terms of the rhs:

$$\begin{aligned}& k^+\sum_{n=0}^{N} n(N-n+1)P_o(n-1,t) - k^+\sum_{n=0}^{N} n(N-n)P_o(n,t) = \\ =\ & k^+\sum_{n=-1}^{N-1} (n+1)(N-n)P_o(n,t) - k^+\sum_{n=0}^{N} n(N-n)P_o(n,t) = \\ =\ & k^+\sum_{n=-1}^{N-1} n(N-n)P_o(n,t) - k^+\sum_{n=0}^{N} n(N-n)P_o(n,t) + k^+\sum_{n=-1}^{N-1} (N-n)P_o(n,t) = \\ =\ & k^+\sum_{n=0}^{N} n(N-n)P_o(n,t) - k^+\sum_{n=0}^{N} n(N-n)P_o(n,t) + k^+\sum_{n=0}^{N} (N-n)P_o(n,t) = \\ =\ & k^+\sum_{n=0}^{N} (N-n)P_o(n,t) = k^+\sum_{n=0}^{N} (N-n)P_c(N-n,t) = k^+\langle N_c\rangle\,,\end{aligned}$$

where has been used the mean value definition $\langle N_c\rangle = \sum_{n=0}^{N}(N-n)P_c(N-n,t)$. Similarly for the last two terms:

$$k^-\sum_{n=0}^{N} n(n+1)P_o(n+1,t) - k^-\sum_{n=0}^{N} n^2 P_o(n,t) = -k^-\langle N_o\rangle\,,$$

Substituting these expressions into the original equation finally leads to:

Alessandro Loppini

$$\begin{aligned}\frac{d\langle N_o\rangle}{dt} &= k^+\langle N_c\rangle - k^-\langle N_o\rangle \\ &= k^+\left(N - \langle N_o\rangle\right) - k^-\langle N_o\rangle\,,\end{aligned}$$

where $\langle N_c\rangle = \sum_{n=0}^{N}(N-n)P_c(N-n,t) = \sum_{n=0}^{N}(N-n)P_o(n,t) = N - \langle N_o\rangle$. Dividing the previous by the total number of channels and considering the mean fraction of open channels $\langle f_o\rangle = \langle N_o\rangle/N$:

$$\frac{d\langle f_o\rangle}{dt} = k^+\left(1 - \langle f_o\rangle\right) - k^-\langle f_o\rangle\,,$$

As it can be seen, the dynamics of the average fraction of open channels is equivalent to the one shown for large ensembles of gating particles in the Hodgkin-Huxley formulation. To fully study the statistics of the number open channels, it is useful to obtain an equation also for the variance of the process $\sigma_o^2 = \sum_{n=0}^{N}(n - \langle N_o\rangle)^2 P_o(n,t)$. Differentiating the latter with respect to time gives:

$$\begin{aligned}\frac{d\sigma_o^2}{dt} &= \sum_{n=0}^{N}\left[-2(n-\langle N_o\rangle)\frac{d\langle N_o\rangle}{dt}P_o(n,t) + (n-\langle N_o\rangle)^2\frac{dP_o(n,t)}{dt}\right] \\ &= \sum_{n=0}^{N}(n-\langle N_o\rangle)^2\frac{dP_o(n,t)}{dt}\,.\end{aligned}$$

Thus, to obtain an ODE for the variance, it is possible to multiply the rhs of the master equation by $(n-\langle N_o\rangle)^2$, summing over all possible values of open channels, in line with the method adopted for the mean value of open channels. Using also the same kind of algebra, it can be shown that the differential equation describing the dynamics of the variance is:

$$\frac{d\sigma_o^2}{dt} = -2(k^+ + k^-)\sigma_o^2 + k^+\left(N - \langle N_o\rangle\right) + k^-\langle N_o\rangle\,.$$

Equilibrium values of the average number of open channel and the variance can be obtained by computing the steady state solutions of the two ODE described above. These are respectively $\langle N_o\rangle^\infty = Nk^+/(k^+ + k^-) = Np$, and $(\sigma_o^2)^\infty = Nk^+k^-/(k^+ + k^-)^2 = Np(1-p)$, that are equal to mean value and variance of the binomial distribution obtained as equilibrium solution of the master equation. Such quantities are related to the equilibrium average value and variance of the macroscopic cell current, whose

analysis of experimental measurements can be used to estimate the number of channel for a specific ion. [25]

3.2.2 Langevin formulation

In some cases, the use of the Markov approach to describe large ensembles of channels can be impractical because each of the ion channels has to be modelled by an independent stochastic process, or a single Markov process with a huge number of states has to be adopted. In such situations, a single stochastic differential equation is used to take into account intrinsic noise caused by channel gating. Such equation is called Langevin equation and was originally used to describe the Brownian motion of particles, subjected to a deterministic friction force plus random fluctuations, both coming from the collisions of many particles in the system. The general form of this equation can be written as:

$$\frac{dx}{dt} = f(x(t)) + \eta(t)\,.$$

where $\eta(t)$ is the random fluctuating term superimposed to the deterministic dynamics, identified as a white noise process. Usually, the noise term is defined by means of a Wiener process $W(t)$. Such process is a special case of continuous-time stochastic processes, whose realisations are normally distributed, with zero mean and variance proportional to time t:

$$\begin{aligned} \langle W \rangle &= 0 \\ \sigma_W^2 &= \langle (W - \langle W \rangle)^2 \rangle = \langle W^2 \rangle = t\,. \end{aligned}$$

Since $W(t)$ is a stochastic process, its increments $dW(dt) = W(t+dt) - W(t)$, computed over a time step dt, represent a random variable, normally distributed and with variance proportional to dt, i.e.:

$$dW(dt) = N(0, dt)\,,$$

where $N(0,1)$ denotes a unit normal random variable. Recalling the normal linear transformation theorem $a + bN(0,1) = N(a, b^2)$, the previous can be written as:

$$dW(dt) = N\left(0, dt^2 \frac{1}{dt}\right) = dtN\left(0, \frac{1}{dt}\right)\,.$$

Alessandro Loppini

Dividing by dt, and taking the limit $dt \to 0$:

$$\lim_{dt\to 0} \frac{dW(dt)}{dt} = \lim_{dt\to 0} N\left(0, \frac{1}{dt}\right) = \lim_{dt\to 0} \eta(dt) = \eta(0)\,.$$

To note that, when dt approaches to 0, $dW(dt)$ tends to a random variable with mean and variance equal to 0, while $\eta(dt)$ seems to tend to a random variable with zero mean and infinite variance.

Thus, $\eta(0)$ is called the white noise random variable, and it is related to the Wiener process by the relation:

$$\frac{dW(t)}{dt} = \eta(0)\,.$$

Such expression needs special care, since stochastic processes are not differentiable in the classical sense, and the previous gives an ill-definition of $\eta(0)$. Langevin equation is usually expressed in terms of the white noise stochastic process, that is the sampling at any time t of the random variable $\eta(0)$, i.e. $\eta(t) = \eta(0)$ for any t.

By definition, the white noise process is characterised by zero mean and by the statistical independence of its realisations, thus, it obeys the following statistics, in terms of mean value and autocorrelation function:

$$\begin{aligned} \langle \eta(t) \rangle &= 0 \\ \langle \eta(t)\eta(t') \rangle &= \delta(t-t')\,. \end{aligned}$$

The second equation can be verified by noticing that $cov\{\eta(t), \eta(t')\} = \langle \eta(t)\eta(t') \rangle - \langle \eta(t) \rangle \langle \eta(t') \rangle = \langle \eta(t)\eta(t') \rangle$. Because of statistical independence, this covariance must vanish for $t \neq t'$, thus validating the autocorrelation function written above in this case. In order to see if the relation hold also for $t = t'$, we can write the autocorrelation function as:

$$\begin{aligned} \langle \eta(t)^2 \rangle &= var\left\{\eta(0)\right\} = var\left\{\lim_{dt\to 0} N\left(0, \frac{1}{dt}\right)\right\} \\ &= \lim_{dt\to 0} var\left\{N\left(0, \frac{1}{dt}\right)\right\} = \lim_{dt\to 0} \frac{1}{dt}\,, \end{aligned}$$

where the last limit, in the framework of the Dirac delta function, can be viewed as $\delta(0)$.

With these assumptions, Langevin equation can be used to model the dynamics of a large number of two-state ion channels, like the one described in the previous section.

Alessandro Loppini

By taking into account the two-state channel kinetics, the Langevin dynamics for the open fraction of channels can be written as:

$$\frac{df_o(t)}{dt} = k^+(1 - f_o(t)) - k^- f_o(t) + \eta(t)\,,$$

where $f_o(t) = N_o(t)/N$ is a stochastic variable. Statistics of the noise term needs special care to correctly model the random openings of channels. Specifically, the fluctuation have zero mean, and autocorrelation function defined as:

$$\langle \eta(t)\eta(t') \rangle = \nu\delta(t - t')\,.$$

The scaling factor ν in the previous equation is strictly linked to the transition rates of the kinetics and to the number of ion channels, and for the considered case takes the form:

$$\nu(f_o) = \frac{k^+(1 - f_o(t)) - k^- f_o(t)}{N}$$

Recalling that $f_o^\infty = k^+/(k^+ + k^-) = p$, the equilibrium value of the factor ν is equal to $\nu_\infty = 2k^+k^-/[(k^+ + k^-)N]$. It is useful to recall also, from the master equation analysis shown above, that the equilibrium variance of the number of open channels is equal to $(\sigma_o^2)^\infty = Np(1-p) = Nk^+k^-/(k^+ + k^-)^2$, and that $var\{f_o\} = \langle (f_o - \langle f_o \rangle)^2 \rangle = \langle (N_o - \langle N_o \rangle)^2 \rangle / N^2 = \sigma_o^2/N^2$. Thus, it can be verified that the equilibrium value of ν and the variance of the open fraction of channels are related by the equation:

$$\nu_\infty = \frac{2(\sigma_o^2)^\infty}{\tau}$$

where $\tau = 1/(k^+ + k^-)$. [25, 27]

Although Langevin equation is a powerful method to evolve the stochastic dynamics of large channels populations, in the following a Markov chain approach will be used to model the stochastic gating of specific ion channels in β-cells because of the non-restrictive size of the ion channels pool.

Alessandro Loppini

Chapter 4

β-cell electrophysiology in mouse

4.1 β-cell electrical activity in mouse

Glucose uptake from β-cells evokes a cascade of processes that trigger a characteristic "bursting" electrical activity. In turn, intracellular calcium oscillations generated by this typical pattern are able to drive a pulsatile insulin release. At low glucose concentrations, i.e. $< 3\,mM$, β-cells are silent and show a resting potential $V_r \simeq -70\,mV$. By increasing the glucose level, the cell depolarises in a concentration-dependent manner, and for concentrations ($> 5-7\,mM$) able to reach the threshold potential $V_{th} \simeq 50\,mV$, it exhibits a bursting electrical activity. In Fig. 4.1(a) a typical bursting oscillation recorded from a mouse β-cell is shown; it is characterised by action potentials separated by silent phases, and can be described by slow oscillations with superimposed fast oscillations. Action potentials in a single burst start from a plateau value of about $-40\,mV$ and reach a peak of about $-20\,mV$. Burst duration, i.e. the time spent in the active phase, increases for increasing glucose levels (as it is shown in Fig. 4.1(b)), reaching a continuous bursting response for concentrations above $16\,mM$. [28]

Several ion channels and currents are involved in burst initiation, duration and termination. The most important ones are listed in the following.

4.1.1 K-ATP channels

K-ATP channels are a particular type of potassium channels whose gating is regulated by the intracellular level of ATP and ADP. These channels are formed by four subunits, each of which contains two domains, the high-affinity sulfonylurea receptor SUR1 and the inward rectifier Kir6.2 channel. Sulfonylureas or increased values of the intracellular ATP/ADP ratio lead to the closure of the channel, and to β-cell depolarization. Single

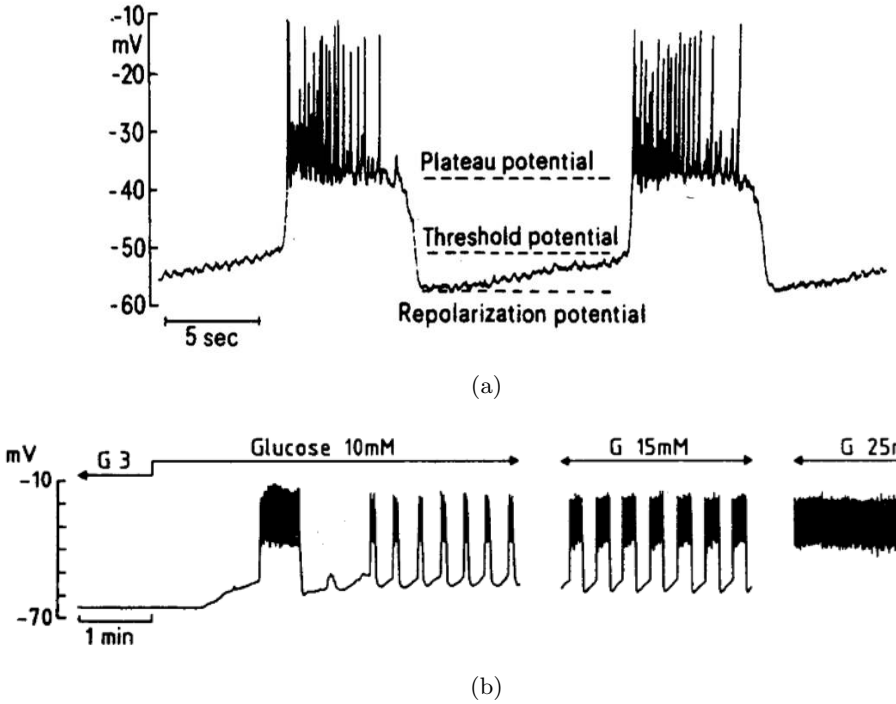

FIGURE 4.1: (a) Bursting oscillation in a mouse β-cell stimulated by a glucose concentration of $10\,mM$. (b) Glucose increasing effect on bursting period and active phase duration, from sub-threshold stimulation up to continuous bursting response. From ref. [28].

channel conductance, measured in symmetrical K^+ concentration of $140\,mM$, is in the range $50 - 80\,pS$. After washout of ATP, measured whole-cell K-ATP conductance is in the range $10 - 20\,nS$, with a single channel conductance of about $20\,pS$ in the same conditions.

The channel is highly selective for K^+ with a low value of Na^+ relative permeability ($P_{Na}/P_K = 0.007$ in rats). Kinetics of the K-ATP channel analysed for inward currents at negative membrane potentials with the use of high extracellular potassium concentration, show channel opening events clustered in bursts. ATP is able to reduce the burst length and increase burst separation, i.e. open probability for the channel is reduced by the nucleotide that acts as an inhibitor (see Fig. 4.2). Such inhibition allows to reach action potential threshold by K^+ cations accumulation so that K-ATP channels have a central role in burst initiation. Mutations in genes coding for SUR1 and Kir6.2 are associated with both hyperinsulinemia and type 2 diabetes. [28–30]

4.1.2 Voltage-gated Ca^{2+} channels

Action potential upstroke is initiated by the opening of voltage-dependent calcium channels (VDCCs) that allows calcium influx. VDCCs in mouse are mainly L-type calcium

Alessandro Loppini

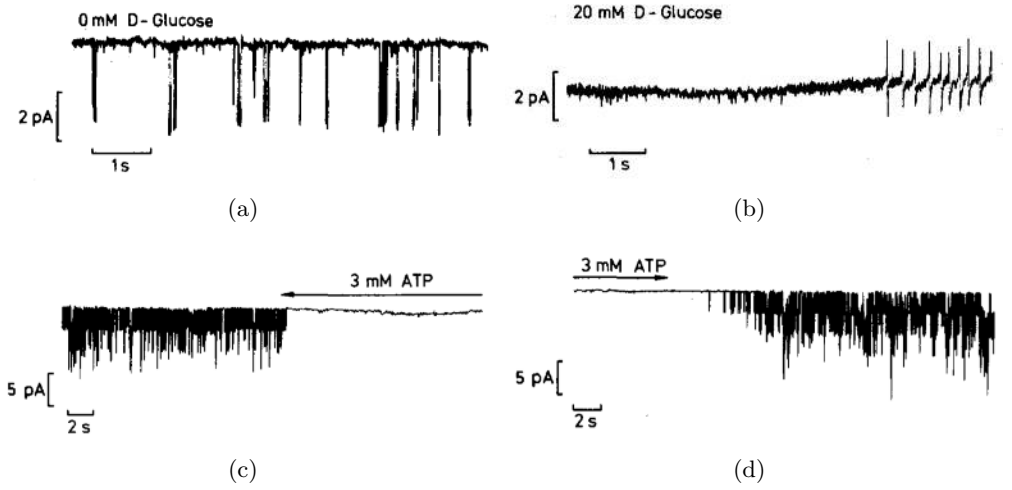

FIGURE 4.2: (a)-(b) Glucose effect on single K-ATP channel current, from a patched mouse β-cell. (c)-(d) ATP effect on single K-ATP channel current, from an isolated membrane patch (inside-out configuration). All data are recorded at the resting potential of $\simeq -70mV$. From ref. [28].

channels, that are multimers formed by five different subunits: α_1, α_2, β, γ and δ. Among these, α_1 subunit can bind dihydropyridines, modulating calcium channels, and sense voltage change. These channels are crucial for insulin secretion and their blocking suppresses hormone release. L-type current is observed for depolarizations from a holding potential between -70 and $-50\,mV$ to potentials greater than $-40mV$, with a current peak in the range $-20-0\,mV$. Single channel conductance in physiological calcium concentrations ($2.6\,mM$) is $\simeq 2\,pS$. Channel's opening times are fitted by a single exponential with $\tau = 0.4\,ms$; closing times are instead fitted by two exponentials, with characteristic times equal to $2\,ms$ and $10-30\,ms$. In addition, inward L-type currents measured between -50 and $+50\,mV$ last for 200-300 ms, indicating slow inactivation. L-type channels are modulated by glucose, and an increase in concentration from 0 to $20\,mM$ evokes a two-fold increase in the current peak, in physiological ion concentrations. Moreover, L-type channels can also be modulated by cAMP-dependent protein kinase that reduces the rate of inactivation. Another type of voltage-sensitive calcium channel found in rats, is the T-type channel. This channel is activated at $-50\,mV$, and show a peak current at -10 to $0\,mV$. Inactivation is faster compared with the L-type, and it lasts from 10 to $100\,ms$. Single channel conductance is $\simeq 8\,pS$ in $100\,mM$ Ba^{2+} solution (L-type channels show a conductance of $\simeq 20\,pS$ in same conditions). [28, 29]

In Figure 4.3 T-type and L-type currents, obtained from a set patch clamp recordings in a rat β-cell, are shown.

Alessandro Loppini

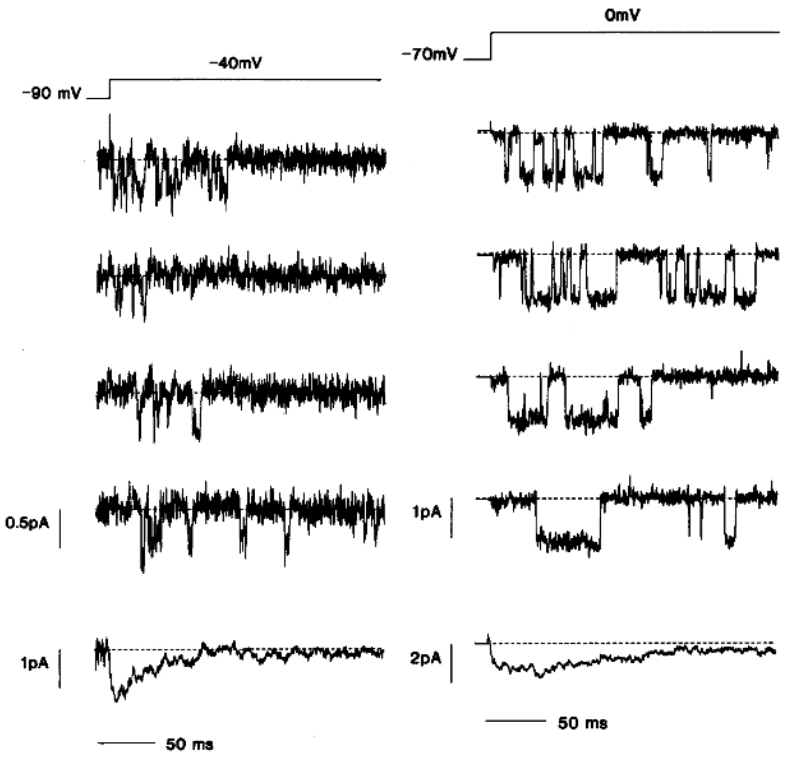

FIGURE 4.3: Patch clamp recordings of T-type (a) and L-type (b) calcium currents in rat β-cell. Bottom sweeps represent the mean current obtained by averaging $\simeq$ 100 recordings. From ref. [28].

4.1.3 Voltage-gated K^+ channels

These potassium channels are usually called delayed rectifying K^+ channels (K-DR). About the $80-90\%$ of the whole-cell delayed outward current flows through them. K-DR currents are elicited at potentials greater than $-30\,mV$. Activation is slow and can be described by a n^2 type kinetics, with a time constant of $2\,ms$ at $0\,mV$. Inactivation also is a slow process, with a time constant of $5\,s$ at $20\,mV$. Single channel recordings show conductance values of $8.5\,pS$ between -40 and $+50\,mV$ under physiological condition. K-DR current is not modulated by sulfonylureas but is inhibited by TEA in a concentration-dependent manner. [28]

4.1.4 K-Ca channels

Calcium-activated potassium channels are K^+ channels whose conductance is regulated by calcium concentration. Two kinds of K-Ca channels have been found in β-cells, low conductance SK channels, and large conductance BK channels. BK channels are thought to have a role in cell repolarization and show a conductance of $200-250\,pS$ in $150mM$

KCl solution. This value lowers to $110 - 155\,pS$ in physiological ion concentrations. Current recordings show a fast activation and an inactivation lasting about $150\,ms$. [28]

As it can be seen in Fig. 4.4, K-Ca channels show both calcium-dependent and voltage-dependent modulation, with increasing open probabilities for increasing concentration of calcium and values of the holding potential.

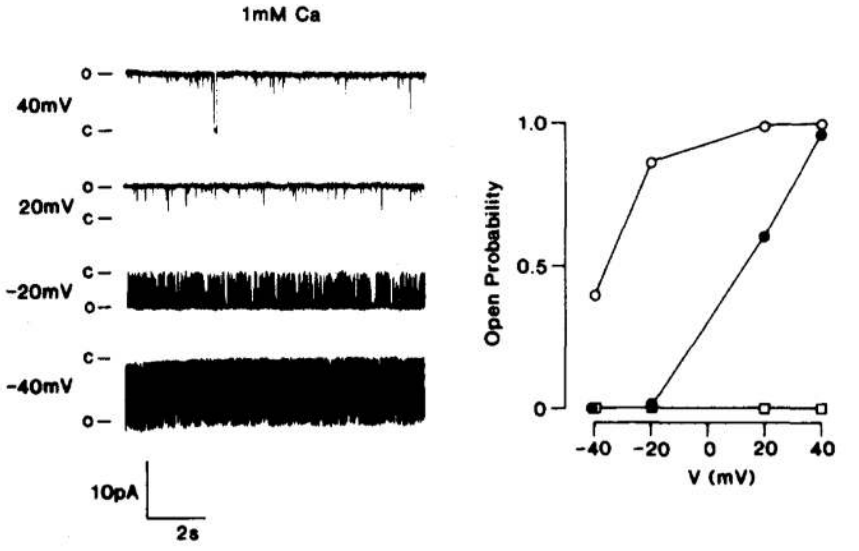

(a)

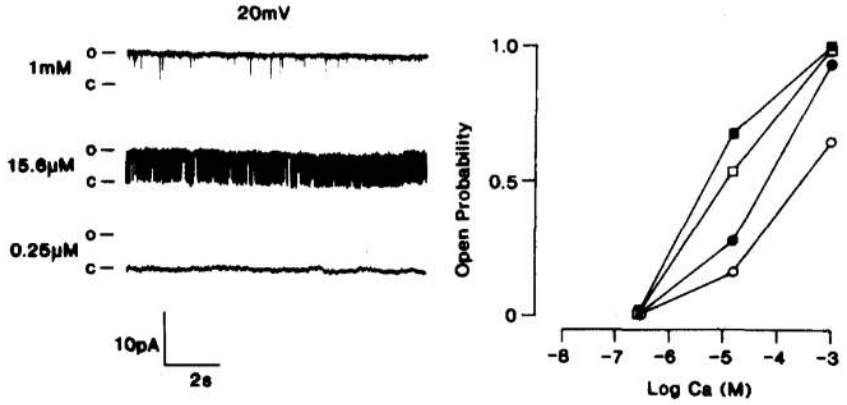

(b)

FIGURE 4.4: (a) Voltage dependence of K-Ca current, recorded with a planar lipid bilayer technique: (left) current recordings in $1\,mM$ Ca^{2+} cis solution at different membrane potentials; (right) open probability at different membrane potentials and at different Ca^{2+} concentrations of the cis solution: $1\,mM$ (white circle), $15.6\,\mu M$ (black circle), $0.25\,\mu M$ (white square). (b) Calcium dependence of K-Ca current, recorded with the same technique: (left) current recordings at a membrane potential of $-20\,mV$ in $1\,mM$, $15.6\,\mu M$, and $0.25\,\mu M$ Ca^{2+} cis solutions; (right) open probability at different cis Ca^{2+} concentrations at a membrane potential of $40\,mV$ (black square), $20\,mV$ (white square), $-20\,mV$ (black circle), $-40\,mV$ (white circle). From ref. [28].

Alessandro Loppini

4.1.5 Na^+ channels

In mouse β-cells, Na^+ current shows unusual inactivation. Half maximum inactivation is recorded at about $-110\,mV$, and at $-70\,mV$, that is about the normal resting potential, the current is totally inactivated. This data are confirmed by the evidence that TTX, a selective blocker of sodium channels, does not affect electrical activity. On the contrary, in rats and humans sodium current is not completely inactivated and plays a role in the generation and in the characterisation of bursting electrical activity. [28]

4.2 Bursting regulation

The exact mechanisms involved in the characterisation of β-cell electrical activity are still debated. However, it is well accepted that bursting electrical activity is triggered by glucose uptake from β-cells, that activates glycolysis and oxidative phosphorylation, causing increased cytoplasmic ATP/ADP ratios. In such conditions, closure of K-ATP channels depolarises the cell, leading the membrane potential to reach the threshold value for L-type calcium channel activation. Voltage-dependent calcium channels are thus responsible for the upstroke of the action potentials within the burst. K-DR and K-Ca currents activation contribute instead to the action potential's downstroke, and cell repolarization at a plateau value of $\simeq -40mV$. At this membrane potential level, potassium current is almost totally inhibited. Slow inactivation of potassium current and reactivation of calcium channels cause then the next action potential. Bursting duration is regulated by a balance between the hyperpolarizing K^+ current from K-ATP channels, and the Ca^{2+} currents. Slow inactivation of calcium currents during the burst leads finally to burst termination while recovery of calcium channels from inactivation regulates the interburst interval. [28]

These aspects are summarised in Fig. 4.5.

Recent studies show however that bursting activity recorded from β-cells is heterogeneous, with reported bursting periods going from several seconds to several minutes. Based on this, bursting activity can be divided into three categories at least (see Fig. 4.6(a)): i) fast bursting, with an oscillation period from 10 to 60s; ii) slow bursting, with a period from one to several minutes; iii) compound bursting, characterised by a fast bursting superimposed on slow oscillations. Because of this heterogeneous behaviour, several hypotheses have been formulated about the effective pacemakers processes involved in bursting activity generation and regulation. In Figure 4.6(b) the cellular signalling pathways and ion currents involved in the glucose-stimulated insulin secretion (GSIS), and possibly linked to the bursting rhythmicity, are reported. These processes

Alessandro Loppini

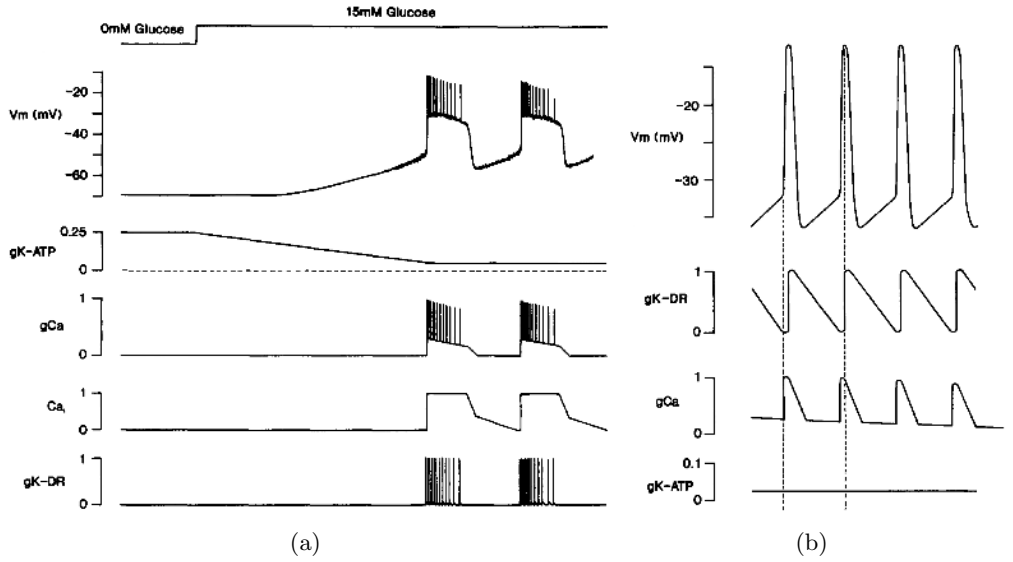

FIGURE 4.5: Qualitative dynamics of ion conductances in mouse β-cell during burst. (a) Ion conductances dynamics during glucose stimulation. (b) Zoom of the ion conductances dynamics within one burst. From ref. [28].

include: activation and inhibition of voltage-dependent calcium currents (as described above) [31–33], activation and inhibition of outward calcium-sensitive potassium currents [34–36], slow changes in the ATP/ADP ratios driven by a calcium feedback [37–39], glycolytic oscillations driving ATP/ADP changes [40–42], Na^+ pump and transporters [43–45], endoplasmic reticulum calcium levels [46–49]. Based on this evidence a large number of β-cells electrophysiological Hodgkin-Huxley type models have been developed with a variable complexity. Between these, the Sherman-Rinzel-Keizer (SRK) model [33] described in Chapter 5, is one of the first model developed able to reproduce mouse fast bursting activity.

4.3 Gap-junctions coupling

Several studies have shown that β-cells within the pancreatic islets present a coordinated and synchronised electrical activity [51–54]. Such coordination leads to a global pulsatile insulin release from the whole islet, whose hypoglycemic effect was shown to be stronger compared to a constant hormone delivery [55, 56]. To achieve synchronisation, β-cells can communicate both via indirect signalling, through molecules diffusing in the extracellular space [57], and via a direct electrical coupling. Between these mechanisms, published literature supports the idea that electrical coupling has a dominant role in synchronising mouse β-cells and improving insulin secretion. The disruption of normal cell contacts and the loss direct coupling leads to decreased or abolished responsiveness to glucose, with a consequent impairment of the insulin release [58]. Such coupling is

Alessandro Loppini

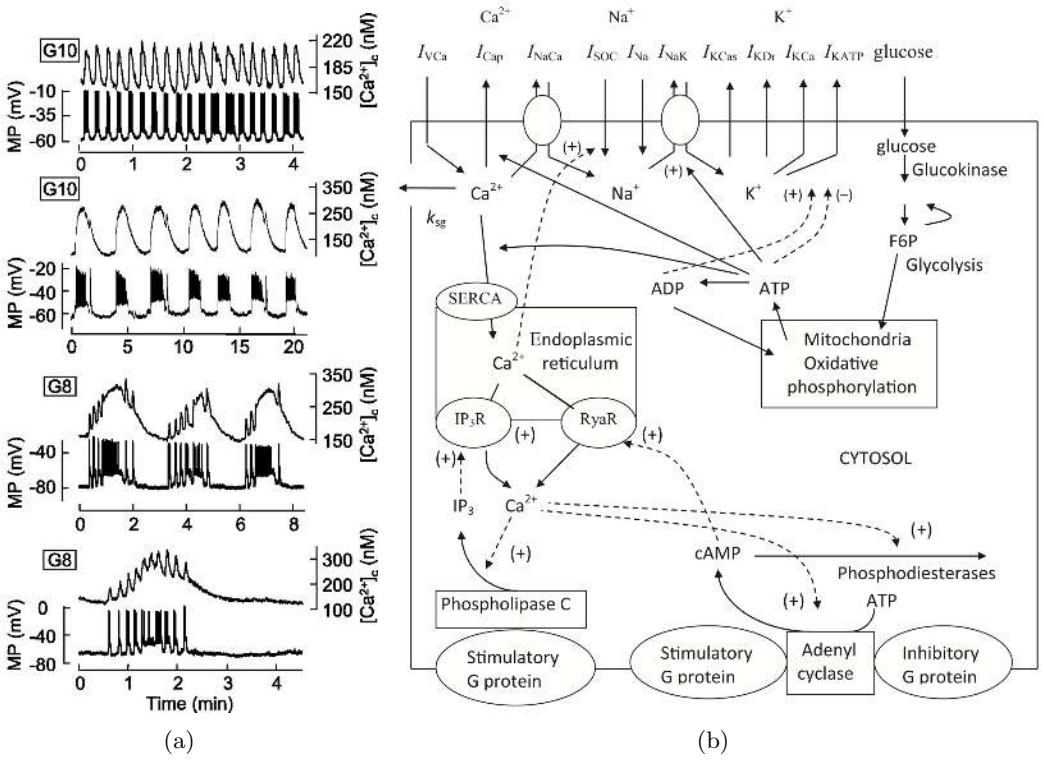

FIGURE 4.6: Burst regulation in mouse β-cell. (a) Heterogenous burst in mouse: fast, slow, and compound bursting (from the top to the bottom) (from ref. [50]). (b) Cellular pathways and ion currents involved in bursting generation and regulation (from ref. [36]).

ensured by specific types of cell surface proteins, forming intercellular junctions between neighbouring β-cells. Gap-junctions ensure communication between cells by coupling of cytosolic components and contribute to the structural property of the islet. Specifically, a gap-junction is an area where the membranes of neighbouring cells are separated by a distance $d \simeq 2 - 3\,nm$. In these conditions, specific hemichannels, i.e. connexons, spanning the membrane of the two cells, can interact and form junctional channels. Each connexon is formed by six proteins called connexins (Cx), and based on the Cx types, the connexon can be homomeric, i.e. formed by the same type of Cx, or heteromeric, i.e. formed by different Cx types. Then, depending on the interacting connexons, junctional channels can be homotypic or heterotypic [59–61].

Such pathways allow the exchange of molecules up to 1kDa. They can conduct metabolites, small peptides and other large molecules as well as ions. In this context, connexons composition is used to fine-tune channel selectivity to specific molecules, regulating parameters such as the size, the charge, and the hydrophilicity of the channel. Efficient discrimination of the purine cyclic monophosphates cGMP and cAMP found in Cx32/26 channels, and permeability differences in nucleotides diffusions between Cx32 and Cx43

channels are examples of this selectivity [62–64]. Several studies have moreover highlighted that the gating of these channels can be modulated by several stimuli, i.e. voltage differences, pH, free intracellular calcium concentration, drugs [59–61].

4.3.1 Cx36 channels in β-cells

Gap junctions in β-cells are tight junctions formed by a small number of connexons. They are mostly formed by Cx36, although also Cx43 expression has been observed in some cases. Cx36 is a protein formed by 321 amino acids, with a long cytoplasmic loop and a short cytoplasmic C-terminal domain that contains recognition sites. This type of connexin does not form junctional channels with other Cx types, and thus connections between β-cells are homotypic [65–67]. In Fig. 4.7 a freeze fracture of a mouse islets, showing these tight junctions between β-cells, is presented.

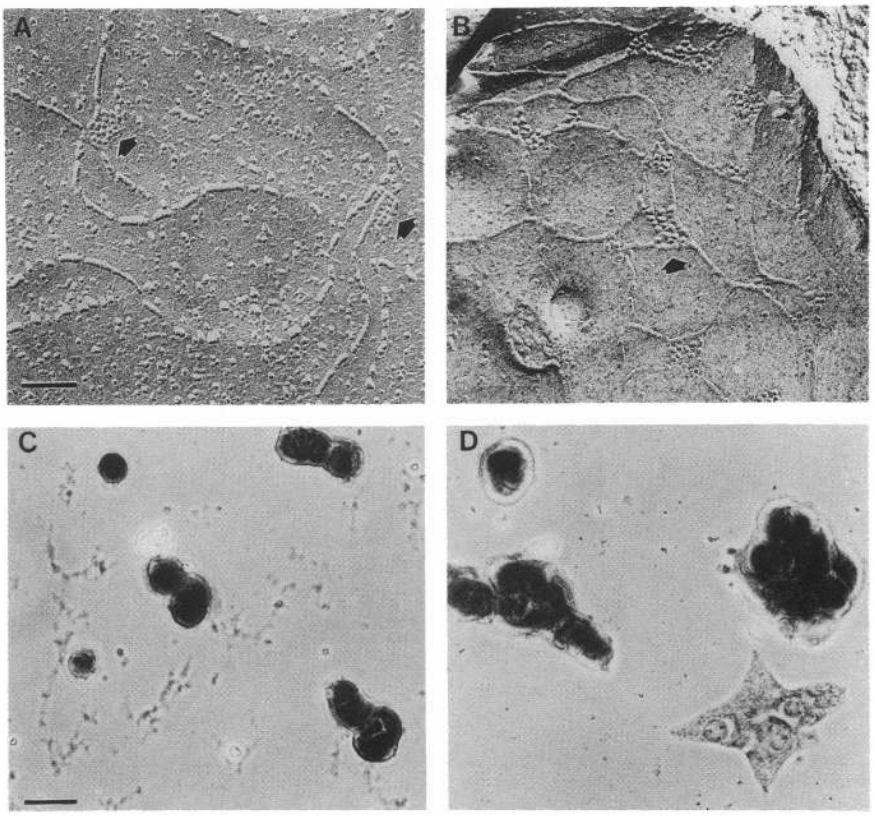

FIGURE 4.7: Ultrastructure of cultured mouse β-cells. (A) Freeze fracture of an isolated mouse islet. (B) Islet cells cultured for 24 h after dissociation. Black arrows highlight gap junctions. (C) β-cell pairs immunostained with anti-insulin antibodies (cells cultured for 12 h after dissociation). (D) As in (C) but with cells cultured for 36 h after dissociation. From ref. [68].

Such channels preferentially exchange cationic molecules, have a small single channel conductance ($\simeq 10\,pS$), and show a minimal voltage sensitivity, despite conserving the

Alessandro Loppini

property to exchange nucleotides and glucose metabolites. To note that also non β-cells in the islet express Cx36, although functional gap junction channels have been found only between β-cells. Interestingly, the minimal voltage dependency ensures a low but permanent level of coupling in both silent, bursting and continuous spiking/bursting regimes evoked by glucose stimulation [65–67].

Genetic regulation of Cx36 is performed by the *Gjd*2 gene, whose expression is regulated at the transcriptional level by the neuron-restrictive silencer element (NRSE). Unfortunately, few studies have focused on the regulation pathways of this gene in β-cells, with just a reported evidence of increased Cx36 expression levels, in conjunction with insulin resistance, in response to the glucocorticoid dexamethasone [69]. Concerning environmental factors, increasing gap junction coupling has been observed during short ($\simeq$ 1 hour) glucose exposure, while decreased gene expressions have been shown for long glucose stimulations ($\simeq$ 24 hours) [70, 71]. Analogously, prolonged exposure to free fatty acids decreases gene expression [72].

Cx36 gap junction channels are probably regulated by C-terminal residues phosphorylation [73]. Connexins phosphorylation evokes changes in permeability, in conductance and in gating of the junctional channels, permitting cells communication. These changes have shown moreover to have an effect on Cx assembly into gap junctions, and on Cx biosynthesis and degradation [74–76]. In mouse retina and in neuronal cells, Cx36 proteins can be phosphorylated by protein kinase A (PKA) and calmodulin-dependent protein kinase II (CAMKII) [73], suggesting similar working mechanisms in β-cells, although further studies should be performed to confirm such thesis. Concerning this aspect, Perez et al. [68] studied electrical properties of Cx36 gap junctions in mouse ruling out a possible modulation of the gating by cAMP-dependent protein kinase. Moreover, they studied freshly dispersed pairs of β-cells with a double patch-clamp techniques noticing as Lucifer Yellow dye diffusion doesn't discriminate junctional coupling, an aspect that is probably linked to the Cx36 channel selectivity with respect to cations. Measurements performed on cells pairs by the authors, show moreover a mean junctional conductance of $215 \pm 110\,pS$ with a distribution following a lognormal-like shape, as it is shown in Fig. 4.8.

4.3.2 Cx36 channels in physiology and pathology

Gap junctions role is not only to synchronise cells electrical activity but is also required for the normal secretory functioning. In stimulatory glucose concentrations, gap junctions synchronise cells depolarization, and calcium oscillations across the islet, while under non-stimulatory glucose concentrations, gap junctions channels can transfer the

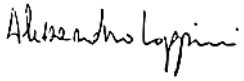

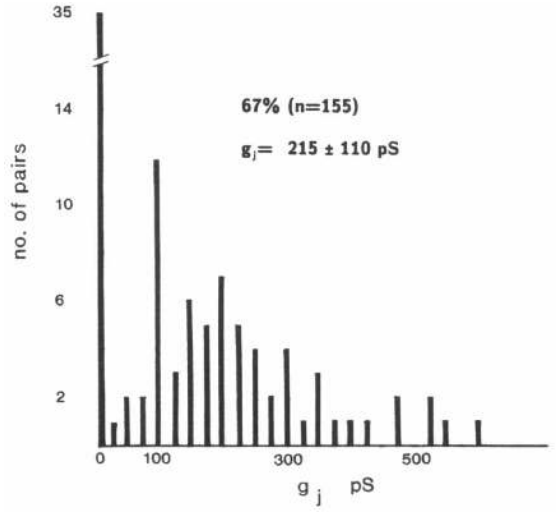

FIGURE 4.8: Double voltage-clamp measurements of gap junction conductance in mouse β-cell pairs. From ref. [68].

K-ATP hyperpolarizing current, homogenising cells responses and suppressing spontaneous calcium elevations [77–80]. Modelling and experimental studies have shown that electrical coupling is required to overcome heterogeneity of such a multicellular system, giving rise to "phase transitions" reminiscent of a critical behaviour in the islet response [81, 82]. Thus, networks of intrinsically inactive and active cells, resembling mouse islets, show an emergent behaviour strictly dependent on coupling strength and on the number of connections. A similar effect of coupling in regulating emergent activity has been observed in the case of islets characterised by subpopulations of non-responsive or overactive β-cells, expressing mutant K-ATP channels [83]. These observations remark that Cx36 coupling has a fundamental role in conserving functional properties of the islet, and its modulation could enhance in some conditions the secretory response. For instance, decoupling the pathological silent cells could recover the activity of normal responsive cells silenced by the non-responsive ones. Pathological lack of coupling leads to a complete loss of the control of heterogeneity and electrical activity coordination, with dramatic effects on cells function. Studies performed on isolated cells, and in islets treated with Cx blockers, have shown that β-cells function is seriously compromised in terms of basal insulin release, responsiveness to glucose, basal insulin expression, insulin biosynthesis and intracellular calcium oscillations [58, 84]. For instance, alterations in insulin release observed in the Cx36 knockout mice, i.e. lacking gap junction channels, are comparable to the alterations observed in prediabetic and Type 2 diabetic states. Such similarities support the idea that an altered expression or function of Cx36 is implicated also in Type 2 diabetes (T2D).

Concerning T2D, a pathogenetic role of Cx36 is also hypothesised by the evidence that

*Gjd*2 gene, coding for Cx36, is located on chromosome 15 (15q14) [85], that has been shown to be a susceptible locus for T2D [86, 87]. Interestingly, a polymorphism on the *Gjd*2 characteristic of hereditary epilepsy is also observed in T2D patients, further suggesting altered Cx36 expression in these pathological conditions [66]. Moreover, glucotoxic and lipotoxic conditions observed in T2D subjects, i.e. sustained exposure to high glucose and free fatty acid concentrations, can have a negative effect on Cx36 as discussed above. Specifically, has been shown as elevated concentrations of the inducible cAMP early repressor (ICER) induced by glucose stimulation, by LDL and by palmitate inhibit *Gjd*2 transcription [71, 72, 88]. On the other hand, specific sulfonylureas that stimulate insulin secretion in T2D subjects have shown instead to promote Cx36 coupling between β-cells [70, 89].

Recent studies have also pointed out a protective role of Cx36 against the proapoptotic environment at the onset of Type 1 diabetes, and against cytotoxic drugs [90–92]. Specifically, a mix of cytokines such as IL-1β, IFN-γ and TNF-α, usually present in islet inflammatory conditions, causes Cx36 down-regulation and increased apoptosis. Down-regulation is mediated by chemical ER (Endoplasmic Reticulum) stressors that through a cascade of processes act on the *Gjd*2 gene coding for Cx36. In this scenario β-cells with high Cx levels can resist to the aggression and remaining functionals. Moreover, Cx36 overexpression increases the basal Ca^{2+} ER concentration, preventing depletion after cytokines exposure. Since cytokines are also present in Type 2 diabetic inflammatory conditions, such protective effect of coupling could also be involved in T2D evolution. Finally, the coupling between β-cells has shown to protect also from mitochondrial apoptosis, possibly implying a cytosolic Ca^{2+} and IP3 diffusion between neighbouring cells to achieve a proper dilution of apoptotic signals.

Alessandro Loppini

Chapter 5

Sherman-Rinzel-Keizer generalised model

In this chapter, the Sherman-Rinzel-Keizer model [33], able to reproduce bursting electrical activity observed in mouse β-cells, is introduced. The original model formulation is here presented and discussed, from the deterministic single cell, up to the stochastic multicellular case. Finally, the model is generalised in order to study in-silico the behaviour of coupled cell populations, in different operating conditions. Emergent bursting is thus analysed in terms of a coherent underlying dynamics, evoked by gap junction electrical coupling. Interestingly, results presented in the last part of the Chapter, suggest that such coherent dynamical regimes are subjected to critical transitions by which a globally synchronised response is achieved throughout the islet.

5.1 The Sherman-Rinzel-Keizer model

The Sherman-Rinzel-Keizer (SRK) model is a Hodgkin-Huxley type electrophysiological model of β-cells activity. It is based on the old assumption that the slow activation and inactivation of K-Ca channels is the process regulating the burst, and does not take into account the K-ATP current. Although such hypotheses have not been confirmed by experimental studies, the model grasps all the quantitative features of fast mouse bursting and, due to its limited complexity, can be used to study deeply dynamical properties of bursting electrical activity in the framework of dynamical systems theory. In general, emergent dynamics of the SRK model is representative of most of the bursting mechanisms proposed in more complex models, where an ad hoc slow dynamics interacts with a fast one to obtain a bursting activity with specific time scales. The model is based

on voltage clamp data coming from mouse (Rorsman and Trube 1986 [93]), and takes into account three types of ion current:

Voltage-dependent Ca^{2+} current. Calcium current is modelled assuming instantaneous activation and inactivation ($\tau_m \simeq 0.1 - 1.5\,ms$), and considering the following steady-state activation and inactivation curves, respectively:

$$\begin{aligned} m_\infty(V) &= \frac{1}{1+\exp[(V_m - V)/S_m]} \\ h(V) &= \frac{1}{1+\exp[(V - V_h)/S_h]}\,. \end{aligned}$$

Voltage-dependent K^+ current. This current activates on a slower time scales ($\tau_n = 20 - 30\,ms$) and it doesn't show inactivation. In order to obtain good agreement with data, voltage effects on the activation time constant and the steady-state activation curve are modelled respectively by the functions:

$$\begin{aligned} \tau_n(V) &= \frac{c}{\exp[(V-\bar{V})/a] + \exp[(V-\bar{V})/b]} \\ n_\infty(V) &= \frac{1}{1+\exp[(V_n - V)/S_n]}\,, \end{aligned}$$

Calcium-dependent K^+ current. K-Ca current is regulated by potassium-sensitive calcium channels. The gating of these channels depends on the binding of a Ca^{2+} ion, and, therefore, it is modelled with the following kinetics,

$$C + Ca \underset{k^-}{\overset{k^+}{\rightleftharpoons}} O\,,$$

that presents an equilibrium fraction of open channels dependent on the intracellular calcium concentration:

$$p = \frac{[O]}{[O]+[C]} = \frac{Ca}{K_d + Ca}\,,$$

where $K_d = k^-/k^+$.

Finally, the intracellular calcium concentration dynamics is modelled taking into account calcium influx via Ca^{2+} channels and a net removal rate due to membrane pumps and exchangers. Oscillation of calcium oscillations, acting on K-Ca channels, are the slow process driving the burst in the model.

With these assumptions, the global set of model's equations is the following:

Alessandro Loppini

$$
\begin{aligned}
C_m \frac{dV}{dt} &= -I_{ion} - \bar{g}_{K-Ca} p (V - V_K) \\
\frac{dn}{dt} &= \lambda \left[\frac{n_\infty(V) - n}{\tau_n(V)} \right] \\
\frac{dCa}{dt} &= f \left[-\alpha I_{Ca} - k_{Ca} Ca \right] \\
I_{ion} &= I_K + I_{Ca} = \bar{g}_K n(V)(V - V_K) + \bar{g}_{Ca} m_\infty(V) h(V)(V - V_{Ca}) \\
p &= \frac{Ca}{K_d + Ca} \\
m_\infty(V) &= \frac{1}{1 + \exp[(V_m - V)/S_m]} \\
h(V) &= \frac{1}{1 + \exp[(V - V_h)/S_h]} \\
n_\infty(V) &= \frac{1}{1 + \exp[(V_n - V)/S_n]} \\
\tau_n(V) &= \frac{c}{\exp[(V - \bar{V})/a] + \exp[(V - \bar{V})/b]}, \\
\alpha &= \frac{1}{2 V_{cell} F};
\end{aligned}
$$

where C_m is the membrane cell capacitance; V is the cell membrane potential; n is the potassium (K^+) activation variable; $n_\infty(V)$ is the steady-state activation curve of voltage-gated potassium channels; $m_\infty(V)$ and $h(V)$ are respectively the steady-state activation and inactivation curves of voltage-gated calcium channels; Ca is the intracellular calcium (Ca^{2+}) concentration; $\bar{g}_K$, $\bar{g}_{Ca}$ and $\bar{g}_{K-Ca}$ are the whole cell ion conductances for potassium, calcium and calcium-sensitive potassium channels, respectively; V_K and V_{Ca} are the potassium and calcium reversal potentials; λ is a parameter used to fine tune the K^+ channels time constant; f is the fraction of free intracellular calcium; α is a conversion factor; k_{Ca} is the calcium removal rate; p represents the fraction of open K-Ca channels; K_d is the ratio of the kinetic constants that regulate the K-Ca channels chemical process of opening and closing; V_m, S_m, V_h, S_h, V_n, S_n, $\bar{V}$, a, b, and c are parameters fine-tuned to obtain good fit of data and to reproduce observed currents dynamics. Complete set of parameters is reported in Tab. 5.1.

5.1.1 Bursting in the SRK model

In figure 5.1 the cell membrane potential, calcium concentration, and K-Ca conductance dynamics in bursting regime, reproduced with the model, are reported. As it can be seen from the simulated time series, the model is able to reproduce bursting oscillations in agreement with the fast bursting recorded from mouse, described in Chapter 4.

Alessandro Loppini

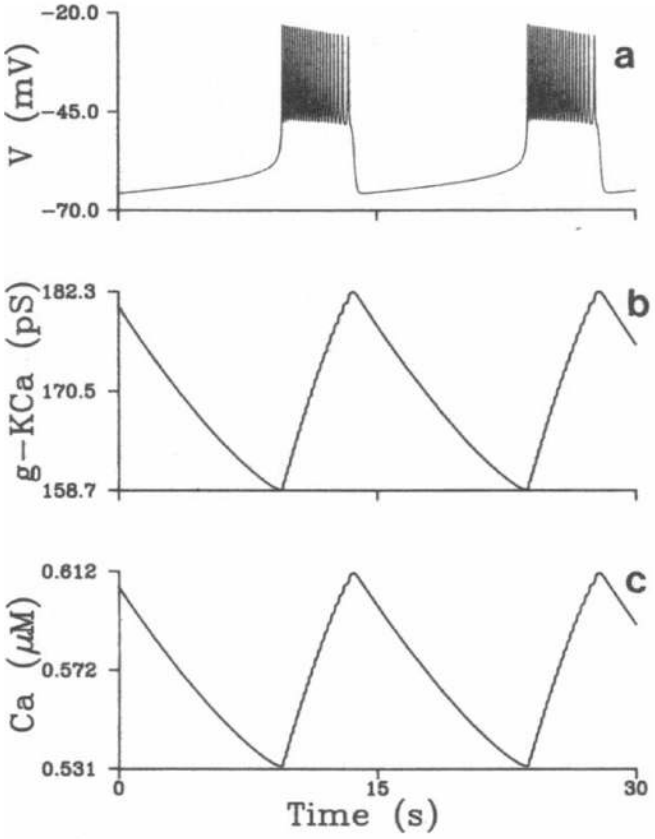

FIGURE 5.1: Bursting in the SRK model. (a) Membrane potential in time. (b) K-Ca conductance in time. (c) Ca^{2+} concentration in time. From ref. [33].

As it can be noticed calcium oscillations in this regime are slow, with a period comparable to the bursting time scale. In the SRK model a fast dynamics, characterised by the membrane potential V and the activation level of potassium channels n, interact with a slow process that is the varying conductance of K-Ca channels driven by the slow calcium oscillations. In order to deeply study bursting mechanism, it is useful to analyse the fixed points of the membrane potential equation treating the g_{K-Ca} conductance (or equivalently the Ca variable) as a parameter, i.e. we have to study the zeros of the function:

$$I_{SS}(V; g_{K-Ca}) = \bar{g}_K n(V)(V - V_K) + \bar{g}_{Ca} m_\infty(V) h(V)(V - V_{Ca}) + g_{K-Ca}(V - V_K)\,,$$

for each fixed value of g_{K-Ca}. This procedure leads to the bifurcation diagram reported in Fig. 5.2(a). For g_{K-Ca} values close to zero, there is only one high voltage steady state solution. For increasing g_{K-Ca}, such branch of stable steady states loses stability through a supercritical Hopf Bifurcation, so that the only stable solution for intermediate g_{K-Ca} levels is a limit cycle, representing a high voltage periodic solution. Increasing further g_{K-Ca}, two other branches of solutions appear through a saddle-node bifurcation

Alessandro Loppini

(SN). Therefore, in a specific range of the parameter, the system shows bistability, i.e. the high voltage periodic solution coexists with a low voltage stable fixed point, separated by an unstable point, that acts as a threshold dividing the high and low voltage basins of attraction. At higher g_{K-Ca} values, i.e. calcium concentrations, the periodic solution collides with the saddle branch and disappears in an homoclinic bifurcation (HC), while the saddle branch eventually connects with the high voltage unstable branch, and the only stable solution is the low voltage branch of fixed points.

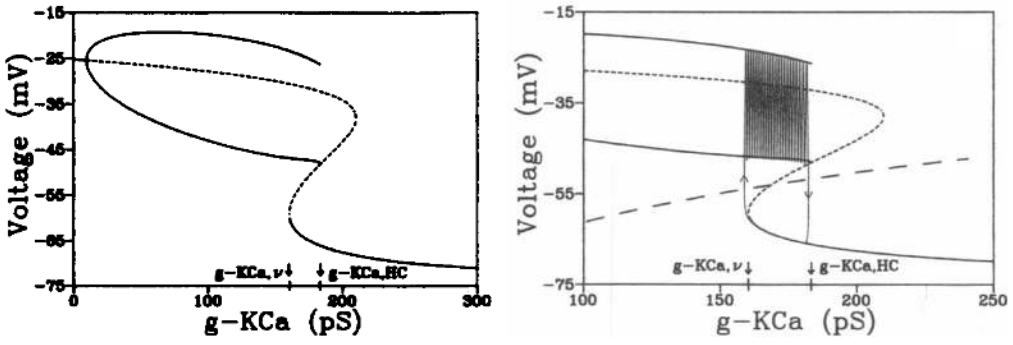

FIGURE 5.2: Bifurcation diagram of the membrane potential in the SRK model. (a) Solutions branches computed by varying g_{K-Ca}: continuos line denote stable solutions, while dashed line unstable solutions. (b) Bifurcation diagram zoom, with superimposed system trajectories (line with arrows) and calcium nullcline (dashed line). The values $g_{K-Ca,\nu}$ and $g_{K-Ca,HC}$ denote the coordinates of the low-voltage saddle-node and homoclinic bifurcations. From ref. [33].

By plotting the calcium nullcline, that is the curve that nullifies calcium derivative, on the bifurcation diagram (see Fig. 5.2(b)), it is possible to investigate emergent trajectories of system analysing changes in calcium concentration and g_{K-Ca} conductance. In a condition with high g_{K-Ca} values (i.e. Ca^{2+}), the system is in a low voltage resting state, and, since such solution is located under the calcium nullcline, calcium derivative is negative, indicating a net efflux of Ca^{2+} form the cell. To track changes of the solution we need to move to the left on the bifurcation diagram since calcium concentration decreases in this condition. Once the SN point is reached, there are no more low voltage stable solutions, and the system must jump on the high voltage periodic stable branch. This jump represents the burst initiation. On the bifurcation diagram, the periodic regime within the burst is located over the calcium nullcline, so that calcium concentration during the burst increases, and consequently the g_{K-Ca} value. Thus, to follow bursting oscillation on the diagram, we need now to move to the right, on the high voltage periodic branch. As before, once the HC point is reached, the system is forced to jump again on the low voltage stable branch, that is the only stable solution at high calcium levels, starting another bursting cycle. This description shows that the bursting oscillation comes from the interaction of a slow process with a fast dynamics.

Alessandro Loppini

As anticipated, such concepts also apply to more complex models of bursting activity, in which more than one slow process can participate to generate rhythmic bursting.

5.2 Stochastic SRK model

Deterministic SRK model introduced above doesn't take into account intrinsic biological noise coming from channel gating (as described in Chapter 3). In this case, noise fluctuations can significantly alter the emergent bursting oscillation, mainly because of the high conductance K-Ca channels. The opening of a small fraction of K-Ca channels can induce strong outward currents so that single channel events may drive the system between active regimes and silent states [33]. Calcium and potassium voltage-dependent currents are also affected by noise due to channel gating. However, the small conductance value presented by these channels compared to the large conductance K-Ca channel allows to keep a deterministic description of the gating, without affecting the validity of the resulting stochastic model. To include this evidence, the deterministic SRK can be modified by modelling K-Ca gating mechanism as a two-state Markov process:

$$C \underset{1/\tau_o}{\overset{1/\tau_c}{\rightleftharpoons}} O \ ,$$

where τ_c and τ_o are the mean closed and open times (as seen in Chapter 3 are related to the inverse of transition rates). At equilibrium, holds the relation $\langle N_o \rangle / \langle N_c \rangle = \tau_o / \tau_c$, where $\langle N_o \rangle$ and $\langle N_o \rangle$ are respectively the mean number of open and closed channels. By comparison with the deterministic gating, it is possible to write the following relations that model the feedback of calcium on channel transition rates:

$$\begin{aligned} \tau_o &= \tau_c \frac{Ca}{K_d} \\ \langle p \rangle &= \frac{\langle N_o \rangle}{\langle N_o \rangle + \langle N_c \rangle} = \frac{Ca}{K_d + Ca} \, , \end{aligned}$$

In the stochastic SRK cell, the fraction of open K-Ca channels is thus calculated evolving such a stochastic process for an ensemble N of K-Ca channels. The ensemble's size can be estimated from channels density and β-cell dimensions, and in the original model is fixed at $N = 600$. Model's simulation performed on such a stochastic cell (shown in Fig. 5.3) reveals a substantially different electrical pattern compared with the deterministic case. As anticipated before, noise due to K-Ca gating is able to drive cell transitions between the active and silent state. It is still possible to observe very fast bursting oscillation, but the clear slow oscillation seen in the deterministic case is totally lost.

Alessandro Loppini

Such behaviour resembles the electrical pattern of individual isolated cell, characterised by chaotic spiking more than a regular busting oscillation.

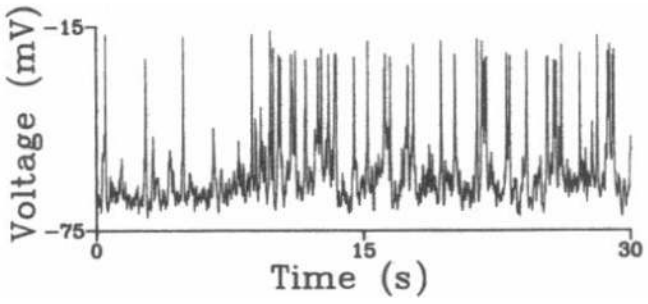

FIGURE 5.3: Single cell simulation of the stochastic SRK model. Membrane potential time series is shown. From ref. [33].

As discussed in Chapter 4, β-cells in the islets are coupled through gap junctions. Such electrical coupling is crucial for normal electrical activity and insulin release, permitting to homogenise cells population, to synchronise burst, to obtain a global pulsatile secretory pattern, etc.; while cells uncoupling leads to a loss of synchronisation, increased basal insulin release and loss of pulsatility. Single cell SRK stochastic model is representative of such scenario, where the isolated cell is no more able to respond with a robust bursting. On the contrary, SRK deterministic model reproduces the electrical behaviour of a β-cell in a fully synchronised islet. In order to analyse stochastic model behaviour for increasing number of coupled cells, Sherman et al. introduced two different generalisations: a simplified "supercell" perspective [33], where all the cells are coupled with infinite coupling conductances, and a "multicell" model [94], that takes into account a finite value of the coupling conductance and topological constraints of the mouse islet architecture.

5.2.1 Supercell model

The supercell model is obtained considering a number N_{cell} of SRK stochastic units coupled by infinite conductance connections, so that all the cells have the same potential. In this case, membrane voltage equation can be rewritten by scaling the single cell equation with the number of cells in the cluster:

$$N_{cell}C_m\frac{dV}{dt} = -N_{cell}I_{ion} - \sum_{i=1}^{N_{cell}} \hat{g}N_o^i(V - V_K)\,,$$

Alessandro Loppini

where $\hat{g} = \bar{g}_{K-Ca}/N$ is the single K-Ca channel conductance, and N_o^i is the number of open channels for the ith-cell. Dividing the previous by N_{cell}, it is possible to obtain:

$$C_m \frac{dV}{dt} = -I_{ion} - \frac{\bar{g}_{K-Ca}}{N_{cell} N} \sum_{i=1}^{N_{cell}} N_o^i (V - V_K) \,.$$

Considering that $p = \frac{1}{N_{cell} N} \sum_{i=1}^{N_{cell}} N_o^i$, such equation has the same form of the single cell SRK membrane equation, but now the factor p represents the fraction of open channels in the entire cluster, as if the cluster is "sharing" the entire pool of stochastic channels [33]. In this way, perturbations coming from channel gating are attenuated by a factor $1/N_{cell}$. All other equations remain the same as in the single cell SRK stochastic model.

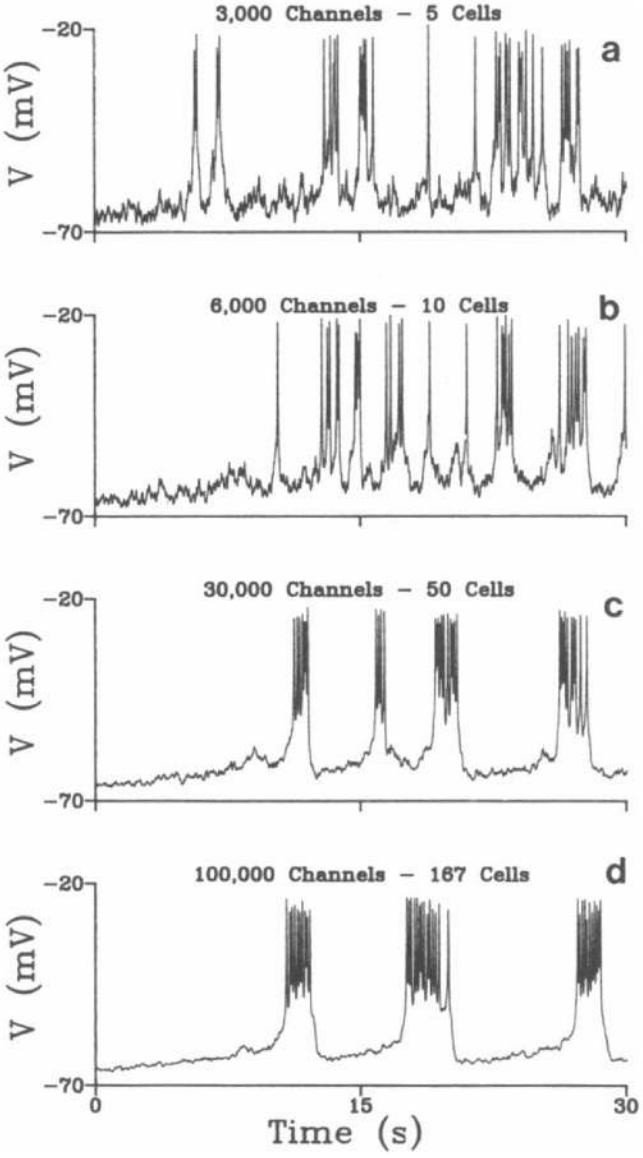

FIGURE 5.4: Simulations of the supercell SRK model. (a)-(d) Membrane potential time series for an increasing number of cells in the cluster. From ref. [33].

Alessandro Loppini

In Fig. 5.4 the results of model simulations, taking into account a variable number of cells in the cluster, are shown. Bursting activity emerges by increasing the cluster size, and a clear organised slow oscillation can be appreciated for clusters of about 50 cells. Because of "channel sharing" the model is thus able to reproduce coherent emergent bursting in β-cells populations, and stochastic spiking of isolated cells. Such considerations are based on the assumption that noise induced by channel gating is a key aspect in the variability of cell response. Other models have focused instead on cells heterogeneity to explain the spiking response of an isolated cell, i.e. by considering deterministic heterogeneous populations. In these models, a robust bursting activity is obtained by coupling a certain number of silent and spiking cells, with only a small percent of cells showing bursting when isolated [95]. Heterogeneity perspective represents an alternate view of emergent bursting coming from coupled populations and probably plays a role, together with ion channel stochasticity, in the modulation of the collective activity of coupled β-cells. In the case of the SRK model, however, noise coming from K-Ca channels would overcome the effect coming from heterogeneity in cells parameters and the addition of such evidence would not be appreciated. In addition, stochasticity can also be viewed as a masked "heterogeneity", further validating such approach [96, 97].

5.2.2 Multicell model

The multicell SRK model [94] generalises the "supercell" model to the case of a variable number of cells coupled by finite value junctional conductances. In this case, the cluster is no more isopotential, and ion concentrations are different between different cells. Model's equations have now to be written for each cell in the cluster, taking care to add properly the gap junction currents. Modified equations for the *ith*-cell are:

$$\begin{aligned}
C_m \frac{dV_i}{dt} &= -I_{ion,i} - \bar{g}_{K-Ca} p_i (V_i - V_K) - g_c \sum_{j \in \Omega_i} (V_i - V_j) \\
\frac{dn_i}{dt} &= \lambda \left[\frac{n_\infty(V_i) - n_i}{\tau_n(V_i)} \right] \\
\frac{dCa_i}{dt} &= f \left[-\alpha I_{Ca,i} - k_{Ca} Ca_i \right] \\
I_{ion,i} &= I_{K,i} + I_{Ca,i} = \bar{g}_K n(V_i)(V_i - V_K) + \bar{g}_{Ca} m_\infty(V_i) h(V_i)(V_i - V_{Ca}) \\
\langle p_i \rangle &= \frac{Ca_i}{K_d + Ca_i},
\end{aligned}$$

where the steady-state activation and inactivation curves $n_\infty(V)$, $m_\infty(V)$, and $h(V)$, and the function $\tau_n(V)$ are the same as before. In the membrane voltage equation, g_c is the gap junction conductance between two cells, and Ω_j is the neighbourhood of the *ith*-cell, i.e. the subset of cells in the cluster connected to the *ith*-cell. In line

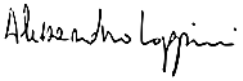

with the mouse islet architecture (see next Chapter for further details), Sherman et al. considered β-cells cluster arranged in a n x n x n cube, in which cells interact via a three-dimensional extension of the Von Neumann neighbourhood, i.e. a central cell is coupled to six neighbours.

The integration of the model requires the resolution of $3N_{cell}$ coupled ODEs, together with the stochastic processes related to the K-Ca channels gating.

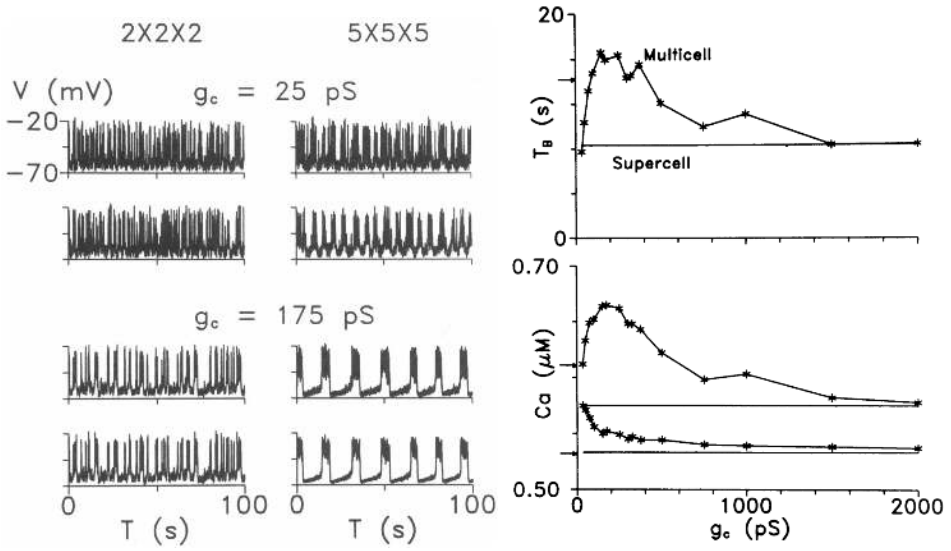

FIGURE 5.5: Simulations of the multicell stochastic SRK model. (a) Membrane potential time series of a 2 x 2 x 2 (left column) and 5 x 5 x 5 (right column), at $g_c = 25\,pS$ (top) and $g_c = 175\,pS$ (bottom) clusters. (b) Bursting period T_B and Ca^{2+} oscillations for g_c in the range $0 - 2000\,pS$. From ref. [94].

In line with the supercell formulation, model's simulations show robust bursting emerging by increasing the number of β-cells in the cluster and the coupling conductance value. In Figure 5.5(a) results published in ref. [94], computed with $n = 2$ (8 cells) and $n = 5$ (125 cells), are shown. Bursting oscillation is completely lost in the 2 x 2 x 2 cluster with low coupling conductance ($g_c = 25\,pS$). Calcium oscillations in this condition are abolished, thus describing a situation with impaired insulin release. By increasing electrical coupling ($g_c = 175\,pS$) it is possible to recover a bursting-like pattern, slightly enhancing calcium oscillations. The 5 x 5 x 5 cluster presents instead a much more robust bursting both for low coupling and high coupling strength, showing in the latter case calcium oscillations comparable in amplitude to the deterministic case. Specifically, the authors show that calcium oscillations and bursting period, depending both on cell number and coupling strength, are enhanced in some conditions compared to both deterministic and supercell case (see Fig. 5.5(b)). They found that for g_c within the range $100 - 400\,pS$ these two values are maximised. This finding takes a great relevance considering that,

as described in Chapter 4, the mean value of junctional conductance between paired β-cells is $\simeq 215\,pS$. Thus, further considering that enhanced calcium oscillations mean enhanced insulin release, biological coupling seems to be set in order to optimise β-cell secretion. It's interesting to note, as pointed out by the authors, that such increasing of the bursting period could be related to the appearance of asymmetrical or aperiodic solutions usually observed in deterministically modelled β-cell pairs [98, 99]. In the bifurcation diagram shown before, such solutions originate from the periodic high voltage solution branch and their collision with the threshold saddle branch is shifted to right respect to the original periodic solution, thus causing longer times spent in the active and silent phases and enhancing the slow oscillation period (and consequently calcium oscillations).

Authors also showed, by modelling cells arranged in $32\,\mathrm{x}\,32$ grid of cells, that the model is able to reproduce bursting waves with phase lags of about $1-2\,s$ across the domain, in line with experimentally recorded activity from cells within mouse islets [51, 100]. Such waves originate mostly from cells in the corners of the grid, where the noise fluctuations are greater because of the low number of neighbours compared to the central cells. Such focusing of noise triggers the bursting that spreads across the grid. More than one bursting wave can originate from different spots, eventually colliding.

In conclusion, the SRK multicell model is a valid description of β-cell activity in the islet. It is able to reproduce the irregular spiking behaviour of isolated cells, and the organised bursting emerging from coupled cells populations. Despite simplistic about the specific sub-cellular pathways involved in the generation and the modulation of the bursting activity, the basic concept is in line with other modelled processes of bursting generation, where a slow dynamics interacts with a fast one. In addition, although the limited complexity, it can reproduce rather faithfully main features of the fast bursting observed in mouse. Because of this, a further generalisation of the SRK multicell model is presented in the following, in order to study emergent bursting and coherent behaviour of coupled cells populations stimulated by varying glucose concentrations, and to analyse architecture effects induced by coupling.

5.3 SRK generalisation: glucose feedback

The original formulation of the SRK model does not take into account the glucose effect on the electrical activity. In order to add this feedback, it is possible to fine-tune opportunely the calcium removal rate (k_{Ca}) parameter in the calcium dynamical equation of the model. In fact, low calcium removal rates evoke accumulation of calcium and increased potassium efflux through K-Ca channels, which in turn forces the cell in a

silent state, as in sub-threshold glucose stimulation. Contrarily, at high calcium removal rates, less calcium is accumulated in β-cells and K-Ca channels are only moderately activated, forcing the cell in a depolarised state through potassium accumulation, in line with the response evoked by increasing glucose concentrations. This effect is also visible in the bifurcation diagram shown in Fig. 5.2. At low values of k_{Ca} the calcium nullcline shifts downward, and intercepts the voltage steady state Z-shaped curve in the low voltage stable branch of solutions; in such situation, the system is in a silent stable state. At higher values of k_{Ca}, calcium nullcline shifts upward, getting closer to the homoclinic bifurcation point. Now the flow is slower near the homoclinic point (Ca^{2+} varies very slowly close to the calcium nullcline), causing more time spent in the bursting depolarised state. At the same time, the distance between the low-voltage saddle-node bifurcation and the calcium nullcline increases, so that flow is faster when the system is in the silent state, giving rise to decreased interburst intervals. Finally, when k_{Ca} is large enough to intersect the periodic high-voltage branch of solutions before the homoclinic point (on the left respect to the HC point), sustained bursting is generated.

Therefore, with the aim to model glucose feedback, a linear relation between the glucose and the calcium removal rate is used, in line with another published study [101]. Specifically, at $[G] \simeq 5.5\,mM$ β-cells show a silent-bursting transition, and at $[G] \simeq 16.6\,mM$ a shift to a continuous bursting can be observed [102]. These behaviours can be obtained in the multicell SRK model, considering a 125 cells cluster, by setting $k_{Ca} = 0.02\,ms^{-1}$ and $k_{Ca} = 0.09\,ms^{-1}$, respectively. Based on this, a simple linear function is adopted to model glycemic feedback:

$$k_{Ca} = C_1[G] - C_2\,,$$

where $C_1 = 6.3 \cdot 10^{-3}\,ms^{-1}mM^{-1}$ and $C_2 = 0.0147\,ms^{-1}$, and $[G]$ is the glucose concentration.

5.4 Coherence in the SRK model

Experimental evidence show that β-cells within mouse islets respond to glucose in a synchronised fashion. Furthermore, it is well-proven that Cx36 gap junction coupling have a lead role in coordinating cellular response, as discussed in Chapter 4 [51–54]. Such coupling ensures that β-cells in mouse act as a functional syncytium, responding to glucose with a clear in-phase bursting. Loss of gap junction coupling leads to a severe decrease in β-cells functionality, causing impaired insulin secretion and usually altered glucose responsiveness [58, 103]. In confirmation of this, isolated β-cells do not exhibit clear bursting activity, but more irregular spiking behaviour. Thus, electrical coupling in mouse seems crucial to achieve cell synchronisation and proper hormone release. In

this framework, it is of interest to analyse the emergence of such coherent activity in response to controlled glucose stimuli, and its sensitivity to variations in the size of the β-cell population. With the multicell stochastic SRK model, Sherman at al. [94] have shown that gap junction coupling can lead to the emergence of robust bursting, by filtering noise fluctuation induced by ion channels gating. By using a generalisation of this model, such phenomena are investigated in the following by varying the stimulating glucose concentration, studying long-range correlations in cellular activity. Specifically, it is shown that β-cells dynamics is characterised by scale-free self-similarity properties in the frequency domain, and in different frequency intervals, suggesting the possible formation of coherent molecular domains, and critical behaviours at different space-time scales. Interestingly such critical behaviour is regulated by environmental conditions and β-cell population size.[1]

In line with the original SRK model [94], β-cell clusters are modelled as cubic clusters of variable size. Cells within the cluster communicate via a three-dimensional Von Neumann neighbourhood, i.e. six neighbours for a central cell. In Fig. 5.6, a typical cluster and the neighbourhood of a representative central cell are shown.

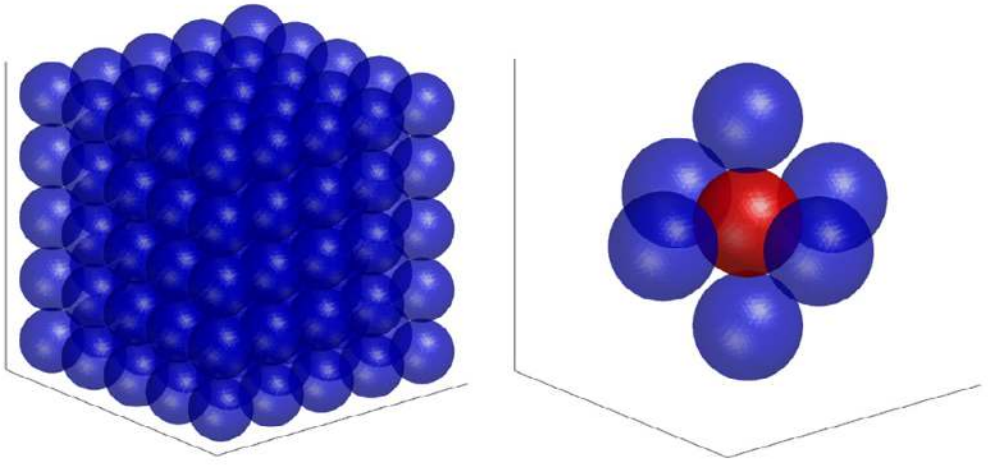

(a) (b)

FIGURE 5.6: (a) Visualization of a 5 x 5 x 5 cluster. (b) Neighbourhood of representative central cell.

In the analyses presented below, the whole model is resolved with a fourth-order Runge-Kutta method with a time step of 0.1 ms. Stochastic gating of K-Ca channels is modelled by considering a total of 600 channels per cell (like in the original formulation [33]) and evolving each channel dynamics with a two-state Markov stochastic process resolved by a Monte Carlo simulation. Thus, the value of open channels per cell, computed at each time step of the numerical integration, is used to compute the open fraction of

[1] The novel study here presented is reported in refs. [104, 105].

Alessandro Loppini

K-Ca channels in the membrane potential dynamical equation. Complete set of model parameters is given in Tab. 5.1.

TABLE 5.1: **SRK model's paramters**. All parameters are set with their default value reported in ref. [33]. In addition are reported parameters used to model glucose feedback.

Parameter	Value	Unit
$Cell\ Radius$	6.5	μm
F	96.487	$C\,mmol^{-1}$
V_{cell}	1150	μm^3
V_K	-75	mV
V_{Ca}	110	mV
$\bar{g}_K$	2500	pS
$\bar{g}_{Ca}$	1400	pS
$\bar{g}_{K-Ca}$	30000	pS
g_c	215	pS
V_n	-15	mV
s_n	5.6	mV
V_m	4	mV
s_m	14	mV
V_h	-10	mV
s_h	10	mV
a	65	mV
b	20	mV
c	60	ms
$\bar{V}$	-75	mV
λ	1.7	
K_d	100	μM
f	0.001	
τ_c	1000	ms
C_1	$6.3 \cdot 10^{-3}$	$ms^{-1}\,mM^{-1}$
C_2	0.0147	ms^{-1}

5.4.1 Correlation in β-cells electrical activity

In order to analyse β-cells coherent activity within the islet and its sensitivity to glucose stimuli, a 5 x 5 x 5 cluster exposed to different glucose concentrations is initially modelled. Figure 5.7 shows computed time series of a representative cell in the cluster at $[G] = 4.7, 9.5, 12.6, 16.6\,mM$. As it can be noticed, the model correctly reproduces the glucose-stimulated electrical activity in β-cells, showing a silent response, bursting oscillations and continuous bursting in line with experimental observations [28, 102]. Different time scales can be noticed in such complex dynamics, i.e. an infinitely small scale due to the stochastic channel gating, a scale of the order of hundreds of milliseconds characterising spiking activity within the burst, and a slow time scale (tens of seconds) due to bursting oscillations. The power density spectra (PDS) of membrane voltage signals presented in Fig. 5.8 are here computed to highlight scaling features of the signals, possibly suggesting an underlying coherent activity in the cluster. Scaling properties

Alessandro Loppini

are analysed by computing log-log slopes of the observed linear trends on these curves. In this framework, the existence of scale-free properties may underly the presence of robust dynamical states in the activity of coupled β-cells, by which they regulate their secretory function.

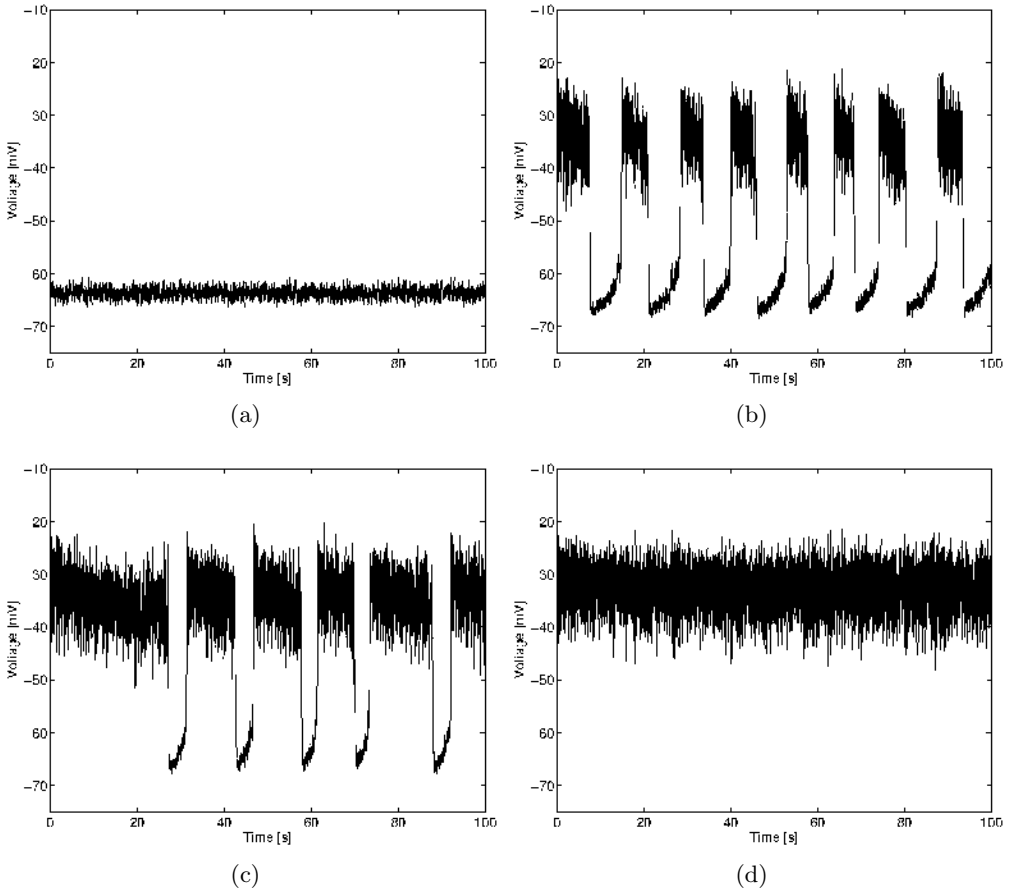

FIGURE 5.7: Simulation of a β-cell mouse $5 \times 5 \times 5$ cluster stimulated by an increasing glucose concentration. The membrane potential time series for a representative cell is shown: (a) $4.7\,mM$, (b) $9.5\,mM$, (c) $12.6\,mM$, (d) $16.6\,mM$.

Interestingly, results show that at mild stimulatory glucose concentrations ($[G] \simeq 9.5\,mM$), the log-log PDS plot presents two clear different linear trends, located at low and high-frequency ranges separated by a transition region. Such frequencies correspond to time scales of seconds and milliseconds, suggesting that scale-free properties are possibly linked to both bursting regime and spiking/channels gating events. In Fig. 5.9(a) the computed slopes of these linear trends at different glucose levels are shown. The high frequency (HF) slope is $S_{HF} \simeq -33\,dB/Hz$ per decade and is almost unaffected by glucose changes. Contrarily, the low frequency (LF) linear trend is nearly absent in the cluster stimulated by sub-threshold and very high glucose concentrations, i.e. for $[G] < 5$ and $[G] > 15\,mM$, while it is clearly observable at intermediate glucose levels

Alessandro Loppini

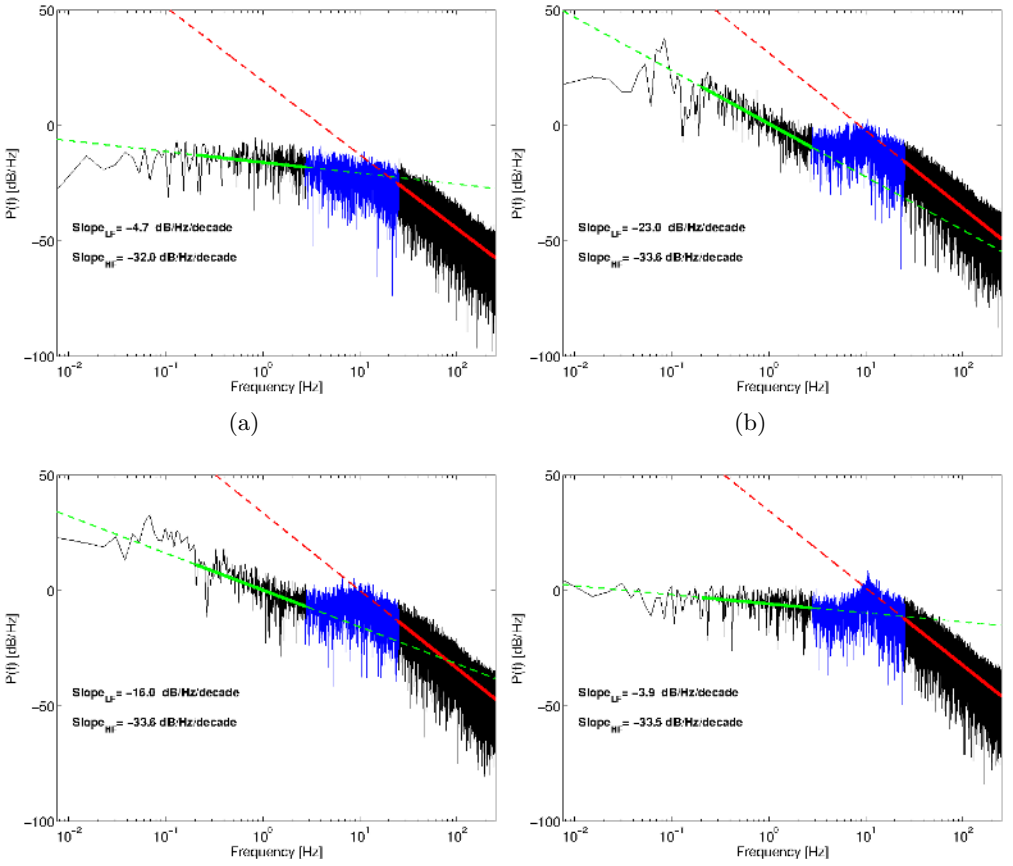

FIGURE 5.8: Power density spectra of simulated membrane potential signals of a representative β-cell in a $5\,x\,5\,x\,5$ cluster exposed to increasing glucose concentrations: (a) $4.7\,mM$, (b) $9.5\,mM$, (c) $12.6\,mM$, (d) $16.6\,mM$. The slope at low (S_{LF}) and high (S_{HF}) frequencies are highlighted in green and red respectively: continuous lines denote the range used for the linear fitting, while dashed lines are used to visualise the computed linear interpolation.

that evoke regular bursting, with $S_{LF} \simeq -20\,dB/Hz$ per decade at almost postprandial glycemic condition ($[G] \simeq 9mM$).

To address the dependency of such scale-free trends on the size of the β-cell coupled population, clusters of increasing size are also modelled and analysed with the use of the log-log PDS plots of the membrane potential, computed for a representative cell. Results obtained for the isolated single cell up to the $10\,x\,10\,x\,10$ cluster, exposed to a mild stimulatory glucose concentration ($[G] = 9.5\,mM$), are shown in Fig. 5.10. As it can be noticed, the HF slope, as observed for different glucose stimulations, is almost independent of the number of coupled cells, showing a value of $S_{HF} \simeq -33\,dB/Hz$ per decade for clusters larger than $\simeq 10$ cells, and slightly lower values in the case of smaller clusters. This threshold is clearer in the LF slope, which is almost zero in the isolated cell, and increases showing an average plateau value of $S_{LF} \simeq -20\,dB/Hz$ per decade

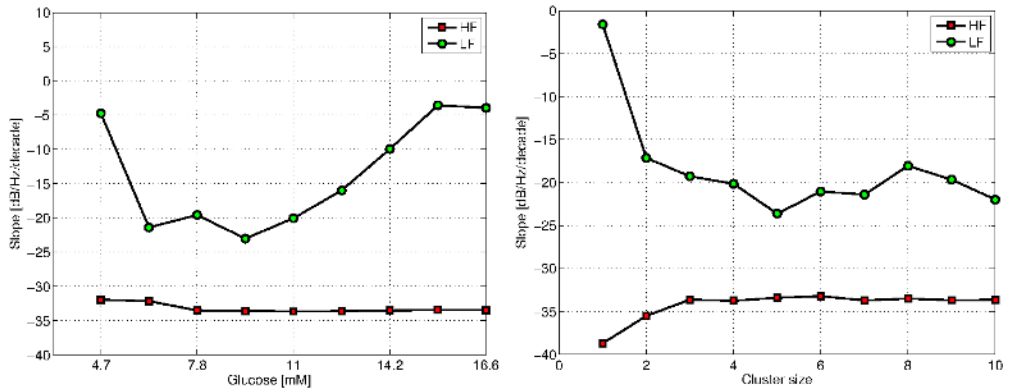

FIGURE 5.9: Power density spectra log-log slopes computed at different glucose concentrations and at increasing cluster size in a representative cell. (a) $5\,\mathrm{x}\,5\,\mathrm{x}\,5$ cluster, and variable glucose concentration. (b) $[G] = 9.5\,mM$, and variable size of the cluster. The value i on the x-axis in (b) stands for $i\,\mathrm{x}\,i\,\mathrm{x}\,i$.

for clusters of proper size (> 10 cells).

To investigate the invariance of such dynamical regimes highlighted by the PDS linear trends, the SRK generalised model is also resolved considering the linear transformation $\hat{V} = V + V_d$, where V_d is treated as a perturbation around V; i.e. the whole dynamical system is resolved under the change of variable $V \to \hat{V}$. Slope values at both low and high frequencies, computed for β-cell clusters of increasing size and stimulated by a glucose concentration of $[G] = 9.5\,mM$, are reported in Tab. 5.2 at different values of the perturbing parameter V_d. As it can be noticed, the imposed change of variables, i.e. the perturbation of the original system, leaves almost unaffected the slope in PDS log plots, thus suggesting that the organised emergent oscillations are representative of a fairly robust state of the system. To note that such observation is not obvious since the Hodgkin-Huxley model represents a nonlinear dynamical system. Translation of the potential affects the steady-state activation and inactivation curves, together with voltage dependence of the time constants leading in general to a different cell dynamics that is not a mere translation of the unperturbed case. Such conclusion can be easily verified by imposing the transformation in the model's equations and by simulation of a single deterministic cell.

These analyses highlight that β-cells dynamics is characterised by scale-free properties of the PDS of cell membrane potential, and that such properties are dependent on operating conditions. It is now interesting to show that such scale-free self-similar characteristics can be expressed in terms of "coherent states". Specifically, a measure of self-similarity is represented by the slope d computed on the linear trends of the PDS plots. In such

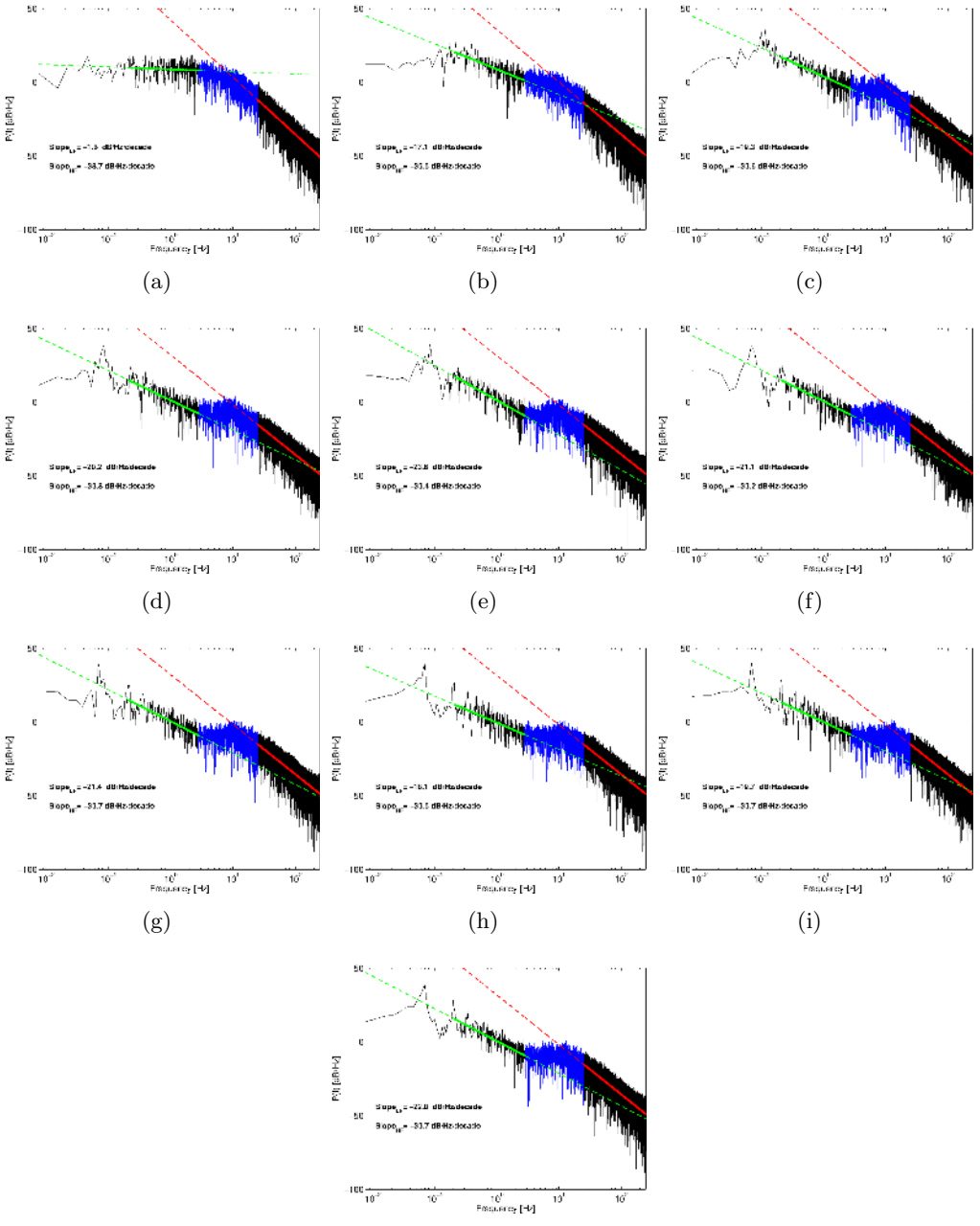

FIGURE 5.10: Power density spectra of simulated membrane potential signals of a representative β-cell in clusters of increasing size, stimulated by a postprandial glucose concentration ($[G] = 9.5\,mM$): (a) single cell, (j) 10 x 10 x 10 cluster, (b-i) intermediate cluster sizes, i.e. n x n x n with $1 < n < 10$. The slope at low (S_{LF}) and high (S_{HF}) frequencies are highlighted in green and red respectively: continuous lines denote the range used for the linear fitting, while dashed lines are used to visualise the computed linear interpolation.

TABLE 5.2: PDS log-log slopes computed at different values of V_d and for increasing β-cell cluster size.

Number of cells	$V_t\,[mV]$	$S_{LF}\,[dB/Hz$ per decade]	$S_{HF}\,[dB/Hz$ per decade]
1	-40	-2.1	-38.8
	-20	-1.9	-38.7
	-10	-0.1	-39.0
	0	-1.6	-38.7
	+10	-2.8	-39.0
	+20	-2.1	-39.2
	+40	-3.5	-38.8
27	-40	-19.2	-33.3
	-20	-19.4	-33.6
	-10	-18.7	-33.6
	0	-19.3	-33.6
	+10	-19.9	-33.5
	+20	-18.5	-33.3
	+40	-19.0	-34.0
64	-40	-19.7	-34.1
	-20	-22.3	-33.8
	-10	-20.9	-33.9
	0	-20.2	-33.8
	+10	-21.9	-34.0
	+20	-21.3	-33.2
	+40	-21.6	-34.0
125	-40	-23.4	-34.2
	-20	-23.6	-34.2
	-10	-22.7	-34.2
	0	-23.0	-33.6
	+10	-22.3	-33.8
	+20	-20.3	-33.4
	+40	-23.4	-34.0

frequency ranges holds the relation:

$$d = \frac{\mathrm{Log}\, P}{\mathrm{Log} F}\,,$$

where $\mathrm{Log}\, F$ and $\mathrm{Log}\, P$ are respectively abscissa and ordinate of the PDS plots, and the ratio d is called self-similarity dimension [106], which is independent of the base of the logarithm. By defining $\alpha \equiv P$ and $q \equiv 1/F^d$, the previous relation can be rewritten in the following self-similarity equation:

$$u_{n,q}(\alpha) \equiv (q\alpha)^n = 1\,, \quad n = 0,\, 1,\, 2,\, ...,$$

where q is called the squeezing parameter [107–109]. Such self-similarity relation is defined in the limit $n \to \infty$. Apart from the normalisation, the functions $u_{n,q}(\alpha)$ represent

the restriction to the real $q\alpha$ of the entire analytic functions

$$\hat{u}_{n,q}(\alpha) = \frac{(q\alpha)^n}{\sqrt{n!}}, \quad n = 0,\ 1,\ 2,\ ...,$$

Indeed, such functions can be used in the Glauber formalism to defined a squeezed coherent state as [107, 110, 111]:

$$\begin{aligned} |q\alpha\rangle &= \exp\left(-\frac{|q\alpha|^2}{2}\right)\sum_{n=0}^{\infty}\frac{(q\alpha)^n}{\sqrt{n!}}|n\rangle \\ |n\rangle &= \frac{1}{\sqrt{n!}}(a^\dagger)^n|0\rangle\,, \end{aligned}$$

where the set $\{|n\rangle\}$ is the eigenkets (i.e. eigenvectors) basis by which is the defined the coherent state, $|0\rangle$ represents the ground state, and a and $a^\dagger$ are the annihilation and creation operators respectively. In this quantum mechanics formalism, each eigenket $|n\rangle$, i.e. energy eigenstate of the system, can be thought to be generated from the n-*th* application of the creation operator $a^\dagger$ to the ground state, since it holds $a^\dagger|n\rangle = \sqrt{n+1}\,|n+1\rangle$. Analogously, annihilation operator acts by lowering the energy eigenstate $a\,|n\rangle = \sqrt{n}\,|n-1\rangle$. Interestingly, when the annihilation operator it's applied to a coherent state $|\alpha\rangle$, defined as above unless the squeezing parameter q, the annihilation process does not change the property of the state. In fact:

$$\begin{aligned} a\,|\alpha\rangle &= a\left[\exp\left(-\frac{|\alpha|^2}{2}\right)\sum_{n=0}^{\infty}\frac{(\alpha)^n}{\sqrt{n!}}|n\rangle\right] = \exp\left(-\frac{|\alpha|^2}{2}\right)\sum_{n=0}^{\infty}\frac{(\alpha)^n}{\sqrt{n!}}\,a\,|n\rangle = \\ &= \exp\left(-\frac{|\alpha|^2}{2}\right)\sum_{n=0}^{\infty}\frac{(\alpha)^n}{\sqrt{n!}}\sqrt{n}\,|n-1\rangle = \exp\left(-\frac{|\alpha|^2}{2}\right)\sum_{n=0}^{\infty}\frac{(\alpha)^n}{\sqrt{(n-1)!}}\,|n-1\rangle = \\ &= \exp\left(-\frac{|\alpha|^2}{2}\right)\sum_{n=-1}^{\infty}\frac{(\alpha)^{(n+1)}}{\sqrt{(n)!}}\,|n\rangle = \alpha\,\exp\left(-\frac{|\alpha|^2}{2}\right)\sum_{n=-1}^{\infty}\frac{(\alpha)^n}{\sqrt{(n)!}}\,|n\rangle = \\ &= \alpha\left[\exp\left(-\frac{|\alpha|^2}{2}\right)\sum_{n=0}^{\infty}\frac{(\alpha)^n}{\sqrt{(n)!}}\,|n\rangle\right] = \alpha\,|\alpha\rangle\,, \end{aligned}$$

where the $n = -1$ eigenstate in the sum is set to zero since it has no meaning to consider energy states lower than the ground state $|0\rangle$. As it can be noticed, the result is a rescaling of the coherent state. Thus, such states are fairly robust upon perturbations. In this framework, the n-*th* power of the self-similarity equation written above can be recovered by the n-*th* application of the operator a to the coherent state $|q\alpha\rangle$, and by considering real $q\alpha$:

$$\langle q\alpha|(a)^n|q\alpha\rangle = (q\alpha)^n\,.$$

Alessandro Loppini

The last equation gives the connection between the self-similarity relation and the coherent state formalism. Thus, scale-free properties in the PDS plots of β-cells membrane potential can be linked to the formation of such coherent states characterising different dynamical regimes, which are modulated by specific parameters such as glucose stimulation and population size. The coherent state parallelism suggests that, as expected, long-range correlations are implied in the emergence of organised bursting oscillation. In confirmation to that, the correlation matrix computed from the simulated electrical activity of a medium cluster (125 cells) shows high correlation levels at a glucose concentration evoking robust bursting (> 0.9). On the contrary, a low degree of correlation is presented at sub-threshold stimulations ($\simeq 0.4$), as it can be noticed in Fig. 5.11.

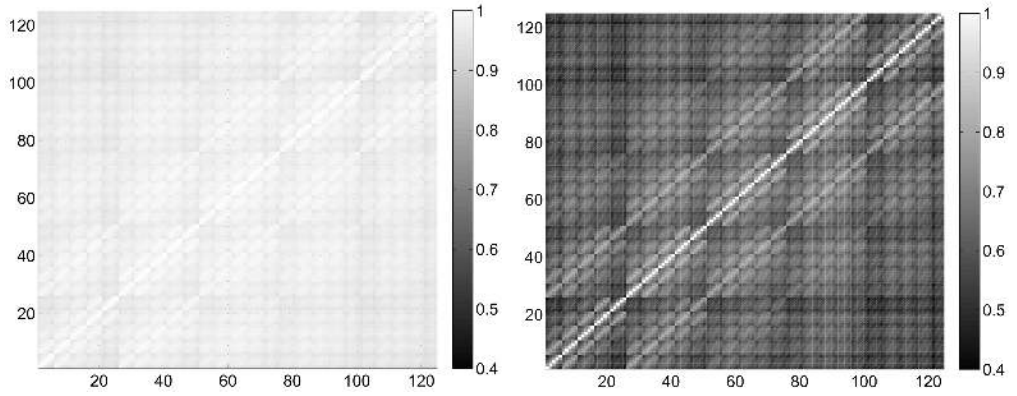

FIGURE 5.11: Correlation matrix plots computed from simulated voltage times series of mouse β-cells in a 5 x 5 x 5: (a) postprandial glucose concentration ($[G] = 9.5\,mM$), (b) sub-threshold glucose concentration ($[G] = 4.7\,mM$). Axis labelling corresponds to a sequential ordering of the cubic cluster from the bottom to the top.

5.4.2 Discussion

As mentioned above, β-cells in mouse islets show a coordinated electrical activity and robust bursting oscillations in response to glucose stimulation. In confirmation of that, experimental recordings show phase lags of only $1 - 2\,s$ between the glucose-stimulated activity of cells located in opposite sites in the islet [51, 100]. In this framework, cells communication via electrical coupling is a fundamental aspect in order to coordinate cells activity. In fact, isolated β-cells, or islets lacking junctional channels, show an altered glucose response and a significant loss of cellular synchronisation, that is a crucial aspect for an oscillatory insulin release [58, 103]. In addition, experimental studies show that glucose level itself seems to regulate cells synchronisation [112].

Alessandro Loppini

With the use of a SRK model generalisation, the analyses presented above show that the formation of coherent dynamical regimes could underlie such coordinated phenomena. Specifically, membrane potential signals of cells within the simulated clusters show scale-free characteristics in the frequency domain, that are regulated by specific system parameters, such as glucose bath concentrations, and the number of units forming the coupled multicellular system. PDS analysis shows that such self-similar behaviours are observed in different frequency ranges, possibly suggesting that scale-free properties are present at different dynamical scales of the system, connected to both stochastic channel gating and bursting dynamics. As shown above, self-similarity in the PDS has a correspondence in terms of squeezed coherent states, usually adopted to describe high correlated quantum systems [113, 114], so that a long-range correlated and robust electrical response can be elicited by proper glucose stimulation (around $\simeq 9\,mM$), and in clusters larger than a certain threshold (> 10 cells). As a confirmation of that, perturbations of the membrane potential V does not almost affect the slopes in the PDS plots (as stated from slope values reported in Tab. 5.2), in line with the stability of coherent states. Thus, HF and LF intervals show that a coherent dynamics is working both at the single cell level and at the β-cell population level, as stated by the correspondent time scales. It is important to note that the squeezed coherent state description suggests a formal analogy between the biological system and quantum physics because of specific characteristics of the emergent dynamics, i.e. self-similarity trends. Within specific regimes, in fact, such parallelism exists although it is not trivial to give a direct biological interpretation. However stochastic, coherent, and coordinated, dynamics is a feature of β-cell activity. Indeed, a strong link between stochastic and quantum systems exists [115], justifying such an approach.

With these assumptions, the clear change of the LF slope in PDS plots by varying control parameters, i.e. cluster size and glucose, is reminiscent of phase transition phenomena observed in many physical systems, such as financial stock markets, vehicular traffic, earthquakes, and epidemics spreading [116–119]. Dynamics of these systems shows self-organised criticality, in the sense that in particular conditions they operate around a critical point so that small scales changes within the system can rapidly be reflected in long range effects. In this framework, is here shown that such dynamics is present also in β-cells coupled clusters. In particular, minimal changes in the HF slope at increasing number of cells and glucose stimulation levels suggest that system dynamics at fast time scales is mainly affected by intrinsic cell properties, and coherence may be linked to intrinsic cellular processes. While the scale-free trend at low frequencies, comparable to bursting time scales, indicates a coherent behaviour in cellular population, since bursting oscillation emerges as a collective phenomenon in the analysed model. Its appearance and variation in particular conditions are consistent with a phase-transition in the cluster

behaviour (Fig. 5.9). At sub-threshold and high glucose stimulations, no detectable slow oscillations can be observed; the same happens in small cell aggregates. In a suitable glucose range, i.e. $5\,mM < [G] < 14\,mM$, and in large enough clusters, a bursting regime arises, as indicated by the LF peak at $\simeq 0.07\,Hz$. Such peak appears in combination with a linear logarithmic decay of the voltage signal power density: the system switch from a decorrelated dynamics to a correlated bursting response. In this sense, phase-transition has to be understood in terms of a dynamical switch to a coherent slow oscillation pattern (with a superimposed spiking activity) driven by selected parameters such as cell numbers and strength of the interacting field, i.e. glucose bath. Taking this into account, the studied phase transitions could be linked to the ones pointed out in other studies on β-cells clusters (see ref. [82]). Specifically, authors have analysed the emergence and suppression of the global electrical activity of multicellular systems composed by a mixture of excitable and non-responsive cells coupled by a variable coupling strength, with the aim to address the effect of mutant ion channels on the whole islet response. In this comparison, results here presented obtained at different glucose concentrations can be linked to the experimentally analysed case of Cx36 +/+ mouse islets, where the whole cells population shifts from a silent to an active state (see Figs. 6 and S8 in the cited reference) by modulation of the KATP conductance with the use of the channel opener diazoxide. A critical transition arises by varying stimulatory conditions. Obtained scale-free relation, its parallelism with the coherent state formalism, and the evidence that suppression and emergence of correlated dynamics happen in a physiological range of parameters support the idea of a system responding to the environment as a functional unit where cellular dynamics shows self-organised criticality. In conclusion, operating around critical points could be the best way to regulate a synchronised and fast response to glucose inputs, leading to a proper insulin release from the whole islet. It is interesting to note that self-organised criticality, coherence, and self-similarity properties can also be found in the brain activity [114, 120–124].

Based on the SRK generalised model here presented, correlations in cells activity are studied in Chapter 6 by taking into account intrinsic differences of islet architecture, and hence β-cell clusters topology, between different species. The electrical response of these complex cellular networks will thus be analysed in response of changes in the coupling conductance strength and intrinsic cellular noise other than by vary glucose stimulation, discussing evoked synchronisation patterns and critical behaviours from a functional point of view.

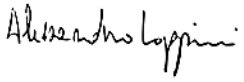

Chapter 6

Structural effects on mouse β-cell networks activity

In the previous Chapter, has been introduced the SRK multicell model and its generalisation, which was used to analyse coherent dynamics in mouse islets. This formulation takes into account the important evidence that β-cells in the pancreatic islets are electrically coupled. A consequent aspect that has to be considered in this context is the cells arrangement in their biological environment, i.e. the islet structure. In fact, cells disposition is crucial for the definition of nearest neighbours interactions ensured by gap junction coupling. As anticipated in Chapter 3, such communications are a key aspect of cell function, filtering noise induced by ion channels stochastic gating, homogenising cells population, enhancing glucose responsiveness, and maximising insulin secretion and pulsatility. Of course, also other pathways of communications can be established between cells, i.e. diffusion of specific molecules in the extracellular space, but the direct electrical coupling represents the more efficient and fastest way through which cells transmit signals. Moreover, such coupling naturally implies a spatial organisation of cells, that assemble in clusters of specific shapes and sizes. Thus, in order to describe such communicating network, it is necessary to analyse endocrine cell disposition within the islets, the size of β-cells clusters, and their local architecture. In this Chapter such topological aspects and their effects on β-cell emergent dynamics are analysed via mathematical modelling.[1]

[1] The novel study here presented is reported in ref. [125].

Alessandro Loppini

6.1 Pancreatic islets architectures

Several studies have highlighted that both islet composition and architecture differs consistently from species to species [5], and can be hypothesised that such differences have implications for the islet function [126]. Fig. 6.1 shows a phylogenetic tree representing islet composition and cells disposition within the islets of different species.

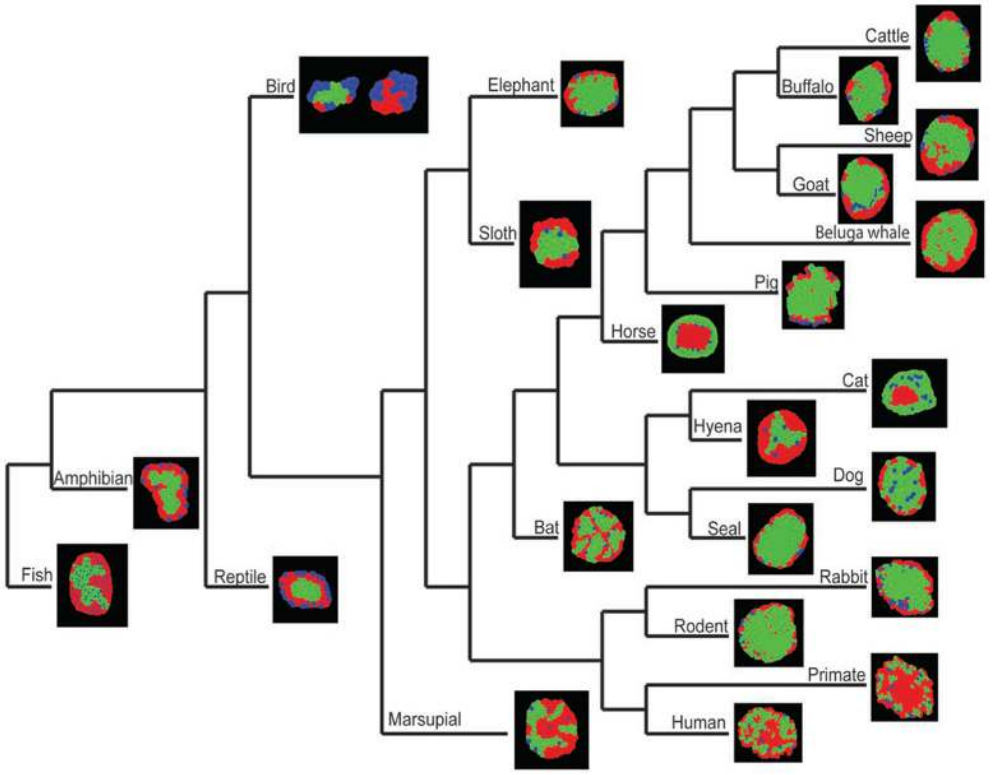

FIGURE 6.1: Phylogenetic tree representing islet compositions and cells dispositions within the islet of different species. From ref. [5].

It is worth noting that some species present a reversed disposition of islet cells compared to other cases. For instance, the horse islet is characterised by a central core of α-cells surrounded by a mantle of β-cells, with PP-cells and δ-cells placed in the islet periphery. The mouse islet instead presents a central core of β-cells surrounded by a mantle formed by other endocrine cells. The reason for such diversity is still not known, but different development mechanisms during islets formation, as well as evolutionary aspects involving different metabolic needs and diets, have been hypothesised [5]. Indeed, several studies have shown islet morphological changes in response to conditions such as pregnancy and obesity, highlighting the fact that the islet is a plastic system able to adapt to environmental changes [127–129].

Because most of the published studies in literature regard mouse and human islets, only these two islet structures are analysed in the following. As anticipated β-cells in the

Alessandro Loppini

mouse are organised in a compact central cluster surrounded by the other islet cells. About $60-80\%$ of islet cells are β-cells, followed in fraction by the α $(15-20\%)$ and δ-cells $(<10\%)$. On the contrary, in humans β and α-cells fractions are much more variable, with mean values of about 50% and 40% respectively, while δ-cells are about 10% of the islet cells [5, 126, 130]. Endocrine cells are not segregated in different areas as in the mouse but are intermingled across the whole islet giving rise to an apparently random configuration.

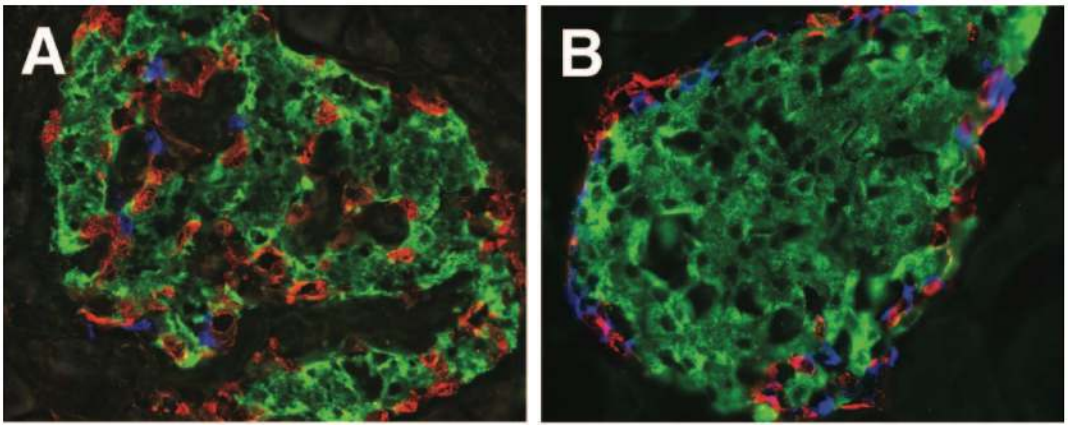

FIGURE 6.2: Histological sections of (A) human and (B) mouse islets, obtained by confocal microscopy. Histological sections ($8\mu m$), magnification x40. From ref. [130].

In Fig. 6.2 are presented two confocal microscopy images showing both human and mouse islet sections, from which is possible to appreciate the differences listed above. These differences have a great impact on cellular communication, both with respect to synchronisation induced by gap junctions coupling and with respect to paracrine interactions. For instance, β-cells in the mouse islet show about 71% and 29% of homotypic and heterotypic contacts respectively, while the 98% of α-cells contacts are heterotypic. Instead in humans, the 71% of β-cells contacts are heterotypic, thus presenting an opposite situation compared to the mouse. Such abundance of heterotypic interactions could be due to different control mechanisms of insulin secretion, maybe requiring paracrine signalling to achieve an optimal function. Such thesis is confirmed by recent studies showing that α-cells in human islets can release acetylcholine and affect insulin secretion via the muscarinic receptor on the β-cell surface, promoting IP3 production and increasing intracellular calcium levels while this function is fulfilled by cholinergic inputs in mouse [131].

Unfortunately, because of a lack of data, it is still not possible to build a model comprising all the complex feedbacks and communication pathways observed in pancreatic islets. Moreover, the interest is not to analyse paracrine effects but to study the impact of these different architectures in the synchronisation of electrically coupled β-cells.

Alessandro Loppini

Such purpose is also motivated by the evidence of gap junctions in human islets (see Chapter 7 for further details on gap junctions in human islets), suggesting that electrical coupling may be the primary way to synchronise cells activity also in this case. On this basis, the work presented in the following aims to study the spatiotemporal behaviour of the emergent bursting activity, via the generalisation of the SRK model described in Chapter 5.

6.1.1 Architecture modelling

In line with the analyses presented in Chapter 5, a mouse pancreatic islet can be represented by a three-dimensional cubic grid of cells. In this configuration, considering a three-dimensional Von Neumann neighbourhood, all cells in the core have 6 neighbours, in agreement with published data of electrical coupling in rodents. In fact, some studies based on Lucifer Yellow dye diffusion pointed out a value of $2-5$ neighbours per cell [132, 133], but such values are probably underestimated because of the limited permeability of the junctional channels to cationic compounds. While a recent study based on electrophysiological measures on mouse islets found a number of $6-7$ neighbours per cell, moreover verifying the limited diffusion of the Lucifer Yellow dye through Cx36 gap junctions [134]. Other modelling studies are instead based on a hexagonal packaging of the cells, where each single unit connects to 12 neighbours [135]. Confirmations of such a large number of neighbours have not been found in the literature. Although, considering that experimental observations on mouse islets pointed out that 33% of adjacent β-cells are not coupled together [68], by taking into account missing couplings the hexagonal cells arrangement can reproduce a number of neighbours close to the measured value ($\simeq 8$). However, in line with other modelling studies [94, 95], a compact cubic structure is used in the following to investigate emergent dynamics of mouse-like β-cells aggregates.

The human islet modelling needs instead special cares in order to correctly reproduce the apparently random distribution of cells. Specifically, taking into account only the β-cells, the human islet can be viewed as a percolated structure. Such β-cell network can be thought to be generated from a compact structure (the islet), by random deletion of cells, i.e. the non β-cells, thus resulting in a non-compact structure. Percolation theory has been widely used and applied in different fields, such as diffusion in porous media, glass transitions, galaxies formation, phase transition on complex networks [136], and can be used in this case to model the sparse β-cells arrangement in humans.

Consider a regular three-dimensional cubic lattice where the cells are located on the grid intersections (sites) and where the lines represent connections between cells (bonds).

Percolation can be performed both on the sites (site percolation), i.e. by eliminating the nodes of the grid, or on the bonds (bond percolation), i.e. by eliminating connections between cells. Elimination of sites or bonds takes place with a probability p defined as "percolation probability". For $p = 0$ the grid is empty or the sites fully decoupled. By increasing p, small coupled sub-clusters can be observed, and at a critical value p_c a coupled cluster, spanning the whole domain, appears. Such value is called "percolation threshold" and the spanning structure takes the name of "percolating cluster". Increasing further p, reduces the number of clusters which become bigger, and for $p = 1$ the regular lattice grid can be recovered. An example performed on a regular two-dimensional lattice is described in Fig. 6.3.

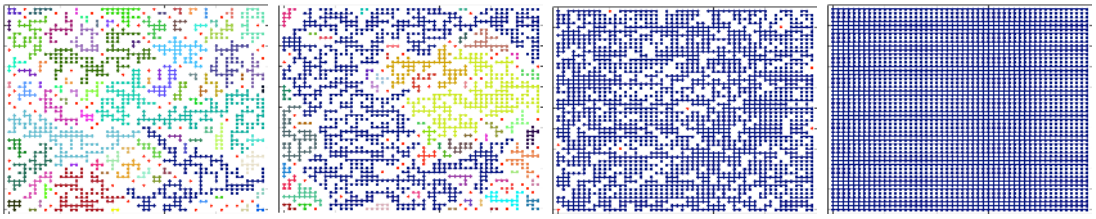

FIGURE 6.3: Site-percolation on a two-dimensional regular lattice: (a) p=0.5; (b) p=0.6; (c) p=0.8; (d) p=1. The bigger connected cluster is coloured in blue.

Based on this approach, a site percolation can be adopted to simulate the human islet random arrangement, starting from an appropriate compact grid. In Fig. 6.4 the whole procedure is shown. In this analysis a regular $10 \times 10 \times 10$ lattice is taken into account, and the percolation probability is set at $p_s = 0.54$. These choices are in line with the real islet size (thousands of cells), and with the mean fraction of β-cells in human islet (54%). Such fraction is also the probability of site occupancy in the percolation process (since sites occupied by α and δ-cells can be viewed as empty). This procedure mimics a random arrangement of β-cells within the islet but doesn't take into account the probability of missing coupling between cells. As stated before, measurements performed on mouse islets show that not all adjacent cell are effectively coupled together. Due to its compactness, the mouse structure is probably insensitive to such fraction of missing couplings, but translating this finding on human islets, where cells have fewer neighbours compared to the mouse, such evidence can have a significative impact on the cluster response. Thus in order to obtain a final representative picture of the human islet, a bond percolation process with a value $p_b = 0.67$ is further performed, besides the site percolation already described. To note that bond percolation on compact structure has already been used in computational studies on mouse islet to study the dependence of calcium wave propagation on islet connectivity [100], while a combined site-bond percolation is adopted in the present study to build a human-like β-cell cluster.

Alessandro Loppini

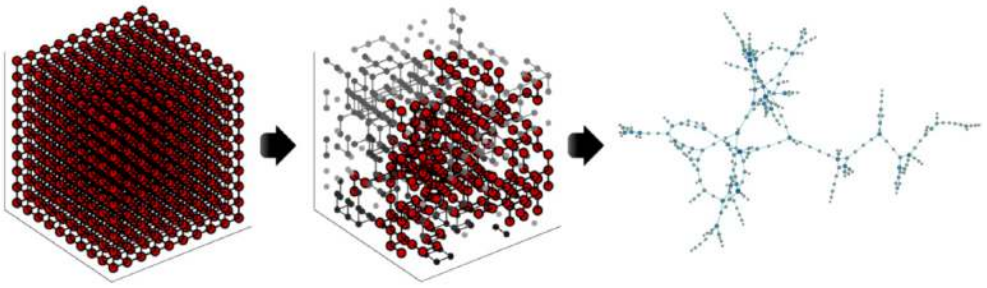

FIGURE 6.4: Human islet modelling via percolation on compact cubic cluster: starting 10 x 10 x 10 cluster (left), intermediated structure formed by decoupled clusters (center), largest component (260 cells) of the human-like islet (right).

Resulting structure (central cluster in Fig. 6.4) it is composed of several decoupled components. Since these are physically disconnected, the interest is to analyse synchronisation patterns within a representative sub-cluster, analysing changes in electrical response due to the non-compact architecture. For this purpose, the bigger sub-cluster (260 cells) is finally extracted from the human-like islet (right cluster in Fig. 6.4). Such architecture presents a mean degree, i.e. a mean number of neighbours per cell, of 2.26, and a maximum value of 5 neighbours. The last is in line with the only reported value of neighbours in human islets measured from diffusion of EB [137], although mean value is considerably lower compared to reported measurements. Thus, analysis performed in the following with such architecture should be validated in future studies in light to more comprehensive histological investigations, fully addressing human β-cell network topology, avoiding possible underestimation of connectivity by considering other cells packaging or percolation procedures.

In their original work Sherman at al. [33, 94] investigated the emergence of organised bursting by increasing the number of coupled β-cells in the cluster while the aim of this study is to characterise the effect of topology on the electrical behaviour. For this purpose, a compact cluster and a linear chain with the same number of cells are here modelled to compare the percolated network response with a case resembling the mouse architecture, and with a degenerate case usually adopted to analyse complex dynamics of coupled oscillators. In order to construct the compact cluster, a 7 x 7 x 7 grid is sequentially filled with cells, stopping the cluster construction once the desired number of units is reached. In Fig. 6.5, a representation of the three final architectures, to be analysed with the generalised SRK multicell model, is given.

Alessandro Loppini

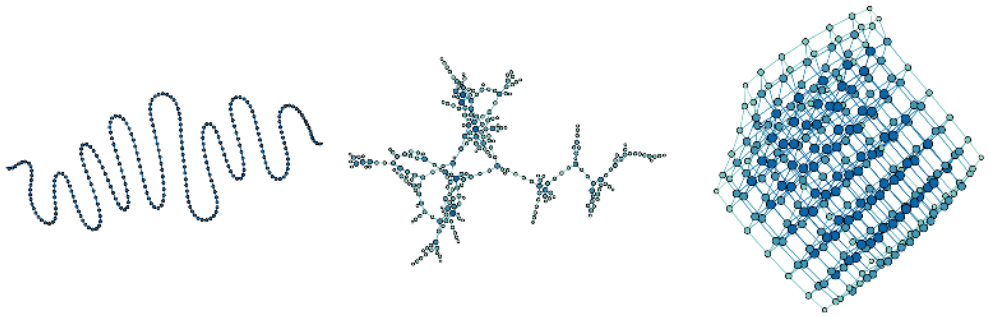

FIGURE 6.5: Modelling of β-cells clusters topology: linear chain (left), percolated cluster (center), compact cluster (right).

6.2 Functional network: a synchronisation measure

Synchronisation analysis is based on a "functional network" approach. A functional network it's different from the underlying physical network, and describes system interactions on the basis of nodal activities correlation. Thus, two cells in a functional network are coupled if their activity is sufficiently correlated, without considering the actual physical interactions. This method is usually applied to the analysis of brain activity, studying functional networks computed on the basis of experimental spatiotemporal data from fMRI (functional Magnetic Resonance Imaging), EEG (Electroencephalography) and MEG (Magnetoencephalography) [138–140]. Only recently it has been applied to the pancreatic islets [112, 141]. Therefore the functional network analysis, used here to study synchronisation patterns, can also be used to inferring system structure from the functional one, being the latter the only one accessible from experiments most of the times. Functional network construction in this study is based on the correlation coefficient R_{ij} between all pairs of β-cells in the cluster, computed on the voltage membrane signals resulting from model simulations:

$$R_{ij} = \frac{\langle \left(V_i\left(t\right) - \langle V_i\left(t\right)\rangle\right)\left(V_j\left(t\right) - \langle V_j\left(t\right)\rangle\right)\rangle}{\sigma_i \sigma_j},$$

where σ_i is the standard deviation of $V_i\left(t\right)$. A link between separate cells is added if the temporal correlation of their electrical signals is greater than a threshold value. Following Stožer et al. [112], this value is here set to 0.8, in order to consider the strongest correlations. Thus, the obtained functional network codes informations on cells synchronisation across the whole cluster. Since, synchronisation properties change with respect to operating conditions, i.e. model parameters, functional networks have a dynamical topology. The study of this varying topology, with the use of the standard statistics usually adopted in the complex network theory, permits to characterise variations in β-cells coordination at different operating regimes. For completeness a list of the observables

used in the analysis are given in the following (see ref. [142, 143]): i) the degree of the *ith*-node (number of neighbours for each cell) $k = \sum_j a_{ij}$, where a_{ij} is the adjacency matrix encoding the topological information of the cluster; ii) the degree distribution computed from the nodes frequency in the network, $P(k) = \frac{N_k}{N}$, where N is the total number of nodes and N_k is the number of nodes with degree k; iii) the cumulative degree distribution $P_{cum}(k) = \sum_{k'=k}^{\infty} P(k')$; iv) the average nearest-neighbour degree as a function of k, i.e. $k_{nn}(k) = \frac{1}{N_k} \sum_{i,k_i=k} k_{nn,i}$, where $k_{nn,i} = \frac{1}{k_i} \sum_j a_{ij} k_j$, that is the average degree of the nearest-neighbours for the node i; v) the average clustering coefficient $C = \frac{1}{N} \sum_i c_i = \frac{1}{N} \sum_i \frac{2e_i}{k_i(k_i-1)}$, where e_i are the number of edges in the subgraph of the neighbours of i, and $k_i(k_i-1)/2$ is the maximum number of edges in the subgraph.

6.3 Structure-function coupling analysis

In Fig. 6.6, the voltage times series, computed with the use of the generalised SRK model, are shown. In this case the clusters are stimulated by a glucose concentration higher than stimulation threshold ($[G] \simeq= 7mM$, i.e. $k_{Ca} = 0.03\, ms^{-1}$ in the model), and the gap junction conductance is set at the physiological mean value ($g_c = 215\, pS$). It is clear that the network topology affects electrical oscillation robustness, with increasing disruptive effect of noise for decreasing compactness of the cluster. This behaviour is due to the "channel sharing" phenomena described by Sherman et al. [33], although in this case the emergent bursting in not affected by the number β-cells in the cluster, but depends on the local connectivity of cells, being the number fixed. The functional network procedure described above is now adopted to study spatial coordination and cell synchronisation. In Fig. 6.7 the obtained results are shown, i.e. the surface plots of the $[N_{cell}\, \mathrm{x}\, N_{cell}]$ correlation matrix computed from the simulated voltage time series, the associated functional networks and the space-time plots of the electrical activity.

In the linear chain, the space-time plot (Fig. 6.7(a)) shows a short-range synchronisation, with several excitation waves arising from different points in space and time, occasionally colliding. This evidence is supported by the structure of the functional network, which presents a mean node degree equal to 4 for the central cells of the chain. The compact cluster shows instead an opposite behaviour (Fig. 6.7(c)), where the space-time plot of the voltage reveals quasi-horizontal bands highlighting a long-range synchronised bursting. The x-axis of this specific plot represents a sequential ordering of the cluster, from the bottom up to the top. In this case, the functional network is characterised by a fully coupled topology, thus correctly captures the globally synchronised activity of the compact structure. The percolated cluster shows an intermediate behaviour compared

Alessandro Loppini

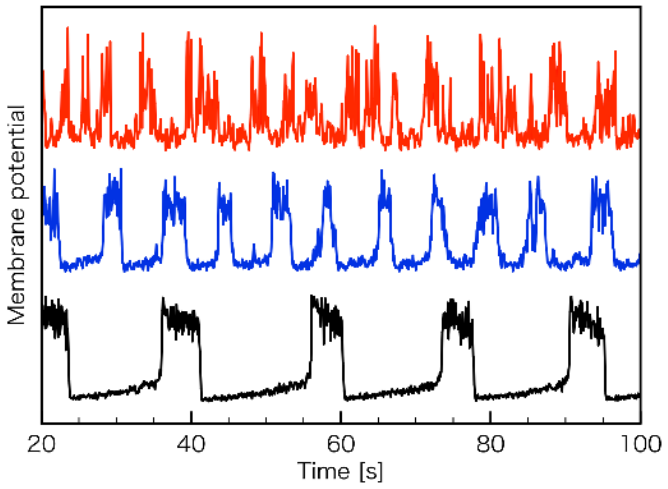

FIGURE 6.6: Membrane potential time series of a representative cell within the three clusters shown in Fig. 6.5: linear chain (top, in red), percolated structure (middle, in blue), compact cluster (bottom, in black).

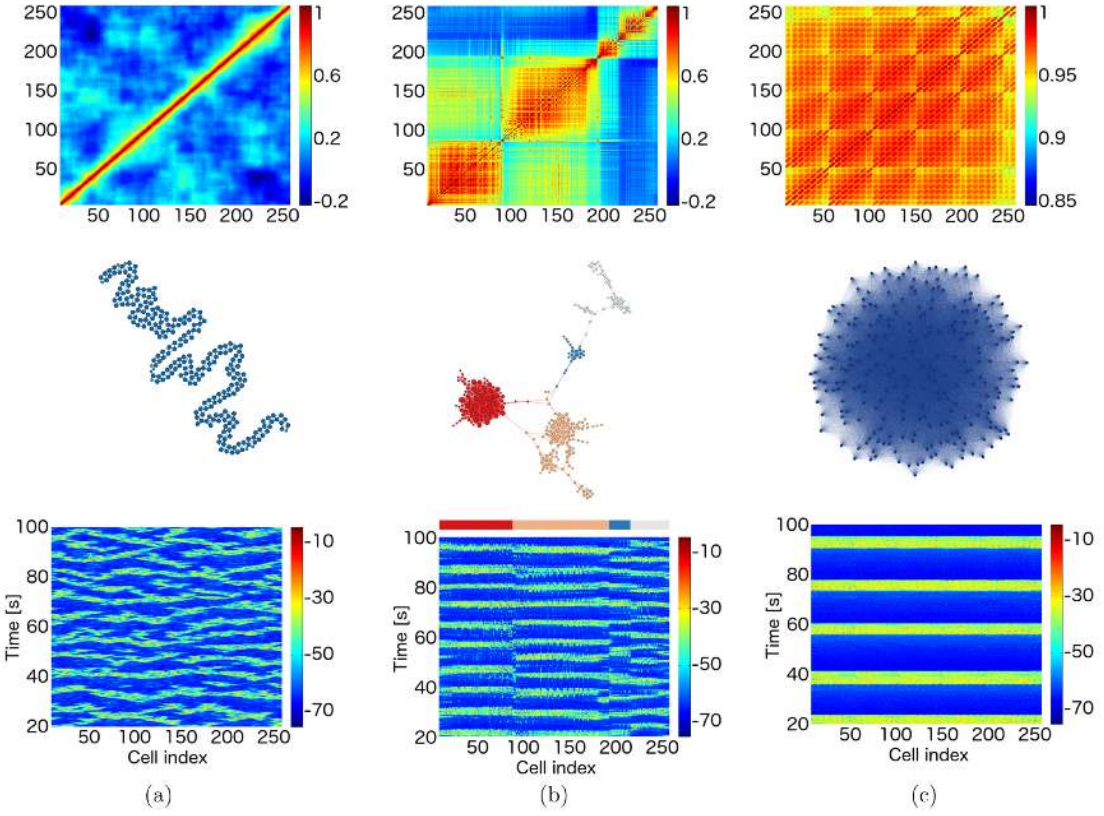

FIGURE 6.7: Correlation matrix (top row), functional networks (central row), and space-time plots (bottom row) computed on β-cells membrane voltage for each simulated topology: (a) linear chain, (b) percolated cluster, (c) compact cluster. In simulations $g_c = 215\,pS$ and $[G] = 7.1\,mM$. Color code of the percolated functional network identifies the corresponding cell subpopulations in the space-time plot.

Alessandro Loppini

to the linear and the compact case. In this case, the functional network presents a modular topology, characterised by at least 4 subpopulations (Fig. 6.7(b)). Spatial ordering in the space-time plot has been performed based on these functional modules without taking care of the internal structure of each module, being that the more efficient way to order unidimensionally such system. Interestingly space-time plots reveal the presence of an out-of-phase bursting and a synchronised activity within each module, and since it is derived from the functional network topology, validates the functional network approach.

It is now interesting to characterise the sensitivity of these functional topologies, to specific model parameters that are related to the operating conditions of the β-cell clusters. Specifically, it is of interest to analyse synchronisation patterns for different glycemic conditions, coupling conductances, and noise levels, trying to characterise bursting robustness in response to such variations. These analyses are described in the following.

6.3.1 Coupling strength effect

Considering that some pathological states can have a negative effect on β-cells gap junction coupling, it is significative to address the impact of the loss of coupling on the electrical activity. At instance, downregulation of Cx36 in glucotoxic islet environment, i.e. in prediabetic or diabetic states, is likely to have a deleterious effect on cells synchronisation. The study of functional networks by varying the coupling strength, can elucidate synchronisation patterns in such pathological scenario. The three clusters described before are now studied at four values of coupling strength $g_c = 100, 215, 300, 400\,pS$, keeping fixed the stimulating glucose concentration $[G] \simeq 7mM$. In Fig. 6.8, simulations results in terms of functional networks are shown. β-cells in the percolated and the linear cluster, at low values of coupling ($g_c = 100\,pS$), do not present correlated activity and a functional disconnection of the cluster can be observed. The compact structure instead seems to be more robust, showing high synchronisation levels also with low coupling strengths.

Increasing g_c at the physiological values leads to a functional connectivity increase in all the three cases analysed, recovering the analysis previously described. It is interesting to note the emergence of such strongly interconnected functional communities from a small number of physical connections. Increasing further g_c over the physiological mean evokes as expected an increasing in the connectivity of the functional networks. Such evidence implies a higher degree of synchrony but is not necessarily beneficial for the islet's global activity. Synchronisation in the compact cluster is not affected by such

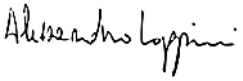

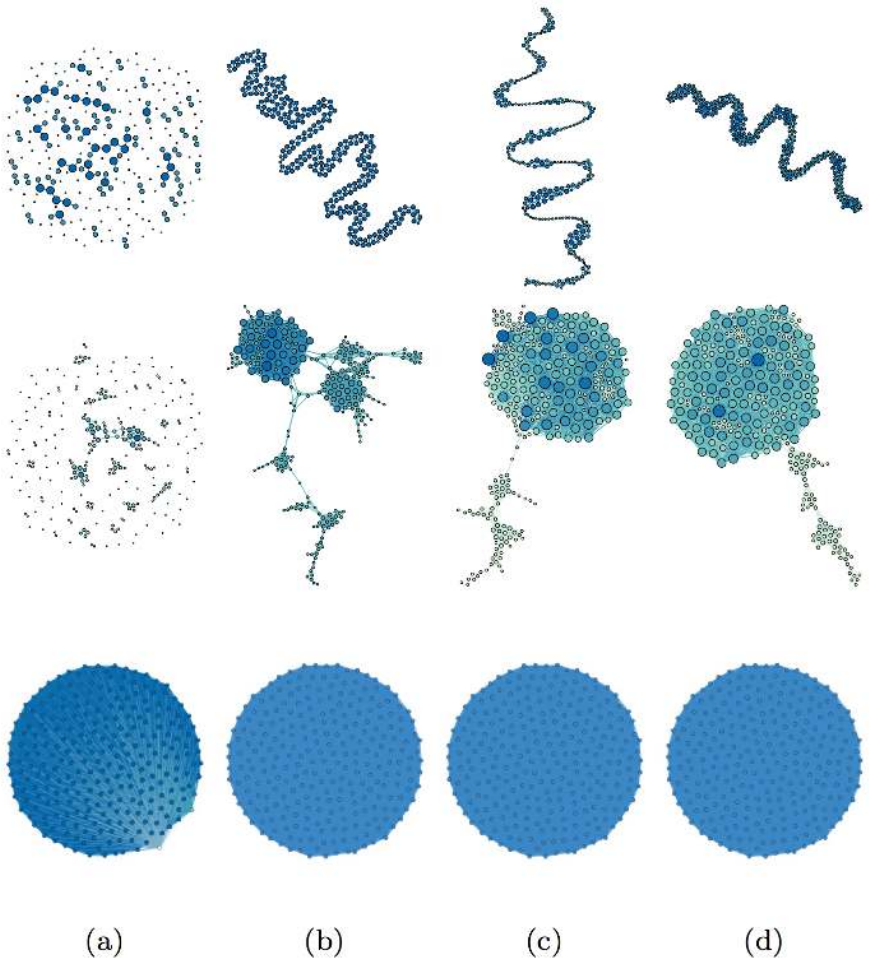

FIGURE 6.8: Computed functional networks at fixed glucose concentration ($[G] = 7.1\,mM$) and increasing coupling strength: (a-d) $g_c = 100, 215, 300, 400\,pS$. Top: linear chain. Center: percolated cluster. Bottom: compact cluster.

increments, showing a fully synchronised state also at a lower coupling, but the human-like cluster, for instance, loses its modularity observed at physiological values of coupling, maybe losing a required property for optimal functioning of the islet. The clustering coefficient of the functional networks computed at different values of g_c is reported in Tab. 6.1, and quantify the described increasing in the correlation of cells activity. The higher is the clustering, the more compact is the functional network, thus indicating synchronisation in this context.

For the non-trivial percolated case, it is interesting to compute other statistics of the network to grasp fully correlations properties. In Fig. 6.9, the degree distribution $P(k)$, the cumulative distribution, and the average nearest neighbours degree (AVNND) of the functional network are reported. For the mean physiological value of coupling, results show that $P(k)$, and thus $P_{cum}(k)$, follow a trend comparable to log-normal/power law decay, indicating strong inhomogeneities in correlated activities, and possibly suggesting

Alessandro Loppini

TABLE 6.1: Clustering coefficient of functional networks computed at increasing coupling strengths ($[G] = 7.1\,mM$). N600: simulations performed with 600 stochastic K-Ca channels per cell. N300: simulations performed with 300 stochastic K-Ca channels per cell.

$g_c\,[pS]$	Linear		Percolated		Compact	
	N600	N300	N600	N300	N600	N300
100	0.00	0.00	0.06	0.00	1.00	0.86
150	0.00	-	0.26	-	1.00	-
215	0.50	0.00	0.72	0.24	1.00	1.00
250	0.50	-	0.73	-	1.00	-
300	0.56	0.01	0.74	0.41	1.00	1.00
350	0.61	-	0.78	-	1.00	-
400	0.63	0.51	0.80	0.70	1.00	1.00

that normal functioning of such architecture is regulated around a criticality point. The computed AVNND as a function of k, show an increasing trend moreover. This behaviour indicates assortative mixing properties, meaning that nodes with a certain degree, i.e. cells with a given number of neighbours, are more likely to be connected to nodes with the same degree. Such behaviour can be related to the fact that synchronisation emerges initially within of small communities, which merge by increasing the coupling strength. Plateau value of AVNND at high values of coupling, presented after a cut-off $k \simeq 30$, is probably due to finite-size effect.

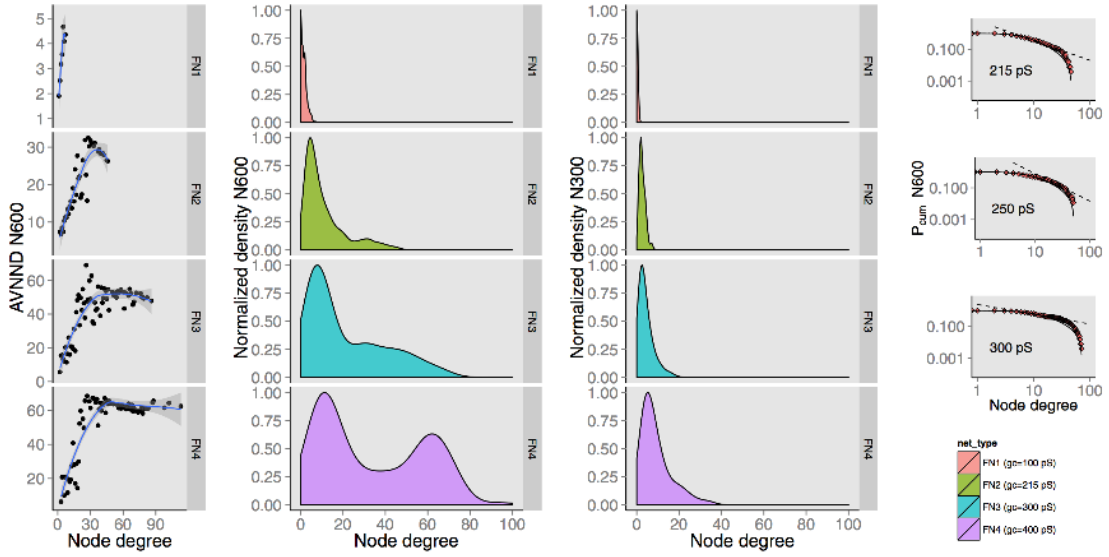

FIGURE 6.9: Degree distribution of functional networks (FN) computed from the percolated cluster activity. Simulations performed by varying the coupling conductance ($g_c = 100, 215, 300, 400\,pS$), and keeping fixed the glucose concentration ($[G] = 7.1\,mM$). A smoothing kernel was used for the normalised histograms fitting. N600 and N300 denote results from simulations performed with 600 and 300 stochastic K-Ca channels per cell, respectively. AVNND: average nearest neighbours degree.

Alessandro Loppini

6.3.2 Glucose effect

β-cells electrical activity changes in response to glucose concentrations, showing silent states, normal bursting and continuous bursting. A consistent effect of such variations on emergent synchronisation is expected (as it was shown in the coherence analysis in Chapter 5). Therefore in this analysis, the functional networks are studied at a fixed value of coupling strength ($g_c = 215\,pS$), and at different glucose concentrations $[G] = 4.7,\ 8.7\,,12.7\,,16.6\,mM$, from the sub-threshold stimulation, up to the concentration evoking sustained activity.

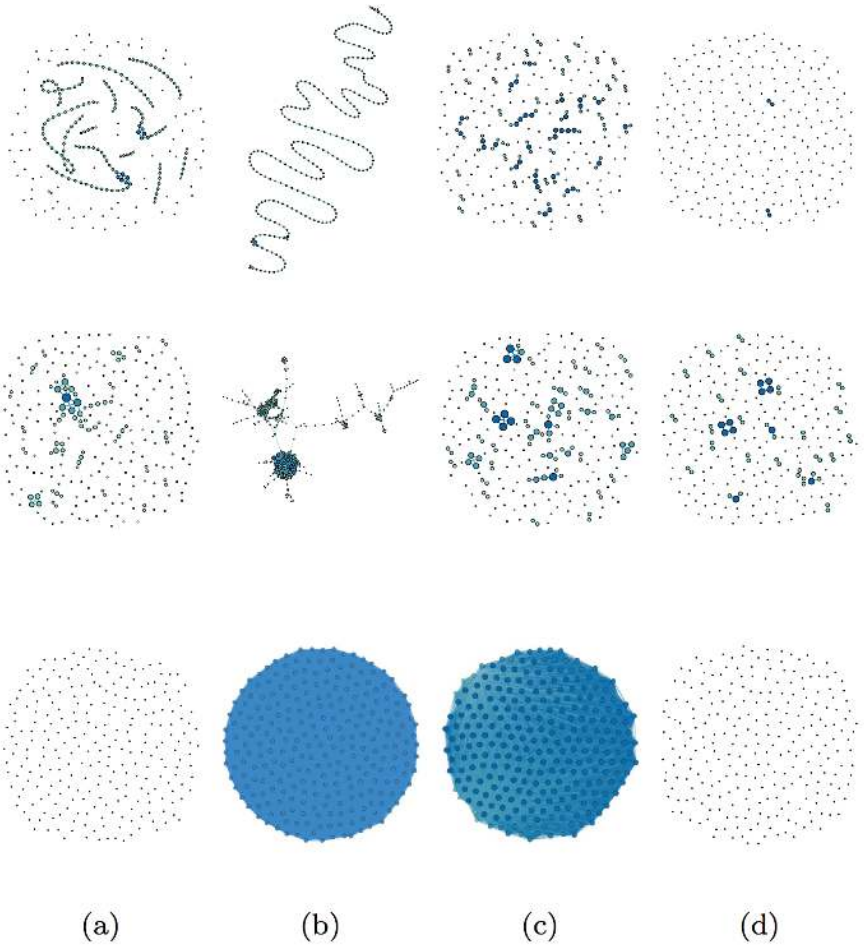

FIGURE 6.10: Computed functional networks at fixed coupling strength ($g_c = 215\,pS$) and increasing glucose concentration: (a-d) $[G] = 4.7,\ 8.7,\ 12.7,\ 16.6\,mM$. Top: linear chain. Center: percolated cluster. Bottom: compact cluster.

In Fig. 6.10, the computed functional networks for the linear chain, percolated and compact clusters are presented. For each of the three cases, at sub-threshold glucose levels, β-cells activity is decorrelated as in the case of low coupling. Similarly, no synchronisation is observed at high glucose stimulatory concentrations. Interestingly, optimal values of the functional connectivity are achieved at intermediate glucose levels, as it

Alessandro Loppini

can be seen qualitatively from the networks shown in Fig. 6.10, and quantitatively from the clustering coefficient values reported in Tab. 6.2. Thus, results suggest an optimal range of glucose ensuring a synchronised activity. Such range is greater in the compact case and shrinks progressively in the percolated cluster and the linear cluster. Also in this analysis, it is interesting to expand the study of the functional network statistic the for percolated structure. The cumulative probability distribution $P_{cum}(k)$ was not computed because of the small number of samples. Results presented in Fig. 6.11 show that both assortative mixing property and inhomogeneity are conserved in the intermediate glucose range previously identified. This evidence could imply that also glucose regulates cells emergent activity around a critical point, in terms of β-cells synchronisation. Strikingly, the glucose range optimising synchronised behaviour is consistent with the glucose peak usually observed after a meal.

TABLE 6.2: Clustering coefficient of functional networks computed at increasing glucose concentrations ($g_c = 215\,pS$). N600: simulations performed with 600 stochastic K-Ca channels per cell. N300: simulations performed with 300 stochastic K-Ca channels per cell.

Glucose $[mM]$	Linear		Percolated		Compact	
	N600	N300	N600	N300	N600	N300
4.7	0.02	0.00	0.03	0.17	0.00	0.00
6.7	0.51	-	0.71	-	1.00	-
8.7	0.03	0.00	0.47	0.21	1.00	1.00
10.7	0.00	-	0.18	-	1.00	-
12.7	0.00	0.00	0.03	0.00	0.97	0.00
14.6	0.00	-	0.00	-	0.00	-
16.6	0.00	0.00	0.00	0.00	0.00	0.00

6.3.3 Noise effect

In Chapter 3 the stochastic process underlying channel gating was discussed. This phenomenon induces an intrinsic noise in β-cell oscillators, which it is likely to have an impact on the clusters synchronisation since it affects membrane voltage oscillations. Noise-induced fluctuations in macroscopic currents are dependent both on single channel properties and on the number of ion channels. In order to study noise impact on functional networks, the same analyses described above are now performed with a reduced population of K-Ca channels (reduced to 300) respect to the original model. This setting has the effect to enhance noise levels by increasing the amplitude of the jumps in the g_{K-Ca} conductance. In Fig. 6.12, the functional networks computed at a fixed value of glucose, and in the range of g_c given previously, are shown. Related clustering coefficients are reported in Tab. 6.1.

As it can be seen, the compact cluster is still able to reach a fully synchronised activity at a physiological value of g_c, losing a small fraction of functional connections at lower

Alessandro Loppini

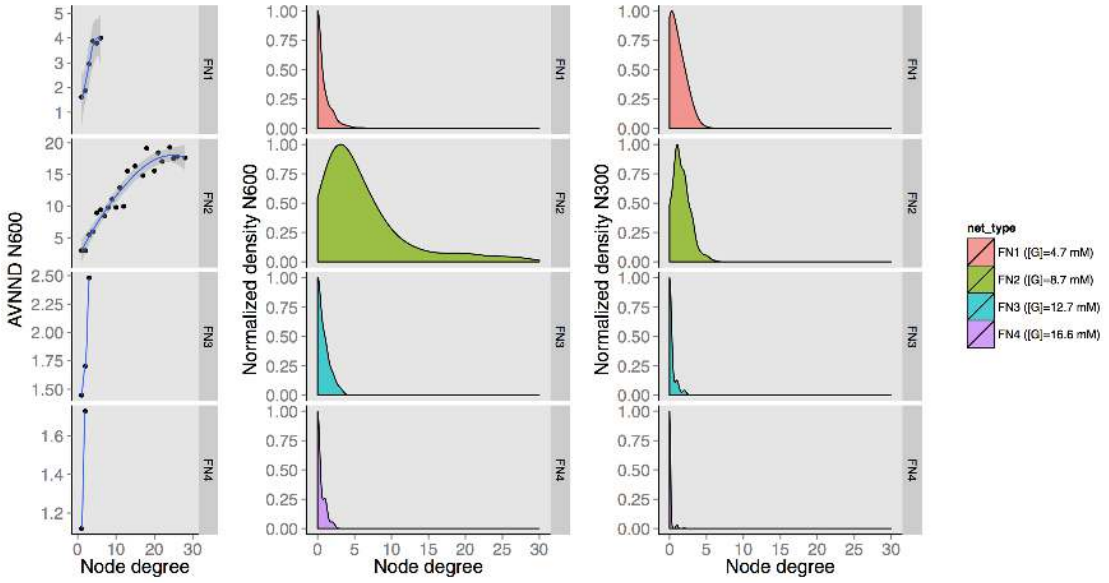

FIGURE 6.11: Degree distribution of functional networks (FN) computed from the percolated cluster activity. Simulations performed by varying the glucose concentration ($[G] = 4.7, 8.7, 12.7, 16.6\,mM$), and keeping fixed the coupling strength ($g_c = 215\,pS$). A smoothing kernel was used for the normalised histograms fitting. N600 and N300 denote results from simulations performed with 600 and 300 stochastic K-Ca channels per cell, respectively. AVNND: average nearest neighbours degree.

values of the coupling. Linear and percolated cluster are not able to reach a high degree synchronisation, showing that doubled values of conductance are needed to reach same values of functional connectivities respect to the 600 K-Ca channels case. Varying glucose level and keeping fixed g_c, show similar behaviours. In Fig. 6.13 and in Tab. 6.2, the computed functional networks and clustering coefficients are presented respectively. As it can be noticed, specific ranges of glucose maximising cells synchronisation are still present. However, increased noise perturbations have a shrinking effect on these ranges, and reduce the level of synchronisation compared to the less noisy case. Degree distribution computed for the percolated cluster, shown in Figs. 6.9 and 6.11, also confirm that inhomogeneity of the functional network is still observed at coupling values almost doubled respect to the physiological mean, and for glucose concentrations $[G] \simeq 8 - 9\,mM$. Thus, functional networks properties seem to be robust respect to noise perturbations despite a lower correlation in the electrical activity is reached.

6.4 Discussion

Networks topology of electrically coupled β-cells differs from species to species [5, 126]. Such differences depend both on the β-cells arrangement within the islet, and on the islet composition. Moreover diabetic states can alter significantly the islet topology, i.e.

Alessandro Loppini

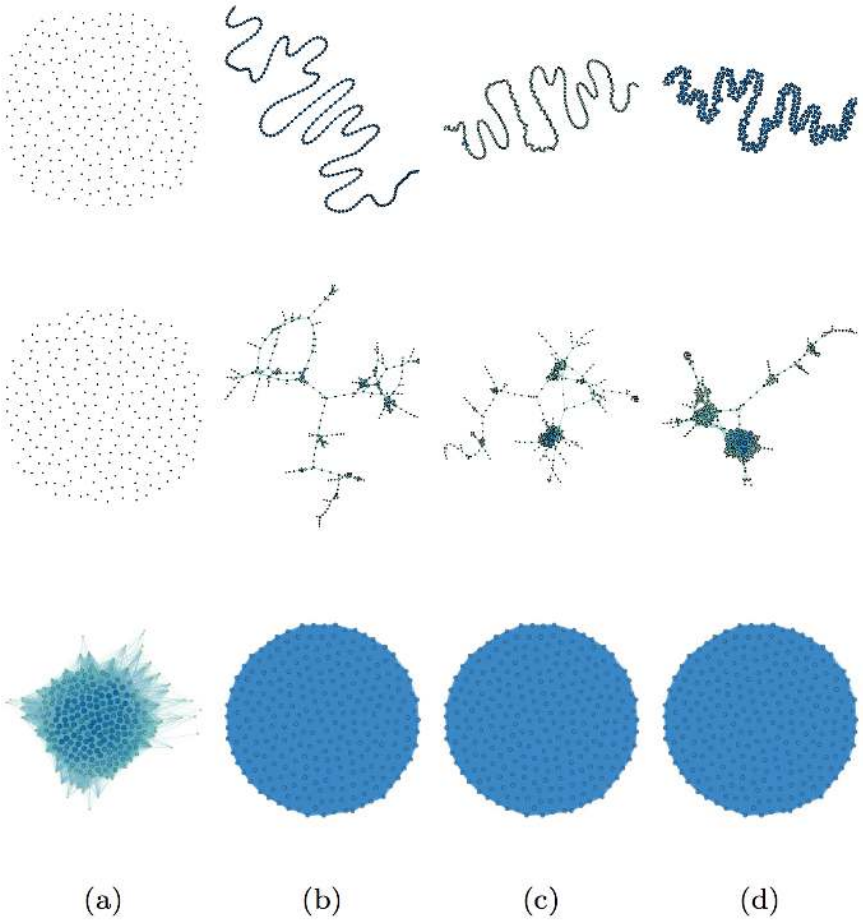

FIGURE 6.12: Computed functional networks at fixed glucose concentration ($[G] = 7.1\,mM$) and increasing coupling strength: (a-d) $g_c = 100, 215, 300, 400\,pS$. Simulations performed by setting the number of K-Ca channels to 300, in order to increase noise strength. Top: linear chain. Center: percolated cluster. Bottom: compact cluster.

the loss of β-cells observed in Type 1 and 2 diabetes can be thought to have an impact both on the number of nodes and on the connectivity of the network, with dramatic effects on insulin release. The original SRK study and other published generalisations were mainly devoted to analyse emergent bursting and synchronisation in β-cells compact cluster, mimicking mouse architecture, by changing the number of clustered units [33, 94]. The aim of the presented work is instead to analyse electrical behaviours of clusters characterised by the same number of cells and different topologies, studying synchronisation sensitivity respect to model parameters changes. In this context, it is fundamental to analyse compact and percolated topologies that mimic β-cells architecture in mouse and human islets, while the linear arrangement is a degenerate case usually adopted to study coupled oscillators, and possibly reflecting hypothetical scenarios of low connectivity configurations in pathological states. Thus, functional networks are used to establish a link between structure and function, in terms of correlated electrical

Alessandro Loppini

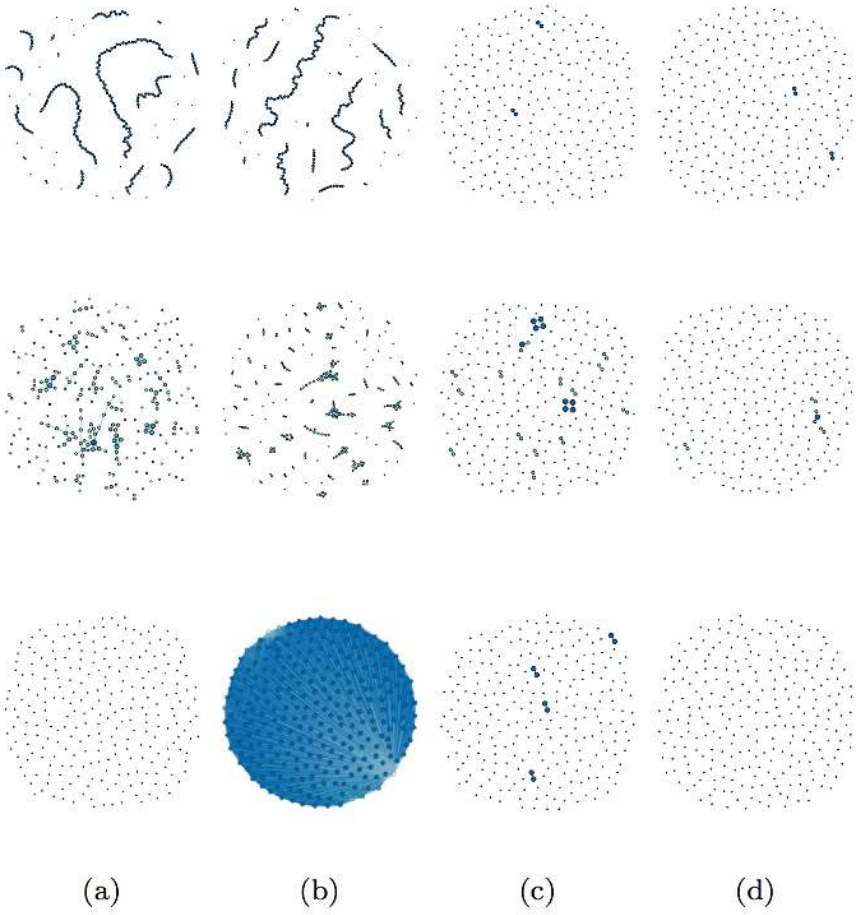

FIGURE 6.13: Computed functional networks at fixed coupling strength ($g_c = 215\,pS$) and increasing glucose concentration: (a-d) $[G] = 4.7,\ 8.7,\ 12.7,\ 16.6\,mM$. Simulations performed by setting the number of K-Ca channels to 300, in order to increase noise strength. Top: linear chain. Center: percolated cluster. Bottom: compact cluster.

activity. Such approach is useful both to characterise the spatiotemporal behaviour of the islet and would permit to validate the results against functional networks constructed from islet experimental data [112].

Results show that linear arrangements ensure a synchronised cellular activity only in a radius of about two cells. In contrast, gap junctions interactions are enough to reach a fully synchronised state in the compact cluster. Such feature is in line with published studies reporting an in-phase burst across the whole mouse islet [51, 54, 144]. Percolated clusters resembling β-cells arrangement in humans show instead intermediate emerging behaviours, characterised by differently synchronised areas. Out-of-phase bursting found in this case, suggests a limited synchronised activity in physiological conditions, coherently with experimental recordings of intracellular calcium concentrations of β-cells within human islets [126]. Specifically, results show that β-cell networks in human could be characterised by a functional modularity, a feature strictly connected

Alessandro Loppini

to system robustness against perturbations [145], for instance, altered nodes dynamics or environmental changes. Specifically, as it was pointed out by Scheferr et al. [146], heterogeneous and modular networks show a high degree of resilience and the capacity to avoid abrupt change of the system functionality in stress conditions. In contrast, homogeneous and highly clustered networks are only apparently robust respect to perturbations, giving rise to a catastrophic collapse of the system until a certain threshold of stress, compromising the whole network function. In this perspective, human islet architecture could respect this design paradigm. Lower values of coupling functionally disconnect the cluster, while higher values increase the connectivity, although affecting the modularity observed at physiological values of g_c. Therefore, an optimal value of coupling strength can be needed to maintain functional features of this system. Studying clusters activity by varying the stimulating glucose concentrations further shows that also an optimal glucose range is required to achieve appropriate synchronisation of cells. Sub-threshold and high concentration stimulations cause an asynchronous β-cell activity in each of the three cluster analysed. Interestingly, glucose range ensuring such synchronisation is consistent with the glucose peak usually observed after meal [147, 148]. Concerning the compact architecture, these observations can be discussed in comparison to experimental functional networks analysed in refs. [112, 141], reconstructed from intracellular calcium imaging of β-cells in mouse pancreatic tissue slices. In line with the emergent synchronisation observed in the modelling study here presented, experimental functional networks statistics support a progressive emergent coordinated behaviour at increasing glucose concentrations (fig. 6 in ref. [141]). Unfortunately published experiments analyse stimulatory glucose concentrations up to $12\,mM$ and, therefore, it is not possible to compare the results obtained with the model at higher glucose concentrations evoking a continuous bursting response, where model results suggest a decorrelation in the electrical activity (Tab. 6.2). In the glucose range $6-12\,mM$, statistics of functional networks computed with the model present sharper transitions and different thresholds compared to experimental ones, which can be ascribed to different aspects. For instance, at low glucose concentrations ($\simeq 7mM$), the results here presented highlight a fully synchronised response in contrast to experimental observations that show a low degree of synchrony. Such discrepancy can be due to a different activating threshold of the modelled β-cells with respect to the analysed mouse islets, i.e. over $7\,mM$ glucose in experiments (fig. 1 in ref. [141]) and $\simeq 5.5\,mM$ in the adopted model. In addition, β-cell clusters are here modelled to respond homogeneously to glucose stimulation, giving rise to the rapid increase in the clustering coefficient at over-threshold stimulatory concentrations, and thus evoking a sharper transition compared to experimental observations at increasing glucose. Furthermore, the different connectivity of the cellular structures may have a role in the observed difference. Concerning this, it has to be noticed that experimental measurements reported in the cited studies are performed on pancreas slices

Alessandro Loppini

that limit the β-cell connectivity naturally expressed in the whole islet. It is likely that this aspect has an effect on the global synchronisation, on the homogenisation of cellular response, and consequently on the sharpness of the observed transition, and it can also explain the higher values of the global clustering coefficient obtained in the model. In this sense, not considering the three-dimensional structure can severely limit the possible pathways through which cells could correlate their activity. Discussed aspects could also motivate the small-world property of the functional networks reconstructed by Stožer et al. [112], and Markovič et al. [141], instead of the complete functional graph obtained via the model. Small-world property emerges in fact from a combination of local and long-range interactions, and it can be viewed as a property of networks that are neither completely regular, neither random. Long-range functional connections in experimental observations could be due to β-cells showing similar sensitivity to glucose although not directly coupled while short-range links are very likely due to local communication ensured by the structure. The limited homogenisation of cellular response in tissue slices may in principle prevent the appearance of fully coupled functional units as in the model, although conserving long range links between cells showing similar intrinsic dose-response characteristics and electrophysiological parameters. Of course, the model itself probably overestimates cellular connectivity since the compact structure does not take into account some morphological aspects of real islets, such as blood vessels, missing contacts, and possible scattering of other cell types within the β-cell cluster. Future studies should be therefore devoted to analyse functional networks taking into account these architectural constraints.

The analysis of functional network statistics from percolated cluster enlightens other interesting properties. Average nearest neighbours degree distributions point out an associative behaviour, where synchronisation seems to come out as a nucleation-like process. For instance, at low values of coupling, low degree nodes are more likely to be connected to low degree nodes, describing a scenario where cells start to be synchronised in small clusters. By increasing the coupling, these synchronised clusters increase in size. Finally, for g_c higher than the physiological mean, high degree nodes and a plateau region in $k_{nn}(k)$ appear, suggesting that the system is moving towards a global synchronisation. Degree distributions further show that physiological values of g_c, and postprandial glucose concentrations, induce a scale-free-like topology of the functional network. In order to understand this emergent property, it is useful to recall that the adopted human architecture comes from a site-bond percolation process on a regular three-dimensional lattice, with the particular choice $p_s^* = 0.54$, $p_b^* = 0.67$. Numerical studies on site-bond percolation show that, in the case of cubic lattice, the point (p_s^*, p_b^*) is very close to the percolation threshold curve in the $p_s p_b$ plane [149]. As anticipated previously, in percolation processes performed on infinite lattices, a connected cluster

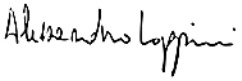

spanning the whole lattice appears at this threshold, and a phase transition can be observed. It's interesting to note that fractal shapes with self-similarity properties can arise at this critical point. Therefore, the scale-free-like topology of the functional network could be due to the underlying self-similar topological structure. Such property can then be enhanced or disrupted by variations of model's parameters, i.e. β-cells operating conditions. Many biological systems can be described by scale-free networks, i.e. metabolic reaction networks, gene regulatory circuits, and the brain [150–152]. Our findings possibly suggest that β-cells in human islet can be added to this list, although such findings should be validated in the future with further topological descriptors of the networks such as the characteristic path length (or average shortest path), eccentricity and centrality not analysed here.

Finally, the analyses performed with increased noise levels show that induced perturbations can considerably desynchronise cells activity in all the clusters analysed. However, topological features of the functional networks seem to be qualitatively conserved for both the human-like and mouse-like architecture, indicating a robustness of the system and conservation of synchronisation patterns.

In conclusion, compact and percolated β-cells clusters correctly describe coordinated cellular activity observed in mouse and human islet network. In this context, the adopted method permits to translate the spatiotemporal analysis of electrical activity to a topological study of the computed functional networks. Such approach highlighted the link between the structural architecture of β-cell aggregates and functionality, analysing this correspondence by varying selected control parameters. Since the purpose of the study was to show differences in emergent activity induced solely by cells network topology, the SRK generalised electrophysiological model was used to reproduce both mouse and human β-cell behaviour. In this framework, emergent synchronisation patterns are mainly due to the different filtering effect induced by the local connectivity with respect to noise fluctuations ("channel sharing" [33, 94]). It would be of interest to expand this study to the case of deterministic heterogeneous models of mouse β-cells, and to electrophysiological models fine-tuned on the human case. In fact published literature shows that humans present some differences in ion channels and currents involved in the membrane potential dynamics compared to the mouse (see Chapter 7). Such differences are also reflected in the emergent electrical activity. Thus, both architectural constraints and different sub-cellular processes can be thought to have an effect on bursting oscillations, cell synchronisation and insulin release.

It is worth noting that in the study here discussed the underlying architecture is studied against a functional network constructed via a descriptor of cells electrical activity correlation encoding informations of the emergent global synchronisation. Thus, the

aim is to analyse the parallelism between the system architecture and its capacity to evoke partial or global β-cells coordination. Results highlight that nearest neighbour interactions can give rise to more complex functional connections and this aspect has to be considered in experiments describing biological networks with the same statistical measures. Such an approach should be extended to a reverse engineering problem able to enlighten causality relations in the functional analysis, inferring properties of the underlying physical structure of connections [153–155]. This aspect is crucial to study in details the connection between the structure and the function of systems composed of a large number of interacting units (nodes), taking a particular relevance in biological systems [156, 157].

In the following chapter, human β-cell electrophysiology will be discussed in order to introduce a mathematical model able to analyse specifically gap junction coupling effect in this case.

Alessandro Loppini

Chapter 7

β-cells electrophysiology in human

7.1 β-cell electrical activity in human

Glucose-stimulated insulin secretion in human β-cells presents similar pathways compared to rodents, but also considerable differences. For instance, glucose uptake in human β-cell is regulated to the GLUT1 and GLUT3 transporters while GLUT2 is the predominant transporter in the mouse. Different kinetics parameters of these transporters imply functional consequences in terms of plasma glucose concentrations in fast and postprandial conditions. In human β-cell, the glucose stimulation threshold is lower than the value observed in mouse, i.e. about $3\,mM$ and $6mM$ respectively, and the half-maximal stimulation is shifted at $\simeq 6\,mM$ ($11\,mM$ in mouse). As in mouse, K-ATP channels are involved in the control of the electrical activity. Resting potential in non-stimulatory glucose concentrations ($< 1\,mM$) is $-70\,mV$, with a resting membrane conductance value equal to $60\,pS\,pF^{-1}$. At glucose concentrations higher than the stimulatory threshold ($6\,mM$), resting conductance reduces of about 70%, inducing cell depolarization. Once the membrane potential reaches the threshold of $-60\,mV$, a regenerative electrical activity is triggered. Compared to mouse, human β-cells electrical activity is more variable, showing both bursting pattern, and spiking oscillations with action potentials firing from a baseline of about $-50\,mV$ [158]. In Fig. 7.1, representative electrical patterns are reported.

Such differences are mainly due to the expression of different types of ion channels in human, some of which are not present or almost inactive in the mouse. In the following are listed main ion channels and currents involved in human β-cells electrical activity.

Alessandro Loppini

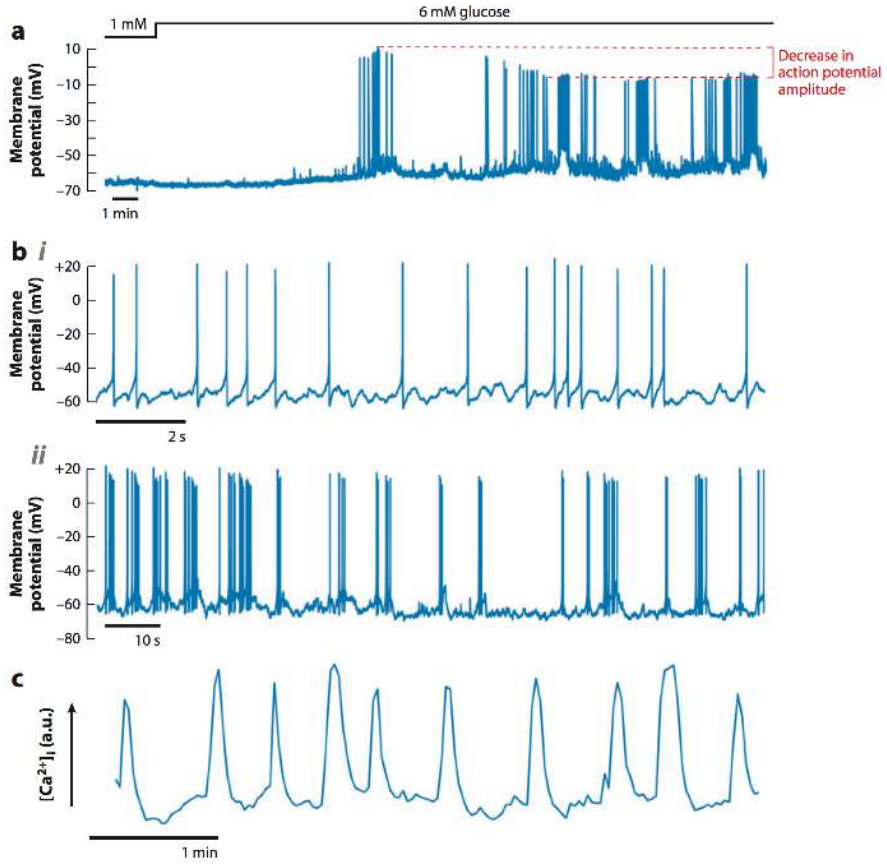

FIGURE 7.1: Glucose induced electrical activity in human β-cells. (a) Electrical activity in a β-cell within an intact islet, stimulated by glucose $6\,mM$. Dashed lines highlight the decrease in action potential amplitude due to voltage and calcium-dependent inactivation of Na^+ and L-type Ca^{2+} currents, respectively. (b) Action potentials and fast bursting in β-cells exposed to $6\,mM$ glucose. (c) Intracellular calcium oscillation in a small cluster of human β-cells exposed to $6\,mM$ glucose. From ref. [158].

7.1.1 K-ATP channels

These metabolically regulated channels are highly selective for potassium and are inhibited by micromolar concentrations of ATP. High concentrations of ADP disinhibit the channels. Thus, as in mouse, such channels are regulated by submembrane levels of both ATP and ADP and respond to sulfonylureas with activity inhibition.

Published data from Misler et al. [159] show a single channel conductance of $17\,pS$ with an extracellular-like solution, and an increase to $60\,pS$ with isotonic KCl solution, in line with mouse data discussed in Chapter 4. About $\simeq 40-50$ channels are open in glucose concentrations of $\simeq 3\,mM$, while raising glucose level up to $6\,mM$, reduces the mean activity by $\simeq 60\%$, suggesting a contribution of about $150\,pS$ in the total membrane conductance (at $6\,mM$ glucose). [159]

Alessandro Loppini

7.1.2 Voltage-gated Ca^{2+} channels

In contrast to mouse, human β-cells express T-type calcium channels. Current flowing through these channels activates at membrane potentials over $-60\,mV$ reaching a peak of $3.5\,pA\,pF^{-1}$ at $-30\,mV$. T-type channel presents voltage-dependent inactivation, that is half-maximal at $-65\,mV$, and characterised by a time constant of $\simeq 40\,ms$ at $-50\,mV$, which decreases at higher membrane potentials. Low-voltage-activated T-type current responds to low concentration of Zn^{2+} and its inhibition stops actions potential firing.

In addition, high-voltage-activated L-type and P/Q-type calcium channels also contribute equally ($\simeq 40\%$) to the whole-cell calcium current. Activation of high-voltage activated Ca^{2+} is fast ($< 5\,ms$) for depolarizations higher than $-40, mV$. L-type channels present calcium-dependent inactivation, characterised by a time constant of $40\,ms$ at $0\,mV$. Inhibition of L-type and P/Q-type currents, respectively by isradipine and ω-agatoxin, abolishes insulin secretion at $6\,mM$ of glucose concentration. Interestingly, isradipine stops action potentials firing, while ω-agatoxin have a weak effect on electrical activity, thus suggesting that P/Q-type channels are directly implicated in insulin exocytosis. [158]

7.1.3 Voltage-gated Na^{+} channels

Human β-cells contain a large number of TTX (tetrodotoxin) sensitive sodium channels. Na^{+} current is about four times larger than the total calcium current and shows a peak $> 40\,pA\,pF^{-1}$ at $0\,mV$. It is elicited by membrane depolarizations to potentials greater than $-30\,mV$, activates rapidly ($< 1\,ms$ to peak, at $-20\,mV$), and inactivates almost completely in $5\,ms$. Moreover, sodium current shows a voltage-dependent inactivation, half-maximal at $-40\,mV$. Inhibition of Na^{+} current affects the action potentials peak, and in some cases suppresses the spiking activity. Insulin secretion in response to glucose concentrations of 6 and $20\,mM$, and with TTX exposure, is reduced by 70% and 50% respectively. [158]

7.1.4 K-Ca channels

Both large-conductance (BK) and small-conductance (SK) calcium-activated potassium channels can be found in human β-cells. BK channels are colocalized with calcium channels on the cell membrane and show voltage and calcium sensitivity. Data obtained with the IbTX (iberotoxin) BK channel blocker show a bell-shaped voltage dependence for this type of current, with a peak value of $\simeq 40\,pA\,pF^{-1}$ at $30\,mV$. Voltage-dependent

Alessandro Loppini

activation of BK current is characterised by a time constant of $\simeq 2\,ms$ for membrane potentials between -20 and $20\,mV$, while for depolarizations to $10\,mV$ the BK current inactivates in $22\,ms$. SK channels can be implicated in fast bursting observed in human β-cells. Both SK4 and SK3 channels type are expressed, with gene levels coding for SK4 10-fold higher than those coding for SK3. Inhibition of SK3 channels by exposure to apamin stimulates action potential firing, and inhibition of SK4 by the channel blocker TRAM34 evokes a two-fold enhancement of insulin secretion in $10\,mM$ of glucose concentration. [158, 160]

7.1.5 Voltage dependent K^+ channels

Human β-cells present a slowly activating, delayed rectifying potassium current. Compared to mouse, which expresses $K_v2.1$ channels, $K_v2.2$ channels seem to drive this current in humans. Blocking BK current with IbTX, the resulting $K_v2.2$ current shows an activation time constant $> 10\,ms$ at $-20\,mV$, suggesting that these channels are only partially activated during the spike upstroke, which lasts less than $10\,ms$. Delayed rectifying current inactivation is very slow, with time constants of about $1.6\,s$ at depolarizations of $10\,mV$. The genes coding for the $K_v7.1$ channels is also expressed at low levels in human β-cells, although it is unclear if it could have a role in electrical activity generation and/or modulation. [158, 160]

Human β-cells also contain HERG potassium channels, similar to the ones found in cardiac cells. These channels activate slowly and carry little outward current. Moreover, inward rectifying K_{ir} channels can be found. Inward currents are inhibited by low Ba^{2+} concentrations, which evoke membrane depolarization and trigger spiking activity in addition to glucose and tolbutamide. [158]

7.2 Spiking/Bursting regulation

Human β-cells show both spiking and bursting activity. Although the identification of the exact mechanisms involved in such heterogeneity needs further studies, recently published works permitted to identify main processes involved in the control of the electrical activity.

At low glucose concentrations ($< 3\,mM$), human β-cells show a resting potential of $-70\,mV$, mainly due to the activity of K_{ir} and K-ATP channels. Concentrations higher than the stimulatory threshold ($3.5-6\,mM$), evoke depolarizations at $-60\,mV$, through changes in ATP-sensitive and inward rectifying currents. Such depolarisations occasionally allow openings of T-type calcium channels, triggering a regenerative response that

Alessandro Loppini

leads to increased depolarisations. L-type calcium channels, followed by sodium channels, are then eventually activated. Thus, these two currents contribute to the upstroke of the action potential, and their inhibition strongly affects electrical activity and insulin release. At potentials above $-20\,mV$, P/Q-type calcium channels activate, triggering insulin exocytosis. Then, the increased intracellular Ca^{2+} concentration activates calcium-sensitive K^+ channels (BK), which, allowing efflux of potassium, contribute to cell repolarization together with sodium channels inactivation. Activation of $K_v2.2$ and HERG channels may also be involved in the action potential repolarisation. These channels are also thought to contribute to the hyperpolarisation usually observed at the end of the spikes, because of their slow inactivation. It is hypothesised that SK calcium channels and K-ATP channels contribute instead to bursting oscillation. Specifically, activation of calcium-sensitive K^+ channels due to calcium influx, or openings ATP-sensitive K^+ channel due to decreased ATP/ADP in response to SERCA pump activity, may have the role of pacemaker processes involved in bursting, as like as the slow pacemaker processes regulating bursting in the mouse. In this context, a computational study has moreover shown that HERG channels may also regulate fast bursting behaviour. [158, 161, 162]

Human β-cells also show a slow bursting pattern resembling the slow bursting observed in mouse, characterised by intracellular calcium oscillations with a period of several minutes ($\simeq 3-5\,min$). Such oscillations could be driven by slow variations of the intracellular ATP/ADP, which has been found to vary on the same time scales. In turn, nucleotides variations are likely to be driven by glycolytic oscillations which in mouse have been shown to be characterised by comparable time scales [158, 162, 163]. Although, exact pacemaker processes involved in the slow rhythm of the electrical activity are not known and such hypotheses should be verified by further experiments.

7.3 Gap-junction coupling

There is evidence that also human β-cells express Cx proteins able to form gap junction channels. Specifically, published literature have shown several connexins types expressed in human islets, i.e. Cx30.3, Cx31, Cx31.1, Cx31.9, Cx36, Cx37, Cx43 and Cx45, with a peaked expression of Cx36. Combined identification of insulin-expressing cells has moreover shown that between these Cx, Cx36 is selectively expressed in β-cells and distributed in small domains where it forms tight junctions similar to the ones observed in murine islets. Dye microinjections, using Lucifer Yellow (LY) and Ethidium Bromide (EB), confirm the limited permeability of gap junctions to LY (1.4 neighbouring cells identified) in line with the mouse case, and moreover reveal a mean number of $\simeq 6$ neighbours per cell, with the use of EB [137].

Alessandro Loppini

Other studies show moreover that such coupling is able to enhance insulin secretion in human, confirming the observations on rodents [164]. In this context, single cell release was compared with cell doublets formed by β-α, β-δ and β-β pairs. Specifically, haemolytic plaque assays show a loss of glucose responsiveness, for concentrations $> 12\,mM$ in single β-cells, i.e. unaltered insulin secretion for high glucose levels compared to the $12\,mM$ stimulation. Interestingly, the increase in insulin release at higher glucose concentrations is recovered in the case of β-β and β-α pairs, suggesting a significant role of both electrical coupling and paracrine effect in hormone secretion, being the latter possibly mediated by acetylcholine stimulation of muscarinic receptor.

The evidence of coupling also comes from experimental recordings showing that β-cells in human islets show coordinated behaviour in small clusters, although cells do not reach a whole islet synchronisation [126, 165]. Considering the different islet architecture between mouse and human, described in Chapter 4, it is likely that gap junction connections have a key role in the appearance of such synchronised clusters.

Thus in humans also, Cx36 seems to be crucial for the normal functioning of the β-cells, ensuring synchronisation and improved secretion. Loss of this type of communications may affect basal and postprandial insulin release. Indeed, as already said, mice expressing low levels of Cx36 are characterised by similar insulin release patterns compared to diabetic human subjects, possibly indicating a similar coupling dysfunction between the causes of impaired insulin release in diabetes. In this context, altered coding for Cx36, or disrupted cell-cell contact due to the extracellular presence of human islet amyloid polypeptide (hIAPP) oligomers in type 2 diabetic conditions can severely compromise cell function [166].

7.4 Mathematical modelling of human β-cell electrophysiology

Human β-cells electrophysiology shows considerable differences compared to the mouse, in terms of both ion currents involved in the generation of electrical activity and pacemaker processes driving bursting rhythm (see above). Mathematical modelling needs to take into account these differences to correctly reproduce human β-cell response to glucose stimulation. In the framework of the Hodgkin-Huxley formulation, a recently published mathematical model fine-tuned on human β-cell data will be presented in the following [161, 162]. The model couples an electrical subsystem and a glycolytic oscillator, in order to reproduce both spiking, fast bursting and slow bursting activity.

7.4.1 Electrical subsystem

The electrical subsystem of the model describes the dynamics of cell membrane voltage, activation and inactivation gating variables of ion channels, and intracellular calcium concentration. Model's parameters were carefully fine-tuned, mostly based on human β-cell electrophysiological data recorded from Braun et al. [160]. In the following, all conductances, hence currents, are normalised by cell size, i.e. by membrane capacitance, which has an average value of $\simeq 10\,pF$. Two compartments are used to describe calcium dynamics: a submembrane compartment where Ca^{2+} changes rapidly in response to the spikes, and a cytosolic compartment where Ca^{2+} integrates many spikes. This choice is due to the SK channels, which are sensitive to calcium concentration and are not strictly co-localised with voltage-dependent calcium channels. Because of this, SK channels gating is supposed to be regulated by the calcium concentration in a submembrane interior shell, with a depth of $\simeq 190\,nm$. With these assumptions, membrane voltage and both submembrane and cytosolic calcium concentrations evolve according to:

$$\begin{aligned}
\frac{dV}{dt} &= -(I_{Kv} + I_{HERG} + I_{KATP} + I_{Na} + I_{CaL} + I_{CaT} + I_{CaPQ} \\
&\quad + I_{BK} + I_{SK} + I_{leak}) \\
\frac{dCa_m}{dt} &= f\alpha C_m(-I_{CaL} - I_{CaPQ} - I_{CaT})/Vol_m \\
&\quad - f(Vol_c/Vol_m)\,[B(Ca_m - Ca_c) + (J_{PMCA} + J_{NCX})] \\
\frac{dCa_c}{dt} &= f[B(Ca_m - Ca_c) - J_{SERCA} + J_{leak}]\,,
\end{aligned}$$

where V is the membrane potential; I_i is the generic ion current; Ca_m and Ca_c are the submembrane and the cytosolic calcium concentrations, respectively; f is the ratio of free calcium; α is a conversion factor from current to concentration units; Vol_m and Vol_c are the submembrane and the cytosolic volumes; J_{PMCA} and J_{NCX} represent the outward calcium fluxes due to the calcium ATPases (PMCA), and to the Na^{2+}-Ca^{2+} exchanger; J_{SERCA} models the calcium removal from the cytosol into the endoplasmic reticulum through SERCA pumps; J_{leak} is a leakage calcium flux from the endoplasmic reticulum to the cytosol; and finally, B is a flux constant.

Ion currents in the membrane potential dynamical equation are modelled based on the specific gating process. Specifically, voltage-dependent currents takes the general form:

$$I_i = g_i m_i h_i (V - V_i)\,,$$

Alessandro Loppini

where i is the channel type, m_i and h_i are the activation and inactivation gating variables for the channel i, and V_i is the reversal potential for the conducted ion. Except when the channel type shows instantaneous activation or inactivation, the dynamics of gating variables is regulated by the equations:

$$\frac{dm_i}{dt} = \frac{m_i^{\infty}(V) - m_i}{\tau_{m_i}}, \quad \frac{dh_i}{dt} = \frac{h_i^{\infty}(V) - h_i}{\tau_{h_i}}.$$

Voltage-dependent steady-state activation and inactivation are instead modelled with sigmoidal Boltzmann functions (with the only exception of L-type calcium current inactivation, as discussed below):

$$m_i^{\infty}(V) = \frac{1}{1 + \exp\left[\frac{(V - V_{m_i})}{n_{m_i}}\right]}, \quad h_i^{\infty}(V) = \frac{1}{1 + \exp\left[\frac{(V - V_{h_i})}{n_{h_i}}\right]}.$$

In the following are listed the specific characteristics of each of the ion currents.

K^+ voltage-dependent currents. Two types of channel contribute to the total potassium current in the model. Among these, the delayed rectifying potassium current presents no inactivation (characterised by slower time scales, i.e. seconds) and a voltage-dependent activation. Specifically, ion current is expressed as $I_{Kv} = g_{Kv} m_{Kv} (V - V_K)$, and the voltage dependence of the activation time constant is fitted by the function:

$$\tau_{m_{Kv}} = \begin{cases} \tau_{m_{Kv,0}} + 10 \exp\left(\frac{-20 \text{ mV} - V}{6\text{mV}}\right) \text{ ms}, & \text{for } V \geq 26.6 \text{ mV}, \\ \tau_{m_{Kv,0}} + 30 \text{ ms}, & \text{for } V < 26.6 \text{ mV}. \end{cases} \tag{7.1}$$

Instead, potassium HERG current activates in $100\,ms$ and inactivates in $50\,ms$. Such current is expressed as $I_{HERG} = g_{HERG} m_{HERG} h_{HERG} (V - V_K)$.

KATP current. In order to reproduce both fast activity and slow bursting, the ATP-sensitive current is modelled in two different ways. When the faster time scales ($\sim$ seconds) are taken into account, slow ATP variations induced by glycolytic oscillations are not considered, and the K-ATP conductance is set to a constant value based on the stimulating glucose level. Instead, when the slow metabolic oscillations are taken into account, the conductance value is modulated by the slow changes in the ATP concentration (see below). Therefore, the current is expressed as $I_{KATP} = g_{KATP}(V - V_K)$.

Na^+ voltage-dependent current. Sodium current is assumed to activate instantaneously, while the inactivation time constant is set to $2\,ms$. The current expression is $I_{Na} = g_{Na} m_{Na}^{\infty}(V) h_{Na} (V - V_{Na})$.

Alessandro Loppini

Ca^{2+} voltage-dependent currents. The model includes all three types of voltage-dependent calcium currents discussed in the previous section. Since total calcium current activates very rapidly, and its activation is almost unaffected by selective channels blockers, both T, L and P/Q-type channels are assumed to active instantaneously. T-type channels inactivate faster, with a time constant of $7\,ms$, followed by L-type channels which inactivate in $20\,ms$. Instead, P/Q type channels do not inactivate. To reproduce the inactivation function of the total Ca^{2+} current, the model assumes that the L-type current follows a calcium-dependent inactivation. Such inactivation is thus modulated by Ca^{2+} in the proximity of L-type channels, hence it's proportional to the activated calcium current through L-type channels. These considerations lead to the expression:

$$h^{\infty}_{CaL}(V) = \max\left(0, \min\left\{1, 1 + [m^{\infty}_{CaL}(V)(V - V_{Ca})]/57\text{mV}\right\}\right) .$$

The equations of the three Ca^{2+} currents are:

$$\begin{aligned} I_{CaL} &= g_{CaL} m^{\infty}_{CaL}(V) h_{CaL}(V - V_{Ca}) , \\ I_{CaPQ} &= g_{CaPQ} m^{\infty}_{CaPQ}(V)(V - V_{Ca}) , \\ I_{CaT} &= g_{CaT} m^{\infty}_{CaT}(V) h_{CaT}(V - V_{Ca}) . \end{aligned}$$

Ca^{2+}-sensitive K^{+} currents. Calcium sensitive SK and BK currents are modelled with two different approaches. Since BK channels are assembled in micro-domains together with voltage-sensitive Ca^{2+} channels, activation is assumed to be directly dependent on the total voltage-dependent calcium current. Calcium-dependent activation is assumed instantaneous while voltage-dependent activation is characterised by a time constant of $2\,ms$. Moreover, BK is assumed to not inactivate, since, during an action potential, such current is blocked by cell repolarization before incurring into inactivation. Therefore, the current is expressed as $I_{BK} = \bar{g}_{BK} m_{BK}(-I_{Ca} + B_{BK})(V - V_K)$, where $I_{Ca} = I_{CaL} + I_{CaT} + I_{CaPQ}$, and B_{BK} models the basal voltage-dependent (calcium-independent) activation. To note that the physical unit of the $\bar{g}_{BK}$ parameter is nS/pA, in contrast to the other ion conductances which are expressed in nS/pF.

Because of the relative position of the SK channels with respect to voltage-dependent Ca^{2+} channels, SK gating is assumed instead to be regulated by the calcium concentration in the submembrane space. Thus, SK activation depends solely on Ca_m concentration and it is expressed by the use of a standard Hill function describing the binding of a molecule/ion to a receptor, i.e the current is expressed as $I_{SK} = g_{SK} \frac{Ca_m^n}{K_{SK}^n + {Ca_m}^n}(V - V_K)$

Leakage current. Such current takes into account all ion fluxes not directly included in the model, due for instance to ion pumps and exchangers activity, nonselective currents, etc. Leakage factor is modelled as a passive current expressed as $I_{leak} = g_{leak}(V - V_{leak})$.

Alessandro Loppini

7.4.2 Metabolic subsystem

Data recorded from human β-cells present, like rodents, a slow bursting oscillation pattern ($\sim min$). As discussed above, it is likely that glycolytic oscillations have a role in driving such slow rhythm, by evoking cyclic variations of the ATP/ADP concentration. In fact, despite some differences, such as glucose transporter type and/or enzymes expression level, electrophysiological studies show that glucose-stimulated insulin secretion follows a similar pathway in human compared to mouse [158, 167]. Therefore, in order to reproduce the human slow response, a glycolytic oscillator, originally built to represent the upper part of glucose metabolism in mouse β-cell, is included in the model and coupled to the electrical subsystem described above [168]. The chain of reactions modelled by the glycolytic subsystem is: 1) glucose phosphorylation into G6P (glucose-6-phosphate), catalysed by glucokinase (GK); 2) conversion of G6P in F6P (fructose-6-phosphate) by the enzyme GPI (glucose-6-phosphate isomerase); 3) F6P phosphorylation into FBP (fructose1,6-bisphosphate), regulated by phosphofructokinase PFK; 4) production of DHAP (dihydroxyacetone-phosphate) and G3P (glyceraldehyde-3-phosphate) from FBP, by the action of the enzyme FBA (fructose-bisphosphate aldolase); 5) DHAP conversion into G3P by TPI (triode-phosphate isomerase); 6) G3P phosphorylation catalysed by the GAPDH (glyceraldehyde-3-phosphate dehydrogenase), which eventually triggers ATP production from mitochondria. In the model GPI and TPI reactions are assumed to be in equilibrium. Dynamical equations describing such scheme are:

$$\begin{aligned}
\frac{d(G6P \cdot F6P)}{dt} &= V_{GK} - V_{PFK} \\
\frac{dFBP}{dt} &= V_{PFK} - V_{FBA} \\
\frac{d(DHAP \cdot G3P)}{dt} &= 2V_{FBA} - V_{GAPDH} \\
\frac{da}{dt} &= V_{GAPDH} - k_A\, a\,,
\end{aligned}$$

where $G6P \cdot F6P$ and $DHAP \cdot G3P$ are dynamical variables denoting the sum of G6P and F6P, and of DHAP and G3P respectively. Such choice is due to the reactions modelled at equilibrium. Because data concerning mitochondrial activity in the human β-cell are unknown, GAPDH reaction rate is directly linked to the growth rate of ATP, whose concentration is mimicked by the variable a. Such variable controls the electrical subsystem by modulating the K-ATP channels conductance:

$$g_{KATP} = \hat{g}_{KATP} \frac{1}{1+a}\,.$$

Alessandro Loppini

Reaction rates V_R are regulated by metabolites concentrations. These dependencies are modelled by the following functions:

$$\begin{aligned}
V_{GK} &= V_{GK,\max}\frac{G^{hGK}}{K_{GK}^{hGK}+G^{hGK}},\\
V_{PFK} &= V_{PFK,\max}\frac{\left(\frac{F6P}{K_{PFK}}\right)^{h(FBP)}}{\left(\frac{F6P}{K_{PFK}}\right)^{h(FBP)}+\frac{1+\left(\frac{FBP}{X_{PFK}}\right)^{hX}}{1+\left(\frac{FBP}{X_{PFK}}\right)^{hX}\alpha_G^{h(FBP)}}},\\
V_{FBA} &= \frac{V_{FBA,\max}\left(\frac{FBP}{K_{FBA}}-\frac{G3P\times DHAP}{P_{FBA}Q_{FBA}K_{FBA}}\right)}{1+\frac{FBP}{K_{FBA}}+\frac{DHAP}{Q_{FBA}}+\frac{G3P\times DHAP}{P_{FBA}Q_{FBA}}},\\
V_{GADPH} &= V_{GADPH,\max}\frac{G3P}{K_{GADPH}+G3P},
\end{aligned}$$

where,

$$\begin{aligned}
F6P &= (G6P\cdot F6P)\frac{K_{GPI}}{1+K_{GPI}},\\
G3P &= (DHAP\cdot G3P)\frac{K_{TPI}}{1+K_{TPI}},\\
DHAP &= (DHAP\cdot G3P)-G3P\\
h(FBP) &= h_{PFK}-(h_{PFK}-h_{act})\frac{FBP}{K_{FBA}+FBP}.
\end{aligned}$$

The metabolic subsystem can oscillate due to the positive feedback of the FBP on the phosphofructokinase reaction rate. Oscillations period is on the order of minutes and can drive variations of the ATP concentration, i.e. of g_{KATP} conductance, with a periodicity comparable to the observed slow bursting period in humans.

All parameters of the model, concerning both ion currents and glycolytic reactions included in the two subsystems, are given in Tab. 7.1. As described in the following, such values fit finely many of the human β-cell properties and permit to reproduce most of the features of the emergent electrical activity correctly.

7.4.3 Single cell model behaviour

When the sole electrical subsystem is resolved without glycolytic coupling, the model is able to reproduce spiking and fast bursting oscillation observed in human β-cells. Concerning spiking activity, the in-silico simulations correctly reproduce action potentials

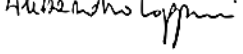

TABLE 7.1: **Human β-cell model parameters**. Values are based on data reported in the indicated references. + indicates parameters adjusted in order to reproduce different electrical behaviours. See also references [161, 162, 168] for a discussion of the parameters of both the electrical and the glycolytic subsystem.

Parameter			Ref.	Parameter			Ref.
V_K	−75	mV	[160]	V_{Na}	70	mV	[161]
V_{Ca}	65	mV	[161]	V_{Cl}	-40	mV	[158]
g_{SK}	0.0/0.03/0.1	nS/pF	+[162, 169]	K_{SK}	0.57	μM	[170]
n	5.2		[170]				
$\bar{g}_{BK}$	0.020	nS/pA	[160]	τ_{mBK}	2	ms	[160]
V_{mBK}	0	mV	[160]	n_{mBK}	-10	mV	[160]
B_{BK}	20	pA/pF	[160]				
g_{Kv}	0.215/0.22/1.0	nS/pF	+[160]	$\tau_{mKv,0}$	2	ms	[160]
V_{mKv}	0	mV	[160]	n_{mKv}	-10	mV	[160]
g_{HERG}	0.0/0.2	nS/pF	+[161, 171]				
V_{mHERG}	-30	mV	[171]	n_{mHERG}	-10	mV	[171]
V_{hHERG}	-42	mV	[171]	n_{hHERG}	17.5	mV	[171]
τ_{mHERG}	100	ms	[172]	τ_{hHERG}	50	ms	[171]
g_{Na}	0.0/0.400	nS/pF	+[160]	τ_{hNa}	2	ms	[160]
V_{mNa}	-18	mV	[160]	n_{mNa}	-5	mV	[160]
V_{hNa}	-42	mV	[160]	n_{hNa}	6	mV	[160]
g_{CaL}	0.140	nS/pF	[160]	τ_{hCaL}	20	ms	[161]
V_{mCaL}	-25	mV	[160]	n_{mCaL}	-6	mV	[160]
g_{CaPQ}	0.170	nS/pF	[160]				
V_{mCaPQ}	-10	mV	[160]	n_{mCaPQ}	-6/-10	mV	+[160]
g_{CaT}	0.050	nS/pF	[160]	τ_{hCaT}	7	ms	[160]
V_{mCaT}	-40	mV	[160]	n_{mCaT}	-4	mV	[160]
V_{hCaT}	-64	mV	[160]	n_{hCaT}	8	mV	[160]
$g_{K(ATP)}$	0.010/0.015	nS/pF	+[159]				
g_{leak}	0.015	nS/pF	[159]	V_{leak}	−30	mV	[161]
$J_{SERCA,\max}$	0.060/0.150	$\mu M/ms$	+[173]	K_{SERCA}	0.27	μM	[173]
$J_{PMCA,\max}$	0.021	$\mu M/ms$	[173]	K_{PMCA}	0.50	μM	[173]
J_{leak}	0.00094	$\mu M/ms$	[173, 174]	$J_{NCX,0}$	0.01867	ms^{-1}	[173, 174]
f	0.01			Vol_c	1.15	$\times 10^{-12}$ L	[162]
B	0.1	ms^{-1}	[162]	Vol_m	0.1	$\times 10^{-12}$ L	[162]
α	5.18×10^{-15}	$\mu mol/pA/ms$					
$V_{GK,\max}$	0.0000556	mM/ms	[168]	K_{GK}	8	mM	[168]
h_{GK}	1.7		[168]	G	10	mM	+
$V_{PFK,\max}$	0.000556	mM/ms	[168]	K_{PFK}	4.0	mM	[168]
h_{PFK}	2.5		[168]	h_{act}	1		[168]
X_{PFK}	0.01	mM	[168]	h_X	2.5		[168]
α_G	5.0		[168]				
$V_{FBA,\max}$	0.000139	mM/ms	[168]	K_{FBA}	0.005	mM	[168]
P_{FBA}	0.5	mM	[168]	Q_{FBA}	0.275	mM	[168]
$V_{GADPH,\max}$	0.00139	mM/ms	[168]	K_{GADPH}	0.005	mM	[168]
K_{GPI}	0.3		[168]	K_{TPI}	0.045455		[168]
k_A	0.0001	ms^{-1}	[162]	$\hat{g}_{KATP}$	0.050	nS/pF	[162]

with comparable firing frequency respect to experiments.

In line with experimental recordings, the model is also able to reproduce the effect of several channel blockers on electrical behaviour. Specifically, blocking sodium current by lowering Na^+ conductance leads to a reduction of the spike amplitude or a suppression

Alessandro Loppini

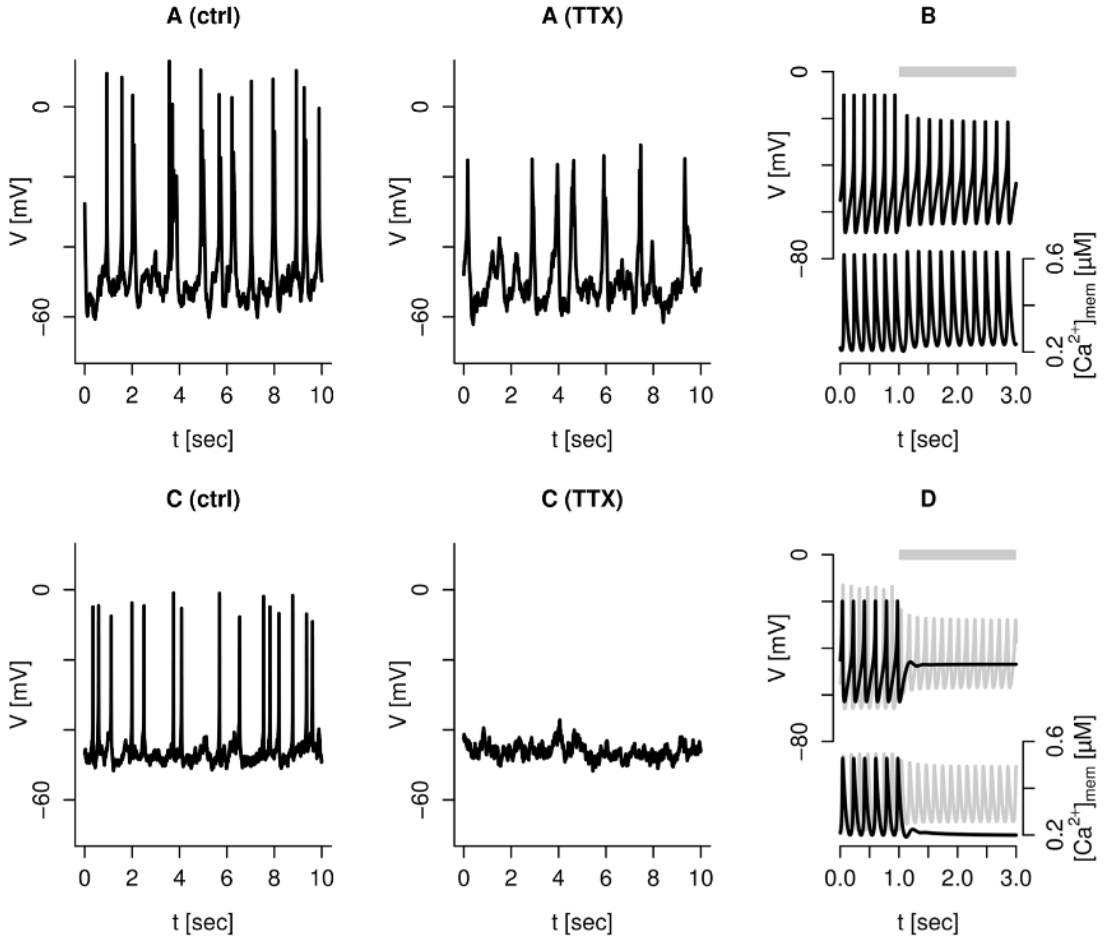

FIGURE 7.2: Effect of TTX on human β-cell spiking. (A) Experimental recordings of a human β-cells showing sustained and reduced spiking activity exposed to TTX. (B) Model results reproducing behaviour in (A). (C) Experimental recordings of a human β-cells showing TTX inhibition of spiking activity. (D) Model results reproducing behaviour in (C). From ref. [162].

of action potentials, as observed from experimental recordings from β-cells exposed to TTX (Fig. 7.2 taken from ref. [162]). Similarly, the model correctly reproduces the effect of the TRAM34 SK4 channel blocker, that leads to unchanged spiking behaviour in the normally stimulated cell, and increases spike frequency in sub-threshold stimulated β-cells. Simulations of the electrical subsystem show moreover that fast bursting can occur via two mechanisms. The first mechanism is based on slow activation of the HERG current and was pointed out in ref. [161]. In this case, when SK current is not taken into account and delayed rectifying conductance is lowered at the 20% of its original value, the model is able to reproduce bursting pattern with a slow oscillation period of $\sim 0.5\,s$. The second mechanism instead, is based on slow periodic variations of the intracellular calcium concentration, driving a slow activation of the SK channels, and was pointed out in ref. [162]. In this second case, when HERG current is not taken into account and

Alessandro Loppini

the SK channel conductance is lowered at the 30% of the original value reported in ref. [169], the model is able to reproduce similar bursting compared to the one generated by the HERG-driven mechanism, with a period of about half a second. In Fig. 7.3, an experimental recording of fast bursting activity and model outcomes (taken from refs. [161, 162]) are shown.

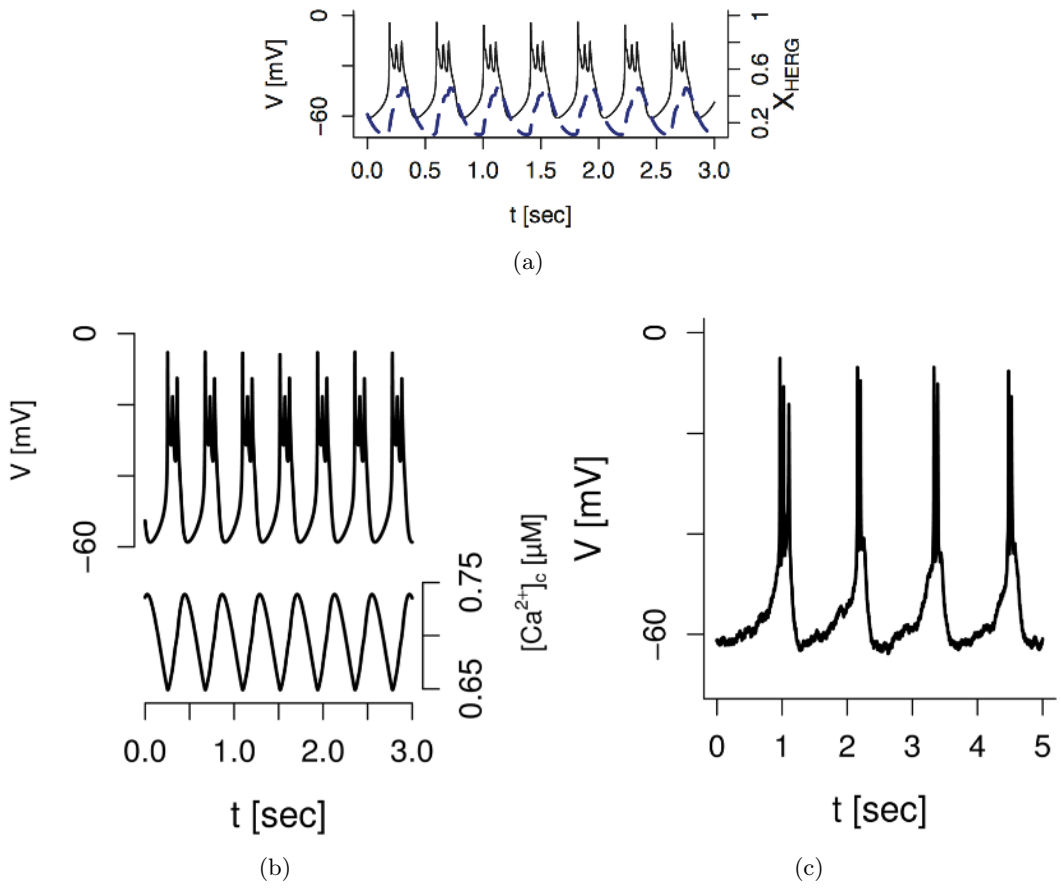

FIGURE 7.3: Bursting behaviour in human β-cell. (a) Model results showing HERG-type bursting mechanism (from ref. [161]). (b) Model results showing SK-type bursting mechanism (from ref. [162]). (c) Experimental recordings of bursting in a human β-cell (from ref. [162]).

Such observations highlight an interesting redundancy in burst-driving mechanisms, in line with the several potential pacemaker processes found in mouse β-cells. Furthermore, these findings show that similar processes underlie burst oscillation, i.e. the interaction of a slow dynamics with a fast one.

When the metabolic subsystem is coupled to the electrical subsystem, the model is able to modulate g_{KATP} conductance via oscillations of the ATP-mimetic variable a, characterised by a period of $\sim 3.5\,min$. Such oscillations give rise to an intermittent spiking behaviour with sustained active and silent phases, thus evoking a slow bursting

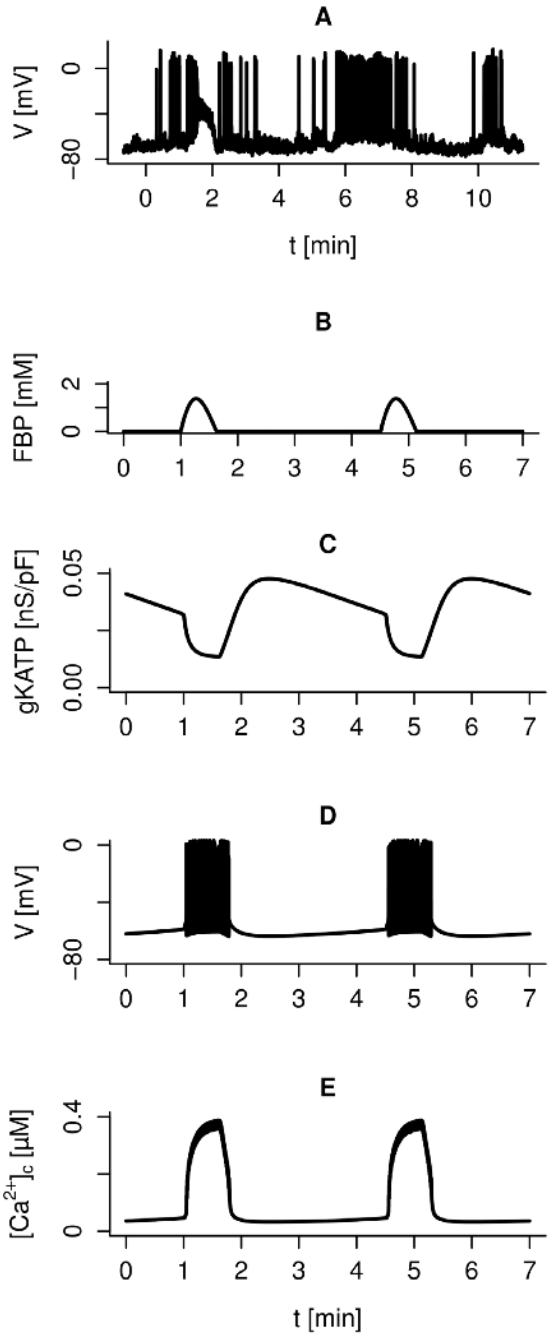

FIGURE 7.4: Slow bursting in human β-cell. (A) Experimental recordings of slow bursting in a human β-cell. (B)-(E) Model results showing membrane potential, cytosolic calcium, FBP, and g_{KATP} computed with the glycolytic driven bursting. From ref. [162].

Alessandro Loppini

response (Fig. 7.4 from ref. [162]). Such slow bursting drives slow oscillations of the cytosolic calcium concentration that in turn can drive slow pulsatile insulin release.

Therefore, the model correctly grasps main features of electrical behaviour recorded from human β-cell, and to date represent the more comprehensive mathematical formulation of human β-cell electrophysiology. In the following Chapter, this model will be generalised to the case of electrically coupled human β-cells. Specifically, this generalisation will be used to give an estimation of the gap junction coupling conductance between paired β-cells, based on experimental data and a parametric study of the model. Such estimate will be then used to investigate emergent behaviour in coupled heterogeneous cells populations.

Alessandro Loppini

Chapter 8

Coupling effects between human β-cells

Despite the evidence of Cx36 forming tight junctions in human islets, electrical properties of such coupling have not been studied as in rodents. Moreover, the observed differences between mouse and human β-cell electrophysiology, i.e. different functional ion channels and evoked bursting, don't allow to translate directly the knowledge accumulated on mouse to the human case. Thus, also gap junction channel may have different properties in humans, where heterotypic Cx channels or homotypic channels formed by other connexin may be present, or where homotypic Cx36 channel gating could be differently regulated. The model presented in Chapter 7 is here used to investigate such aspects. Specifically, an estimate of the coupling conductance between human β-cells is obtained based on experimental data. This finding is then used to study the effect of gap junction coupling on the emergent electrical activity of heterogeneous cell clusters in different electrical regimes.[1]

8.1 Experimental observations

The estimate of the gap junction conductance is mainly based on atypical electrical patterns recorded from a patched human β-cell within a tiny cluster of cells, stimulated by $6\,mM$ of glucose. In Fig. 8.1 these experimental patterns are shown.

As it can be noticed it consists of small amplitude oscillations of the membrane potential ($\simeq 10\,mV$), starting from a baseline of about $-50\,mV$, with an occasional firing of action potentials. Such oscillations are still present even when the cluster is exposed to the

[1] The novel study here presented is reported in ref. [175].

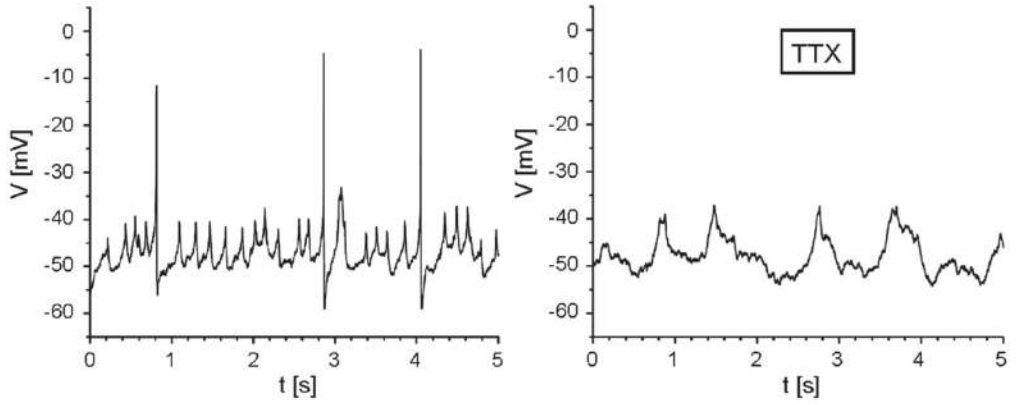

FIGURE 8.1: Perforated-patch whole-cell recordings in a human β-cell within a tiny cluster, in (a) control condition, and (b) with exposure to $0.1\,\mu g/ml$ of TTX. Extracellular solution (mM): $3.6\,KCl$, $140\,NaCl$, $0.5\,MgSO_4$, $1.5\,CaCl_2$, $10\,HEPES$, $0.5\,NaH_2PO_4$, $5\,NaHCO_3$ and 6 glucose (pH 7.4). Pipette solution (mM): $76\,K_2SO_4$, $10\,KCl$, $10\,NaCl$, $1\,MgCl_2$, $5\,HEPES$ (pH 7.35), plus amphotericin B ($0.24\,mg/ml$).

selective sodium channel blocker TTX, although an increase in the oscillation period can also be observed. This particular behaviour is representative of 3 out of 10 different recordings (both with and without TTX). In the other cases the patched cell showed: 1) spiking activity in control condition but reduced oscillations ($10-15\,mV$) with TTX (2 cells); 2) spiking activity both in control condition and with TTX exposure (4 cells); 3) no activity both in control condition and with TTX exposure (1 cell). Probably the observed differences are partly due to the heterogeneity in glucose sensitivity, and a certain glucose concentration can be stimulatory for some cells, evoking action potential firing, but subthreshold for other β-cells, that remain silent. Therefore, a reasonable hypothesis that justifies the observed atypical pattern is that the patched cell is a silent cell, that is not responding to glucose stimulation, and that the small amplitude low voltage oscillations are due to gap junction currents coming from active neighbouring cells, in which glucose triggers spiking activity. In this perspective, the occasional potential firing observed in control condition is not of interest, being probably due to random threshold-crossing events evoking isolated action potentials. To note that such hypothesis is in line also with the evidence of sustained spiking activity in some cells exposed to TTX (see Chapter 7 or ref. [162]), despite the reduced amplitude of action potentials, thus justifying the persistence of the small amplitude low-voltage oscillations.

8.2 Gap junction estimate

By using the electrophysiological model of human β-cell activity discussed in the previous Chapter, it is possible to investigate the effect of gap junction currents in-silico. In line

with previous works performed on mouse models of β-cell electrophysiology, like the generalised SRK model described in Chapter 5, model's equation describing membrane potential dynamics can be easily modified to take into account electrical coupling:

$$\frac{dV_i}{dt} = -I_{ion,i} - g_c \sum_{j \in \Omega_i} (V_i - V_j) \,,$$

where $I_{ion,i}$ is the sum of the ionic currents through the cell membrane and include all the currents described in Chapter 7, Ω_i is the neighbourhood of cell i, and g_c is the coupling conductance.

The aim is to investigate the conditions for which an active cell can induce $\simeq 10\,mV$ oscillations in a silent coupled cell. Therefore, to reproduce experimental data, a system of two coupled cells (doublet), one silent and one active, can be simulated with the model, analysing for different coupling strengths the induced perturbations in the silent cell, i.e. the patched cell in the experiment (see Fig. 8.2).

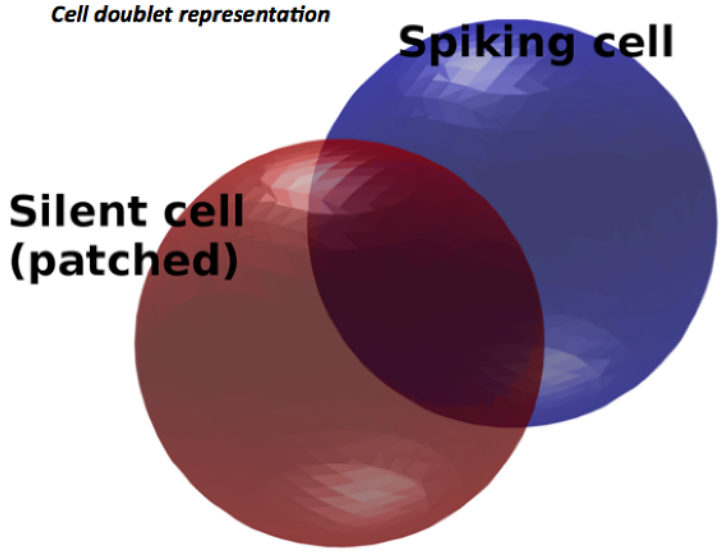

FIGURE 8.2: Cell doublet representation: silent patched cell in red, and active coupled cell in blue.

For this study, only the electrical subsystem of the model is taken into account, since the purpose is to reproduce fast spiking oscillations, not affected by slow variations ($\sim min$) of the ATP concentration. In this context, active and silent responses are obtained by a proper fine-tuning of the K-ATP cell conductance, since high g_{KATP} values block cell depolarization silencing the cell while low values evoke spiking activity. Moreover, this parameter represents the natural choice to introduce heterogeneity in glucose sensitivity. Specifically g_{KATP} is here varied in the ranges $0.003 - 0.005\,nS/pF$ and $0.02 - 0.035\,nS/pF$, to respectively model the active and silent cell.

Alessandro Loppini

8.2.1 Cell doublet: times series analysis

In Fig. 8.3, representative results of numerical integration of the cell doublet system, performed with the XPPAUT software (using the CVODE numerical scheme), are shown. In this case silent and active cells are modelled by setting the g_{KATP} value to 0.02 and $0.005\,nS/pF$ respectively. In Fig. 8.3(a), the two cells are coupled with a fixed conductance $g_c = 0.010\,nS/pF$ and the emerging spiking oscillations are analysed both without and in the presence of the TTX channel blocker. Specifically, TTX effect is simulated by setting at zero the sodium channels conductance ($g_{Na} = 0\,nS/pF$). While, in Figs. 8.3(b) and (c) emergent oscillations are analysed for different values of the coupling conductance both with and without TTX.

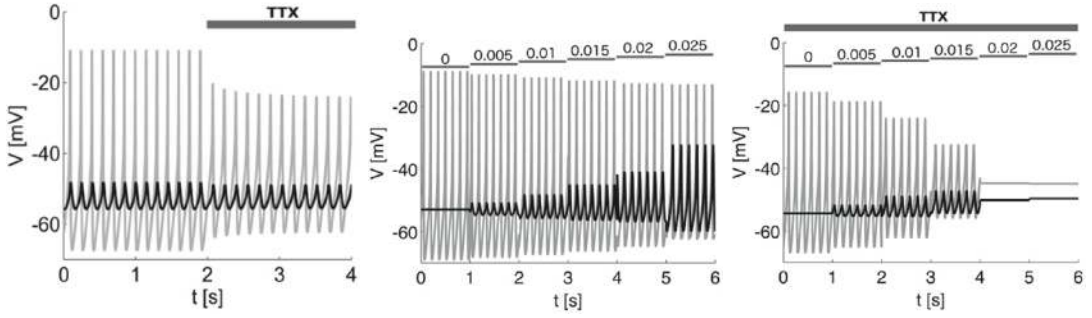

FIGURE 8.3: Simulation of a human β-cell doublet formed by an active cell ($g_{KATP,a} = 0.005\,nS/pF$, grey line) coupled to a silent cell ($g_{KATP,s} = 0.02\,nS/pF$, black line). In the time interval highlighted by the grey bar, TTX exposure is simulated setting $g_{Na} = 0\,nS/pF$, while other parameters are set at default values (see Tab. 7.1). (a) Simulation with $g_c = 0.01\,nS/pF$. (b) Simulations for g_c in the range $0 - 0.025\,nS/pF$ without TTX. (c) Simulations for g_c in the range $0 - 0.025\,nS/pF$ in the presence of TTX.

As it can be noticed, at proper values of the gap junction conductance, the active cell is able to induce small voltage perturbations in the otherwise silent cell. Moreover, TTX exposure does not significantly affect the amplitude of the induced oscillations. When the doublet is studied at different values of g_c without TTX, the oscillation amplitude in the silent cell increases for increasing values of the junctional conductance. Only within a proper interval of g_c ($0.010 - 0.020\,nS/pF$) are recovered induced oscillations of $\simeq 10mV$ like the ones noticed in experimental recordings. Instead, for g_c out of this range induced oscillations are too small or too large. Simulations with TTX exposure confirm such finding since at low values of coupling the active cell induces oscillations in the silent cell with a too low amplitude compared to the experiment ($\simeq 3\,mV$ at $g_c = 0.005\,nS/pF$ versus $10\,mV$). In this case, at high coupling strengths the effect of the silent cell is dominant, trapping the active cell in a silent state. Thus, oscillations comparable to experiments are recovered only in an optimal range of values for the gap

Alessandro Loppini

junction conductance. Moreover, as shown below, this conclusion is independent of the particular choice of the parameters used to model the active and the silent cell.

8.2.2 Cell doublet: bifurcation diagrams analysis

To correctly quantify the optimal range of coupling strength that evokes proper oscillations in the silent cell, the sensitivity of the induced oscillations with respect to the single-cell parameters is here analysed with the use of bifurcation diagrams.

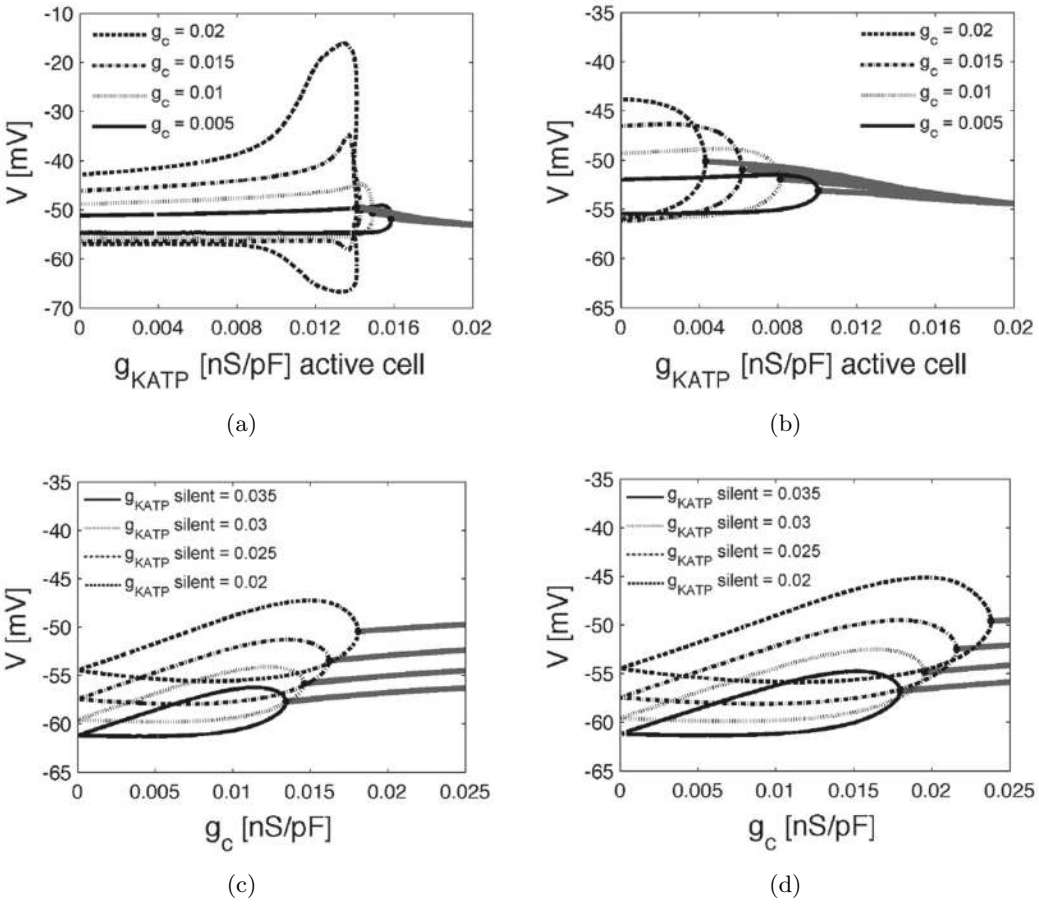

FIGURE 8.4: Bifurcation diagrams for the silent cell in the doublet system. (a) Diagrams computed without TTX, with $g_{KATP,s} = 0.020\,nS/pF$, and by varying $g_{KATP,a}$. (b) As in (a) but in the presence of TTX. (c) Diagrams computed in the presence of TTX, with $g_{KATP,a} = 0.005\,nS/pF$, and by varying g_c. (d) As in (c) but with $g_{KATP,a} = 0.003\,nS/pF$.

Such diagrams permit to track maximum and minimum of the evoked oscillations by varying the K-ATP conductance of the silent and active cell ($g_{KATP,a}$ and $g_{KATP,s}$ respectively), and the coupling conductance g_c. In Fig. 8.4, the computed diagrams for the silent cell are shown. As it can be seen, suitable induced oscillations appear only under specific conditions. Treating $g_{KATP,a}$ as the bifurcation parameter, and

Alessandro Loppini

in control conditions, the coupled system with $g_{KATP,s} = 0.020\,nS/pF$ oscillates when $g_{KATP,a} < 0.015\,nS/pF$ and the coupling strength is higher than zero. However, in order to observe oscillations of $\simeq 10\,mV$ in the silent cell, the coupling conductance has to be greater than $0.010\,nS/pF$, while values higher than $0.015\,nS/pF$ evoke oscillations too large in amplitude for a range of $g_{KATP,a}$ values.

In the presence of TTX the conclusion is the same. In fact, although the spiking threshold of the active cell moves to lower values of $g_{KATP,a}$ (0.008 nS/pF for $g_c = 0.010\,nS/pF$), a coupling conductance $g_c > 0.010\,nS/pF$ is still need to obtain evoked oscillations $> 5\,mV$. When g_c is treated as the bifurcation parameter, sensitivity analysis with respect to $g_{KATP,a}$ and $g_{KATP,s}$ in the presence of TTX, show moreover that for $g_{KATP,s} = 0.02 - 0.035\,nS/pF$ and for $g_{KATP,a} = 0.003 - 0.005\,nS/pF$, evoked oscillations of $\simeq 10mV$ are recovered for $g_c = 0.010 - 0.020\,nS/pF$.

Considering that the membrane capacitance of human β-cells is $\simeq 10pF$, such estimate corresponds to a non-normalised range of $100 - 200\,pS$, surprisingly in line with measures of coupling conductance between mouse β-cells, both in islets and in isolated pairs [68, 134, 176]. Such estimate is used in the following to investigate the effect gap junction coupling on the activity of heterogeneous human β-cell clusters.

8.2.3 Three-cells configuration: effects on the estimate

In the analysis presented above, coupling conductance is estimated from a doublet cell system. Unfortunately, informations on the exact number of cells in the experimental cluster are not available; thus, in this paragraph, the estimate of g_c is tested by increasing the cell number. The purpose of this analysis is also to give a plausible explanation for the slower oscillation period observed in the silent cell, in the presence of TTX. Specifically, simulations are here performed modelling three coupled β-cells (triplet), organised in a line (only the central cell is coupled to the others) or in a triangle (each cell is coupled to the others). One cell is modelled as normal spiking cell, one cell is silent, and the third cell is a slowly spiking cell, i.e. a cell characterised by a lower spiking frequency respect to a normal spiking cell. The silent cell is supposed to be the patched cell in the experiment as before.

In Figs. 8.5 and 8.6 computed voltage traces for the linear and triangular configuration are presented respectively. In the triangular configuration, when cells are coupled with $g_c = 0.01\,nS/pF$ the slow spiker seems to be overwhelmed by the normal spiking cell, and it switches to a normal spiking response. In the presence of TTX ($g_{Na} = 0\,nS/pF$), the normal spiker is inhibited and presents only evoked oscillations driven by the slow spiker. Although, interestingly such oscillations are characterised by the normal spiker

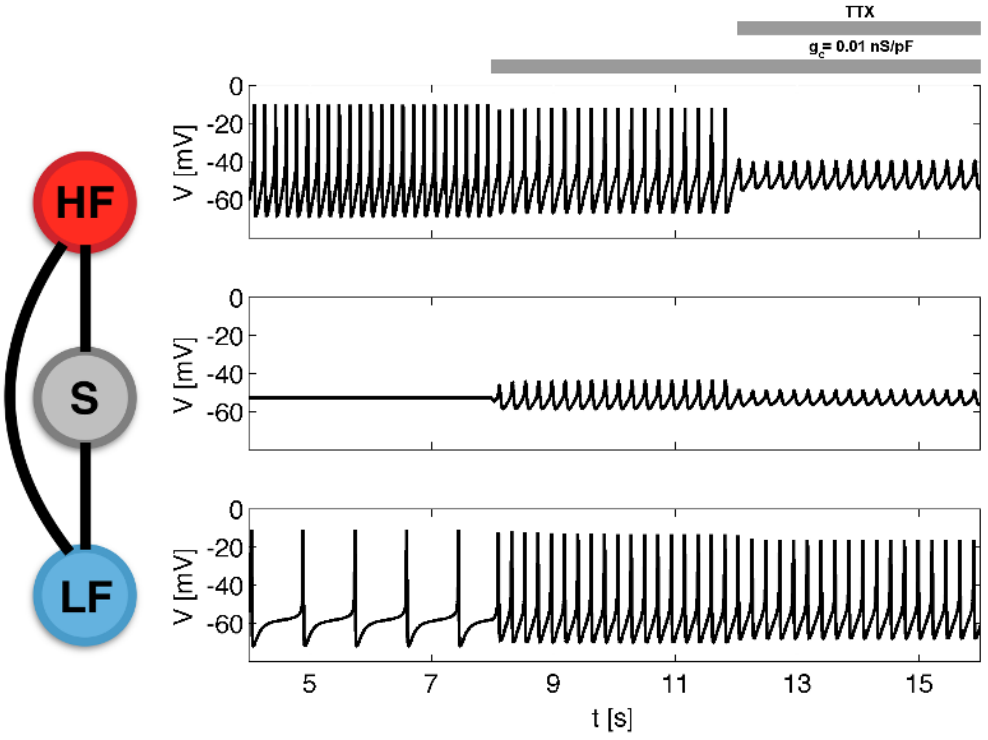

FIGURE 8.5: Simulations of three cells coupled in a triangular configuration. The central cell is the silent cell (S, $g_{KATP} = 0.020\,nS/pF$), the top cell is the high frequency spiker (HF, $g_{KATP} = 0.010\,nS/pF$), and the bottom cell is the low frequency spiker (LF, $g_{KATP} = 0.025\,nS/pF$, plus $g_{leak} = 0.0075\,nS/pF$ and $g_{Na} = 0\,nS/pF$ respect to default parameters given in Tab 7.1). Grey bars denote the time interval during which the coupling is turned on, or the TTX exposure is simulated.

endogenous rhythmicity. Thus, this configuration does not reproduce the increase in the period of the evoked oscillations, despite the amplitude is comparable to the experimental tracks. When the triplet is coupled in a chain configuration, i.e. when only the central silent cell (patched cell) is mutually coupled to the other cells, a more complex behaviour arises. In this case, cells coupling ($g_c = 0.010\,nS/pF$) both increases the spiking frequency of the slow spiker, as in the triangular case, and evokes irregular oscillations in the silent cell ($\simeq 5 - 10\,mV$). When TTX exposure is simulated, the normal spiker is silenced, and the remaining cells oscillate at a lower frequency compared to the triangular arrangement, still preserving an amplitude of $\simeq 10\,mV$ in the otherwise silent cell. Such behaviour may be explained by the fact that the extra link in the triangle configuration leads to a stronger activation of the normal spiker inhibited by TTX, which in turn is able to "beat the beat". While in the chain configuration, the silenced normal spiker is only minimally activated because of the missing direct coupling with the active slow spiker. Therefore, during TTX exposure, the slow spiker is able to fire at a frequency closer to its intrinsic rhythm, as reflected from the slower induced

Alessandro Loppini

oscillations in the silent patched cell.

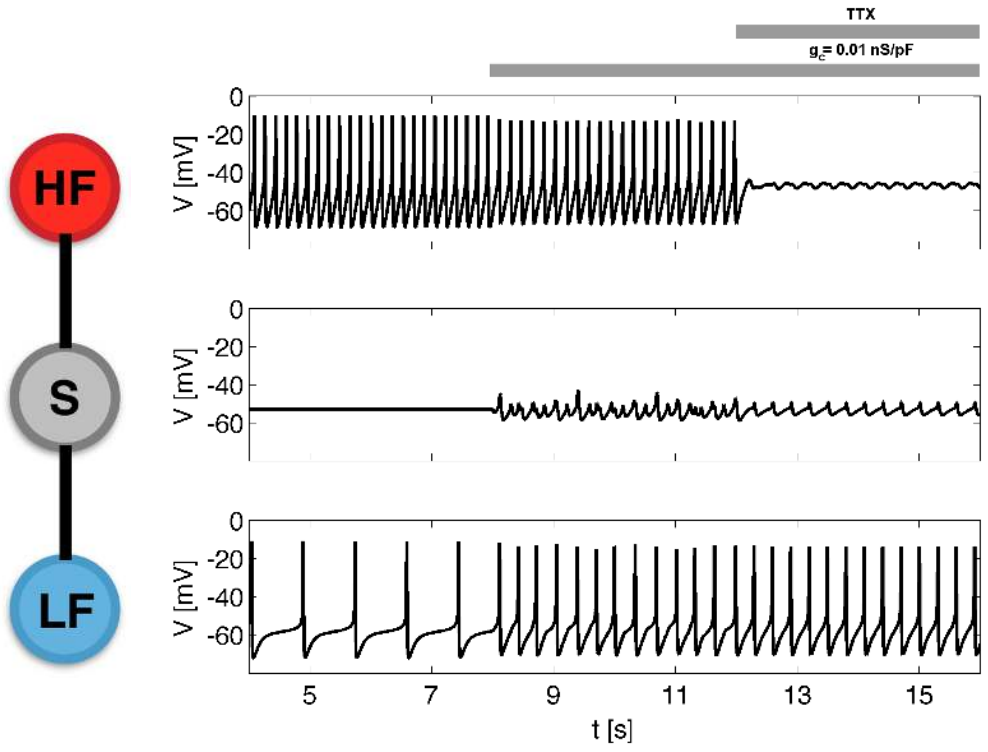

FIGURE 8.6: Simulations of three cells coupled in a chain configuration. The central cell is the silent cell (S, $g_{KATP} = 0.020\,nS/pF$), the top cell is the high frequency spiker (HF, $g_{KATP} = 0.010\,nS/pF$), and the bottom cell is the low frequency spiker (LF, $g_{KATP} = 0.025\,nS/pF$, plus $g_{leak} = 0.0075\,nS/pF$ and $g_{Na} = 0\,nS/pF$ respect to default parameters given in Tab 7.1). Grey bars denote the time interval during which the coupling is turned on, or the TTX exposure is simulated.

Therefore, this analysis validates the range of g_c estimated in cell doublets also for arrangements of three cells. An explanation for the increase in the oscillation period evoked in the silent cell is also given, despite other mechanisms could be involved in the observed change. For instance, specific slow ion currents not taken into account in the electrophysiological model, whose effect in normal conditions is overwhelmed by sodium currents, may have a role. However, since it is more likely that the gap junction conductance has an effect on the evoked oscillation amplitude more than the evoked period, mechanisms underlying the frequency change in response to TTX will not be discussed further. Such choice is further validated by the evidence that by using both experiments performed with and without TTX, the coupling conductance estimate is almost unaffected; thus frequency change does not have a significant impact on model's prediction and consequent conclusions.

Alessandro Loppini

8.3 Coupling effects on fast activity

As mentioned in Chapter 7, β-cells in human islet show an heterogeneous electrical activity, characterised by spiking, fast bursting, and slow bursting oscillations. The estimate obtained above for g_c is used in this section to investigate coupling effect on heterogeneous 3 x 3 x 3 β-cell clusters reproducing these behaviours. In line with the SRK generalised model (see Chapter 5), cell clusters are built as regular three-dimensional grids, and cells within the clusters communicate via a three-dimensional Von Neumann neighbourhood, i.e. six neighbours for a central cell, in agreement with experimental observations. Cluster size is in line with the sparse architecture of human islets compared to mouse (see Chapter 6), suggesting that β-cells in human islets are coupled in small cluster through Cx36 channels. Thus, instead of reconstructing large percolated networks, as in the study reported in Chapter 6, the human β-cell cluster is built here as a compact small cluster. Moreover, such a multicellular system is modelled by imposing heterogeneity on single cell parameters in order to obtain heterogeneous populations of normal spiking and fast bursting cells ("spikers" and "bursters" respectively in the following). Specifically, the delayed rectifying and the K-ATP conductance values are randomly extracted from a Gaussian distribution with a small standard deviation. This choice is due to the fact that g_{KATP} directly control glucose sensitivity, and g_{Kv} have the major effect on the qualitative emergent electrical behaviour (spiking or bursting). Furthermore, simulations performed by imposing heterogeneity also in the other parameters lead to similar results. As done for the g_c estimate, in this analysis only the electrical subsystem is resolved, since the interest is to analyse fast activity, not affect by slow oscillations driven by metabolic processes. Resulting ODE system is resolved with a fourth order Runge-Kutta scheme with a time step of $0.02\,ms$, implemented in a C++ numerical code.

8.3.1 Spiking

The effect of coupling on the synchronisation of heterogeneous spikers is here presented. To obtain such multicellular cluster the g_{Kv} and the g_{KATP} are normally distributed with a standard deviation equal to 10% their mean values ($\bar{g}_{Kv} = 1.0\,nS/pF$ and $\bar{g}_{KATP} = 0.010\,nS/pF$, where the bar denotes mean value), while other parameters are set at default values (see Tab. 7.1). When such spikers are uncoupled, they fire asynchronously since are characterised by different intrinsic spiking frequency. Instead, when β-cells are coupled with a $g_c = 0.010\,nS/pF$, i.e. a value equal to the lower limit of the range previously estimated, the cluster shows a global synchronous spiking behaviour. While a ten-fold lower value of the coupling conductance ($g_c = 0.001\,nS/pF$) is not able to

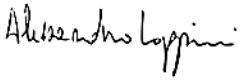

synchronise the spiking activity. Simulations results reporting the emergent activity of the cluster are shown in Fig. 8.7(a).

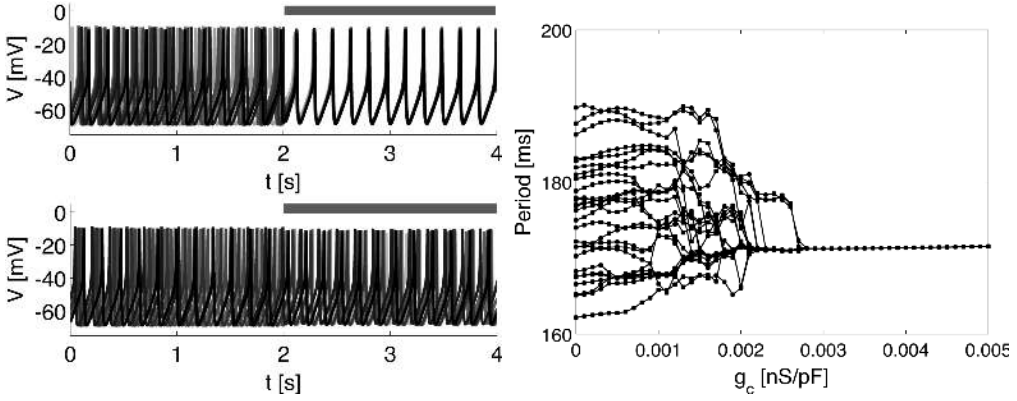

FIGURE 8.7: Simulations of a 3 x 3 x 3 cluster of human spiking β-cells. (a) Membrane potential of cells within the top plane of the cluster (9 cells) coupled with $g_c = 0.010\,nS/pF$ (top), and $g_c = 0.001\,nS/pF$ (bottom). (b) Spiking period of the 27 cells of the cluster for g_c in the range $0 - 0.005\,nS/pF$. Grey bars in (a) denote the time interval during which the coupling is turned on.

The spiking period is also computed for different values of the coupling conductance to investigate the minimum amount of coupling strength able to achieve cells synchronisations. Computed periods for each of the 27 spikers in the cluster are reported in Fig. 8.7(b). As it can be noticed, the variability of the spiking frequency is minimal for $g_c = 0.002\,nS/pF$, and a coupling conductance of about $g_c = 0.003\,nS/pF$ is enough to achieve a full cluster synchrony. Thus, the estimated coupling strength is definitely enough to ensure synchronisation of small β-cells populations showing spiking activity.

8.3.2 Bursting

As discussed in Chapter 7 (see refs. [161, 162]), it was suggested that two different mechanisms are able to drive fast bursting in human β-cells. These mechanisms involve slow activation of the HERG current, and slow oscillations of the cytosolic Ca^{2+} evoking a slow activation of the SK channels. In this paragraph, the effect of coupling is studied when a heterogeneous population of HERG-type or SK-type bursters are coupled together. Specifically, HERG-type bursters are modelled by setting $g_{SK} = 0\,nS/pF$, and by extracting the g_{Kv} parameter from a Gaussian distribution with mean $\bar{g}_{Kv} = 0.22\,nS/pF$ and a standard deviation equal to 5% of mean value; SK-type bursters are instead modelled by setting $\bar{g}_{Kv} = 0.215\,nS/pF$ (the standard deviation is set to $\simeq 1\%$ of mean value, due to high sensitivity of the SK-burst to variations of $\bar{g}_{Kv}$), $n_{mPQ} = -10\,mV$, and $g_{SK} = 0.03\,nS/pF$. Other parameters are equal to the default values reported in

Alessandro Loppini

Tab. 7.1. Emergent bursting is thus analysed in terms of cells synchronisation and bursting period.

Interestingly, when the SK-type bursters are coupled with a $g_c = 0.010\,nS/pF$ cells show a high voltage sustained oscillations, as if they remain trapped in the active phase of the burst (see Fig. 8.8(a)). In this case, action potentials of different cells appear to be almost phase locked. Such situation is observed in all the range of coupling estimated above, and a normal bursting pattern is recovered only for g_c values fairly higher than the upper limit estimated previously.

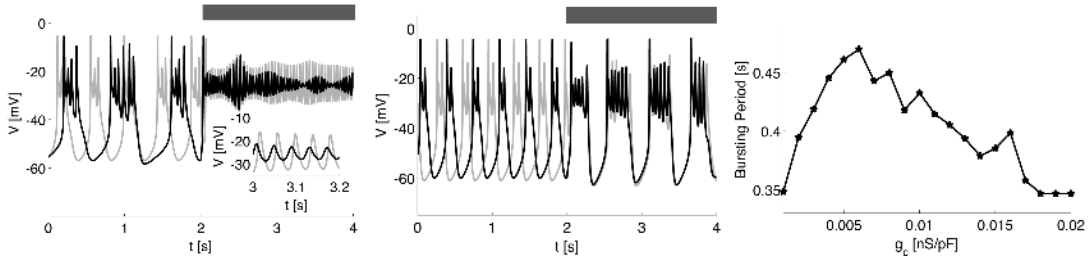

FIGURE 8.8: Simulations of a 3 x 3 x 3 cluster of human bursting β-cells. (a) Membrane potential of two representative neighbouring cells of the cluster considering SK-type bursters. (b) Membrane potential of two representative neighbouring cells of the cluster considering HERG-type bursters. (c) Dependence of bursting period on the coupling conductance g_c for the HERG-type bursters. Grey bars in (a) and (b) denote the time interval during which the coupling is turned on ($g_c = 0.010\,nS/pF$).

A different behaviour is instead observed when HERG-type bursters are coupled together. Simulations results show that when the coupling factor is switched on ($g_c = 0.010\,nS/pF$) the cells are not trapped in a continuous bursting response, and show almost synchronous bursting (Fig. 8.8(b)). Most interesting aspect is that the bursting period increases and the value reached by the potential in the repolarization phase at the end of the burst is slightly more negative respect to the uncoupled case. Analysis of the emergent bursting period for all the estimated range of g_c is presented in Fig. 8.8(c) and enlightens an interesting dependency of the bursting period on the coupling conductance. Within an optimal range of g_c, in agreement with the estimate obtained above, fast bursting period significantly increases. A similar behaviour was pointed out in the SRK stochastic model and in other modelling studies of mouse β-cells [94, 95], suggesting a similar underlying mechanism of bursting enhancement, i.e. the possible appearance of asymmetrical or out-of-phase branches of solutions characterised by longer times spent in the active phase [98, 99]. However, the higher dimensionality and complexity of the considered electrophysiological model does not permit a trivial verification of such hypothesis with the usually adopted methods.

Alessandro Loppini

8.3.3 Mixed populations and non-responsive cells

In human β-cell clusters it is likely that spikers and bursters are randomly intermingled. Therefore, cells showing intrinsic fast bursting and spiking activity can be coupled together. Moreover, there could be situations where normally responsive cells are coupled to β-cells expressing non-functional K-ATP channels, i.e. mutant channels that present limited sensitivity to ATP-inhibition and are overactive forcing the cell in a silent state, as it was experimentally noticed in mouse [83]. It is interesting to study how gap junction coupling affects emergent electrical activity in such situations.

In order to investigate the first point, a β-cells cluster is here modelled with an approximately equal number of spikers (13 out of 27 cells) and bursters (14 out of 27 cells). When the cells are coupled with a $g_c = 0.010\,nS/pF$, numerical simulations show that all the cells shift to a spiking response, both in the case of HERG-type and SK-type bursters (SK case presented in Fig. 8.9(a)). Such spiking activity is characterised by a higher minimum of the spiking oscillation compared to the uncoupled spiker, suggesting a slightly different behaviour respect to the uncoupled case. Although, this result demonstrates that the spiking solution is a much more robust state of activity compared to the fast bursting, and a spiking cell could easily force a coupled burster to switch its activity in a spiking response.

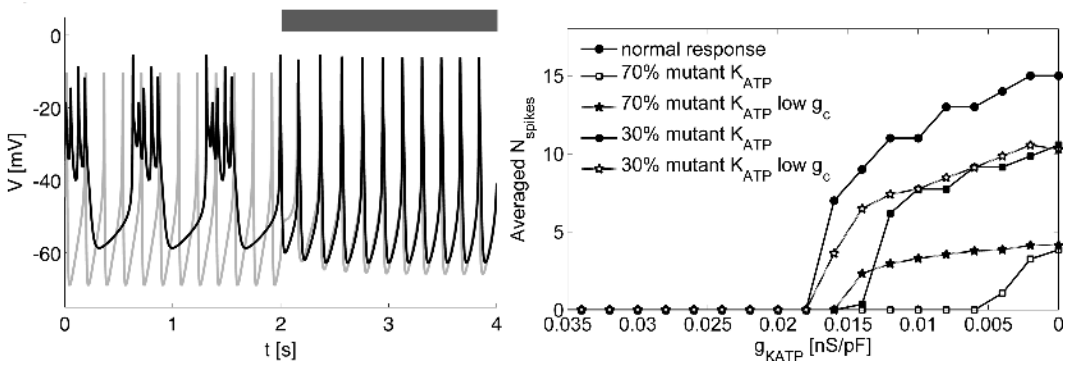

FIGURE 8.9: Simulations of 3 x 3 x 3 mixed clusters of human β-cells. (a) Membrane potential of two representative neighbouring cells (one spiker and one SK-type burster) of the cluster. (b) Dose-response curves (mean number of spike per cell vs g_{KATP} of the active cells) for different fractions of silent cells, considering a low coupling conductance ($g_c = 0.001\,nS/pF$) and a value in agreement with the estimated range ($g_c = 0.01\,nS/pF$). "Normal response" denotes the case with no silent cells and with $g_c = 0.01\,nS/pF$. Grey bar in (a) denotes the time interval during which the coupling is turned on ($g_c = 0.010\,nS/pF$).

In order to investigate coupling effect in the presence of mutant cells, clusters formed by normal spikers and silent β-cells (due to the overactivity of the K-ATP channels) are built considering a variable fraction of mutant cells (30% and 70%), and analysing their

response for different values of g_c ($0.001\,nS/pF$ and $0.010\,nS/pF$). The mean cluster response is here quantified by constructing a dose-response-like curve: the mean number of spikes per cell is computed for each value of glucose stimulation, i.e. the g_{KATP} value of the normal responsive cells. Specifically, the spikes number is averaged over 3 seconds of simulated activity. This choice is due to the fact that spiking activity is linked to calcium influx into the cell and to insulin release, thus, the mean number of spikes represents a valid indicator of the cluster response. Non-responsive cells are instead modelled with a fixed K-ATP conductance $g_{KATP} = 0.03\,nS/pF$. Computed dose-response curves are presented in Fig. 8.9(b). When cells are coupled with $g_c = 0.010\,nS/pF$, the presence of mutant cells significantly alter the mean number of spikes. In the case of 30% mutant cells, considering a medium glucose stimulation ($g_{KATP} = 0.01\,nS/pF$), the mean number of spikes is $\simeq 8$, while the normal responsive cluster (no mutant cells) shows a mean number of spikes equal to $\simeq 11 - 12$. When the cluster contains 70% of mutant cells, no response can be observed in this condition. Inhibition of the response, in the presence of mutant cells, seems to be evident in the whole range of glucose stimulation.

Interestingly, when the coupling conductance is significantly lowered (ten-fold in this case), the mean number of spikes is enhanced and is possible to recover a residual response from the cluster. Such phenomenon is mainly due to the trapping effect that the silent cells exert on the normal spiking cells via gap junction coupling. Thus, the analysis shows that the estimated value of coupling conductance could be deleterious in such pathological scenario, leading to a detrimental inhibition of normal functioning cells at glucose levels that should trigger insulin release. Lowering of the coupling conductance could, in this case, recover cells response by suppression of this inhibitory pathway.

8.4 Coupling effects on slow oscillations

Despite fast bursting, human β-cells also present a slow bursting pattern, whose oscillation period is $\simeq 3-5\,min$. As discussed above it was hypothesised that slow variations of the intracellular ATP, which has been found to vary on the same time scale, evoke such pattern by slow inhibition and activation of the K-ATP current, and it was numerically shown that metabolic oscillations can potentially drive the slow burst in humans [162]. In this section, the interest is to study how coupling can affect such oscillatory pattern of activity. To this purpose both the electrophysiological and the glycolytic subsystems of the model are resolved here in the case of $2\,x\,2\,x\,2$ heterogeneous clusters (cluster size is reduced due to computational issues). Specifically, cells heterogeneity is implemented by random extraction from Gaussian distributions of both the g_{Kv} and the glucokinase

reaction rate (V_{GK}) parameters. This particular choice is due to the variability in the glucokinase expression level between β-cells, that is reflected in heterogeneity in glucose sensitivity. Thus, for a certain glucose concentration, a cell can either be silent or slowly bursting with her own intrinsic rhythm. In the following, such system is resolved considering the sole electrical coupling (as done in the previous analyses), and in addition also metabolic coupling. In fact, as discussed in Chapter 5, Cx36 channels allow the diffusion of specific metabolites. In this case, the glycolytic subsystem can be modified to take into account a gap junction mediated metabolic coupling, in line with the procedure adopted to introduce the electrical coupling factor in the dynamics of the membrane potential. Specifically, in agreements with other modelling study [177] and based on data of G6P and F6P diffusion between coupled mouse β-cells [178], the metabolic coupling is here implemented by modifying the $G6P \cdot F6P$ dynamics, introduced in Chapter 7, according to:

$$\frac{d(G6P \cdot F6P_i)}{dt} = V_{GK} - V_{PFK} - p_{G6P \cdot F6P} \sum_{j \in \Omega_i} (G6P \cdot F6P_i - G6P \cdot F6P_j)$$

where $p_{G6P \cdot F6P}$ is the metabolic coupling factor, estimated to be $\simeq 0.01\, ms^{-1}$ from experimental data [178]. Concerning numerical simulations the metabolic subsystem is here resolved in parallel to the electrical subsystem, adopting a Euler scheme with a fixed time step of $0.02\, ms$ due to the non-restrictive slow dynamics of the glycolytic oscillator. With these assumptions, the interest is to study the effect of both couplings on the emergent electrical activity, both separately and in combination.

When the sole electrical coupling is studied, the model shows an interesting behaviour. Simulations results are presented in Fig. 8.10(a). Electrical coupling does not affect glycolytic oscillations as it can be noticed from the FBP oscillations, which continue to drift when the coupling is activated ($g_c = 0.010\, nS/pF$). In contrast, cells membrane potential shows an irregular behaviour, with clear perturbations induced in the silent phase of the slow burst when the coupled cell is in the active phase. In this case, shorter isolated groups of action potentials can be observed within the slow bursting pattern. Such "fragmentation" of the burst elicits intracellular calcium oscillations with a reduced amplitude. Interestingly such behaviour resembles some experimentally recorded slow pattern (see Fig. 8.11).

Contrarily when cells are coupled with the sole metabolic coupling (Fig. 8.10(b)), glycolytic oscillators are perfectly synchronised, as it can be noticed by the in-phase FBP oscillations. Membrane potential, in this case, does not present perturbations and calcium oscillation are only minimally affected by the metabolic coupling, mainly because the duration of the active and silent phases of the burst slightly varies in response of

glycolytic synchronisation. To note that the action potentials (or fast bursting oscillations) within the active phase of the slow burst are not synchronised due to the missing electrical coupling.

When both electrical and metabolic coupling is considered, cells are able to synchronise both their metabolic oscillations and their electrical activity. Interestingly, when cells are modelled as SK-type bursters, cells membrane potential shows sustained oscillations in a depolarised state (Fig. 8.10(c)). Such effect is mainly due to the electrical coupling of the SK-type bursters, which was shown before to be able to trap cells in the active phase of the fast burst. In this condition, calcium oscillations are not only synchronised but also show a significant increase in amplitude, possibly suggesting an increase in the insulin release. To note that such pattern is also experimentally observed in some human β-cells as shown in Fig. 8.11.

Finally, the gap junction estimate obtained in the first analysis with the sole electrical subsystem is here validated considering the complete model, with both electrical e metabolic coupling. Specifically, an active-silent cell doublet is here modelled by fine-tuning the glucokinase reaction rate ($V_{GK} = 0.00005\, mM/ms$ for the silent cell, and default value for the active cell). Results are shown in Fig. 8.12. When both electrical and metabolic coupling are switched on ($g_c = 0.01\, nS/pF$ and $p_{G6P\cdot F6P} = 0.01\, ms^{-1}$), the active cell evokes small amplitude voltage oscillations in the silent cell, with an amplitude consistent with the experimental data in Fig. 8.1. The evoked electrical activity is, in turn, able to drive slow calcium oscillations in the otherwise silent cell. Moreover, metabolic coupling induces perturbations in the FBP dynamics, showing slow oscillations in the silent cell also in this case. Interestingly, FBP oscillations amplitude in the active cell is significantly enhanced in this condition. However, such variations are not discussed further here, since a dedicated study on the coupled dynamics of glycolytic oscillators should be performed to address this effect correctly. This last analysis shows that the estimated range of coupling conductance can reproduce experimental data also by considering the slow activity driven by metabolic oscillations.

8.5 Discussion

The key role of gap junction coupling in mouse β-cells has been largely proven. Dedicated studies have been performed to characterise electrophysiological properties of these channels and their role and dysfunction in diabetic conditions [68, 89, 90, 179]. Such evidence raises questions about gap junction role in human islets. Even though Cx36 gap junction channels were shown to be present between human β-cells [137], no experimental studies have been performed to investigate electrophysiological properties of

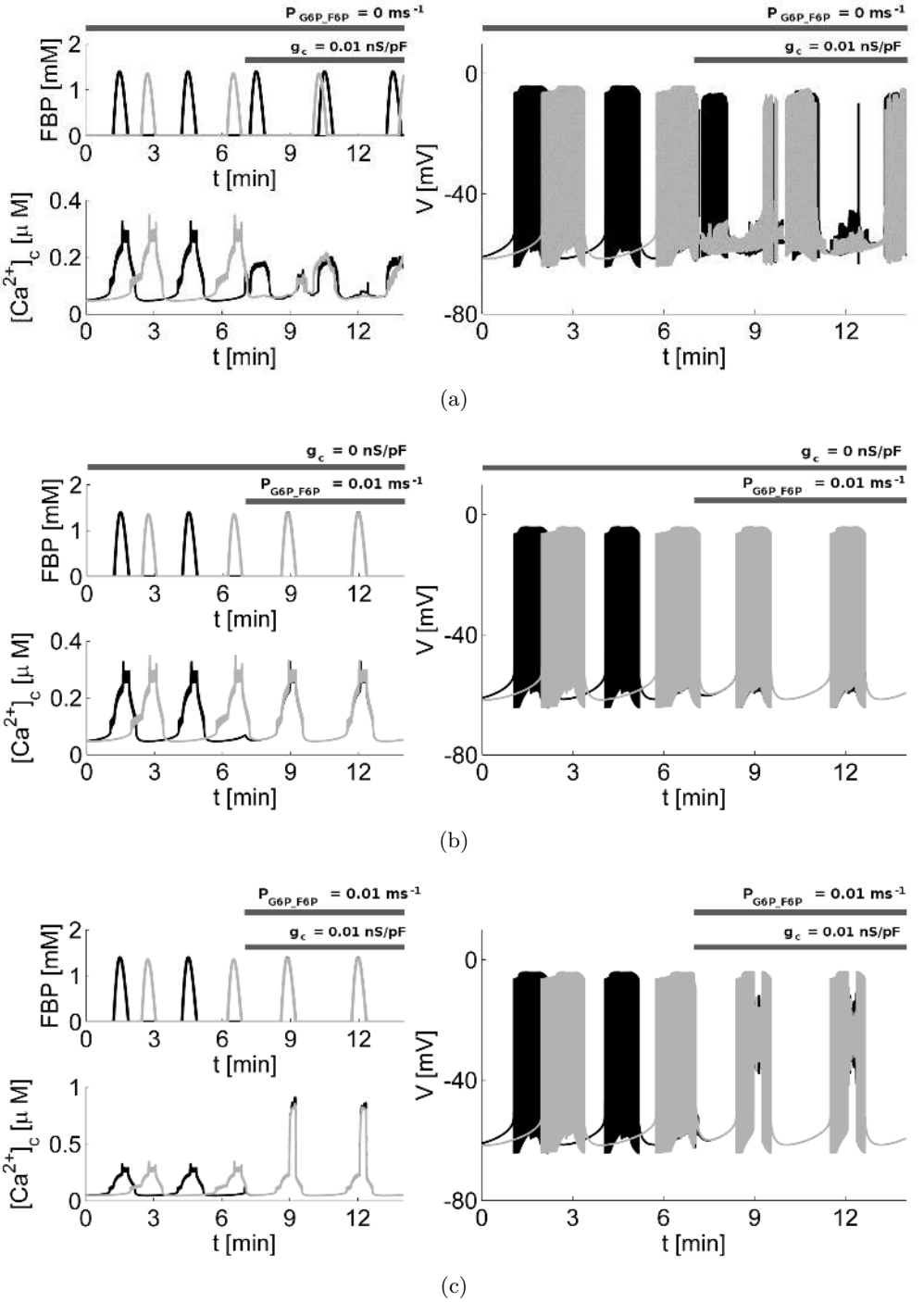

FIGURE 8.10: Simulations of 2 x 2 x 2 clusters of human slow bursting β-cells. Membrane potential, FBP and cytosolic calcium time series of two representative cells. (a) Cells response with only electrical coupling ($g_c = 0.01\,nS/pF$). (b) Cells response with only metabolic coupling ($p_{G6P\cdot F6P} = 0.01\,ms^{-1}$) electrically electrical. (c) Cells response considering both electrical and metabolic coupling ($g_c = 0.01\,nS/pF$ and $p_{G6P\cdot F6P} = 0.01\,ms^{-1}$). Simulations performed considering SK-type bursters. Grey bars denote the time interval during which the coupling is turned on.

Alessandro Loppini

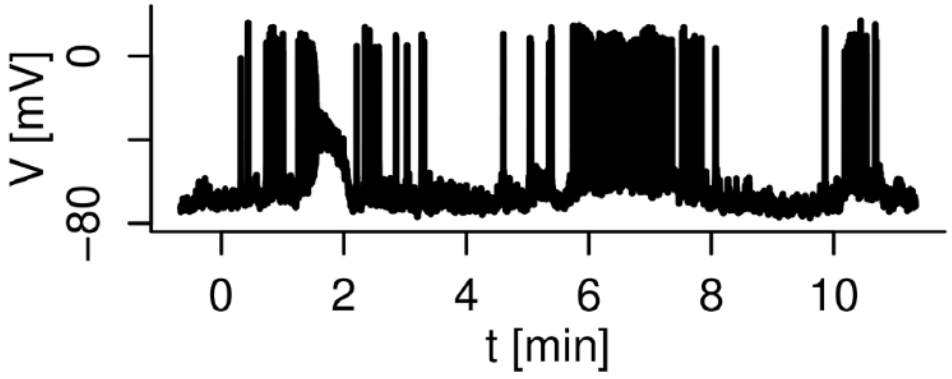

FIGURE 8.11: Experimental recording of a human β-cell showing slow bursting. Both sustained high voltage oscillations and fragmentation of the slow burst can be noticed, as reproduced from simulations. From ref. [162].

such coupling. The analyses here presented were based on a mathematical modelling approach to investigate this aspect. Specifically, a generalised version of the human β-cell electrophysiological model presented in Chapter 7 (see refs. [161, 162]), was used here to reproduce experimental recordings of β-cells, showing atypical small amplitude oscillations. It is important to note that the obtained estimate of g_c relies on the assumption that a silent cell can be coupled to an active cell without being activated in turn, underlying the importance of gap junction coupling in synchronising cells more than activate otherwise silent cells. Such hypothesis seems to be confirmed by mouse islet recording showing coexistence of active and silent cells in response of glucose gradients [54, 141], and by β-cell recordings from humans islets, where cells characterised by long quiescent periods in response to glucose are coupled to cells showing a more active behaviour [180]. Hence such evidence supports the study's assumptions.

Performed analyses suggest that a coupling conductance of $g_c = 100 - 200\,pS$ is required to reproduce experimentally observed oscillations. Surprisingly, this value is in line with the measured value of gap junction conductance between mouse β-cells [68, 134, 176]. Such estimate is fairly robust, both respect to the single cell parameters and to the cell number, and it is obtained via the use of a highly reliable mathematical model carefully fine-tuned to reproduce heterogeneous response of human β-cell. Based on these facts the obtained result takes a great relevance. To note that it is not obvious a similar coupling conductance between mouse and human gap junction channels since Cx36 channels may differ in expression, have different properties or be differently regulated in human islets; moreover other types of Cx junctional channels may result in different global values of electrical coupling between human neighbouring cells. For instance, K-ATP channel conductance is largely different between mouse and human [158].

Alessandro Loppini

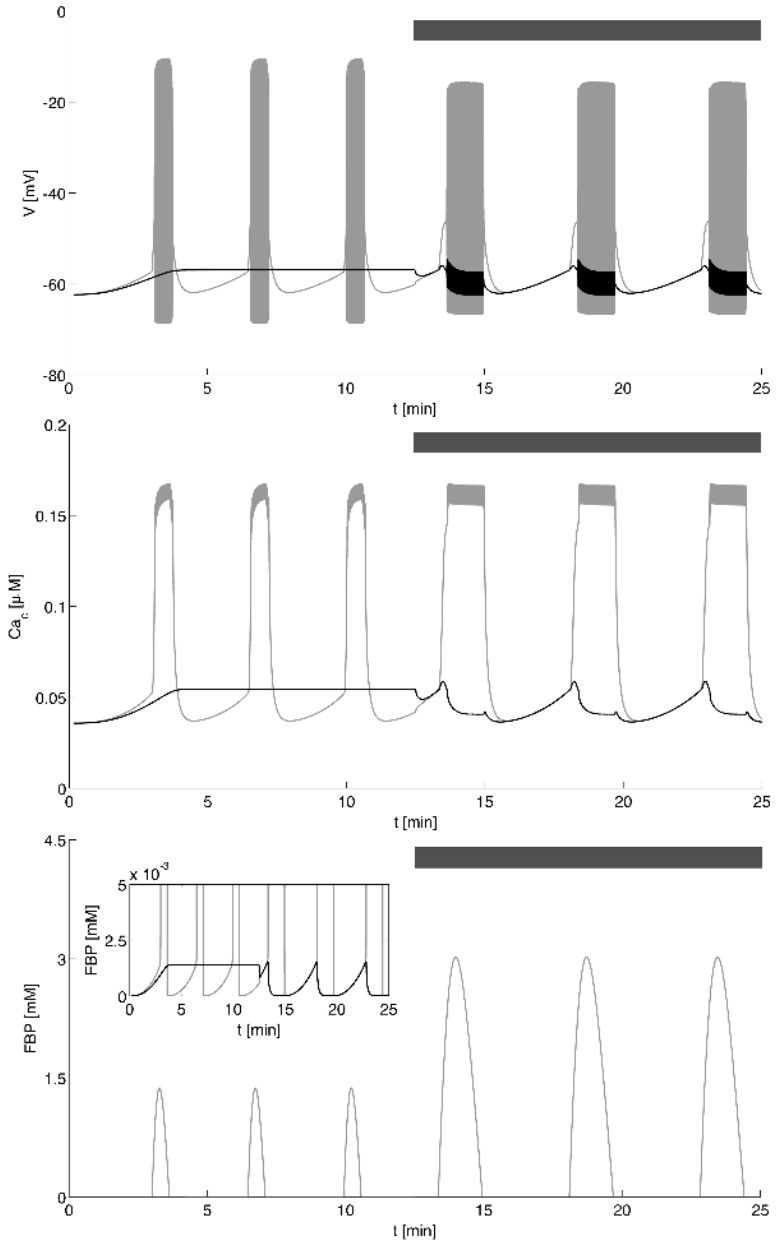

FIGURE 8.12: Simulations of cell doublets driven by the glycolytic oscillator. Membrane potential (top), cytosolic calcium concentration (centre), and FBP (bottom) time series for the silent (black) and active (grey) cell.

Alessandro Loppini

Results show that a value of coupling equal to the lower limit of the estimated range is enough to achieve synchronisation of small heterogeneous clusters of spiking and bursting human β-cells. Interestingly, the emergent effect of enhanced bursting period is reminiscent of coupling effect on mouse β-cells models, and is probably due to the partial synchronisation effect of the action potentials within the burst. It is important to note that sustained bursting activity is linked to increased calcium oscillations and consequently to enhanced insulin secretion. The evidence that the here estimated coupling is able to synchronise small human β-cell cluster is in line with the partial degree of synchrony observed in human islets [126, 165], and with the evidence of an oscillatory pattern of insulin release recorded from the whole islet [181].

In the case of mixed clusters of bursting and spiking cells, the analyses show moreover that bursting behaviour is a less robust dynamics in human compared to the mouse. In fact, results suggest that the bursting state is unstable respect to the perturbation induced by the spiking oscillation. However, a more comprehensive dynamical study should be performed to address correctly this point, but such approach is not so trivial due to the high complexity and dimensionality of the adopted model. One could speculate that limited connectivity in human islet could also serve to preserve bursting regime in β-cells subpopulation within the islet. When the coupling estimate is applied to mixed coupled clusters of normally spiking cells and silent cells, resembling β-cells expressing mutant K-ATP channels, model results seem to suggest a similar emergent dynamics compared to experimental observations on mutant rodent islets [83]. Therefore, also in human gap junction coupling could be deleterious in such pathological conditions, where mutant silent cells are in principle able to inhibit the whole cluster, silencing the otherwise active cells.

Concerning slow activity patterns, simulations of electrically coupled β-cells showing glycolytic-driven bursting are surprisingly in agreement with some experimental recordings, further validating the obtained estimate. In this case, heterogeneity in the glycolytic intrinsic rhythm of cellular oscillators and limited diffusion of metabolites seem to be required to reproduce the fragmentation of the action potentials grouping induced by the slow variations in ATP concentration. In addition, because of coupling, the out-of-phase glycolytic oscillators give rise to the appearance of small amplitude oscillation ($\simeq 10\,mV$) in the membrane potential during the silent phases of the slow pattern, comparable to the oscillations experimentally observed in human fast activity, and on which the gap junction estimation was based. These observations suggest that metabolic coupling could not be required to the normal activity of human β-cells. As a confirmation, diffusion of metabolites, whose properties are estimated here from a published study on rat [178], rapidly synchronises metabolic oscillations giving rise to a too regular electrical behaviour compared to experimental evidence. Nonetheless, when the metabolic

coupling is taken into account, sustained oscillations from a high voltage plateau can be reproduced, resembling some other atypical pattern observed in slowly bursting cell; although aspects other than coupling could underlie such observation.

Results obtained are not in contrast with the published studies on human islets. The fact that the estimated coupling conductance is able to synchronise β-cells within small clusters is in line with human islet recordings showing the existence of coordinated activity within limited spatial ranges [126, 165]. Such findings have been suggested to have strong implications for islet functions [126]. In this scenario, the small clusters here studied are in agreement with the limited functional synchrony and with the architectural constraints of the human islet. Results show that even in such small clusters electrical coupling can have an impact on emergent electrical activity, affecting insulin release. In this perspective, human islet architecture could serve to achieve a certain degree of heterogeneity in cellular response, maybe pursued with functionally distinct modules of insulin-releasing β-cells. However, further experimental studies should be performed to confirm the goodness of the estimate and the results here presented. For this purpose, it is interesting to note that in human islet it is not possible to adopt a single patch-clamp technique usually adopted to estimate gap junction coupling between mouse β-cells [134, 182]. Such approach, in fact, is based on a combination of a voltage and current-clamp performed on a β-cell within a coupled cluster, and in order to be used requires a regular bursting activity not perturbed by experimentally injected currents. This assumption holds in the mouse case, but contrarily β-cell electrical activity in human clusters is significantly perturbed by coupling, and is not possible to extrapolate a conductance value from the emergent non-physiological behaviour. Thus, in this case, a more sophisticated dual patch-clamp technique should be adopted to confirm coupling conductance estimate, in line with other experimental studies performed in mouse [68].

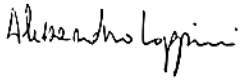

Chapter 9

Conclusions

Despite a large amount of research on the topic, the complex dynamics of pancreatic β-cells is far from being well understood. In this context, the studies on rodents allowed the identification of the main regulatory processes involved in insulin secretion, but some aspects remain unresolved. Gap junction coupling is one of them. In vivo and in-vitro experiments converge to the evidence that such coupling is an important regulator of β-cells function, and recently has been suggested that gap junction dysfunction is also implicated in the physiopathology of diabetes. Such evidence accumulated on rodents has to be necessarily validated in humans, in order to enrich our understanding of the diabetic syndrome and possibly suggesting new therapeutical perspectives.

In the presented work, the effect of gap junction coupling on β-cells function has been analysed with a mathematical modelling approach, trying to elucidate further gap junction effect in mouse islet, and to investigate gap junction coupling in the human islet.

9.1 Novel results and implications

Results obtained have clarified interesting aspects of the emergent dynamics in coupled population of mouse β-cells, and represents the first attempt to estimate the gap junction coupling in human islets.

The simulations of cubic mouse β-cell cluster have highlighted important features of coherent dynamics. Such coherence is a robust dynamical state that ensures long range correlations in cellular activity. It is interesting to note that the coherent emergent dynamics is strictly dependent on cluster size and glucose stimulation level, thus synchronised and robust bursting is achieved only at proper sizes of the β-cell population and in a specific range of the stimulating glucose concentrations. The β-cell cluster is

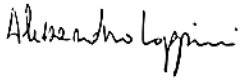

able to switch from coherent to uncorrelated dynamics resembling phase transition and critical phenomena also observed in other physical systems. This aspect has a great relevance if we think that also other biological networks regulate their dynamics around a critical point and show coherent dynamics, i.e. neurons. In such dynamical regimes a small scale variation can quickly be reflected at large scale, and in multicellular systems this property can be used to achieve an efficient organisation. In the presented work coherence and criticality was pointed out also in β-cells systems.

The analysis of the topological effects in electrically coupled networks of β-cells has moreover pointed out the role of the structure in the emergence of organised electrical activity. In this context, it was shown that the mouse β-cells compact architecture can be viewed as a fully coupled functional unit while the human architecture shows a substantially different behaviour. A percolated cluster resembling β-cells arrangement in human islet gives rise to an emergent electrical activity characterised by distinct functional modules. In this case, a scale-free similarity in the synchronisation pathways was observed, possibly due to the underlying percolated structure. Such functional properties are interestingly promoted for glucose stimulations and coupling strengths in physiological ranges. The adopted functional network technique is moreover a new approach by which the structure-function coupling problem can be analysed against functional experimental studies on whole islet recordings.

With the use of experimental data and via a generalised electrophysiological model of human β-cell electrical activity, it was moreover estimated the gap junction coupling in the human islet. Interestingly, such estimate is in line with measure performed in rodent islet, suggesting that gap junction channels could have similar electrical properties between the two species. Results, in this case, have shown that such coupling is enough to achieve synchronisation of small human β-cells population, and that can significantly alter emergent dynamics of cells in different electrical regimes.

9.2 Study limitations

The adopted Sherman-Rinzel-Keizer model represents one of the first electrophysiological models of β-cell electrical activity. It is based on a bursting mechanism underlying slow variations in intracellular calcium oscillation, and it can reproduce mouse fast bursting. The model is not able to reproduce slow bursting and compound bursting also observed in mouse islet, thus, more realistic models should be used to analyse synchronisation properties considering all the possible bursting regimes. Moreover, bursting emergence was studied in the framework of intrinsically stochastic coupled cells. A

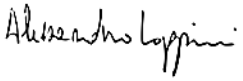

deterministic heterogeneous approach should also be used to investigate possible variations in the emergent dynamics. Concerning the study of coupling between human β-cells, two main limitations are the limited number of observations similar to the one used to estimate the gap junction conductance, and the assumption that the observed atypical pattern of oscillations is due to the occurrence of an active and a silent cell. Unfortunately, no other data were available, and the formulated hypothesis could not be verified from experiments; although, it is in line with the evidence of β-cell heterogeneity in glucose sensitivity, and with the coexistence of neighbouring silent and active cells in pancreatic islets.

9.3 Future perspectives

Future works should take into account more comprehensive models of mouse β-cells electrical activity, analysing coherence and synchronisation pathways in the different bursting regimes observed in mouse. In line with other studies, it would also be of interest to resolve these models in the case of degenerative pathologies that have a significative impact on cellular architecture, such as Type 1 diabetes. Moreover, the interest is also to study β-cell populations coupled with the α-cells. To this purpose dedicated mathematical models reproducing α-cell electrophysiology should be considered, taking into account paracrine signalling based on the current knowledge. With this approach, topological differences between species, as well as the topology destruction of the islet, could also be studied analysing heterotypic cells interaction. In addition, in the framework of functional network analysis it will be of interest to further analyse the structure-function problem by using such an advanced mathematical modelling, reconstructing causal pathways of cellular interactions by adopting more suitable techniques such as partial correlations analysis. Accordingly, it will be possible to infer in a consistent way structural property from cells activity directly validating obtained results, with possible applications to whole islet data used to investigate functional connectivities.

In order to investigate possible variations in the emergence dynamics, electrophysiological models fine-tuned on human data should also be tested on percolated clusters resembling human islet architecture, comparing results with the case of small compact clusters. Moreover, considering the abundance of heterotypic interactions, and the cholinergic input coming from α-cells in human islets, the modelling should take into account the paracrine interactions. Such approach could give in this case a more comprehensive picture of the whole islet activity, by analysing electrical response and hormones secretion in different operating conditions, from the physiological up to the diabetic state. To note that in this perspective, electrophysiological models reproducing

the endocrine cells activity could be coupled to mathematical models describing cellular mass dynamics and islet plasticity, thus resolving both the dynamics the network topology and the evoked electrophysiological response.

Alessandro Loppini

Publications

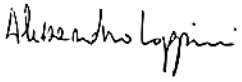

Physics Letters A 378 (2014) 3210–3217

Contents lists available at ScienceDirect

Physics Letters A

www.elsevier.com/locate/pla

On the coherent behavior of pancreatic beta cell clusters

Alessandro Loppini [a], Antonio Capolupo [b,*], Christian Cherubini [a,c], Alessio Gizzi [a], Marta Bertolaso [d], Simonetta Filippi [a,c], Giuseppe Vitiello [b]

[a] *Nonlinear Physics and Mathematical Modeling Lab, University Campus Bio-Medico, Via A. del Portillo 21, I-00128 Rome, Italy*
[b] *Physics Department, University of Salerno, Fisciano (SA), 84084, Italy*
[c] *International Center for Relativistic Astrophysics, University Campus Bio-Medico, Via A. del Portillo 21, I-00128, Rome, Italy*
[d] *Faculty of Engineering and Institute of Philosophy of Scientific and Technological Practice, University Campus Bio-Medico, Via A. del Portillo 21, I-00128 Rome, Italy*

ARTICLE INFO

Article history:
Received 23 July 2014
Received in revised form 11 September 2014
Accepted 15 September 2014
Available online 27 September 2014
Communicated by Z. Siwy

Keywords:
Nonlinear dynamics
Coherent states
Pancreatic beta-cells

ABSTRACT

Beta cells in pancreas represent an example of coupled biological oscillators which via communication pathways, are able to synchronize their electrical activity, giving rise to pulsatile insulin release. In this work we numerically analyze scale free self-similarity features of membrane voltage signal power density spectrum, through a stochastic dynamical model for beta cells in the islets of Langerhans fine tuned on mouse experimental data. Adopting the algebraic approach of coherent state formalism, we show how coherent molecular domains can arise from proper functional conditions leading to a parallelism with "phase transition" phenomena of field theory.

1. Introduction

Islets of Langerhans in the pancreas are ellipsoidal clusters of excitable endocrine cells that ensure blood glucose homeostasis. Alpha, beta, delta and PP cells form this particular structure. Specifically beta cells are able to lower glycemic level by releasing insulin [1]. In rodents, these cells are clustered in the central core of the islet surrounded by peripheral alpha cells, and are coupled through specific connections, the gap junctions [2–5]. In response to glucose uptake from extracellular space, beta cells within the islet modify their membrane potential, exhibiting slow oscillations with superimposed action potentials (bursting activity) [1]. This characteristic behavior leads to oscillations of the intracellular calcium concentration that triggers pulsatile insulin release [6,7]. On the other hand, isolated beta cells show an irregular spiking activity in response to glucose stimuli. Experimental measurements show moreover that beta cells electrical activity is synchronized over the islet [6,8,9]. Such an observed feature highlights that a coherent intercellular correlation extending over the islet's volume can be established under proper functional conditions and glucose concentrations, providing the motivation for the study presented in this paper. We indeed analyze such a behavioral property of the cells in the frame of a Hodgkin–Huxley [10] type model also considering the kinetics of the stochastic K–Ca channels [11] (calcium-dependent potassium channels; here Ca stands for the ion Ca^{2+}). We thus focus our study on the dynamics of the membrane potential in variable scale clusters in connection with intracellular calcium concentration and the activation of potassium and calcium channels. Our numerical simulations agree with the observed possibility of formation of coherent molecular domains and show how this depends on glucose concentrations and on the islet size. In particular, we find that the power density spectrum (PDS) of membrane voltage exhibits scale free self-similarity features with respect to frequency occurring with different self-similarity dimension in different frequency intervals and show how such a feature is indeed an evidence of coherent molecular dynamics. In our discussion, we use the algebraic approach of the coherent state formalism through which the isomorphism is shown to exist between the linear fit of the log–log plot of PDS/frequency and the squeezed coherent state algebraic structure. The plan of the paper is the following. The mathematical modeling is introduced in Section 2, while numerical simulations and results are presented in Section 3. The notions of (fractal) self-similarity dimension and squeezed coherent states are given in Section 4, where the algebraic isomorphism between self-similarity and coherent states is also discussed. Section 5 is devoted to conclusions.

* Corresponding author.
E-mail addresses: a.loppini@unicampus.it (A. Loppini), capolupo@sa.infn.it (A. Capolupo), c.cherubini@unicampus.it (C. Cherubini), a.gizzi@unicampus.it (A. Gizzi), m.bertolaso@unicampus.it (M. Bertolaso), s.filippi@unicampus.it (S. Filippi), vitiello@sa.infn.it (G. Vitiello).

http://dx.doi.org/10.1016/j.physleta.2014.09.041
0375-9601/

Alessandro Loppini

2. Mathematical modeling

An extended version of the stochastic multi-cell SRK (Sherman–Rinzel–Keizer) model [12], based on mouse electrophysiological data, was adopted to study bursting activity of beta cells cubic clusters of variable size for different glycemic levels. Such a Hodgkin–Huxley type model permits to reproduce isolated and coupled dynamics of beta cells. This is because of the stochastic formulation of the high conductance K–Ca channel gating. Single gating events of this specific type of channel can lead the cell to an active or a silent state, making possible to observe a spiking activity in an isolated cell. Thanks to "channel sharing", coupled cells are able to share the entire population of K–Ca channels [11,12], overcoming noise and giving rise to bursting behavior, a characteristic electrical pattern observed experimentally in beta cells within the islet. The model's equations for the i-th cell are:

$$C_m \frac{dV}{dt} = -I_{ion} - \bar{g}_{K\text{-}Ca} p (V - V_K) - g_c \sum_{j \in \Omega} (V - V_j)$$

$$\frac{dn}{dt} = \lambda \left[\frac{n_\infty - n}{\tau_n(V)} \right]$$

$$\frac{dCa}{dt} = f[-\alpha I_{Ca} - k_{Ca} Ca]$$

$$\langle p \rangle = \frac{Ca}{K_d + Ca}$$

$$I_{ion} = I_K + I_{Ca} = \bar{g}_K n (V - V_K) + \bar{g}_{Ca} m_\infty(V) h(V) (V - V_{Ca})$$

$$m_\infty(V) = \frac{1}{1 + \exp[(V_m - V)/S_m]}$$

$$h(V) = \frac{1}{1 + \exp[(V - V_h)/S_h]}$$

$$n_\infty(V) = \frac{1}{1 + \exp[(V_n - V)/S_n]}$$

$$\tau_n(V) = \frac{c}{\exp[(V - \bar{V})/a] + \exp[(V - \bar{V})/b]},$$

where the dynamical variables V, n, Ca have to be understood as V_i, n_i, Ca_i. The ODE system models the dynamics of the membrane potential V, the potassium channel activation level n and the intracellular calcium concentration Ca. C_m represents the membrane capacitance; $m_\infty(V)$ and $n_\infty(V)$ are sigmoid functions defined upon constant values of the voltage; in particular, they represent the steady states of the calcium and potassium currents, respectively, once a step function of the voltage is imposed; $h(V)$ is the inactivation curve of calcium channels; $\tau_n(V)$ is the voltage dependent time constant of potassium channels fine tuned by the parameter λ; $\bar{g}_K$, $\bar{g}_{Ca}$ and $\bar{g}_{K\text{-}Ca}$ represent the whole cell conductances of potassium, calcium and potassium–calcium dependent ionic channels, respectively; g_c is the strength (conductance) of coupling between two adjacent cells due to gap junctions, in a 3D Von Neumann neighborhood (Ω) of the cell modified to take account of different communication rules on the boundary region (in Fig. 1 is shown a $5 \times 5 \times 5$ cluster and the neighborhood considered for a central cell); p is the fraction of open K–Ca channels whose transition events are obtained as evolution of a stochastic process described in the following; V_K and V_{Ca} are the potassium and calcium equilibrium potentials; f is a fixed parameter which slows down intracellular calcium dynamics; the factor α converts current units in concentration units; k_{Ca} represents the rate at which calcium is pumped out from cytosol to extracellular space; K_d is a factor that depends on K–Ca channels kinetics; a, b, c, and $\bar{V}$ are parameters used to fine tune the dependence of the potassium channel time constant on the membrane voltage; V_n, V_m, V_h, S_n, S_m and S_h are parameters used to fit the activation and inactivation curves of the ion channels.

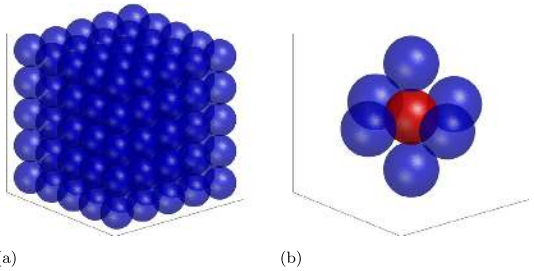

(a) (b)

Fig. 1. 3D view of a $5 \times 5 \times 5$ cluster (a) and Von Neumann neighborhood (b) for a central cell, plotted in red. (For interpretation of the references to color in this figure legend, the reader is referred to the web version of this article.)

2.1. Stochastic gating of K–Ca channels

Transition events of the K–Ca channels were computed with the use of a two state Markov process for each ionic channel. Following [11], a two-state kinetics was adopted, i.e.:

$$\mathcal{C} \underset{1/\tau_o}{\overset{1/\tau_c}{\rightleftharpoons}} \mathcal{O}, \qquad \tau_o = \tau_c \frac{Ca_i}{K_d}.$$

Here τ_o and τ_c are the mean opening and closing times. Keeping τ_o fixed, τ_c varies as a function of intracellular calcium. The probabilities that a channel in a specific state makes a transition in a fixed time window are given by:

$$\frac{\Delta t}{\tau_c} = \text{Prob}\{s(t) = \mathcal{O}, t + \Delta t \mid s(t) = \mathcal{C}, t\},$$

$$\frac{\Delta t}{\tau_o} = \text{Prob}\{s(t) = \mathcal{C}, t + \Delta t \mid s(t) = \mathcal{O}, t\};$$

where $s(t) \in \{C, O\}$ is a stochastic variable and Δt is the considered time step [13]. Considering 600 channels of K–Ca type per cell, each two-state process was resolved with the use of a Monte Carlo simulation, computing the fraction of open channels at every integration time step of the model equations.

2.2. Glucose feedback

As in Ref. [14], glucose feedback was modeled tuning the calcium removal rate parameter in order to reproduce experimentally observed beta cells activity at specific blood glucose concentrations $[G]$. At about $[G] = 5.5$ mM and $[G] = 16.6$ mM, a silent-bursting and a bursting-continuous spiking transition, respectively, can be observed in beta cells membrane potential. These behaviors can be obtained in the model setting $k_{Ca} = 0.02\ \text{m s}^{-1}$ and $k_{Ca} = 0.09\ \text{m s}^{-1}$. Considering these observations, a simple linear function was adopted to achieve the feedback:

$$k_{Ca} = A[G] - B \quad \text{for } [G] \geq 2.33\ \text{mM},$$

where $A = 6.3 \cdot 10^{-3}\ \text{m s}^{-1}\,\text{mM}^{-1}$, $B = 0.0147\ \text{m s}^{-1}$ and $[G]$ is the glucose concentration. A full list of the adopted parameters is given in Appendix A.

3. Numerical simulations

A fourth order Runge–Kutta method with a fixed time step of 0.1 ms was adopted to solve the ODE system. The global model was implemented in a C++ code. Cells' voltage membrane signals

Alessandro Loppini

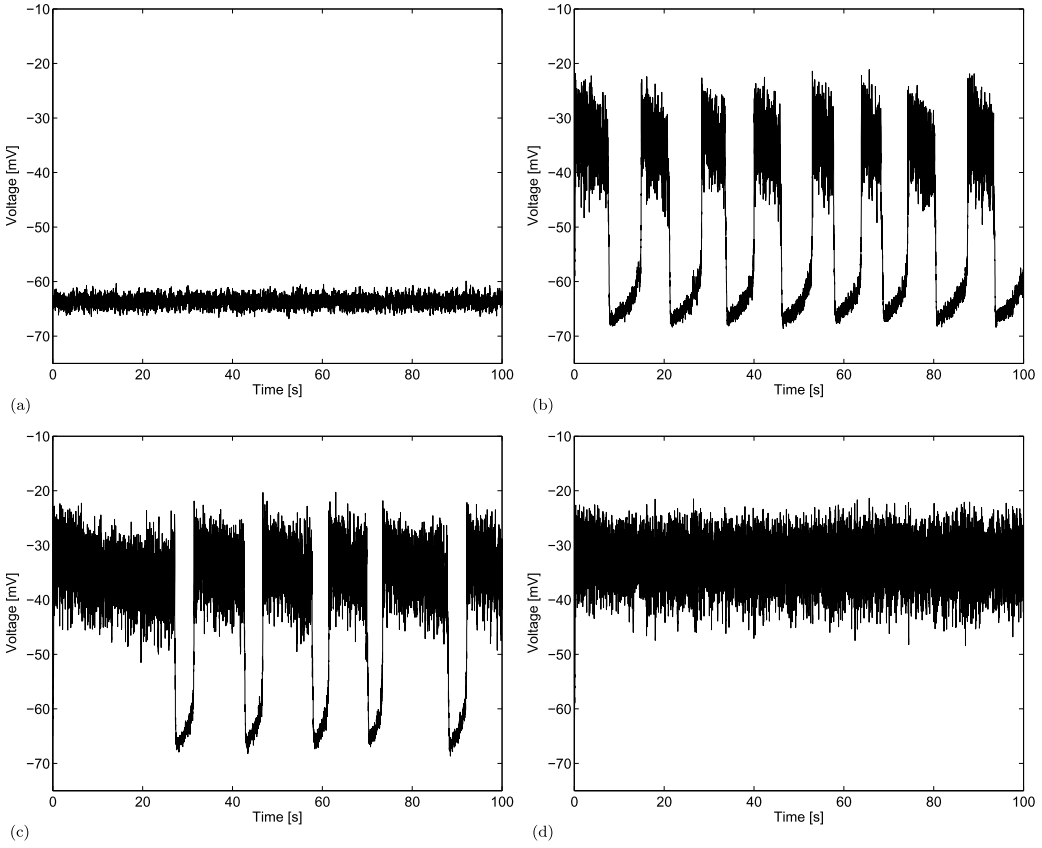

Fig. 2. Membrane potential signals of a representative cell in a $5 \times 5 \times 5$ cluster, stimulated by different glucose concentrations: (a) $[G] = 4.7$ mM; (b) $[G] = 9.5$ mM; (c) $[G] = 12.6$ mM; (d) $[G] = 16.6$ mM.

obtained from simulations were analyzed with the Matlab® software, computing signals spectra with the use of the FFT algorithm here implemented. Our analysis shows how the activity of beta cells depends on the glucose bath concentration $[G]$ and on the islet size (cluster population).

Dependence of the beta cell activity on glucose bath concentration. In order to investigate a coherent activity of beta cells in the islet and its possible correlation with glucose stimuli, we initially modeled a 125 cells cubic cluster in glucose baths of different concentrations. Specifically, the cluster response was studied for glycemic levels in the range $[G] = 4.7$ mM–16.6 mM, analyzing a representative cell of the network. In Fig. 2 the computed membrane potentials in time for $[G] = 4.7, 9.5, 12.6, 16.6$ mM are shown (Fig. 2a, b, c, and d, respectively). As can be seen, the model correctly reproduces silent, bursting and continuous bursting behavior experimentally observed at increasing glucose levels. Three characteristic time scales can be noticed: the bursting slow wave with a period of tens of seconds, the spiking activity of the order of hundreds of milliseconds, and an infinitely low time scale due to stochastic channel gating. The power density spectrum (PDS) of voltage signals was computed to highlight scaling features of the signals as an observable phenomena of coherent activity in the cluster. In Fig. 3 the PDS of signals reported in Fig. 2 are plotted in a log scale. Scaling properties were then analyzed computing log–log slopes of linear trends observed in PDS. Performed analysis have shown that a representative cell of the cluster, stimulated by typical postprandial glucose concentration ($[G] \simeq 9.5$ mM, Fig. 3b), presents two different linear trends in the log–log plot of PDS, at low and high frequency ranges, respectively, with an intermediate transition region (highlighted in blue in the PDS plots). The slopes in the log–log plots were then computed with a linear fitting of data in these two ranges of frequencies (red and green lines in the PDS plots represent the computed slopes), at different glucose levels. Results obtained are reported in Fig. 4. As can be seen, the slope at high frequencies (HF) is $S_{HF} \simeq -33$ dB/Hz per decade and seems to be independent on glucose level. The slope at low frequencies (LF) instead is nearly absent in the clustered cells stimulated by both subthreshold and very high glucose concentrations, while can be observed at intermediate glucose levels that ensure regular bursting, where $S_{LF} \simeq -20$ dB/Hz per decade at postprandial glycemic level.

Dependence of the beta-cell activity on cluster population. With the aim to support the coherence hypothesis, a Pearson's correlation matrix was obtained from data, treating membrane potential time series of the modeled cells as multiple observations from different stochastic variables. In Fig. 5, the surface plots of the correlation matrix for the 125 cells cubic cluster in subthreshold and postprandial glucose concentrations are shown. As can be noticed, the

Alessandro Loppini

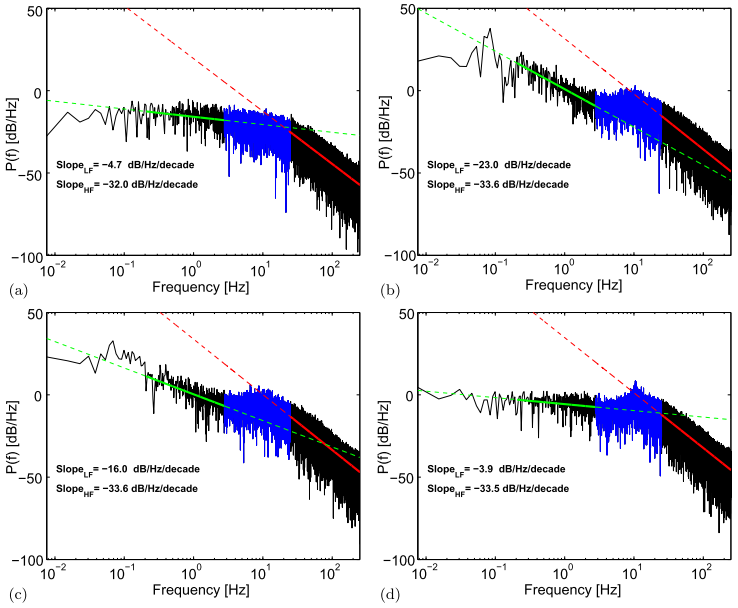

Fig. 3. Log–log power density spectra of membrane potential signals of a representative cell in a $5 \times 5 \times 5$ cluster, stimulated by different glucose concentrations: (a) $[G] = 4.7$ mM; (b) $[G] = 9.5$ mM; (c) $[G] = 12.6$ mM; (d) $[G] = 16.6$ mM. The slope at low frequencies (S_{LF}) is highlighted in green, the slope at high frequencies (S_{HF}) in red. Continuous lines segments highlight the PDS points used for the linear fitting; dotted lines segments are the extrapolation of the linear estimation. The transition region between the two linear zones is highlighted in blue. (For interpretation of the references to color in this figure, the reader is referred to the web version of this article.)

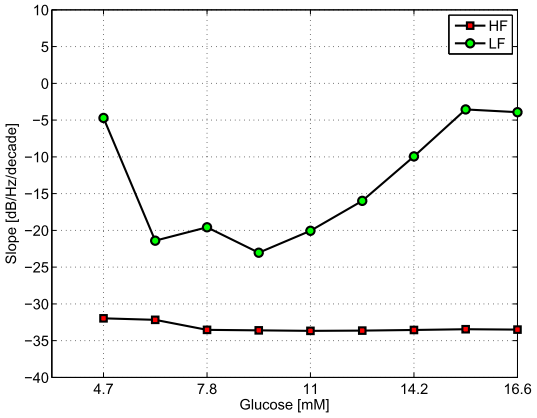

Fig. 4. Computed slopes at low (green circles) and high (red squares) frequencies for increasing glucose concentrations. (For interpretation of the references to color in this figure, the reader is referred to the web version of this article.)

correlation indexes of cells' voltage signals are quite high (all above 0.9) for suitable glucose levels (Fig. 5a), both for neighboring cells and for different cellular planes of the cluster; considering low glucose concentration instead, correlation indexes get lower with minimum values of about 0.4 (Fig. 5b).

Because of channel noise, a minimum size of the cluster (minimum cell population) is required to achieve robust bursting. With the aim to study cell population effect on slopes in the log–log PDS plots, we modeled clusters of increasing sizes starting from the single isolated cell up to the 1000 cells case, stimulated by a postprandial glucose concentration. In Fig. 6 the PDS plots of voltage signals for a representative cell of each cluster are reported. From results in Fig. 7, the slope at high frequencies seems to be also independent on cluster size with $S_{HF} \simeq -33$ dB/Hz per decade for clusters bigger than about ten cells; slightly lower values were obtained for the isolated cell and for the $2 \times 2 \times 2$ cluster. This threshold value for the cluster size can be noticed also in S_{LF} that is almost zero in the single cell, while it increases in modulus starting from the $2 \times 2 \times 2$ cluster.

In order to test slope invariance under perturbations, δV, of the single cell membrane potential V, model equations were solved considering the new variable (linear transformation) $\widetilde{V} = V + V_t$, with $V_t \equiv \delta V$ a constant perturbation parameter. Clusters containing 1, 27, 64 and 125 cells stimulated by postprandial glucose concentration were modeled analyzing log–log PDS plots of $\widetilde{V}$ for different values of V_t. Results are summarized in Table 1. As it can be seen, apart for the case of 1 cell, there are very little changes in the values of slopes, which signals the slope invariance under the V_t perturbation.

4. Self-similarity analysis

In the previous sections, we have found that power density spectra exhibit a log–log linear behavior in function of frequency with different slopes in different frequency intervals (cf. Figs. 3 and 6). In this section we show that an isomorphism exists between the log–log linear behavior and the coherent state formalism, which confirms the experimental observation of coherent cellular activity in the clusters.

Let $\mathrm{Log}\, P$ and $\mathrm{Log}\, f$ denote the ordinate and the abscissa, respectively, in Figs. 3 and 6. Also, in each of the cases considered in the figures, let a convenient translation of the reference frame be done, so that the straight line crosses the origin of the axis, which is equivalent to divide the abscissa (or multiply the ordinate) by a real number c, with $\mathrm{Log}\, c = s$, where s is the point intercepted

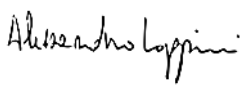

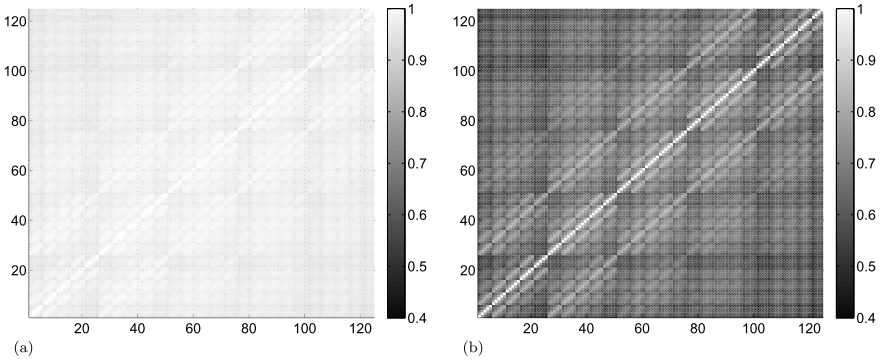

Fig. 5. Surface plots of the correlation matrix for (a) postprandial and (b) subthreshold glucose concentration in a $5 \times 5 \times 5$ beta cells cluster. The labeling of the axes has to be understood as a sequential numbering of the cubic cluster: 1–25 first cluster plane; 26–50 second plane; 51–75 third plane; 76–100 fourth plane; 101–125 fifth plane.

by the line on the abscissa axis. A measure of self-similarity is provided by the value of the slope d of the fitting straight line, $\mathrm{Log}\, P = d\, \mathrm{Log}\, f$, in each of the frequency intervals. Thus, we have

$$d = \frac{\mathrm{Log}\, P}{\mathrm{Log}\, f}. \tag{1}$$

Since the ratio d in this equation does not depend on the logarithm base we may switch to the natural base. We will also use the notation $\alpha \equiv P$ and $q \equiv 1/f^d$. Eq. (1) is equivalent to

$$u_{n,q}(\alpha) \equiv (q\alpha)^n = 1, \quad \text{for } n = 0, 1, 2, 3, \ldots, \text{ with } q \equiv \frac{1}{f^d}, \tag{2}$$

where the frequency f belongs to a given considered interval of linear behavior in the considered plots. Eq. (2) is the self-similarity relation aimed. In each of the linearity intervals, the constancy of the angular coefficient d and its independence of n express the scale free nature and the self-similarity properties of the phenomenon. Indeed, d is called the self-similarity or fractal dimension [15] and q is called the deformation or squeezing parameter [16–18]. We recall that, self-similarity is properly defined only in the $n \to \infty$ limit (cf. Eq. (2)) and it expresses therefore the highly nonlinear dynamical property of the system under study (confusion should not be made between the linearity of the log–log plot and the nonlinearity of the power law equation (2)). The results in Figs. 3 and 6, therefore, show that different values of d in different frequency linearity intervals correspond to different nonlinear dynamical regimes of the system under study arising from different values of the control parameters such as glucose concentrations and/or cluster size.

The analysis presented in the previous sections, based on the ODE model of the cell membrane potential V, stochastic gating K–Ca channels and numerical simulations is now complemented with the algebraic methods analysis proper of coherent state formalism [19]. We observe that the functions $u_{n,q}(\alpha)$ in Eq. (2) are, apart for the normalization factor $1/\sqrt{n!}$, the restriction to real $q\alpha$ of the entire analytic functions in the complex α-plane

$$\tilde{u}_{n,q}(\alpha) = \frac{(q\alpha)^n}{\sqrt{n!}}, \quad n = 0, 1, 2, 3, \ldots \tag{3}$$

Thus, the self-similarity implied by our result can be studied in the space $\mathcal{F}$ of the entire analytic functions, by restricting, at the end, the conclusions to real $q\alpha$, $q\alpha \to Re(q\alpha)$ [20,21]. As well known, the entire analytic functions provide the key tool for the construction of (Glauber) coherent states $|\alpha\rangle$ [19,22,23].

To see that a mathematical isomorphism indeed exists between the observed self-similarity properties and the (q-deformed) coherent states, we note that $\mathcal{F}$ provides the representation of the Weyl–Heisenberg algebra of elements $\{a, a^\dagger, 1\}$ with number operator $N = a^\dagger a$ and the Fock–Bargmann representation (FBR) [19,22] of the coherent states. More explicitly, the FBR is the Hilbert space $\mathcal{K}$ generated by the basis $\tilde{u}_n(\alpha) \equiv \tilde{u}_{n,q}(\alpha)|_{q=1}$, i.e. the space $\mathcal{F}$ of entire analytic functions. A one-to-one correspondence exists between any normalized vector $|\psi\rangle$ in $\mathcal{K}$ and a function $\psi(\alpha) \in \mathcal{F}$. The vector $|\psi\rangle$ is then described by the set $\{c_n;\ c_n \text{ complex numbers};\ \sum_{n=0}^{\infty} |c_n|^2 = 1\}$ defined by its expansion in the complete orthonormal set of eigenkets $\{|n\rangle\}$ of N:

$$|\psi\rangle = \sum_{n=0}^{\infty} c_n |n\rangle \to \psi(\alpha) = \sum_{n=0}^{\infty} c_n \tilde{u}_n(\alpha), \tag{4}$$

$$|n\rangle = \frac{1}{\sqrt{n!}} (a^\dagger)^n |0\rangle, \tag{5}$$

where $|0\rangle$ is the ground state vector, $a|0\rangle = 0$, $\langle 0|0\rangle = 1$. Putting $q = e^\zeta$, with ζ a complex number, the q-deformed coherent state $|q\alpha\rangle$ is obtained by applying q^N [24], called *the fractal operator* [20,21], to $|\alpha\rangle$

$$q^N |\alpha\rangle = |q\alpha\rangle = \exp\left(-\frac{|q\alpha|^2}{2}\right) \sum_{n=0}^{\infty} \frac{(q\alpha)^n}{\sqrt{n!}} |n\rangle. \tag{6}$$

Note that $|q\alpha\rangle$ is actually a squeezed coherent state [16,24] with $\zeta = \ln q$ the squeezing parameter. Thus, q^N acts in $\mathcal{F}$ as the squeezing operator. Notice the high nonlinearity of q^N and $|q\alpha\rangle$. As observed in Refs. [17,18,20,21], the n-th power component $u_{n,q}(\alpha)$ of the self-similarity Eq. (2) is obtained by applying $(a)^n$ to $|q\alpha\rangle$ and restricting to real $q\alpha$

$$\langle q\alpha | (a)^n | q\alpha \rangle = (q\alpha)^n = u_{n,q}(\alpha), \quad q\alpha \to Re(q\alpha). \tag{7}$$

Eqs. (6) and (7) are the aimed result. They indeed establish the one-to-one formal correspondence between the n-th power component $u_{n,q}(\alpha)$ with $n = 0, 1, 2, \ldots, \infty$, Eq. (2), and the n-th term in the q-deformed coherent state series. In other words, they provide the isomorphism relation between self-similarity properties of the observed phenomenology and the q-deformed algebra of the squeezed coherent states [17,18,20,21].

In conclusion, the cellular activity of beta cells analyzed in the previous sections can be described in terms of coherent state formalism. The low frequency (long wavelength) behavior which has been identified as a signal of collective effect due to the islet cell population finds then a description in terms of long range cellular correlation modes.

Alessandro Loppini

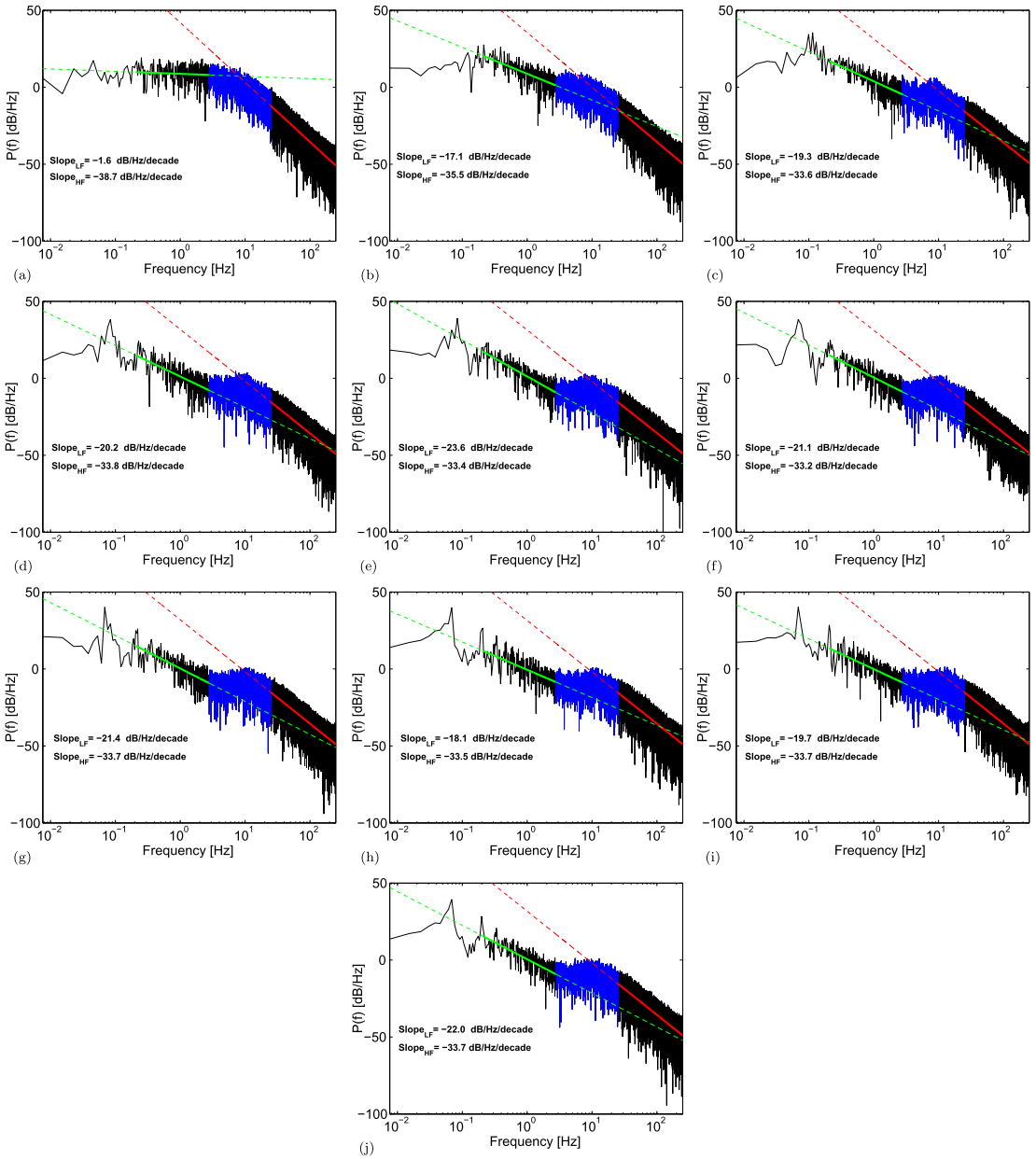

Fig. 6. Log–log power density spectra of membrane potential signals of a representative cell in clusters of increasing size, stimulated by a postprandial glucose concentration ($[G] = 9.5$ mM): (a) single cell; (j) $10 \times 10 \times 10$ cluster; (b)–(i) intermediate cases $n \times n \times n$ (with n integer and $1 < n < 10$). The slope at low frequencies (S_{LF}) is highlighted in green, the slope at high frequencies (S_{HF}) in red. As in Fig. 3 continuous lines segments highlight the PDS points used for the linear fitting; dotted lines segments are the extrapolation of the linear estimation. The transition region between the two linear zones is highlighted in blue. (For interpretation of the references to color in this figure legend, the reader is referred to the web version of this article.)

Alessandro Loppini

Table 1
Computed slopes for different values of V_t and increasing cells number.

Number of cells	V_t [mV]	S_{LF} [dB/Hz per decade]	S_{HF} [dB/Hz per decade]
1	−40	−2.1	−38.8
	−20	−1.9	−38.7
	−10	−0.1	−39.0
	0	−1.6	−38.7
	+10	−2.8	−39.0
	+20	−2.1	−39.2
	+40	−3.5	−38.8
27	−40	−19.2	−33.3
	−20	−19.4	−33.6
	−10	−18.7	−33.6
	0	−19.3	−33.6
	+10	−19.9	−33.5
	+20	−18.5	−33.3
	+40	−19.0	−34.0
64	−40	−19.7	−34.1
	−20	−22.3	−33.8
	−10	−20.9	−33.9
	0	−20.2	−33.8
	+10	−21.9	−34.0
	+20	−21.3	−33.2
	+40	−21.6	−34.0
125	−40	−23.4	−34.2
	−20	−23.6	−34.2
	−10	−22.7	−34.2
	0	−23.0	−33.6
	+10	−22.3	−33.8
	+20	−20.3	−33.4
	+40	−23.4	−34.0

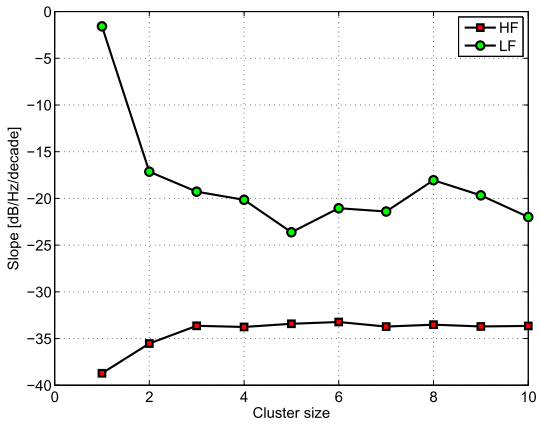

Fig. 7. Computed slopes at low (green circles) and high (red squares) frequencies for increasing cluster size. The value n on the x axis has to be understood as $n \times n \times n$. (For interpretation of the references to color in this figure legend, the reader is referred to the web version of this article.)

5. Conclusions

As mentioned in Section 1, experimental measurements [6,8,9] show that the electrical activity of beta cells is synchronized over the islet provided convenient conditions on the glucose concentrations and islet size are satisfied. It has been also observed [11,12] that coupled cells may share the entire population of K–Ca channels [11,12] ("channel sharing", cf. Section 2), and thus are able to overcome noise and give rise to bursting behavior with a characteristic electrical pattern observed experimentally in beta cells within the islet. Motivated by these experimental observations, and by resorting to an extended version of the stochastic multi-cell SRK model [12], of Hodgkin–Huxley type, we have studied the bursting activity of beta cells cubic clusters of variable size for different glycemic levels. Our analysis has been based on such ODE model of the membrane potential V with the stochastic gating of K–Ca channels and numerical simulations to reproduce the activity of single cells and clusters of variable size have been performed. In particular, we have studied the power density spectra in function of the frequency in terms of log–log plots and reached the following results. We have evidenced a linear log–log behavior with different slopes in different frequency intervals (cf. Figs. 3 and 6). We have shown then that such a behavior highlights that scale free (power law) dynamics with self-similarity properties works at a basic level of the system components, in each of the different dynamical regimes identified by the different slopes (cf. Figs. 3 and 6 and Section 3). Indeed, in Section 4, we have shown the existence of an isomorphism of the self-similarity properties of such a behavior with squeezed coherent states, with different slopes corresponding to different values of the squeezing parameter, consistently with the results of [17,18,20,21]. The changeable working conditions used in the numerical simulations, such as the modulation of glycemic level and different cluster sizes thus appear to drive the formation/modulation/disappearance of coherent structures at a microscopic level. One interesting consequence of our results concerns the "robustness" of coherent activity in each of the frequency intervals once the log–log linearity is established. As numerical simulations (cf. the comment at the end of Section 3) and inspection of the values reported in Table 1 show, fluctuations in the membrane potential V leave almost unaffected the value of the slope, which is consistently reflected in the coherent state dynamical stability at a given squeezing parameter value. Moreover, a critical transition occurs at the point in the plots where slope changes. This is consistent with the criticality of the variations of the squeezing parameter value [23]. Namely, by expressing such a scenario in the jargon of many-body physics, we might say that as the number of cells in cluster increases (up to thousand in our numerical simulation) we are in the presence of a typical field theory "phase transition" phenomenon triggered by changes in the concentration of the glucose bath in which cell clusters are embedded. We recall indeed that squeezed coherent states with different squeezing parameters (different slopes in Figs. 3 and 6) belong to different dynamical regimes (phases) [24]. It is interesting to observe that the linear behavior in log–log PDS/frequency plots in specific intervals of frequencies found in the present system, also appears in brain studies where assemblies (clusters) of large number of neurons with phase locked amplitude modulated oscillations and self-similarity properties are observed as well [21,25–30]. Our expectation is that, in addition to its specific biochemical and cellular composition, coherent dynamics and self-similarity properties would play a crucial role in the evolution of a biological system through non-equilibrium processes driven by external inputs and boundary conditions.

Acknowledgements

C.C. and S.F. acknowledge the International Center for Relativistic Astrophysics Network (ICRANet) and the National Group of Mathematical Physics (GNFM-INdAM); A.G. and A.L. acknowledge the support by National Group of Mathematical Physics (GNFM-INdAM); G.V. and A.C. acknowledge Istituto Nazionale di Fisica Nucleare (INFN) for support.

Appendix A

Here a full list of model's parameters and adopted values is given:

Alessandro Loppini

Parameter	Dimensional unit	Value
V_K	mV	−75
V_{Ca}	mV	110
$\bar{g}_K$	pS	2500
$\bar{g}_{Ca}$	pS	1400
$\bar{g}_{K-Ca}$	pS	30 000
g_c	pS	215
V_n	mV	−15
S_n	mV	5.6
V_m	mV	4
S_m	mV	14
V_h	mV	−10
S_h	mV	10
a	mV	65
b	mV	20
c	ms	60
$\bar{V}$	mV	−75
λ	–	1.7
K_d	μM	100
f	–	0.001
α	$\mathrm{mmol\,C^{-1}\,\mu m^{-3}}$	$4.506 \cdot 10^{-6}$
τ_c	ms	1000
A	$\mathrm{m\,s^{-1}\,mM^{-1}}$	$6.3 \cdot 10^{-3}$
B	$\mathrm{m\,s^{-1}}$	0.0147

References

[1] F.M. Ashcroft, P. Rorsman, Prog. Biophys. Mol. Biol. 54 (1989) 87.
[2] M. Brissova, M.J. Fowler, W.E. Nicholson, A. Chu, B. Hirshberg, D.M. Harlan, A.C. Powers, J. Histochem. Cytochem. 53 (2005) 1087.
[3] D.J. Steiner, A. Kim, K. Miller, M. Hara, Islets 2 (2010) 135.
[4] L. Orci, R.H. Unger, A.E. Renold, Cell. Mol. Life Sci. 29 (1973) 1015.
[5] R.L. Michaels, J.D. Sheridan, Science 214 (1981) 801.
[6] J.V. Rocheleau, G.M. Walker, W.S. Head, O.P. McGuinness, D.W. Piston, Proc. Natl. Acad. Sci. USA 101 (2004) 12899.
[7] P. Gilon, R.M. Shepherd, J.C. Henquin, J. Biol. Chem. 268 (1993) 22265.
[8] R.M. Santos, L.M. Rosario, A. Nadal, J. Garcia-Sancho, B. Soria, M. Valdeolmillos, Pflügers Arch. Eur. J. Physiol. 418 (1991) 417.
[9] M.G. Pedersen, R. Bertram, A. Sherman, Biophys. J. 89 (2005) 107.
[10] A.L. Hodgkin, A.F. Huxley, J. Physiol. 117 (1952) 500.
[11] A. Sherman, J. Rinzel, J. Keizer, Biophys. J. 54 (1988) 411.
[12] A. Sherman, J. Rinzel, Biophys. J. 59 (1991) 547.
[13] C.P. Fall, E.S. Marland, J.M. Wagner, J.J. Tyson (Eds.), Computational Cell Biology, 2002.
[14] R. Portuesi, C. Cherubini, A. Gizzi, R. Buzzetti, P. Pozzilli, S. Filippi, Diabetes Metab. Res. Rev. 29 (2013) 194.
[15] H.O. Peitgen, H. Jürgens, D. Saupe, Chaos and Fractals. New Frontiers of Science, Springer-Verlag, Berlin, 1986.
[16] H.P. Yuen, Phys. Rev. 13 (1976) 2226.
[17] G. Vitiello, Phys. Lett. A 376 (2012) 2527.
[18] G. Vitiello, Systems 2 (2014) 203.
[19] A. Perelomov, Generalized Coherent States and Their Applications, Springer-Verlag, Berlin, 1986.
[20] G. Vitiello, in: P. Bruza, D. Sofge, et al. (Eds.), Quantum Interaction, in: Lecture Notes in Artificial Intelligence, Springer-Verlag, Berlin, Heidelberg, 2009, p. 6, Edited by R. Goebel, J. Siekmann, W. Wahlster.
[21] G. Vitiello, New Mathematics and Natural Computation 5 (2009) 245.
[22] J.R. Klauder, B. Skagerstam, Coherent States, World Scientific, Singapore, 1985.
[23] M. Blasone, P. Jizba, G. Vitiello, Quantum Field Theory and its macroscopic manifestations, Imperial College Press, London, 2011.
[24] E. Celeghini, S. De Martino, S. De Siena, M. Rasetti, G. Vitiello, Ann. Phys. 241 (1995) 50;
E. Celeghini, M. Rasetti, G. Vitiello, Phys. Rev. Lett. 66 (1991) 2056.
[25] V. Braitenberg, A. Schüz, Anatomy of the Cortex: Statistics and Geometry, Springer-Verlag, Berlin, 1991.
[26] K. Linkenkaer-Hansen, V.M. Nikouline, J.M. Palva, R.J. Iimoniemi, J. Neurosci. 15 (2001) 1370.
[27] R.C. Hwa, T. Ferree, Phys. Rev. E 66 (2002) 021901.
[28] X.F. Wang, G.R. Chen, IEEE Circuits Syst. 31 (2003) 6.
[29] W.J. Freeman, Biol. Cybern. 92 (6) (2005) 350.
[30] D. Plenz, T.C. Thiagaran, Trends Neurosci. 30 (2007) 101.

Alessandro Loppini

PHYSICAL REVIEW E **92**, 042702 (2015)

Role of topology in complex functional networks of beta cells

Christian Cherubini,[1,2] Simonetta Filippi,[1,2] Alessio Gizzi,[1] and Alessandro Loppini[1]
[1]*Nonlinear Physics and Mathematical Modeling Laboratory, University Campus Bio-Medico of Rome, I-00128, Rome, Italy*
[2]*International Center for Relativistic Astrophysics Network—I.C.R.A.Net, University Campus Bio-Medico of Rome, I-00128, Rome, Italy*
(Received 4 February 2015; revised manuscript received 28 July 2015; published 5 October 2015)

The activity of pancreatic β cells can be described by biological networks of coupled nonlinear oscillators that, via electrochemical synchronization, release insulin in response to augmented glucose levels. In this work, we analyze the emergent behavior of regular and percolated β-cells clusters through a stochastic mathematical model where "functional" networks arise. We show that the emergence and robustness of the synchronized dynamics depend both on intrinsic and extrinsic parameters. In particular, cellular noise level, glucose concentration, network spatial architecture, and cell-to-cell coupling strength are the key factors for the generation of a rhythmic and robust activity. Their role in the functional network topology associated with β-cells clusters is analyzed and discussed.

DOI: 10.1103/PhysRevE.92.042702 PACS number(s): 87.18.Hf, 64.60.ah, 05.45.Xt, 64.60.aq

I. INTRODUCTION

The function of many biological systems underlies an intrinsic rhythmic activity [1–3]. These systems are not isolated but interact with the environment and other systems and show collective dynamics that emerges from a communicating network. Communication is the basis for the occurrence of synchronization or phase-locked dynamics of separate components in complex dynamical systems. Specifically, the role of structural and physical connections versus functional connectivity is currently investigated to understand and categorize the observed emerging behavior. In particular, the role of local heterogeneities [4], the spatial organization of the connectivity [5], and the inverse problem of extracting structural information from functional one [6] all aim at unveiling the key mechanisms responsible for synchronization and desynchronization in highly interconnected networks.

The β cells (BCs), in the endocrine islets of the pancreas, are an example of coupled nonlinear oscillators that show such a coordinated rhythmic activity. Pancreatic islets are ellipsoidal cells' aggregates characterized by a complex architecture. The islet contains at least three other types of cells other than BCs, i.e., α cells (ACs), δ cells (DCs), and pancreatic-polypeptide (PP) cells [7]. Several studies show that cells within the islet communicate both by autocrine and paracrine signaling, and by ultrastructural connections [7–9]. These communications finely control cells function, smooth cells heterogeneity, synchronize cells, etc. Specifically, BCs modify their electrical activity in response to changes in blood glycemic levels, triggering intracellular calcium oscillations and insulin secretion. The typical membrane voltage pattern observed in BCs is a "bursting" oscillation [7]. A key concept for this characteristic behavior is the interaction of fast and slow dynamics. The fast subsystem shows a bistability, i.e., the coexistence of two stable states, a periodic high-voltage solution, and a silent low-voltage steady state. Changes in the slow variable drive the fast subsystem between these two states, achieving a pattern of sustained high-voltage oscillations separated by quiescent phases. In this context, glucose acts like a control parameter that regulates the dynamics of the network itself. Glucose, in addition, exerts a crucial feedback on β-cell proliferation *in vitro* and *in vivo* [10].

In association with intrinsic biological noise and heterogeneity, the network topology strongly affects the single-node dynamics [5,11]. In fact, isolated BCs exhibit irregular spiking, but electrically coupled BCs in compact clusters show regular synchronous bursting leading to pulsatile insulin release [12,13]. In between these opposite behaviors, several emergent spatiotemporal patterns of electrical activity can arise from different network structures in terms of nodes number and connectivity. This aspect has a great relevance if one considers the dramatic topological effects that some pathological conditions can induce in BCs networks. Irregular behaviors caused by loss of coupling and degeneration of BCs is an example [14–16]. For instance, in type-1 diabetes, the loss of β-cell mass and communication leads to an insufficient insulin secretion and impaired pulsatility. This unstable phase can last from a few months up to several years [17], because β-cell populations larger than a critical size can still maintain the blood glycemic level in a physiological range [18,19]. Additionally, the islet architecture and composition, and hence the BCs networks, differ from species to species. In rodents, about 75% of islet cells are BCs and form a compact central core surrounded by ACs and DCs. In humans, BCs are about 54% of the islet cells and are organized in a sparse configuration [20–22]. These structural differences can play a key role in the generation of robust rhythmic behavior and the onset of local and/or global synchronous states. This thesis is corroborated by experimental evidences of (i) faster bursting [23] and (ii) spatially limited synchronization of intracellular calcium oscillations [21] in human BCs compared to rodents. Moreover, differences between mouse and human BCs in terms of ion currents also play a role in bursting oscillations.

In this work, bursting activity in BCs networks is studied via a stochastic mathematical model fine-tuned to reproduce mouse bursting activity [24]. The model is built through a percolation approach mimicking the physiological architecture of the islet. Emergent dynamics of BCs clusters are investigated by analyzing temporal correlations of cells' electrical activity and by deriving and constructing a functional network linking the BCs cluster structure to the emergent behavior. Through such an analysis, we provide a complete and quantitative description of the spatiotemporal synchronization properties

Alessandro Loppini

and their relation with experimental evidences. We show that very simple communication rules can give rise to complex functional coupling patterns within a stochastic framework and that the topology of these functional networks is very sensitive to changes in specific control parameters, i.e., the coupling conductance strength, the glucose concentration, and the noise strength. Such an approach, usually adopted to study the functional structure of the brain in physiological and pathological states [25–27], has been experimentally used to analyze the activity of BCs in islets from mouse pancreas tissue slices [28].

The paper is organized as follows. In Sec. II, the adopted stochastic mathematical model is presented. Glucose feedback and topological and functional networks architectures are described. In Sec. III, numerical simulations and results are presented. In Sec. IV, outcomes, limitations, and future perspectives are discussed. Conclusions are drawn in Sec. V.

II. MATHEMATICAL MODELING

In this section, we introduce a modified version of the minimal electrophysiological murine model SRK [24,29] that grasps many quantitative features of β-cells ensembles. The original model was designed to study isopotential cell populations and not fully synchronized cubic clusters in fixed normoglycemic conditions. As said before, the generalized version of the model here presented takes into account a fine-tuned glucose feedback and network structure based on cytoarchitecture evidences [20–22,30]. We finally explain how construct functional networks from the computed dynamics of these coupled oscillators.

A. SRK multicell model

SRK model equations are based on a Hodgkin-Huxley-type formulation [31], where a fast and a slow dynamics are nonlinearly coupled. Via this minimal modeling, it is possible to reproduce both the behaviors of isolated cells and the typical bursting electrical activity of cell clusters, thanks to the noise-filtering effect of BCs network. Each cell is described by three ordinary differential equations (ODE) and is coupled to other contiguous cells (see Appendix for details). The membrane potential and the potassium channels characterize the fast dynamics while the intracellular calcium concentration represents the slow variable that turns the cell in a silent or bursting regime. Several stochastic processes were implemented to model the gating of calcium-dependent potassium channels (K-Ca). This choice is originally due to the high conductance of this type of ion channels. Because of this, its stochastic gating leads to stronger perturbations of the membrane potential compared to K^+ and Ca^2+ channels. Following Portuesi *et al.* [11] and Loppini *et al.* [32], glucose feedback was modeled tuning the calcium removal rate parameter as a linear function of glycemic states. Heterogeneity is another important biological evidence. However, considering the intrinsic noise due to the stochastic gating of K-Ca channels, simulations performed on heterogeneous cells populations did not show significant differences from the activity observed in clusters of identical cells. Although, alternative approaches have been proposed in the literature [5], noise itself induces local heterogeneities [33] that overcome the effect of heterogeneity in cells parameters. For these reasons, in the following we consider homogeneous cells populations.

B. Numerical implementation

We have adopted the SRK model in order to simulate the BCs activity of different networks architectures. The numerical algorithm (see Appendix) for the integration of the network dynamics was implemented in C++ language. The Gephi software [34] and Matlab numerical environment were used for networks and data analysis, respectively. The *R* statistical tool was used for graphical purposes.

C. β-cell networks topology

The architectural organization of β cells in the islets differs from species to species [20]. BCs in murine islets are usually confined in a central core with a surrounding mantle of ACs and DCs. For the horse is exactly the opposite. Human islets instead are characterized by apparently random distributions of β, α, and δ cells, resulting in more complex islet structures [20]. In addition, also the islet composition is variable. As anticipated, the percentage of BCs in murine and human islets is about 75% and 54% [20–22], respectively. Another important architectural feature is that not all the adjacent BCs are coupled. In particular in mouse, about 33% of adjacent cells are not coupled [30]. Assuming a similar coupling distribution in human islets, we developed a β-cell insular geometry with a site-bond percolation [35] performed on a compact cubic cluster with a site occupancy probability of 54% ($p_s = 0.54$) and with a bond occupancy probability of 67% ($p_b = 0.67$). This procedure has been recently adopted in the context of pancreatic islet cellular networks [5]. In particular, phase transitions of BCs networks under different percolation conditions with the onset of type-1 diabetes have been related there. In this study, our aim is different. We fix the topological architecture of the network upon a given site-bond percolation and explore cells synchronization and emergent bursting, investigating the influence of architecture and parameters' changes on BCs functions.

The bond percolation effect has been experimentally studied in the literature [36,37], modeling the emergent dynamics with the use of deterministic BCs clusters. In particular it has been observed that: (1) in physiological conditions not all adjacent BCs are coupled; (2) inhibition or genetic knockout of gap junctions compromises synchronized cell activity; (3) cell aggregates size seems to be correlated with coordinated cells activity. We address this particular aspect with a complex network perspective, combined with stochastic dynamics and comparing and contrasting different representative architectures in terms of emergent behaviors for linear chains, compact clusters, and percolated structures.

D. Functional network analysis: A synchronization measure

Synchronization phenomena have been investigated computing the correlation index between all pairs of BCs

Alessandro Loppini

membrane potential signals [28,38]:

$$R_{ij} = \frac{\langle (V_i(t) - \langle V_i(t)\rangle)(V_j(t) - \langle V_j(t)\rangle)\rangle}{\sigma_i \sigma_j}, \qquad (1)$$

where σ_i is the standard deviation of $V_i(t)$. In the functional network approach, a new network, different from the structural physical cluster, is constructed on the basis of the correlation matrix obtained. Specifically, we add a link between separate cells if the temporal correlation of their electrical signals is greater than a threshold value. Following Stožer *et al.* [28], and filtering the stronger correlations, this value in our analysis is set to 0.8. From the functional network, one can achieve qualitative and quantitative information on the BCs emergent dynamics in terms of synchronized activity. In particular, the presence of synchronized subpopulations, the quantification of the temporal correlation of the global oscillatory activity, and several features of the emergent behavior can be derived.

For the sake of clarity, we list the observables specifically used in this study (see Refs. [39,40]): (i) the degree of the ith node $k_i = \sum_j a_{ij}$, where a_{ij} is the adjacency matrix associated to the network; (ii) the degree distribution $P(k)$ and the cumulative degree distribution $P_{\rm cum}(k) = \sum_{k'=k}^{\infty} P(k')$; (iii) the average nearest neighbors degree as a function of k, i.e., $k_{\rm nn}(k) = \frac{1}{N_k} \sum_{i,k_i=k} k_{{\rm nn},i}$, where $k_{{\rm nn},i} = \frac{1}{k_i} \sum_j a_{ij} k_j$, that is the average nearest-neighbors degree for the node i, and N_k is the node number of degree k; (iv) the average clustering coefficient $C = \frac{1}{N} \sum_i c_i = \frac{1}{N} \sum_i \frac{2e_i}{k_i(k_i-1)}$, where e_i are the edges in the subgraph of the neighbors of the ith node and $k_i(k_i - 1)/2$ is the maximum number of edges in the subgraph.

As anticipated, the functional network topology is driven by cells synchronization, and we move from totally uncorrelated electrical activity to almost full synchronized behavior. Because of this, at least if the standard definition of the observables hold, we will also consider nodes of degree 0 (the isolated nodes) in the computation of the networks' statistics.

III. RESULTS

With the use of the site-bond percolation described above [35], a human-like insular structure was constructed from a compact cubic lattice of 1000 β cells. This procedure led to a fragmentation of the original architecture into separate components characterized by structural networks of different sizes and connectivities. The numerical study focuses on the analysis of the biggest component obtained, extracted from the percolated architecture, and formed by 260 cells (see Fig. 1). Two other simple topologies were constructed taking into account the same number of nodes: a linear 1D chain and a 3D compact cluster. In the latter case, a $7 \times 7 \times 7$ grid was sequentially filled with cells, stopping the cluster construction once the desired number of units was reached. A representation of the different topologies is shown in Fig. 2.

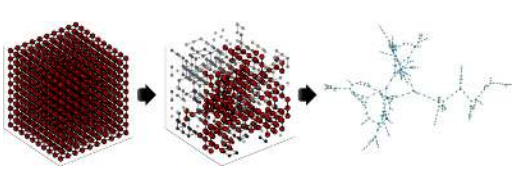

FIG. 1. (Color online) Construction of the percolated topology. Starting from a compact cubic cluster (left) a human-like architecture is obtained via a site-bond percolation (center) and the biggest connected component is extracted (right).

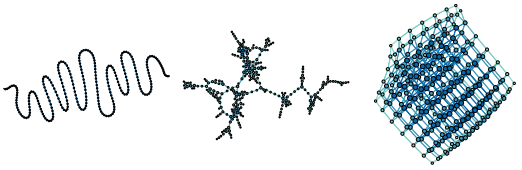

FIG. 2. (Color online) Different network topologies: linear chain (left), percolated architecture (center), compact structure (right).

In Fig. 3 the voltage time series computed for the stochastic SRK model is shown for a representative cell of any of the three simulated topologies. For these simulations a glucose concentration slightly above the BCs activation threshold was imposed ($[G] = 7.1$ mM, i.e., $k_{\rm Ca} = 0.03\,{\rm ms}^{-1}$), setting the coupling conductance between cells at a physiological value ($g_c = 215$ pS). Clearly, network topology strongly affects voltage oscillations. This effect is due to the different filtering properties induced by the "channel sharing" mechanism [24] with respect to the noise produced by stochastic channel gating. More organized structures give rise to longer bursting periods with lower variability of the interburst interval.

In order to extract information on the synchronization properties, in Fig. 4 we provide the correlation matrix, the computed functional network, and the space-time plots of voltage signals for each simulated structure. Bursting activity in the linear chain, Fig. 4(a), presents a short-range synchronization with excitation waves arising from different points in space and time, occasionally colliding. These evidences are supported by the structure of the functional network, which presents a mean node degree equal to 4 for the central cells of the chain. The opposite emergent behavior can be seen in the compact cluster, Fig. 4(c): the appearance of quasihorizontal bands in the voltage space-time plot highlights a long-range synchronization of the bursting. In this case, the

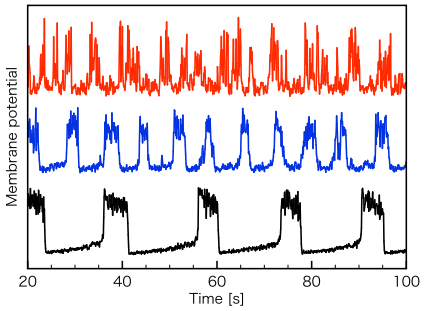

FIG. 3. (Color online) Membrane potential time series for a representative cell in: linear chain (top), percolated structure (middle), compact cluster (bottom).

Alessandro Loppini

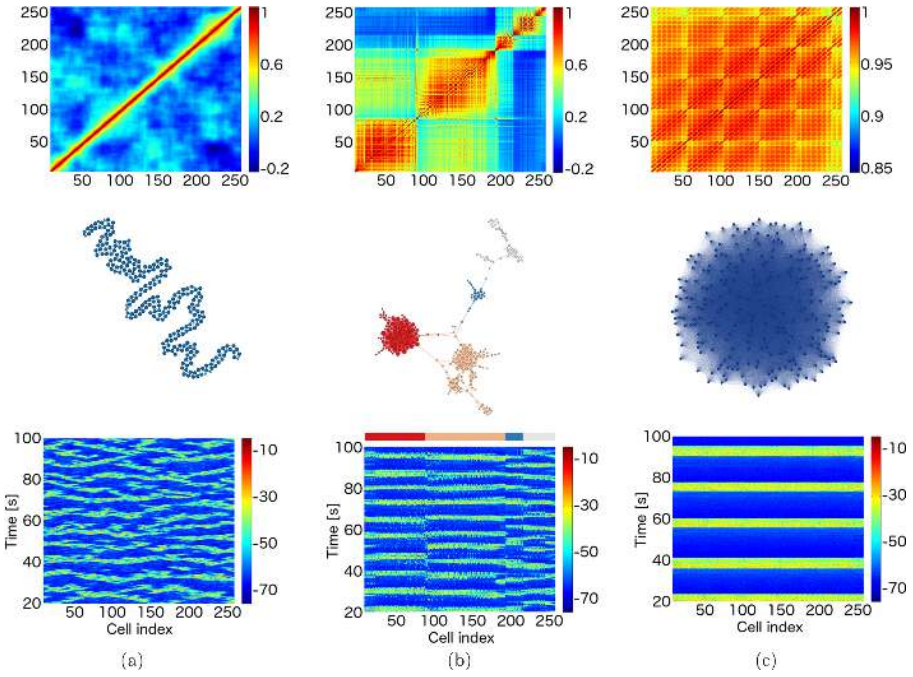

FIG. 4. (Color online) Correlation matrix (top row), reconstructed functional network (central row), and space-time plot of membrane voltage (bottom row) for each topology. (a) Left column: linear chain. (b) Central column: percolated topology. (c) Right column: compact structure. Physiological conditions are considered: $g_c = 215\,\mathrm{pS}$ and $[G] = 7.1\,\mathrm{mM}$. The color code of the percolated functional network identifies the subpopulations in the space-time plot.

x axis of the plot is a one-dimensional ordering of the cells obtained with a sequential indexing from the bottom to the top of the cluster. Functional network in such a situation is a fully connected network. The percolated topology shows instead an intermediate and very interesting behavior, Fig. 4(b). From the correlation matrix and the reconstructed functional network, four subpopulations with different bursting regimes can be identified (highlighted with different colors). The spatial coordinates of the space-time plot in this case were reordered on the basis of the macro subpopulations leading to the appearance of different out-of-phase bands of bursting activity. Each subpopulation is identified along the x axis by the same color used in the corresponding functional network.

A. Fixed glucose and variable gap junction conductance

Different functional networks were constructed analyzing the electrical activity of the BCs structures previously described, by varying the coupling strength (link strength of the structural network) and keeping fixed the glucose concentration ($[G] = 7.1\,\mathrm{mM}$). Figure 5 shows three functional networks sequences for the linear chain, the percolated network, and the compact cluster, respectively. The analysis shows that lowering g_c below a specific threshold causes the functional disconnection of the network. In this scenario, BCs do not show correlated activities nor robust bursting. Increasing the coupling conductance gives rise, instead, to functional connections that reveal a much more complex organization compared to the bare physical topology of the BCs cluster. Strongly interconnected functional communities appear from a limited number of junctional connections for the linear, the percolated, and the compact topology. The compact cluster gives rise to a fully connected functional network for all the coupling strengths considered, losing just a few connections at $g_c = 100\,\mathrm{pS}$, thus exhibiting a robust and synchronized bursting. The linear and the percolated cases, instead, do not reach a complete functional connectivity, even by increasing coupling strength. However, the study of the "functional" clustering coefficient computed for each operating condition highlights a similar trend in the network synchronization, as reported in Table I.

In order to further explore the emergent dynamics on the percolated topology, the degree distributions $P(k)$ of the functional networks are computed and shown in Fig. 6. Numerical results highlights that for a coupling conductance close to the physiological value ($g_c = 215\,\mathrm{pS}$), the distribution seems to match similar trends with respect to log-normal density functions and power-law decays. In order to better analyze this aspect, cumulative degree distributions were also computed for different coupling strengths. Log-Log plots of $P_{\mathrm{cum}}(k)$ are also reported together with a log-normal and a power law fit (straight line) of the data. Linear fitting seems

Alessandro Loppini

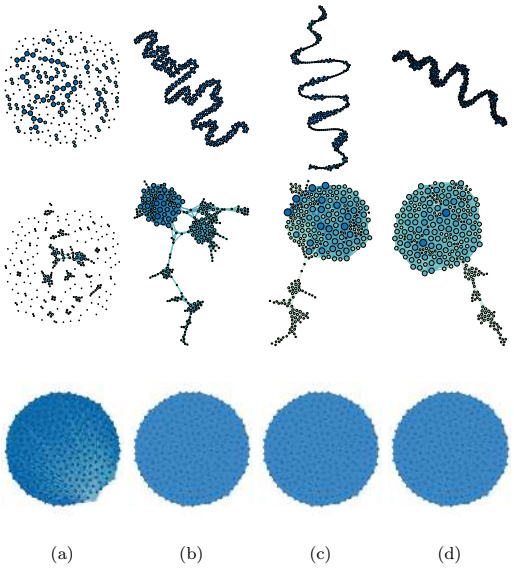

FIG. 5. (Color online) Functional networks sequences for increasing coupling strength, (a–d) $g_c = 100, 215, 300, 400$ pS, and fixed glucose concentration $[G] = 7.1$ mM. Top row, linear chain; center row, percolated structure; bottom row, compact cluster.

to hold for a central range of values while log-normal fit suits better for low degree nodes and the tail.

Although bigger cells populations should be studied to mitigate finite-size effects and to deeply investigate cumulative distributions behavior, our results highlight a strong inhomogeneity of the network and suggest that scale-free properties may be involved in the synchronization pathways. A bimodal distribution underlines bigger and more clustered synchronized communities, increasing the coupling strength further above the physiological value.

With the aim to study functional network correlations between degrees of connected nodes, the average nearest neighbor degree distributions $k_{nn}(k)$ are also computed and provided in Fig. 6. For a coupling strength in the range 100–215 pS, $k_{nn}(k)$ is an increasing function. For stronger coupling, the increasing trend reaches a plateau after a cutoff of $k \simeq 30$, probably linked to structural issues. However, this observation suggests an assortative mixing property of the network [39,41] for optimal coupling strength: nodes are mostly linked to other nodes with the same degree. Additionally, such assortative tendency is conserved in lower degree nodes for stronger coupling. Degree-preserving random rewiring (not shown) does not show increasing trend in $k_{nn}(k)$, suggesting that assortative mixing is not induced by the structure, but other processes may be involved [41].

TABLE I. Clustering coefficient for increasing coupling strengths ($[G] = 7.1$ mM). N600, simulations performed with 600 stochastic K-Ca channels per cell; N300, simulations performed with 300 stochastic K-Ca channels per cell.

	Linear		Percolated		Compact	
g_c [pS]	N600	N300	N600	N300	N600	N300
100	0.00	0.00	0.06	0.00	1.00	0.86
150	0.00	—	0.26	—	1.00	—
215	0.50	0.00	0.72	0.24	1.00	1.00
250	0.50	—	0.73	—	1.00	—
300	0.56	0.01	0.74	0.41	1.00	1.00
350	0.61	—	0.78	—	1.00	—
400	0.63	0.51	0.80	0.70	1.00	1.00

B. Fixed gap junction conductance and variable glucose

The emergent activity of the three structures was also analyzed for different values of glucose concentrations, ranging from low subthreshold stimulation values up to high glycemic levels that evoke a continuous spiking response. In this analysis, the coupling conductance was set at 215 pS. Figure 7 shows a functional networks sequence of the analyzed structures at different glycemic levels. Subthreshold values of glucose concentration functionally decouple the network as for low coupling strength values. In the same way, high values of glucose concentration decrease BCs temporal correlation causing functional decoupling of the network at high glycemic states. Optimal functional connectivity is obtained for glycemic levels slightly greater than the stimulation threshold. The computed clustering coefficient for each structure (see Table II) confirms these observations.

These results suggest that the glucose range ensuring cells functional synchronization is greater in the compact case, shrinking progressively in the percolated and the chain network. The analysis of the network degree distribution of the percolated cluster is computed for different glycemic states, see Fig. 8, showing that log-normal trends and possibly scale-free properties may also arise in the range of glucose values that maximize cells correlation. Cumulative distributions were not computed in this analysis because of the limited number of samples. In addition, although functional decoupling of the cells causes a lack of data for the computation of the average nearest-neighbor degree distribution in subthreshold stimulation and in overstimulation regimes, the computed $k_{nn}(k)$ shows an increasing trend for glucose concentrations just above the stimulation threshold. This result suggests an assortative property of the network as shown in the case of variable coupling strength discussed in the previous section.

C. Noise effect

Ion channel gating is a stochastic process, and the macroscopic currents observed originate from the opening and closing of large channel populations distributed on the cell membrane. Therefore, these biological systems can be viewed as intrinsically stochastic oscillators. Macroscopic membrane current fluctuations strongly depend on single-channel properties and on the numerosity of the population. Noise level is expected to have a great impact on cells synchronization.

On these bases, we investigate the noise effect on functional networks by varying the channel population size. Specifically,

Alessandro Loppini

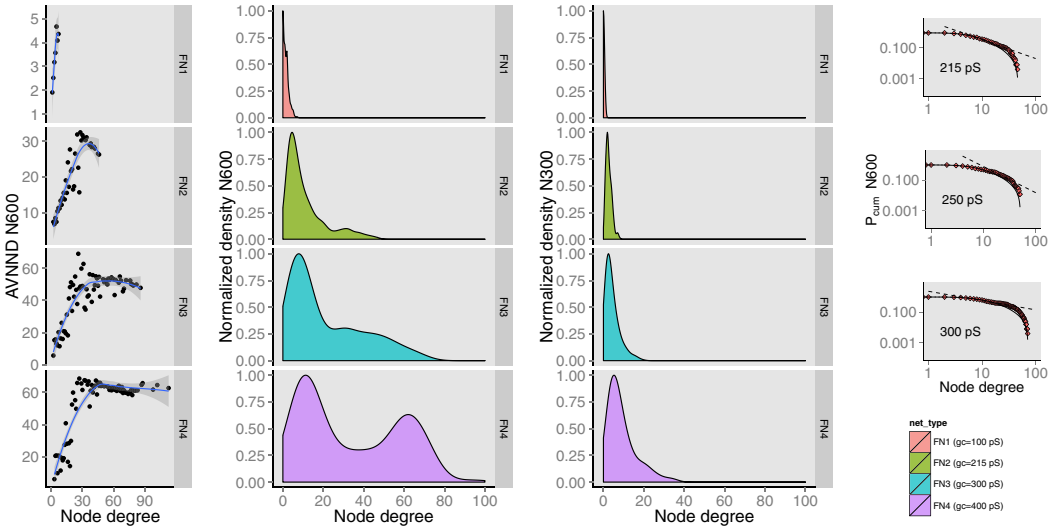

FIG. 6. (Color online) Degree distribution for different functional networks (FN) of the percolated structure varying the coupling strength ($g_c = 100, 215, 300, 400$ pS) and keeping fixed the glucose concentration ($[G] = 7.1$ mM). A smoothing kernel was used for the histograms fitting, previously normalizing the occurrences with the maximum value reached in each case. N600, observables computed from simulations performed with 600 stochastic K-Ca channels per cell; N300, observables computed from simulations performed with 300 stochastic K-Ca channels per cell; AVNND, average nearest neighbor degree; P_{cum}, cumulative degree distribution. Dotted line and continuous line in the AVNND plots represent a power law and a log-normal fit of the data (colored square), respectively.

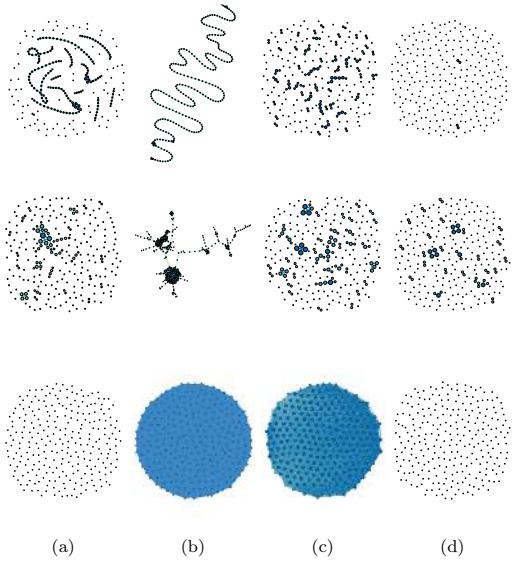

FIG. 7. (Color online) Functional networks sequences for increasing glucose concentration, (a–d) $[G] = 4.7, 8.7, 12.7, 16.6$ mM from left to right and fixed gap junction conductance $g_c = 215$ pS. Top row, linear chain; center row, percolated structure; bottom row, compact cluster.

the size of K-Ca channels population was lowered to half of the original value (from 600 to 300) in order to increase current fluctuations. Functional network sequences were similarly analyzed as presented above, i.e., (1) keeping fixed the glucose concentration and varying coupling strength, (2) keeping fixed the coupling strength and varying the glucose level. Numerical results show a similar trend with respect to lower noise levels. Figure 9 shows that increasing the coupling conductance enhances the connectivity of the network. Although, compared to the 600 K-Ca channels case, doubled values of the coupling strength are needed to achieve a similar functional connectivity for the linear and percolated structures. These observations are

TABLE II. Clustering coefficient for increasing glucose concentrations ($g_c = 215$ pS). N600, simulations performed with 600 stochastic K-Ca channels per cell; N300, simulations performed with 300 stochastic K-Ca channels per cell.

	Linear		Percolated		Compact	
Glucose [mM]	N600	N300	N600	N300	N600	N300
4.7	0.02	0.00	0.03	0.17	0.00	0.00
6.7	0.51	—	0.71	—	1.00	—
8.7	0.03	0.00	0.47	0.21	1.00	1.00
10.7	0.00	—	0.18	—	1.00	—
12.7	0.00	0.00	0.03	0.00	0.97	0.00
14.6	0.00	—	0.00	—	0.00	—
16.6	0.00	0.00	0.00	0.00	0.00	0.00

Alessandro Loppini

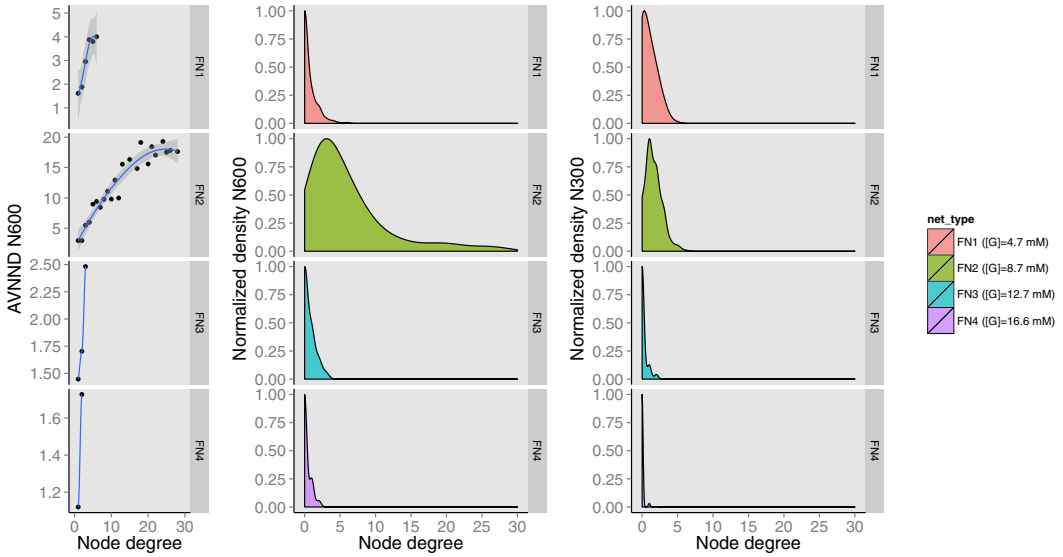

FIG. 8. (Color online) Degree distribution for different functional networks (FN) of the percolated structure varying the glucose concentration ($[G] = 4.7, 8.7, 12.7, 16.6$ mM) and keeping fixed the coupling conductance ($g_c = 215$ pS). As for variable coupling strength, a smoothing kernel was used for the normalized histograms fitting. N600, observables computed from simulations performed with 600 stochastic K-Ca channels per cell; N300, observables computed from simulations performed with 300 stochastic K-Ca channels per cell; AVNND, average nearest-neighbor degree.

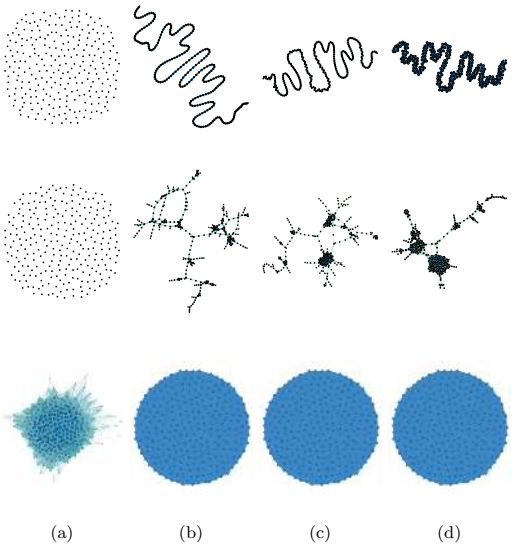

FIG. 9. (Color online) Functional networks sequences for increasing coupling strength, (a–d) $g_c = 100, 215, 300, 400$ pS from left to right at fixed glucose, i.e., $[G] = 7.1$ mM. The number of K-Ca channels per cell was set to 300 to increase noise strength. Top row, linear chain; center row, percolated structure; bottom row, compact cluster.

summarized by the computed clustering coefficients reported in Table I. The compact cluster resulted more robust to noise perturbation, and a fully functional connectivity was reached for physiological values of the coupling conductance. The analysis was limited to selected values of the conductance due to computational issues.

Similar behaviors are also observed varying the glucose level (Fig. 10 and Table II). An optimal range of glucose concentration maximizing cells synchronization is still present. However, higher noise perturbations strongly reduce this range and the degree of synchronization.

The degree distribution analysis of the functional networks computed from the percolated structure (Figs. 6 and 8) shows similar topological properties also for enhanced noise levels. Log-normal and power-law behaviors of the degree distributions are obtained for coupling conductances higher than the physiological value and glucose concentrations of about 8–9 mM. However, also for higher noise levels the maximum degree of the nodes is significantly lowered. This result underlines the robustness of the functional topology with respect to perturbations.

IV. DISCUSSION

Experimental studies have shown that β cells in pancreatic islets exploit several pathways of communication in order to coordinate and synchronize their secretory activity, from electrical to autocrine and paracrine coupling. This evidence implies a specific structural organization of cells within the islet. Such a structure varies from species to species

Alessandro Loppini

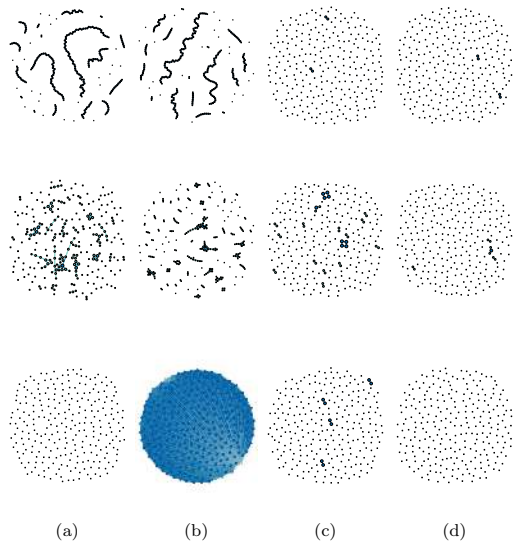

FIG. 10. (Color online) Functional networks sequences for increasing glucose, (a–d) $[G] = 4.7, 8.7, 12.7, 16.6$ mM from left to right at fixed gap junction conductance, i.e., $g_c = 215$ pS. The number of K-Ca channels per cell was set to 300 to increase noise strength. Top row, linear chain; center row, percolated structure; bottom row, compact cluster.

and can be substantially altered by degenerative pathologic processes like type-1 diabetes [42]. The existing literature on mouse and human data highlights that the emergent electrical activity in time and its coordination in space may vary significantly considering different species. Additionally, the loss of communication and degeneration of the cellular network in diabetic subjects strongly affect insulin release.

The present study analyzed the relation between structure and function in BCs networks, considering normal conditions and varying selected control parameters with respect to the physiological limits. In this framework, it is fundamental to analyze compact and percolated clusters since they clearly resemble mouse and human BCs architectures. The linear chain case, instead, is the representative example of a degenerate case, usually adopted to study the dynamics of coupled oscillators [43].

A. Bursting robustness

In the physiological state, numerical results show that temporal robustness of bursting activity is strongly affected by network architecture. This aspect was highlighted in the original work of Sherman *et al.* [24,29], studying cubic clusters of increasing size. They showed that coupled cells can "share the pool of stochastic channels" lowering noise strength. Similar behaviors were studied experimentally in cardiac coupled cells [44] and numerically in coupled networks of stochastic oscillators [24,29,45,46]. In these studies, an enhancement of the temporal precision was achieved for specific properties of the network, e.g., topology and number of nodes N. In particular, the standard deviation of the inter-beat intervals was shown to follow a $1/\sqrt{N}$ scaling law. Similar properties also arise in the stochastic gating of K-Ca channels in the "supercell" version of the SRK model [24]. Since the gating is modeled as a two-state process, it is possible to write the master equation for the evolution of the probability to find n channels in an open state in a population of size N [47]. The master equation is a set of $(N + 1)$ ODE of the form

$$\frac{dP_o(n,t)}{dt} = K_1 P_o(n-1,t) - K_2 P_o(n,t) + K_3 P_o(n+1,t),$$

where $K_1 = k^+(N - n + 1)$, $K_2 = k^+(N - n) + k^- n$, $K_3 = k^-(n + 1)$, and $k^{+/-}$ are the transition rates from the closed to the open state (see Appendix).

The equilibrium solution is given by the well-known binomial distribution:

$$P_o^{\infty}(n) = \binom{N}{n} p^n (1-p)^{N-n},$$

with $p = k^+/(k^+ + k^-)$. The coefficient of variation of this distribution is $\mathrm{CV} = \mathrm{SD}/m = \sqrt{(1-p)/(Np)}$, where SD and m are the standard deviation and the mean value, respectively. For the supercell model, the total number of stochastic channels is given by the number of channels per cell times the number of cells within the isopotential cluster. Using CV as a noise measure, for an increasing number of cells a lower spreading of P is obtained and the decrease of noise fluctuations is proportional to $1/\sqrt{N_{\mathrm{cell}}}$. A similar intuitive approach was also pointed out by Clay *et al.* [45]. These observations underline scaling laws similar to the one found in the variation of temporal precision, which are embedded in the intrinsic stochastic process of channel gating on the cell membrane. In this study, we show that the attitude of noise spreading and filtering, which gives rise to a robust bursting in time, is also dependent on the clustering of the network and not only on the population size. Our approach is in line with the heterogeneity studies recently discussed in Ref. [4].

B. Cluster synchronization

Synchronization analysis of bursting activity reveals interesting features. In particular, the linear chains do not ensure a long-range synchronization of cells and the functional network analysis suggests that a significant correlation in the activity ($R \geqslant 0.8$) holds just in a radius of about two cells. Alternatively, the compact structure shows that fully functional connectivity can be reached even considering only nearest-neighbors interactions. Of note is that such a feature is in line with recorded signals in mouse islets, showing an in-phase bursting over the whole islet [12,13]. Interestingly, the percolated topology (the closest to the human physiological one) presents intermediate behaviors where several synchronized areas arise. A globally synchronized activity is not achieved in this case as demonstrated by the degree distribution of the functional network (Fig. 6) and the out-of-phase bands in the space-time plot of membrane voltage signals (Fig. 4). These results suggest a limited and partially synchronized activity in human-like β-cell networks under

Alessandro Loppini

physiological conditions, in line with experimental recordings of intracellular calcium [21].

Could these results be a symptom of modularity? It is known that many biological networks show such a feature, which is strictly connected to the system robustness against system's perturbations [48], i.e., environment changes or altered dynamics of some nodes in the network. The functional network structure changes dynamically when the operating conditions change. The numerical analyses we conducted in this study demonstrate that if the cluster structure is not compact, values of the coupling conductance below a certain threshold are not able to synchronize cells anymore. In fact, the functional network for the linear and percolated cases are almost totally disconnected. On the other hand, higher values of the coupling are able to recover cells synchronization though the functional network loses its modularity. These evidences suggest the hypothesis of an optimal value of coupling strength, peaked at the physiological value, to maintain the functional features of the system.

In addition, other interesting properties arise keeping fixed the coupling strength while increasing glucose concentration. Glycemic levels that keep β cells in a silent state or evoke a continuous bursting lead to cells desynchronization in all the topologies analyzed; i.e., the corresponding functional networks are almost totally disconnected. For intermediate values of glucose concentration, however, the clustering coefficient for all three structures reaches a clear maximum. This last result suggests an optimal value, again, of the glucose-synchronization feedback. This level is above the stimulatory threshold and for the percolated and compact clusters is very close to the peak of glucose concentration usually observed after a meal [49,50]. These outcomes are consistent with experimental based functional network analyses in mouse islets [28], where time correlations of intracellular calcium variations between β cells are analyzed.

C. Percolated clusters and self-similarity

The associative behaviors pointed out for the average nearest-neighbor degree distributions highlight interesting aspects of synchronization pathways. The node-degree correlation suggests somehow that the emergent coordinated activity does not appear as a sharp transition in response to parameters changes but comes out as a nucleation-like process. For low values of the coupling strength, high-degree nodes are absent and low-degree nodes are coupled with other low-degree nodes, i.e., functional cell doublets and small coordinated pools. Increasing the coupling strength, the distribution of $k_{nn}(k)$ shows a plateau and high-degree nodes appear. These nodes are equally linked to other nodes, suggesting that the system is reaching a global synchronization.

Degree distributions analysis performed for the different operating conditions reveal that physiological coupling strength values and postprandial glucose concentrations induce a scale-free-like topology of the functional network. Our representative human-like cluster, in fact, comes from a particular occurrence of the percolation process performed on a regular 3D lattice of cells [5]. Specifically, in order to match biological and histological evidences, a site percolation with $p_s^* = 0.54$ and a bond percolation with $p_b^* = 0.67$ was performed. Numerical studies about mixed site-bond percolation performed on different lattices showed that the pair (p_s^*, p_b^*) is very close to the percolation threshold curve in the p_s-p_b plane for the cubic lattice (Fig. 1 in Ref. [51]). Moreover, finite-size effects have been pointed out also in Ref. [5]. In typical percolation problems performed on infinite lattices, once this threshold is reached a big connected cluster spanning all the lattice emerges; the process can be viewed as a phase transition in physical systems [35]. Near this critical threshold, fractal shapes can arise characterized by self-similarity properties. Scale-free topology of the functional network may then be reminiscent of the underlying self-similar topological structure, and variations of the model parameters could enhance or disrupt such a property in this perspective. Experimental studies have highlighted the appearance of scale-free networks in many biological complex systems like metabolic reaction networks, gene regulatory networks, and functional connectivity in the brain [52–54]. In the latter case, the scale-free properties are associated with characteristic states of the neural activity.

In the pancreatic islets, such a functional structure highlights substantial differences between mouse and human. A modularity and scale-free topology of synchronization (we are talking about functional networks) could represent the best way to regulate cells' electrophysiological activity. In addition, the analyses performed with increased noise levels suggest that perturbations of the voltage dynamics can considerably desynchronize cells' activity due to stochastic fluctuations of ion currents. However, numerical simulations also highlight that the observed topological features of the functional networks are conserved both for the percolated and the compact structure. These evidences suggest that the system is robust, and synchronization patterns are qualitatively conserved when the intrinsic noise due to cell properties is enhanced. Though these results have been derived on simplified topological BCs networks and adopting a murine-based stochastic mathematical model, due to the similarity of the reaction-diffusion formulation, ionic currents and the order of magnitude of the coupling conductances [55] we expect, by analogy, our results may have relevance within a complete and more reliable human-based framework.

V. CONCLUSIONS

The functional network analysis performed on different cluster topologies of coupled BCs highlighted a deep connection between structure and function. Results on cell synchronization are in line with experimental studies performed on human and mouse islets, in which a partial and a complete synchronization was found, respectively. The degree of synchronization is not constant but varies together with operating conditions. The compact cluster acts as a unique functional unit that is very robust over a degeneration of coupling and desegregates only for subthreshold and very high values of glucose concentration. The percolated structure gives rise to limited synchronization of cells as observed in human. In this case, physiological values of coupling conductance and glucose concentration maximize cells synchronization also preserving modularity and scale-free properties of the functional connectivity.

Alessandro Loppini

In the present study, we adapted a well-known murine-based electrophysiological model to different cluster configurations in order to highlight the relation between structural and physical topology and functionality [6]. A fine-tuning of the model parameters matching different electrophysiological behavior is out of the scope of this work. Moreover, synchronization and emergent dynamics need further exploitation in future studies taking into account that the analysis of the functional connectivity, different from the physical one, requires a careful interpretation of the statistical analyses. However, it is important to remark that modularity and scale-free properties shown in this work arise only for physiological values of the parameters, thus implying a correct interpretation of the results. In addition, synchronization and emergent dynamics are fundamental for the correct functioning of β cells and their alteration is related to pathological conditions, i.e., diabetes.

Model limitations rely with the absence of the autocrine and paracrine communication pathways within the islet and the different endocrine cells. In this perspective, more realistic coupled network topologies of the islet should be reconstructed [56] or based on local dependencies [57,58], analyzing the functional response of the cells with human electrophysiological models [55,59,60] and analyzing networks properties from observed dynamics [61]. Accordingly, the model should be tuned on human data and different percolation structures should be studied in the context of evolutionary studies [62]. In addition, weighted networks without a correlation cutoff need also to be considered in forthcoming contributions in order to better characterize the in-phase and out-of-phase bursting behaviors, as well as partial synchronization phenomena.

ACKNOWLEDGMENTS

We acknowledge the support from the International Center for Relativistic Astrophysics Network (ICRANet) and Gruppo Nazionale per la Fisica Matematica (GNFM-INdAM).

APPENDIX

1. Electrophysiological SRK model

Here we list the SRK model's equations [24,29], expressed for a single cell. For the sake of notation, we denote variables V_i, n_i, Ca_i, simply as V, n, Ca; C_m the cell membrane capacitance; V the membrane potential; n is the potassium (K^+) channel gating variable; n_∞ the steady-state activation curve for the potassium channel; Ca the intracellular calcium (Ca^{2+}) concentration; $\bar{g}_K$, $\bar{g}_{\mathrm{Ca}}$, and $\bar{g}_{\text{K-Ca}}$ the whole cell ionic channels conductances for K^+, Ca^{2+}, and K-Ca, respectively; g_c the coupling conductance; V_{K} and V_{Ca} the potassium and calcium reversal potentials; λ a parameter used to fine tune the K^+ channels time constant; f is the fraction of free intracellular calcium; α is a conversion factor; k_{Ca} the calcium removal rate; K_d the ratio of the kinetic constants that regulate the K-Ca channels chemical process of opening and closing; V_{cell} and S_{cell} the volume and the surface of the cell, respectively, assuming a spherical geometry; F the Faraday constant and the factor 10 in the membrane capacitance expression is the capacitance per unit area ($f\,F\,\mu\mathrm{m}^{-2}$).

$$
\begin{aligned}
C_m \frac{dV}{dt} &= -I_{\mathrm{ion}} - \bar{g}_{\text{K-Ca}}\, p(V - V_{\mathrm{K}}) - g_c \sum_{j\in\Omega}(V - V_j)\\
\frac{dn}{dt} &= \lambda\left[\frac{n_\infty - n}{\tau_n}\right]\\
\frac{d\mathrm{Ca}}{dt} &= f[-\alpha I_{\mathrm{Ca}} - k_{\mathrm{Ca}}\mathrm{Ca}]\\
\langle p\rangle &= \frac{\mathrm{Ca}}{\mathrm{K}_d + \mathrm{Ca}}\\
I_{\mathrm{ion}} &= I_{\mathrm{K}} + I_{\mathrm{Ca}} = \bar{g}_{\mathrm{K}} n(V - V_{\mathrm{K}}) + \bar{g}_{\mathrm{Ca}} m_\infty h(V - V_{\mathrm{Ca}})\\
m_\infty &= \frac{1}{1 + \exp[(V_m - V)/S_m]}\\
h &= \frac{1}{1 + \exp[(V - V_h)/S_h]}\\
n_\infty &= \frac{1}{1 + \exp[(V_n - V)/S_n]}\\
\tau_n &= \frac{c}{\exp[(V - \bar{V})/a] + \exp[(V - \bar{V})/b]}\\
\alpha &= \frac{1}{2\,\mathrm{F}\,V_{\mathrm{cell}}}\\
C_m &= 10\,S_{\mathrm{cell}}.
\end{aligned}
$$

The adopted formulation considers three particular ionic channels: (i) the delayed rectifier K^+ channel (allows ions flux in a specific direction), (ii) the Ca^{2+} channel, and (iii) the K-Ca channel. The Ca^{2+} conductance is defined by the product of two sigmoidal functions: a steady-state activation curve m_∞, and a factor h, introduced to achieve a reasonable fit of experimental data. The K^+ conductance is regulated by the activation level n with time constant τ_n. The K-Ca conductance at a particular instant is given by the total K-Ca conductance $\bar{g}_{\text{K-Ca}}$ times the fraction of open channels p calculated by a parallel stochastic process described in the following section.

The last term in Eq. (2) takes into account the ultrastructural connections (gap junctions) between cells and tends to homogenize the voltage gradients between neighboring cells. The summation is evaluated in a neighborhood Ω of the cell and defined as a three-dimensional expansion of a two-dimensional Von Neumann neighborhood [63]. The numerical integration of the ODE system was carried out using a fourthorder Runge-Kutta solver and a fixed time step of 0.1 ms. A complete list of the model parameters can be found in Table III.

2. Coupled stochastic processes

The opening and closure events of each K-Ca channel were modeled as a Markov stochastic process [47]. For a single channel the following two-state kinetics was considered:

$$
C \underset{1/\tau_o}{\overset{1/\tau_c}{\rightleftharpoons}} O,
$$

where τ_o and τ_c are the mean time spent by the channel in an opened and a closed state, respectively. Considering a stochastic variable $s \in \{C, O\}$ in a time interval Δt, the

Alessandro Loppini

TABLE III. Model parameters.

Parameter	Unit	Value
Cell radius	μm	6.5
F	C mmol^{-1}	96.487
V_K	mV	-75
V_{Ca}	mV	110
$\bar{g}_K$	pS	2500
$\bar{g}_{Ca}$	pS	1400
$\bar{g}_{K-Ca}$	pS	30 000
g_c	pS	See text
V_n	mV	-15
s_n	mV	5.6
V_m	mV	4
s_m	mV	14
V_h	mV	-10
s_h	mV	10
a	mV	65
b	mV	20
c	ms	60
$\bar{V}$	mV	-75
λ		1.7
K_d	μM	100
f		0.001
τ_c	ms	1000
C_1	ms^{-1} mM^{-1}	6.3×10^{-3}
C_2	ms^{-1}	0.0147

probability that a channel in a closed state makes a transition in an opened state is given by

$$\frac{\Delta t}{\tau_c} = \text{Prob}\{s = \mathcal{O}, t + \Delta t \mid s = \mathcal{C}, t\}.$$

Vice versa the probability that a channel in an opened state makes a transition to a closed one is given by

$$\frac{\Delta t}{\tau_o} = \text{Prob}\{s = \mathcal{C}, t + \Delta t \mid s = \mathcal{O}, t\}.$$

A Monte Carlo simulation scheme [47] was adopted to evolve such a stochastic process. To ensure probability conservation, the resulting summation over the transition probabilities must be 1, so one can split the interval $[0,1]$ in regions related to a specific transition of the channel. A random number extracted uniformly in the interval $[0,1]$ can then be used to impose the change of the single channel state. A number of 600 K-Ca channels *per cell* was considered, and the state of every single channel at each integration time step was evaluated. As in Ref. [24], mean closing time was kept fixed and mean opening time was defined as a function of calcium concentration:

$$\tau_o = \tau_c \frac{\text{Ca}_i}{\text{K}_d}.$$

We remark that the calcium feedback is achieved directly weighing the transition probability of the channel. The number of opened channels at each time t was used to obtain the factor p in the membrane potential equation. A congruential generator characterized by a relatively high value of the period was adopted using the *ran2* routine given in Ref. [64] to ensure the randomness of the generated number sequence.

3. Glucose feedback

By varying the k_{Ca} parameter, a silent regime or an emergent bursting with increasing active phases can be obtained. Following Portuesi *et al.* [11], we fine tuned this property to model glycemic inputs. Setting $k_{Ca} = 0.02\,\text{ms}^{-1}$ and $k_{Ca} = 0.09\,\text{ms}^{-1}$ the model responds with a silent-active transition and an active-continuous spiking transition, respectively. These transitions in BCs occur at glucose concentrations of 5.5 mM and 16.6 mM, respectively. On these evidences, we assumed for simplicity a monotonic linear trend of k_{Ca} given by

$$k_{Ca} = C_1[G] - C_2 \quad \text{for} \quad [G] \geqslant 2.33\,\text{mM},$$

where

$$C_1 = 6.3 \times 10^{-3}\,\text{ms}^{-1}\,\text{mM}^{-1}, \quad C_2 = 0.0147\,\text{ms}^{-1},$$

and $[G]$ is the glucose concentration.

[1] L. Glass, Nature **410**, 277 (2001).
[2] S. H. Strogatz and I. Stewart, Sci. Am. **269**, 102 (1993).
[3] S. H. Strogatz, SIAM J. Appl. Math. **50**, 1645 (1990).
[4] F. Scafuti, T. Aoki, and M. di Bernardo, Phys. Rev. E **91**, 062913 (2015).
[5] I. J. Stamper, E. Jackson, and X. Wang, Phys. Rev. E **89**, 012719 (2014).
[6] W. Lin, Y. Wang, H. Ying, Y. C. Lai, and X. Wang, Phys. Rev. E **92**, 012912 (2015).
[7] F. M. Ashcroft and P. Rorsman, Prog. Biophys. Mol. Bio. **54**, 87 (1989).
[8] L. Orci, R. H. Unger, and A. E. Renold, Cell. Mol. Life Sci. **29**, 1015 (1973).
[9] R. L. Michaels and J. D. Sheridan, Science **214**, 801 (1981).
[10] M. R. Metukuri, P. Zhang, M. K. Basantani, C. Chin, R. E. Stamateris, L. C. Alonso, K. K. Takane, R. Gramignoli, S. C. Strom, R. M. O'Doherty, A. F. Stewart, R. C. Vasavada, A. Garcia-Ocaña, and D. K. Scott, Diabetes **61**, 2004 (2012).
[11] R. Portuesi, C. Cherubini, A. Gizzi, R. Buzzetti, P. Pozzilli, and S. Filippi, Diabetes Metab. Res. Rev. **29**, 194 (2013).
[12] J. V. Rocheleau, G. M. Walker, W. S. Head, O. P. McGuinness, and D. W. Piston, Proc. Natl. Acad. Sci. U.S.A. **101**, 12899 (2004).
[13] P. Gilon, R. M. Shepherd, and J. C. Henquin, J. Biol. Chem. **268**, 22265 (1993).
[14] P. Meda, D. Bosco, M. Chanson, E. Giordano, L. Vallar, C. Wollheim, and L. Orci, J. Clin. Invest. **86**, 759 (1990).
[15] C. Vozzi, S. Ullrich, A. Charollais, J. Philippe, L. Orci, and P. Meda, J. Cell Biol. **131**, 1561 (1995).
[16] A. Nittala and X. Wang, Theor. Biol. Med. Model. **5**, 17 (2008).
[17] M. Knip, R. Veijola, S. M. Virtanen, H. Hyöty, O. Vaarala, and H. K. Åkerblom, Diabetes **54** (Suppl. 2), S125 (2005).
[18] A. Jansen, F. Homo-Delarche, H. Hooijkaas, P. J. Leenen, M. Dardenne, and H. A. Drexhage, Diabetes **43**, 667 (1994).
[19] F. C. Jonkers, J. C. Jonas, P. Gilon, and J. C. Henquin, J. Physiol. **520**, 839 (1999).

Alessandro Loppini

[20] D. J. Steiner, A. Kim, K. Miller, and M. Hara, Islets **2**, 135 (2010).
[21] O. Cabrera, D. M. Berman, N. S. Kenyon, C. Ricordi, Per-Olof Berggren, and A. Caicedo, Proc. Natl. Acad. Sci. U.S.A. **103**, 2334 (2006).
[22] M. Brissova, M. J. Fowler, W. E. Nicholson, A. Chu, B. Hirshberg, D. M. Harlan, and A. C. Powers, J. Histochem. Cytochem. **53**, 1087 (2005).
[23] L. C. Falke, K. D. Gillis, D. M. Pressel, and S. Misler, FEBS Lett. **251**, 167 (1989).
[24] A. Sherman, J. Rinzel, and J. Keizer, Biophys. J. **54**, 411 (1988).
[25] M. P. Van Den Heuvel, and H. E. Hulshoff Pol, Eur. Neuropsychopharm. **20**, 519 (2010).
[26] W. de Haan, Y. A. Pijnenburg, R. L. Strijers, Y. van der Made, W. M. van der Flier, P. Scheltens, and C. J. Stam, BMC Neuroscience **10**, 101 (2009).
[27] C. J. Stam, Neurosci. Lett. **355**, 25 (2004).
[28] A. Stožer, M. Gosak, J. Dolenšek, M. Perc, M. Marhl, M. S. Rupnik, and D. Korošak, PLoS Comput. Biol. **9**, e1002923 (2013).
[29] A. Sherman and J. Rinzel, Biophys. J. **59**, 547 (1991).
[30] M. Perez-Armendariz, C. Roy, D. C. Spray, and M. V. Bennett, Biophys. J. **59**, 76 (1991).
[31] A. L. Hodgkin and A. F. Huxley, J. Physiol. **117**, 500 (1952).
[32] A. Loppini, A. Capolupo, C. Cherubini, A. Gizzi, M. Bertolaso, S. Filippi, and G. Vitiello, Phys. Lett. A **378**, 3210 (2014).
[33] M. G. Pedersen, J. Theor. Biol. **235**, 1 (2005).
[34] M. Bastian, S. Heymann, and M. Jacomy, ICWSM **8**, 361 (2009).
[35] D. Stauffer and A. Aharony, *Introduction to Percolation Theory* (CRC Press, Boca Raton, FL, 1994).
[36] R. K. P. Benninger, M. Zhang, W. S. Head, L. S. Satin, and D. W. Piston, Biophys. J. **95**, 5048 (2008).
[37] T. H. Hraha, A. B. Bernard, L. M. Nguyen, K. S. Anseth, and R. K. P. Benninger, Biophys. J. **106**, 299 (2014).
[38] J. Lee Rodgers and W. A. Nicewander, Am. Stat. **42**, 59 (1988).
[39] A. Barrat, M. Barthélemy, and A. Vespignani, *Dynamical Processes on Complex Networks* (Cambridge University Press, Cambridge, 2008).
[40] S. Boccaletti, V. Latora, Y. Moreno, M. Chavez, and D. U. Hwang, Phys. Rep. **424**, 175 (2006).
[41] A. L. Barabási, *Network Science* (Cambridge University Press, Cambridge, UK, 2016), http://barabasi.com/networksciencebook/.
[42] G. C. Weir, D. R. Laybutt, H. Kaneto, S. Bonner-Weir, and A. Sharma, Diabetes **50**, S154 (2001).
[43] A. Pikovsky, M. Rosenblum, J. Kurths, and R. C. Hilborn, *Synchronization: A Universal Concept in Nonlinear Sciences* (Cambridge University Press, Cambridge, 2001).
[44] J. R. Clay and R. L. DeHaan, Biophys. J. **28**, 377 (1979).
[45] J. R. Clay and L. J. DeFelice, Biophys. J. **42**, 151 (1983).
[46] H. Kori, Y. Kawamura, and N. Masuda, J. Theor. Biol. **297**, 61 (2012).
[47] C. P. Fall, E. S. Marland, J. M. Wagner, and J. J. Tyson (eds.), *Computational Cell Biology* (Springer, Berlin, 2002).
[48] A. L. Barabási and Z. N. Oltvai, Nature Rev. Genet. **5**, 101 (2004).
[49] J. C. Brand-Miller, K. Stockmann, F. Atkinson, P. Petocz, and G. Denyer, Am. J. Clin. Nutr. **89**, 97 (2009).
[50] B. W. Wolf, P. M. Humphrey, C. W. Hadley, K. S. Maharry, K. A. Garleb, and J. L. Firkins, J. Nutr. **132**, 1219 (2002).
[51] Y. Y. Tarasevich and S. C. van der Marck, Int. J. Mod. Phys. C **10**, 1193 (1999).
[52] H. Jeong, B. Tombor, R. Albert, Z. N. Oltvai, and A. L. Barabási, Nature **407**, 651 (2000).
[53] N. Guelzim, S. Bottani, P. Bourgine, and F. Képès, Nature Genet. **31**, 60 (2002).
[54] V. M. Eguiluz, D. R. Chialvo, G. A. Cecchi, M. Baliki, and A. V. Apkarian, Phys. Rev. Lett. **94**, 018102 (2005).
[55] M. G. Pedersen, Biophys. J. **99**, 3200 (2010).
[56] A. Caicedo, Semin. Cell. Dev. Biol. **24**, 11 (2013).
[57] S. Shao, X. Huang, H. E. Stanley, and S. Havlin, New J. Phys. **17**, 023049 (2015).
[58] S. Havlin, H. E. Stanley, A. Bashan, J. Gao, and D. Y. Kenett, Chaos, Solitons Fractals **72**, 4 (2015).
[59] M. Riz, M. Braun, and M. G. Pedersen, PLoS Comput. Biol. **10**, e1003389 (2014).
[60] M. Riz, M. Braun, X. Wu, and M. G. Pedersen, Biochem. Biophys. Res. Comm. **459**, 284 (2015).
[61] M. Timme and J. Casadiego, J. Phys. A: Math. Theor. **47**, 343001 (2014).
[62] L. G. Alvarez Zuzek, H. E. Stanley, and L. A. Braunstein, Sci. Rep. **5**, 12151 (2015).
[63] J. Von Neumann, *Theory of Self-reproducing Automata* (University of Illinois Press, Champaign, 1966).
[64] W. H. Press, B. P. Flannery, S. A. Teukolsky, and W. T. Vetterling, *Numerical Recipes in C, The Art of Scientific Computing* (Cambridge University Press, Cambridge, 1992).

Alessandro Loppini

IOP Publishing *Phys. Biol.* **12** (2015) 066002 doi:10.1088/1478-3975/12/6/066002

Physical Biology

PAPER

RECEIVED
3 June 2015

REVISED
17 August 2015

ACCEPTED FOR PUBLICATION
18 August 2015

PUBLISHED
25 September 2015

Mathematical modeling of gap junction coupling and electrical activity in human β-cells

Alessandro Loppini[1], **Matthias Braun**[2,4], **Simonetta Filippi**[1] **and Morten Gram Pedersen**[3]

[1] Nonlinear Physics and Mathematical Modeling Laboratory, University Campus Bio-Medico, I-00128, Rome, Italy
[2] Alberta Diabetes Institute, Department of Pharmacology, University of Alberta, Edmonton, Alberta, Canada
[3] Department of Information Engineering, University of Padua. Via Gradenigo 6/B, I-35131 Padova, Italy
[4] Deceased

E-mail: pedersen@dei.unipd.it

Keywords: pancreatic islets, connexin-36, insulin secretion, mathematical model, bursting, syncrony

Supplementary material for this article is available online

Abstract

Coordinated insulin secretion is controlled by electrical coupling of pancreatic β-cells due to connexin-36 gap junctions. Gap junction coupling not only synchronizes the heterogeneous β-cell population, but can also modify the electrical behavior of the cells. These phenomena have been widely studied with mathematical models based on data from mouse β-cells. However, it is now known that human β-cell electrophysiology shows important differences to its rodent counterpart, and although human pancreatic islets express connexin-36 and show evidence of β-cell coupling, these aspects have been little investigated in human β-cells. Here we investigate theoretically, the gap junction coupling strength required for synchronizing electrical activity in a small cluster of cells simulated with a recent mathematical model of human β-cell electrophysiology. We find a lower limit for the coupling strength of approximately 20 pS (i.e., normalized to cell size, $\sim$2 pS pF^{-1}) below which spiking electrical activity is asynchronous. To confront this theoretical lower bound with data, we use our model to estimate from an experimental patch clamp recording that the coupling strength is approximately 100–200 pS (10–20 pS pF^{-1}), similar to previous estimates in mouse β-cells. We then investigate the role of gap junction coupling in synchronizing and modifying other forms of electrical activity in human β-cell clusters. We find that electrical coupling can prolong the period of rapid bursting electrical activity, and synchronize metabolically driven slow bursting, in particular when the metabolic oscillators are in phase. Our results show that realistic coupling conductances are sufficient to promote synchrony in small clusters of human β-cells as observed experimentally, and provide motivation for further detailed studies of electrical coupling in human pancreatic islets.

Introduction

At raised glucose levels insulin is secreted in a coordinated, pulsatile fashion from human pancreatic β-cells located in islets of Langerhans [1, 2]. As in their murine counterparts, a well-characterized pathway underlies glucose-stimulated insulin secretion in human β-cells [3–6]. Glucose metabolism leads to production of ATP, closure of ATP-sensitive potassium channels (K(ATP)-channels) and electrical activity, which activates voltage-gated calcium channels. The resulting influx of Ca^{2+} leads to insulin release through Ca^{2+}-dependent exocytosis [7].

In order to obtain an overall pulsatile secretion pattern from the islets scattered throughout the pancreas, the β-cells should be synchronized both within and between islets [8]. Concerning intra-islet synchrony, it is well-established that the strong synchrony seen in mouse islets is due to electrical gap junction coupling [9–11]. Gap junctions in the islets are mainly composed of connexin-36 (Cx36) [9, 12], and Cx36 knock-out mice show reduced intra-islet synchrony of Ca^{2+} oscillations [13]. Similarly, human pancreatic islets express Cx36 [14] that form gap junctions [14, 15], which might synchronize the β-cells in human islets. In contrast to the well-studied role of

Alessandro Loppini

IOP Publishing Phys. Biol. 12 (2015) 066002 A Loppini et al

gap junctions within islets, the mechanisms of inter-islet synchronization are still poorly understood in both mice and humans.

Although the overall mechanisms underlying glucose-stimulated insulin secretion is similar in humans and mice, the electrophysiological characteristics of human and murine β-cells show important differences [3, 5, 6]. Also the organization of pancreatic islets differs between humans and mice, which has been shown to have functional consequences [16–18]. In addition, the electrical properties of gap junction coupling have been studied in mouse β-cells [19–22], but is so far unexplored in human islets. Human β-cells show heterogeneous behavior with no clear burst patterns [3, 5, 23]. Moreover, the β-cell population in human islets show less coordinated behavior than mouse islets, although sub-islet clusters of human β-cells are synchronized [17, 18]. These facts highlight that findings obtained in mice can not be immediately transferred to human islet physiology, which must therefore be studied directly, based on the knowledge accumulated from rodents.

While theoretical studies of electrical patterns in mouse β-cells have a long history [24, 25], mathematical models of single human β-cells were developed only recently to provide insight in the electrophysiological patterns observed in human β-cells [23, 26]. The role of gap junction coupling in mouse β-cells has also been the subject of mathematical modeling [8, 27], with studies investigating heterogeneity in the islet β-cell population [28–30], the role of noise [31–34], scale free self-similarity [35], and wave propagation [36–40].

Here, we use our model of electrical activity in human β-cells [23] to investigate the amount of gap junction coupling needed for synchronizing small, electrically coupled clusters of human β-cells. We find a lower bound on the required gap junction conductance, and show that this prediction is in agreement with the electrical coupling strength between human β-cells, as estimated from a model-based investigation of an atypical membrane potential recording from a patched cell within a small cell cluster. We analyze the robustness of our findings with bifurcation diagrams, and find that our estimate is in good agreement with previous results for the coupling strength between mouse β-cells. We then investigate emergent synchrony in a human β-cells cluster model with different kinds of electrical behavior including spiking and rapid bursting, and very slow bursting driven by a glycolytic oscillator [23, 41].

Methods

Modeling

We build on our recent mathematical model of human β-cell electrophysiology and Ca^{2+} dynamics [23], and add gap junction coupling between adjacent cells. Specifically, we simulate two mutually coupled cells, and $3 \times 3 \times 3$ clusters of cells. The cells of the clusters are coupled via a three-dimensional Von Neumann neighborhood, i.e., six neighbors for a center cell, in decent agreement with studies estimating that β-cells in mouse islets are coupled to ~7 cells [22], considering that the fraction of β-cells is lower in human than in mouse islet [16, 17]. Regarding the cluster size, we performed control simulations with $5 \times 5 \times 5$ clusters of cells, and found that our conclusions remained valid, though tiny quantitative changes were seen. We note that the poorly synchronized β-cell dynamics seen in human islets, which contain ~1000 β-cells, and the arrangement with β-cells intermingled with non-β-cells [16–18], suggest that human β-cell clusters are composed of, at most, a few tens of cells.

The modified equation for the membrane potential dynamics of the ith cell is

$$\frac{dV_i}{dt} = -I_{\text{ion},i} - g_c \sum_{j \in \Omega_i} \left(V_i - V_j\right), \qquad (1)$$

where $I_{\text{ion},i}$ is sum of the ionic currents through the membrane, Ω_i is cell i's neighborhood and g_c is the coupling conductance. All model equations and parameters can be found in the supplementary material.

To simulate slow oscillations we included a glycolytic oscillator [41] as in our previous work [23]. Oscillations in glycolysis is in this model the result of positive feedback on the central enzyme phosphofructokinase (PFK) by its product fructose-1,6-bisphosphate (FBP). Cell coupling was either electrical as in equation (1), or metabolic due to diffusion of glycolytic metabolites [42]. Our interest was to study the effects of synchronized metabolic oscillators [43] rather than to investigate the exact mechanism of metabolic coupling. We therefore chose to model diffusion of glucose-6-phosphate (G6P) as in a previous modeling study [44], even if we have no direct evidence for G6P diffusion. G6P is the product of glucokinase (GK), which phosphorylates glucose at the first step of glycolysis. We assume that G6P is in equilibrium with fructose-6-phosphate (F6P), the substrate for PFK, and G6PF6P, the sum of G6P and F6P, in cell i follows

$$\frac{d\ \text{G6PF6P}_i}{dt} = V_{\text{GK},i} - V_{\text{PFK}} - P_{\text{G6PF6P}} \times \sum_{j \in \Omega_i} \left(\text{G6PF6P}_i - \text{G6PF6P}_j\right), \qquad (2)$$

where $V_{\text{GK},i}$ is the glucokinase rate, varying between cells, and V_{PFK} is the PFK rate. The strength of metabolic coupling $P_{\text{G6PF6P}} = 0.01\ \text{ms}^{-1}$ was estimated based on data of diffusion of glycolytic metabolites between β-cells [42].

Numerics

The cell doublet system was numerically solved with the XPPAUT software [45], using the AUTO tool [45, 46] for the computation of bifurcation diagrams.

Alessandro Loppini

Numerical integration of the model for cell clusters was implemented in a C++ algorithm using a fourth-order Runge–Kutta scheme for the electrical subsystem. The metabolic subsystem was resolved in parallel with an Euler scheme due to the non-restrictive slow dynamics of the glycolytic oscillator. In each case a fixed time step of 0.02 ms was used. Numerical accuracy was verified with stand-alone XPPAUT implementations of both the glycolytic compartment and the electrical one, using the CVODE integration method. In order to reproduce 10 s of electrical activity, computing time was of the order of seconds for the cells doublets and the $3 \times 3 \times 3$ cells clusters, considering the electrical subsystem only. For the simulation of 10 min of activity in the case of $2 \times 2 \times 2$ clusters, considering both metabolic and electrical subsystems, the computing time was ∼10 min on a standard laptop computer. Cell heterogeneity was implemented by distributing selected parameters drawn from normal distributions.

All expressions of the model and computer code can be found in the supplementary material.

Data analysis

Spike and burst periods of the simulated voltage time series for coupled mixed populations with different fractions of spikers and bursters were computed by analyzing when the simulated membrane potential crossed a threshold, adjusted manually to avoid false crossings, and calculating the time duration of each oscillation cycle. The single durations were then averaged to obtain a mean period for each simulated cell.

Experiments

Human pancreatic islets were obtained with ethical approval and clinical consent from non-diabetic organ donors. All studies were approved by the Human Research Ethics Board at the University of Alberta. The islets were dispersed into single cells and small cell clusters by incubation in Ca^{2+} free buffer and plated onto 35 mm plastic Petri dishes. The cells were incubated in RPMI 1640 culture medium containing 7.5 mM glucose for >24 h prior to the experiments. Patch-pipettes were pulled from borosilicate glass to a tip resistance of 6–9 MΩ when filled with intracellular solution. The membrane potential was measured in the perforated-patch whole-cell configuration, using an EPC-10 amplifier and Patchmaster software (HEKA, Lambrecht, Germany). The cells were constantly perifused with heated bath solution during the experiment to maintain a temperature of 31 °C–33 °C. The extracellular solution consisted of (in mM) 140 NaCl, 3.6 KCl, 0.5 $MgSO_4$, 1.5 $CaCl_2$, 10 HEPES, 0.5 NaH_2PO_4, 5 $NaHCO_3$ and 6 glucose (pH was adjusted to 7.4 with NaOH). The pipette solution contained (in mM) 76 K_2SO_4, 10 KCl, 10 NaCl, 1 $MgCl_2$, 5 HEPES (pH 7.35 with KOH) and 0.24 mg ml^{-1} amphotericin B. β-cells were identified by immunostaining or by size when immunostaining was not possible (cell capacitance >6 pF, [5]). Tetrodotoxin (TTX) was purchased from Alomone Labs (Jerusalem, Israel).

Results

Estimating coupling strength between human β-cells

We analyzed the effect of gap junction coupling in a heterogeneous population of spiking human β-cells by simulation of a cluster of 27 β-cells ($3 \times 3 \times 3$ cube), which were modeled with our recent data-based model [23] and coupled by gap junctions. We added heterogeneity by extracting values for the conductances of the delay rectifier (g_{Kv}) and the K(ATP)-channels (g_{KATP}) from normal distributions with small variance. Cellular heterogeneity was introduced on these parameters because glucose-sensitivity is directly related to g_{KATP}, and because the value of g_{Kv} controls the quantitative behavior of the model, i.e., whether a simulated cell shows spiking or rapid bursting electrical activity [26]. Control simulations confirmed that our conclusions are valid also when imposing variability on all model parameters.

Due to the heterogeneity in the K^+-currents the uncoupled β-cell population fired action potentials asynchronously (figure 1(A)). The average gap junction conductance between pairs of mouse β-cells has been estimated to fall in the interval 150–215 pS [19, 22, 47]. In our simulations, gap junction coupling with a strength slightly below this range ($g_c = 0.010$ nS pF^{-1} when normalizing to cell size, considering that the cell capacitance of human β-cells is ∼10 pF [5]) rapidly synchronized action potential firing throughout the cluster. In contrast, a ten fold lower coupling strength ($g_c = 0.001$ nS pF^{-1}) was unable to synchronize the cells (figure 1(B)). To investigate the lower bound on g_c for obtaining synchrony we plotted the spike period for all cells in the cluster for different values of g_c between 0 and 0.005 nS pF^{-1}. We found that the cell periods became identical for coupling strengths above ∼0.002 nS pF^{-1}, indicating that synchrony was obtained above this threshold (figure 1(C)).

However, this lower bound is purely theoretical and does not provide information on actual human β-cell electrophysiology. We therefore attempted to estimate the coupling strength from a particular pattern seen in a human β-cell located in a tiny cluster of a few cells (figure 2(A)). The membrane potential showed small oscillations of ∼10 mV around the resting potential with occasional action potential firing. We hypothesized that the small oscillations were because of gap junction currents coming from a neighboring cell with regular spiking activity, while the occasionally observed action potentials were due to stochastic events, which were not analyzed further. When the

Alessandro Loppini

IOP Publishing *Phys. Biol.* **12** (2015) 066002 A Loppini *et al*

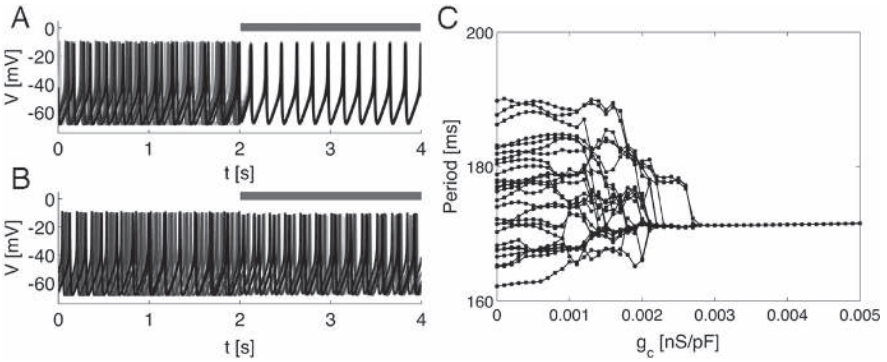

Figure 1. (A) Twenty-seven simulated spiking human β-cells, which are initially out of phase, synchronize when coupled with gap junction conductance $g_c = 0.010$ nS pF^{-1}. (B) As in panel (A), but with $g_c = 0.001$ nS pF^{-1}. (C) Spike period for all cells in a representative cluster at various coupling strengths. Identical periods for g_c above ~0.002 nS pF^{-1} indicate synchrony of the cluster.

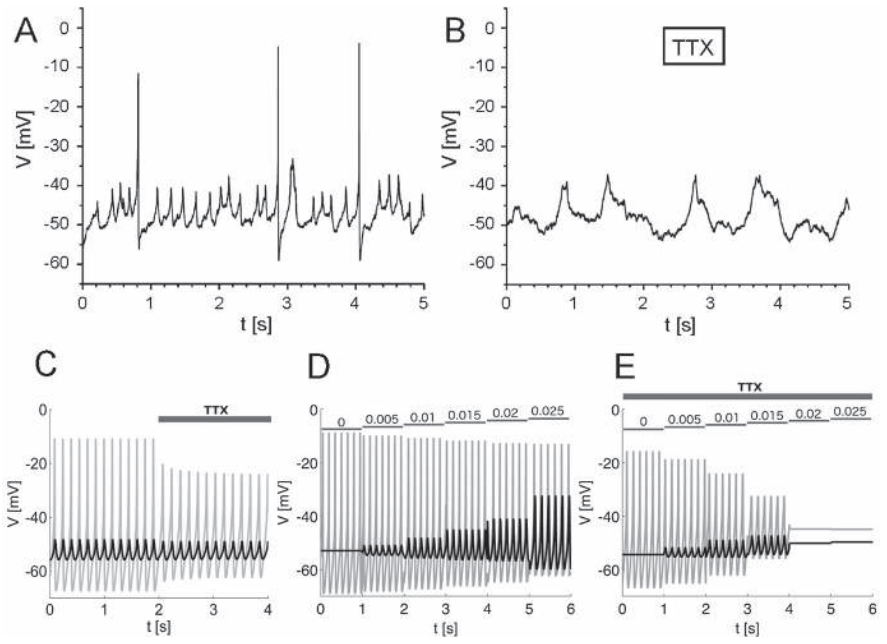

Figure 2. (A) Patch clamp recording of the membrane potential in a human β-cell in a cell cluster under control conditions. (B) Recording of the membrane potential in the same human β-cell as in panel (A) in the presence of TTX (0.1 μg ml^{-1}). (C) Model simulation of a doublet of human β-cells coupled with gap junction conductance $g_c = 0.010$ nS pF^{-1} in the absence and presence of TTX ($g_{Na} = 0$ nS pF^{-1}) as indicated. One cell was assumed to be silent when uncoupled ($g_{KATP} = 0.020$ nS pF^{-1}; black trace); the other was active when uncoupled ($g_{KATP} = 0.005$ nS pF^{-1}; gray trace). Other parameters took default values. (D) Model simulation of the same couple of β-cells as in panel (C) in the absence of TTX with varying coupling strength g_c (nS pF^{-1}) as indicated. (E) As panel (D), but in the presence of TTX.

same human β-cell cluster was exposed to the Na^+ channel blocker TTX, the amplitude of the oscillations observed in the patched cell was unchanged, and no action potentials were seen (figure 2(B)). In support of our hypothesis that the small-amplitude oscillations reflect gap junction coupling, such behavior has to the best of our knowledge not been observed in isolated human β-cells (see e.g. [48, 49]).

The behavior in figures 2(A) and (B) is representative of 3 out of 10 human β-cells monitored in absence and presence of TTX. Other two cells showed rapid action potential firing in control conditions but small-

Alessandro Loppini

amplitude (10–15 mV) oscillations when exposed to TTX. Of the remaining cells, four were active both in absence and presence of TTX, precluding the possibility of observing small amplitude oscillations as a result of incoming gap junction currents. One cell was silent in both control and TTX conditions, but showed no small amplitude oscillations, suggesting that it was either uncoupled to its neighbors (i.e., an isolated cell), or that also the neighboring cells were silent.

We simulated two human β-cells coupled by gap junctions with a strength of 0.010 nS pF^{-1}. One of the cells, corresponding to the monitored cell in the patch-clamp experiment, was assumed to be silent in the absence of coupling, while the other cell was modeled as a spiking cell. When coupled with the right amount of gap junction conductance, the spiking cell was able to induce small oscillations in the otherwise silent cell (figure 2(C)), as seen experimentally (figure 2(A)). When TTX application was simulated by setting $g_{Na} = 0$ nS pF^{-1}, small oscillations were still seen.

We varied the coupling strength for the simulations without TTX (figure 2(D)). The oscillation amplitude in the silent cell increased with increasing gap junction conductance, and only for g_c in the interval 0.010–0.020 nS pF^{-1} were oscillations with amplitudes comparable to the experimental recording (figure 2(A)) reproduced. In the presence of TTX, the coupled pair of simulated human β-cells stopped oscillating if the coupling strength was too large, since the effect of the silent cell on the spiking one became sufficiently strong to stop action potential firing (figure 2(E)). On the contrary if g_c was too small, the incoming gap junction currents from the spiking cell caused oscillations in the silent cell with too low amplitude ($\sim$3 mV at $g_c = 0.005$ nS pF^{-1}, figure 2(E)) compared to experiments ($\sim$10 mV, figure 2(B)). Thus, oscillations in the silent cell comparable to experiments were seen only for a range of gap junction conductances. This conclusion was independent of the single-cell parameters chosen for the silent and spiking cells, although the numerical values of this range varied with single-cell parameters.

To analyze the sensitivity of our estimate of the coupling strength to the single-cell parameters, we varied the K(ATP)-conductance of the active ($g_{KATP,a}$) and silent ($g_{KATP,s}$) cells, and created bifurcation diagrams showing the maximum and minimum, hence the amplitude, of the oscillations in the silent cell (figure 3). Without TTX, the coupled system with $g_{KATP,s} = 0.020$ nS pF^{-1} oscillated when $g_{KATP,a}$ was below $\sim$0.015 nS pF^{-1} for a range of coupling strengths. However, in order to have oscillations of $\sim$10 mV in the silent cell, the coupling strength had to be above $g_c = 0.010$ nS pF^{-1} (figure 3(A)). This conclusion was also reached from the bifurcation diagrams in the presence of TTX (figure 3(B)). To obtain such oscillations in the presence of TTX the K(ATP)-conductance of the active cell had to be below $g_{KATP,a} = 0.008$ nS pF^{-1} for $g_c = 0.010$ nS pF^{-1}, and even lower for stronger coupling. To investigate how the range of compatible coupling strengths varied with the K(ATP)-conductance of the silent cell, we created bifurcation diagrams for different values of $g_{KATP,s}$ for $g_{KATP,a} = 0.005$ nS pF^{-1} (figure 3(C)) and $g_{KATP,a} = 0.003$ nS pF^{-1} (figure 3(D)) in the presence of TTX ($g_{Na} = 0$ nS pF^{-1}). These diagrams showed that oscillations with an amplitude of $\sim$10 mV were seen when $g_{KATP,s}$ was in the range 0.020–0.025 nS pF^{-1}, and for coupling strengths g_c around 0.010–0.020 nS pF^{-1}.

In summary, we found that the gap junction conductance should be of the order $g_c \approx$ 0.010–0.020 nS pF^{-1} in order to simulate oscillations with amplitudes similar to the experimentally observed values. This interval of coupling strengths is comparable to but above the theoretically estimated lower bound ($g_c \approx 0.002$ nS pF^{-1}) for synchrony in a 27 cell cluster of spiking human β-cells. With a cell size of $\sim$10 pF [5], the range corresponds to a gap junction coupling strength between two cells of 100–200 pS, in excellent agreement with estimates of g_c in intact mouse islets ($\sim$170 pS [22]) and pairs of mouse β-cells ($\sim$150 pS [19], $\sim$215 pS [47]).

Synchronization of human β-cell clusters

We extended our theoretical analysis of synchrony in human β-cell clusters composed of spiking cells (figure 1) to other types of behavior. Electrical activity in some human β-cells shows rapid bursting activity where a few action potentials are clustered together, and fire from a slightly depolarized plateau [3, 23]. We have suggested [26] that this behavior could be driven by slow activity of the human ether-a-go-go (HERG) potassium channels operating in human β-cells [50, 51], or, alternatively, that Ca^{2+} dynamics and activation of SK-channels could be the underlying mechanism [23].

We performed simulations of a cluster of 27 heterogeneous human β-cells showing rapid bursting driven by SK-channels when uncoupled. Surprisingly, the introduction of gap junction coupling changed the electrical behavior to a depolarized, spiking pattern, as if the cells became trapped in the active phase of the bursts (figure 4(A)). This did not depend of the strength of the gap junction coupling in the range estimated above ($g_c = 0.010$–0.020 nS pF^{-1}). For very high coupling strengths the cells completely synchronized in a bursting pattern (not shown).

In contrast, when we simulated a 27-cell cluster of human β-cells where rapid bursting was driven by HERG channels, coupling did not interrupt the burst pattern, but synchronized the heterogeneous cells in a common bursting behavior (figure 4(BI)). We found that the period of the emerging synchronized pattern depended on the gap junction coupling strength (figure 4(BII)), as has been found previously for models of bursting in mouse β-cells [27, 28, 31].

Alessandro Loppini

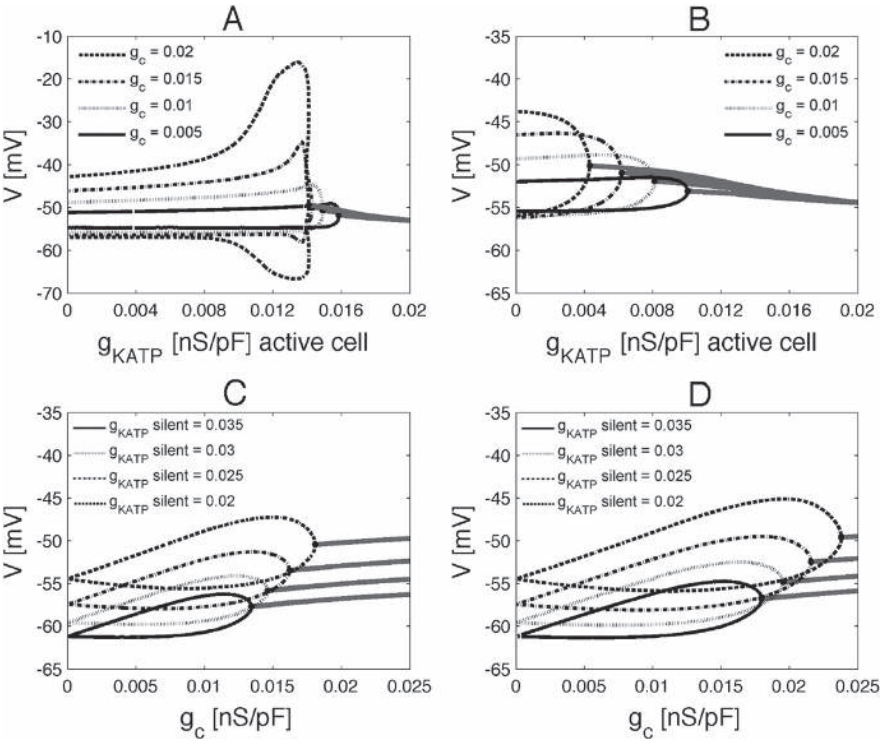

Figure 3. Bifurcation diagrams of the silent cell. (A) Without TTX with $g_{KATP,s} = 0.020$ nS pF^{-1} and varying $g_{KATP,a}$, for four different values of coupling strengths. (B) As panel (A), but in the presence of TTX. (C) In the presence of TTX with $g_{KATP,a} = 0.005$ nS pF^{-1} and varying g_c, for four different values of $g_{KATP,s}$. (D) As panel (C), but with $g_{KATP,a} = 0.003$ nS pF^{-1}.

Experimentally, spiking and rapid bursting human β-cells are observed equally often, i.e., approximately 50% of human β-cells with electrical activity are spikers, and ∼50% are rapid bursters. We simulated a cluster of 27 β-cells of which approximately half (14 of 27) of the cells were spikers and the remaining ones were rapid bursters (driven by SK-channels) when uncoupled. Gap junction coupling resulted consistently in an emerging, synchronous spiking pattern (figure 4(C)), showing that bursting is less stable than spiking. This conclusion was confirmed also in the case when bursting was driven by HERG-channels (not shown).

Slow oscillations

In vivo insulin release is pulsatile with a period of ∼5 min [1], and this rhythmic secretion pattern is also seen in isolated human pancreatic islets [2]. It is believed that the periodic release of insulin is due to Ca^{2+} oscillations observed in human β-cells [18, 52], which in turn have been suggested to be caused by slow patterns of electrical activity [23, 26, 53]. In order to obtain an overall pulsatile secretion profile from the pancreas or group of islets, individual β-cells should be synchronized [8]. Recent studies show that in isolated *ex vivo* human islets, the total β-cell population is not synchronized, but smaller clusters of β-cells within the islet show synchronous Ca^{2+} oscillations [18]. Interestingly, exposing human islets to an oscillating glucose profile results in a clearer pulsatile insulin secretion pattern [54], which we have suggested to be because of entrainment and synchronization of the individual, cellular, metabolic oscillators [55], a mechanism possibly involved in synchronization of insulin pulses also *in vivo* [1, 8].

In our earlier work [23] we showed that the electrophysiological model can produce slow electrical burst patterns when coupled to a glycolytic oscillator [41]. We now couple 8 ($2 \times 2 \times 2$) of such slowly oscillating cells. Besides cell-to-cell variation in g_{Kv} we also impose heterogeneity in the glucose kinase rate V_{GK} to simulate differences in metabolism. The glycolytic oscillator creates pulses of FBP (figure 5(A), upper trace), which via ATP production and closure of K (ATP)-channels, leads to bursts of electrical activity figure 5(B)) and Ca^{2+} oscillations (figure 5(A), lower trace).

Alessandro Loppini

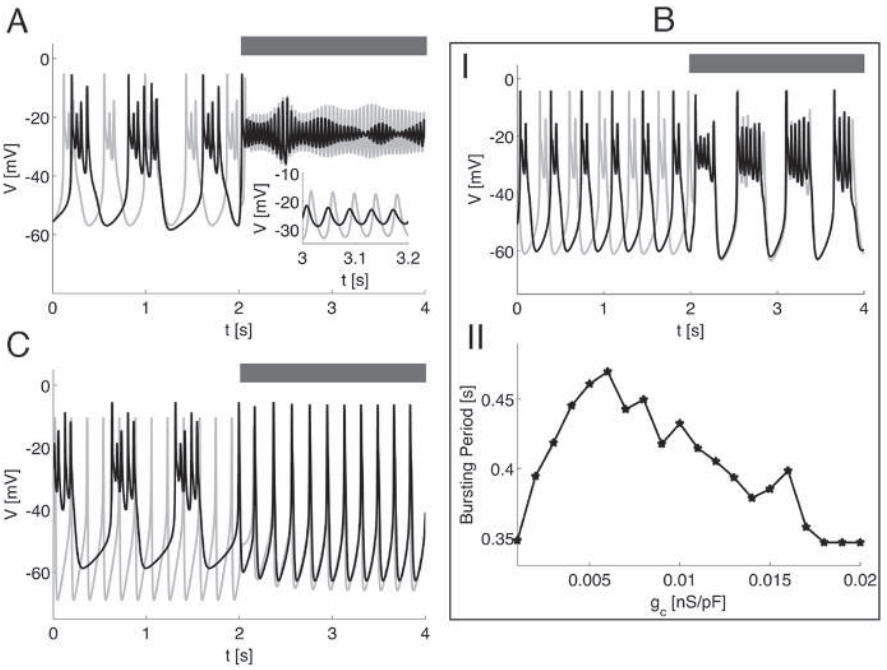

Figure 4. Simulations of $3 \times 3 \times 3$ cubic cluster of human β-cells. (A) Bursters (shown 2 of 27) driven by Ca^{2+} and SK-channels become trapped in the active phase when coupled. The inset shows a zoom on the oscillations during coupling. (B) Bursters driven by HERG-channels continue bursting with longer periods when coupled, as seen in simulated traces (shown 2 of 27 cells, subpanel (I)), and from the relationship between coupling strength and average burst period (subpanel (II)). (C) A mixed population of spikers and bursters, driven by Ca^{2+} and SK-channels, all exhibit spiking when coupled. The bars indicate the interval where the simulated β-cells were coupled, in all cases with gap junction strength $g_c = 0.010$ nS pF^{-1}.

With purely electrical coupling the glycolytic oscillators continue to drift while electrical activity and Ca^{2+} oscillations nearly synchronize (figures 5(A) and (B)). The electrical burst pattern is more irregular after coupling is turned on with occasional shorter periods of action potentials (figure 5(B)), resembling experimental recordings [6, 23, 53].

When coupling is purely metabolic, the glycolytic oscillators synchronize rapidly, which yields synchronous electrical activity and Ca^{2+} excursions that are similar in shape before and after coupling is turned on (figures 5(C), (D)). In contrast, combined metabolic and electrical coupling not only synchronize metabolism, electrical activity and Ca^{2+} oscillations, but change the shape of the bursts, which in the presence of coupling spend time in a depolarized state with smaller oscillations (figures 5(E), (F)). This pattern is similar in origin to the effect of coupling on bursters shown in figure 4(A).

Finally, we investigated whether the conclusions drawn from figure 2 are valid in the case of slow oscillations and metabolic coupling, in addition to ohmic gap junction coupling. We coupled two cells, one of which was silent because of reduced glycolytic flux (modeled by lowering the maximal GK rate V_{GK}), while the other cell exhibited glycolytic oscillations and slow bursting when uncoupled (figure S1 in the supplementary material). Due to metabolic coupling, deflections in the FBP levels of the silent cell were observed, which modulated the membrane potential, resulting in small Ca^{2+} oscillations. As in figure 2, electrical coupling introduced low-amplitude excursions in the membrane potential of the silent cell due to incoming gap junction currents.

Discussion

Although it is well-established that human β-cells are coupled by gap junctions [15] formed by Cx36 [14], no electrophysiological studies of electrical coupling have been performed in human islets. Mouse models have shown that Cx36-mediated coupling is important for normal β-cell function [56, 57], and a recent article suggested that gap junction coupling is involved in incretin responses in human islets [58]. It is therefore of clinical interest to understand the biophysical properties of gap junction coupling between human β-cells.

Here we used mathematical modeling to investigate the gap junction conductance required for

Alessandro Loppini

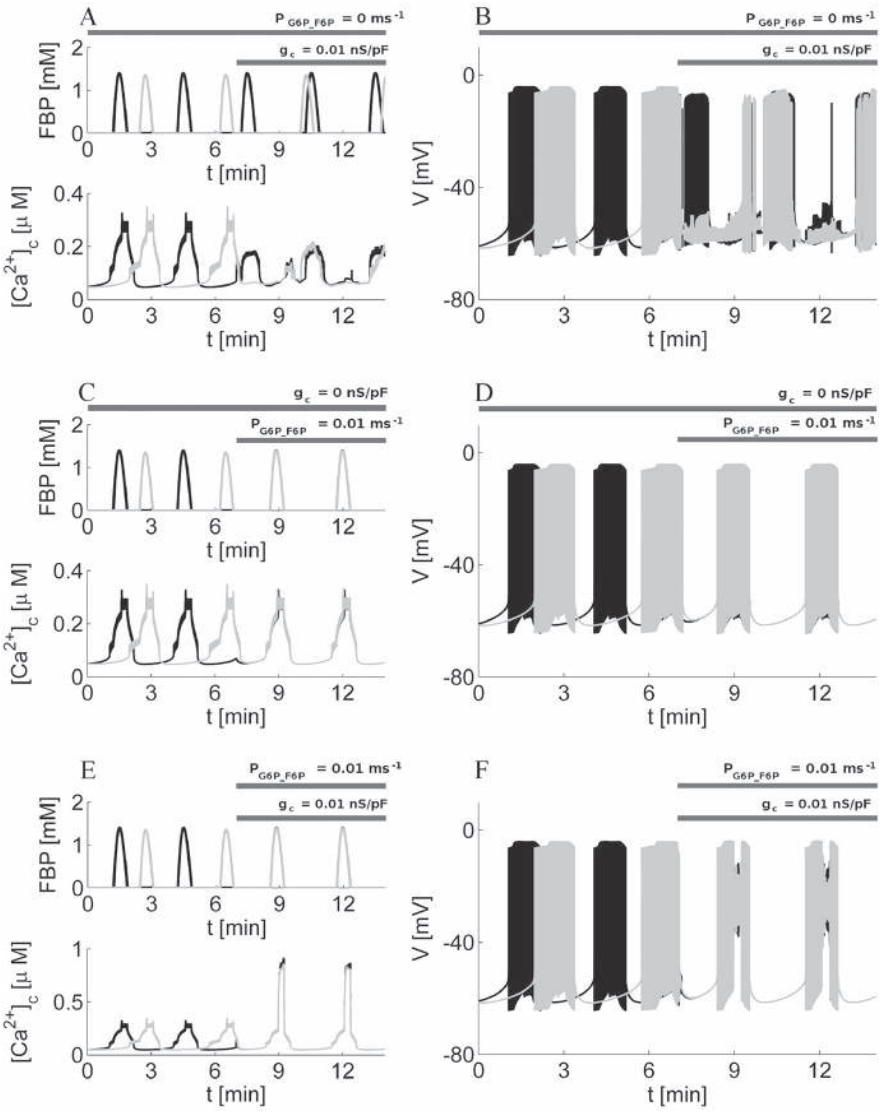

Figure 5. Simulations of 2 × 2 × 2 cubic cluster of human β-cells driven by heterogenous glycolytic oscillators. Membrane potential, FBP and cytosolic calcium time series of two representative cells are shown for three different coupling conditions. (A), (B) Electrical coupling alone does not synchronize metabolic oscillations. The out-of-phase slow bursts evoke a mutual entrainment effect between cells, giving rise to small amplitude oscillations and burst fragmentation. Reduced Ca^{2+} oscillations are observed in this condition. (C), (D) The sole metabolic coupling synchronize glycolytic oscillators, giving rise to in phase slow bursting and Ca^{2+} oscillations. Spikes and fast burst observed in the active phase are not synchronized (not shown). The amplitude of Ca^{2+} oscillations is not affected in this condition. (E), (F) The combined effect of metabolic and electrical coupling synchronize both glycolytic oscillations and bursting activity. The simulations were performed with bursters driven by SK-channels. Therefore, when the coupling is turned on, the bursting cells are trapped in an high-voltage oscillating regime during the active phase (see figure 4(A)). During coupling, Ca^{2+} oscillations are in phase and have higher amplitude compared to the uncoupled scenario.

synchronizing electrical activity in clusters of human β-cells. To confront our theoretical findings with data, we went on to estimate the gap junction coupling strength between human β-cells from an experimental trace, representative of a subset of experiments, investigated with our model. We found that the gap junction conductance should be of the order 100–200 pS (0.010–0.020 nS pF^{-1} when normalized to cell size) in

Alessandro Loppini

order to simulate small amplitude oscillations reproducing the experimental recording of the membrane potential in a human β-cell (figure 2(A)).

The coupling of a silent and an active cell is a crucial assumption for our estimation approach. Imaging experiments in intact human islets have shown coordinated Ca^{2+} oscillations in two active β-cells separated by a third β-cell whose behavior was not reported [18]; it is tempting to speculate that this third cell did not show Ca^{2+} excursions, i.e, it was a silent cell located between two active cells. Further, β-cells in glucose-stimulated human islets show long stretches of quiescence in spite of neighboring cells being active as revealed by Ca^{2+} imaging [59]. In addition, β-cells in the strongly coupled and synchronized mouse islets have different activation thresholds with respect to glucose, i.e., at a certain glucose concentration some cells are silent and others are active [60, 61]. These results suggest that gap junction coupling serves to synchronize active cells, not to activate otherwise silent cells, and provide strong support to our assumption of coupled silent and active β-cells.

In order to use a dynamical mathematical model to estimate the gap junction conductance, it is of crucial importance that the single-cell model is a precise, reliable and verified description of the electrophysiology of each cell. When constructing our human β-cell model [23, 26], we took great care in fitting individual currents to experimental recordings, both with respect to current amplitudes and kinetics. The ability of the model to reproduce a wide range of patterns of electrical activity [23, 26] gives us confidence in the model construction and parameters. However, cellular heterogeneity is a biological fact, corresponding to different parameters in our model [23], which should be considered when estimating gap junction conductance. We used bifurcation diagrams for various combinations of parameters to show that our estimate of the coupling strength is fairly robust to variations of selected parameters (figure 3). Control simulations confirmed that the conclusions remained valid when parameter variation was imposed globally. Although based on a small subset of experiments, our estimate of gap junction coupling in human β-cells corresponds nicely to previous results found in rodents [19, 22, 47]. Thus, several lines of support suggest that our estimate of $g_c \approx 100$–200 pS is not strongly dependent on our single-cell model. We note that it is not *a priori* obvious that g_c is similar in human and mouse islets; in these species e.g. the K(ATP)-channel conductance differs by an order of magnitude [6].

Our simulations showed that gap junction coupling with strength in the weak end of the estimated range easily synchronized both spiking and bursting human β-cells (figures 1 and 4). In addition, the burst period increased slightly for a range of coupling strengths (figure 4(B)). We showed further that slow electrical oscillations, likely underlying Ca^{2+} oscillations and pulsatile insulin secretion, can synchronize partly because of electrical coupling, which yields simulated traces (figure 5) resembling experimental recordings of slow oscillations in human β-cells [6, 23, 53]. Metabolic coupling is thus not strictly necessary for cell-to-cell synchrony. Further, synchronization of the metabolic oscillators results in completely synchronized responses that appear too regular compared to experiments, although this might be due to experimental noise not accounted for in our model. It will be interesting to investigate if human β-cells show metabolic synchronization as seen in mouse islets [43].

At first glance, our results are in apparent contrast to the low degree of synchrony observed in human islets [17, 18], but it should be noted that smaller clusters of β-cells within the islets were reported to be synchronized [18]. Together, these findings suggest that the human islets are composed of clusters of gap junction coupled β-cells, while such clusters are separated by other cell types, notably α-cells and vascular cells [17]. The active β-cells in each cluster are readily synchronized by electrical, and possibly metabolic, coupling via gap junctions. *In vivo*, these clusters could then be synchronized via other mechanisms. Of note, human islets show low amplitude insulin oscillations when stimulated by constant glucose [54] *in vitro*. Periodic exposure to glucose improves the pulsatility of insulin secretion [54], indicative of entrainment of a metabolic oscillator as in mouse islets [55].

Patch clamp experiments with combined voltage- and current-clamp recordings of β-cells in intact murine islets have also been used to estimate gap junction coupling [20, 22], but this approach is dependent on the typical and highly synchronized burst pattern seen in mouse islets [62]. Because of the lack of regular bursting electrical activity, and less synchrony, in human β-cells, the whole-islet approach to estimate gap junction coupling is not immediately feasible in human islets. In particular, the holding current injected during voltage-clamp recordings might disturb the relatively few electrically coupled β-cells in a locally synchronized cell cluster. Indeed, a simulation shows that voltage-clamping a surface cell in a $3 \times 3 \times 3$ human β-cell cluster strongly reduces the action potential amplitude in the neighboring cells (figure S2 in the supplementary material). Thus, electrical activity in the neighbor cells could be non-physiological, and hence, the inflowing gap junction currents would not yield reliable estimates of the coupling strength [62]. Alternatively, dual-patch experiments could be used to find the coupling strength between couples of human β-cells, as done previously for mouse β-cells [19]. Although more laborious than single-cell patching, the dual-patch approach could be used to verify and improve our estimate of the electrical coupling strength directly and model independently. This approach could also quantify how often neighboring human β-cells are electrically coupled.

Alessandro Loppini

In summary, we have shown how a model-based investigation of synchronized activity in human β-cell clusters, in particular when combined with membrane potential recordings, can give bounds on gap junction coupling strength. Hopefully, our results will encouraged detailed biophysical studies on electrical coupling in human islets.

Acknowledgments

We dedicate this manuscript to our co-author, the late Dr Matthias Braun. Thanks to his insight and skills, we have been able to carefully develop our model of human β-cells and investigate the various aspects of islet physiology presented here. MB was supported by the CIHR (MOP-106435). MGP was supported by the University of Padova (PRAt 2012, Progetto Strategico 2011 'DYCENDI'), and the European Union's Seventh Framework Programme (FP7-ICT-2011-9) under grant agreement no. 600914 (the MOSAIC consortium).

Author contributions

AL performed modeling, implemented the model, and performed computer simulations, prepared figures, contributed to drafting the manuscript, and corrected the final manuscript. MB designed and performed all experiments, and contributed to formulating the general idea of the work. SF contributed to study design and modeling, contributed to drafting the manuscript, and corrected the final manuscript. MGP conceived the general idea of the work, designed the theoretical studies, contributed to modeling, interpreted results, and wrote the final manuscript.

Supporting citations

References [63–67] appear in the supporting material.

References

[1] Pørksen N 2002 The in vivo regulation of pulsatile insulin secretion *Diabetologia* **45** 3–20
[2] Ritzel R A, Veldhuis J D and Butler P C 2003 Glucose stimulates pulsatile insulin secretion from human pancreatic islets by increasing secretory burst mass: dose–response relationships *J. Clin. End. Metab.* **88** 742–7
[3] Misler S, Barnett D W, Gillis K D and Pressel D M 1992 Electrophysiology of stimulus-secretion coupling in human beta-cells *Diabetes* **41** 1221–8
[4] Henquin J-C, Dufrane D and Nenquin M 2006 Nutrient control of insulin secretion in isolated normal human islets *Diabetes* **55** 3470–7
[5] Braun M, Ramracheya R, Bengtsson M, Zhang Q, Karanauskaite J, Partridge C, Johnson P R and Rorsman P 2008 Voltage-gated ion channels in human pancreatic β-cells: electrophysiological characterization and role in insulin secretion *Diabetes* **57** 1618–28
[6] Rorsman P and Braun M 2013 Regulation of insulin secretion in human pancreatic islets *Annu. Rev. Physiol.* **75** 155–79
[7] Braun M, Ramracheya R, Johnson P R and Rorsman P 2009 Exocytotic properties of human pancreatic beta-cells *Ann. New York Acad. Sci.* **1152** 187–93
[8] Pedersen M G, Bertram R and Sherman A 2005 Intra- and inter-islet synchronization of metabolically driven insulin secretion *Biophys. J.* **89** 107–19
[9] Bosco D, Haefliger J-A and Meda P 2011 Connexins: key mediators of endocrine function *Physiol. Rev.* **91** 1393–445
[10] Meissner H P 1976 Electrophysiological evidence for coupling between beta cells of pancreatic islets *Nature* **262** 502–4
[11] Eddlestone G T, Goncalves A and Bangham J 1984 Electrical coupling between cells in islets of Langerhans from mouse *J. Membr. Biol.* **77** 1–14
[12] Serre-Beinier V, le Gurun S, Belluardo N, Trovato-Salinaro A, Charollais A, Haefliger J A, Condorelli D F and Meda P 2000 Cx36 preferentially connects beta-cells within pancreatic islets *Diabetes* **49** 727–34
[13] Ravier M A, Guldenagel M, Charollais A, Gjinovci A, Caille D, Sohl G, Wollheim C B, Willecke K, Henquin J C and Meda P 2005 Loss of connexin36 channels alters β-cell coupling, islet synchronization of glucose-induced Ca^{2+} and insulin oscillations, and basal insulin release *Diabetes* **54** 1798–807
[14] Serre-Beinier V *et al* 2009 Cx36 makes channels coupling human pancreatic beta-cells, and correlates with insulin expression *Hum. Mol. Genetics* **18** 428–39
[15] Orci L, Malaisse-Lagae F, Amherdt M, Ravazzola M, Weisswange A, Dobbs R, Perrelet A and Unger R 1975 Cell contacts in human islets of Langerhans *J. Clin. End. Metab.* **41** 841–4
[16] Brissova M, Fowler M J, Nicholson W E, Chu A, Hirshberg B, Harlan D M and Powers A C 2005 Assessment of human pancreatic islet architecture and composition by laser scanning confocal microscopy *J. Histochem. Cytochem.* **53** 1087–97
[17] Cabrera O, Berman D M, Kenyon N S, Ricordi C, Berggren P-O and Caicedo A 2006 The unique cytoarchitecture of human pancreatic islets has implications for islet cell function *Proc. Natl Acad. Sci.* **103** 2334–9
[18] Quesada I, Todorova M G, Alonso-Magdalena P, Beltrá M, Carneiro E M, Martin F, Nadal A and Soria B 2006 Glucose induces opposite intracellular Ca2+ concentration oscillatory patterns in identified alpha- and beta-cells within intact human islets of Langerhans *Diabetes* **55** 2463–9
[19] Pérez-Armendariz M, Roy C, Spray D C and Bennett M V 1991 Biophysical properties of gap junctions between freshly dispersed pairs of mouse pancreatic beta cells *Biophys. J.* **59** 76–92
[20] Mears D, Sheppard N F Jr, Atwater I and Rojas E 1995 Magnitude and modulation of pancreatic beta-cell gap junction electrical conductance in situ *J. Membr. Biol.* **146** 163–76
[21] Moreno A P, Berthoud V M, Pérez-Palacios G and Pérez-Armendariz E M 2005 Biophysical evidence that connexin-36 forms functional gap junction channels between pancreatic mouse β-cells *Am. J. Physiol. Endoc. M.* **288** E948–56
[22] Zhang Q, Galvanovskis J, Abdulkader F, Partridge C J, Göpel S O, Eliasson L and Rorsman J 2008 Cell coupling in mouse pancreatic beta-cells measured in intact islets of Langerhans *Phil. Trans. A: Math. Phys. Eng. Sci.* **366** 3503–23
[23] Riz M, Braun M and Pedersen M G 2014 Mathematical modeling of heterogeneous electrophysiological responses in human β-cells *PLoS. Comput. Biol.* **10** e1003389
[24] Chay T R and Keizer J 1983 Minimal model for membrane oscillations in the pancreatic beta-cell *Biophys. J.* **42** 181–90
[25] Sherman A 1996 Contributions of modeling to understanding stimulus-secretion coupling in pancreatic β-cells *Am. J. Physiol. Endoc. M.* **271** E362–72
[26] Pedersen M G 2010 A biophysical model of electrical activity in human β-cells *Biophys. J.* **99** 3200–7
[27] Sherman A and Rinzel J 1991 Model for synchronization of pancreatic β-cells by gap junction coupling *Biophys. J.* **59** 547–59
[28] Smolen P, Rinzel J and Sherman A 1993 Why pancreatic islets burst but single β cells do not. The heterogeneity hypothesis *Biophys. J.* **64** 1668–80
[29] de Vries G and Sherman A 2001 From spikers to bursters via coupling: help from heterogeneity *Bull. Math. Biol.* **63** 371–91
[30] Zimliki C L, Mears D and Sherman A 2004 Three roads to islet bursting: emergent oscillations in coupled phantom bursters *Biophys. J.* **87** 193–206

Alessandro Loppini

[31] de Vries G and Sherman A 2000 Channel sharing in pancreatic beta -cells revisited: enhancement of emergent bursting by noise *J. Theor. Biol.* **207** 513–30
[32] Pedersen M G 2005 A comment on noise enhanced bursting in pancreatic beta-cells *J. Theor. Biol.* **235** 1–3
[33] Pedersen M G 2007 Phantom bursting is highly sensitive to noise and unlikely to account for slow bursting in beta-cells: considerations in favor of metabolically driven oscillations *J. Theor. Biol.* **248** 391–400
[34] Jo J, Kang H, Choi M Y and Koh D-S 2005 How noise and coupling induce bursting action potentials in pancreatic beta-cells *Biophys. J.* **89** 1534–42
[35] Loppini A, Capolupo A, Cherubini C, Gizzi A, Bertolaso M, Filippi S and Vitiello G 2014 On the coherent behavior of pancreatic beta cell clusters *Phys. Lett.* A **378** 3210–7
[36] Aslanidi O V, Mornev O, Skyggebjerg O, Arkhammar P, Thastrup O, Sørensen M, Christiansen P, Conradsen K and Scott A 2001 Excitation wave propagation as a possible mechanism for signal transmission in pancreatic islets of Langerhans *Biophys. J.* **80** 1195–209
[37] Pedersen M G 2004 Homogenization of heterogeneously coupled bistable ODE's-applied to excitation waves in pancreatic islets of Langerhans *J. Biol. Phys.* **30** 285–303
[38] Pedersen M G 2005 Wave speeds of density dependent Nagumo diffusion equations-inspired by oscillating gap-junction conductance in the islets of Langerhans *J. Math. Biol.* **50** 683–98
[39] Pedersen M G and Sørensen M P 2008 Wave-block due to a threshold gradient underlies limited coordination in pancreatic islets *J. Biol. Phys.* **34** 425–32
[40] Benninger R K P, Zhang M, Head W S, Satin L S and Piston D W 2008 Gap junction coupling and calcium waves in the pancreatic islet *Biophys. J.* **95** 5048–61
[41] Westermark P O and Lansner A 2003 A model of phosphofructokinase and glycolytic oscillations in the pancreatic beta-cell *Biophys. J.* **85** 126–39
[42] Kohen E, Kohen C, Thorell B, Mintz D H and Rabinovitch A 1979 Intercellular communication in pancreatic islet monolayer cultures: a microfluorometric study *Science* **204** 862–5
[43] Merrins M J, van Dyke A R, Mapp A K, Rizzo M A and Satin L S 2013 Direct measurements of oscillatory glycolysis in pancreatic islet β-cells using novel fluorescence resonance energy transfer (FRET) biosensors for pyruvate kinase M2 activity *J. Biol. Chem.* **288** 33312–22
[44] Tsaneva-Atanasova K, Zimliki C L, Bertram R and Sherman A 2006 Diffusion of calcium and metabolites in pancreatic islets: killing oscillations with a pitchfork *Biophys. J.* **90** 3434–46
[45] Ermentrout B 2002 *Simulating, Analyzing, and Animating Dynamical Systems: A Guide to XPPAUT for Researchers and Students* (Philadelphia: SIAM)
[46] Doedel E J AUTO: software for continuation and bifurcation problems in ordinary differential equations (http://indy.cs.concordia.ca/auto/)
[47] Andreu E, Bernat S and Sanchez-Andres J V 1997 Oscillation of gap junction electrical coupling in the mouse pancreatic islets of Langerhans *J. Physiol.* **498** 753–61
[48] Barnett D W, Pressel D M and Misler S 1995 Voltage-dependent Na+ and Ca2+ currents in human pancreatic islet beta-cells: evidence for roles in the generation of action potentials and insulin secretion *Pflugers Arch.* **431** 272–82
[49] Misler S, Dickey A and Barnett D W 2005 Maintenance of stimulus-secretion coupling and single beta-cell function in cryopreservedthawed human islets of Langerhans *Pflugers Arch.* **450** 395–404
[50] Rosati B, Marchetti P, Crociani O, Lecchi M, Lupi R, Arcangeli A, Olivotto M and Wanke E 2000 Glucose- and arginine-induced insulin secretion by human pancreatic beta-cells: the role of HERG K(+) channels in firing and release *FASEB J.* **14** 2601–10
[51] Hardy A B, Fox J E M, Giglou P R, Wijesekara N, Bhattacharjee A, Sultan S, Gyulkhandanyan A V, Gaisano H Y, MacDonald P E and Wheeler M B 2009 Characterization of Erg K+ channels in alpha- and beta-cells of mouse and human islets *J. Biol. Chem.* **284** 30441–52
[52] Martin F and Soria B 1996 Glucose-induced $[Ca^{2+}]_i$ oscillations in single human pancreatic islets *Cell Calcium* **20** 409–14
[53] Braun M, Ramracheya R and Rorsman P 2012 Autocrine regulation of insulin secretion *Diabetes Obesity Metab.* **14** 143–51
[54] Ritzel R A, Veldhuis J D and Butler P C 2006 The mass, but not the frequency, of insulin secretory bursts in isolated human islets is entrained by oscillatory glucose exposure *Am. J. Physiol. Endoc. M.* **290** E750–6
[55] Pedersen M G, Mosekilde E, Polonsky K S and Luciani D S 2013 Complex patterns of metabolic and Ca2+ entrainment in pancreatic islets by oscillatory glucose *Biophys. J.* **105** 29–39
[56] Cigliola V, Chellakudam V, Arabieter W and Meda P 2013 Connexins and β-cell functions *Diabetes Res. Clin. Pract.* **99** 250–9
[57] Farnsworth N L and Benninger R K P 2014 New insights into the role of connexins in pancreatic islet function and diabetes *FEBS Lett.* **588** 1278–87
[58] Hodson D J *et al* 2013 Lipotoxicity disrupts incretin-regulated human β cell connectivity *J. Clin. Invest.* **123** 4182–94
[59] Rutter G A and Hodson D J 2013 Minireview: intraislet regulation of insulin secretion in humans *Mol. End.* **27** 1984–95
[60] Rocheleau J V, Walker G M, Head W S, McGuinness O P and Piston D W 2004 Microfluidic glucose stimulation reveals limited coordination of intracellular Ca^{2+} activity oscillations in pancreatic islets *Proc. Natl Acad. Sci.* **101** 12899–903
[61] Markovič R, Stožer A, Gosak M, Dolenšek J, Marhl M and Rupnik M S 2015 Progressive glucose stimulation of islet beta cells reveals a transition from segregated to integrated modular functional connectivity patterns *Sci. Rep.* **5** 7845
[62] Sherman A, Xu L and Stokes C L 1995 Estimating and eliminating junctional current in coupled cell populations by leak subtraction. A computational study *J. Membr. Biol.* **143** 79–87
[63] Chen L, Koh D S and Hille B 2003 Dynamics of calcium clearance in mouse pancreatic β-cells *Diabetes* **52** 1723–31
[64] Jacobson D A, Mendez F, Thompson M, Torres J, Cochet O and Philipson L H 2010 Calcium-activated and voltage-gated potassium channels of the pancreatic islet impart distinct and complementary roles during secretagogue induced electrical responses *J. Physiol.* **588** 3525–37
[65] Maylie J, Bond C T, Herson P S, Lee W-S and Adelman J P 2004 Small conductance Ca2+-activated K+ channels and calmodulin *J. Physiol.* **554** 255–61
[66] Schönherr R, Rosati B, Hehl S, Rao V G, Arcangeli A, Olivotto M, Heinemann S H and Wanke E 1999 Functional role of the slow activation property of ERG K+ channels *Eur. J. Neurosci.* **11** 753–60
[67] Chen Y, Wang S and Sherman A 2008 Identifying the targets of the amplifying pathway for insulin secretion in pancreatic beta-cells by kinetic modeling of granule exocytosis *Biophys. J.* **95** 2226–41

Alessandro Loppini

ELECTROMAGNETIC BIOLOGY AND MEDICINE

http://informahealthcare.com/ebm
ISSN: 1536-8378 (print), 1536-8386 (electronic)

Electromagn Biol Med, 2015; 34(2): 138–140
 DOI: 10.3109/15368378.2015.1036069

informa healthcare

ORIGINAL ARTICLE

The role of coherence in emergent behavior of biological systems

Marta Bertolaso[1], Antonio Capolupo[2], Christian Cherubini[3,4], Simonetta Filippi[3,4], Alessio Gizzi[3], Alessandro Loppini[3], and Giuseppe Vitiello[2]

[1]Faculty of Engineering and Institute of Philosophy of Scientific and Technological Practice, University Campus Bio-Medico, Rome, Italy, [2]Department of Physics "E.R. Caianiello", University of Salerno and INFN Gruppo Collegato Salerno, Fisciano (SA), Italy, [3]Nonlinear Physics and Mathematical Modeling Laboratory, University Campus Bio-Medico, Rome, Italy, and [4]ICRA and ICRANet, University Campus Bio-Medico, Rome, Italy

Abstract

In his research activity, Emilio Del Giudice explored the possibility to move towards a unified view of some long-range dynamics in nature, ranging from quantum field theory in physics up to biology. Such a view is adopted in this contribution by discussing a mathematical model for synchronized electrical behavior of pancreatic beta cells. The stochasticity is a fundamental component of the physiological synchronized behavior of this system. On the contrary, in a pathological type I diabetes scenario, the cells are destroyed by the autoimmune system and their coherent behavior is lost. This phenomenology conceptually links to ideas of coherent dynamics in quantum physics. Possible implications both for physical sciences and for the epistemology of life sciences are outlined.

Keywords

Collective dynamics and coherence, electromagnetic interactions in biological systems, long-range interactions, quantum physics

History

Received 26 January 2015
Accepted 27 March 2015
Published online 9 June 2015

Introduction

Two recent papers published by Emilio Del Giudice have inspired this paper. The first one was dealing with ''The Role of Coherence in a Systems View of Cancer Development'' (Plankar et al., 2012) and the second one was a quantum approach applied to ''Communication and the Emergence of Collective Behavior in Living Organisms'' (Bischof and Del Giudice, 2013). Inspired by the quantum field theory mechanism of spontaneous breakdown of symmetry and the consequent generation of long range correlations in physical systems, Del Giudice explored the possibility to move towards a unified view of some long-range dynamical systems in nature including biological systems. The differences between living organisms and non-living systems led him to analyze two main features of biological behaviors. ''The first one is the capability of self-movement, namely a living organism is able to pursue autonomously the direction of its own motion, whereas a non-living object can be only pushed or pulled by an externally applied force. The second difference is that the dynamics of each component depends on the simultaneous dynamics of the other components, so that the ensemble of components behaves in unison in a correlated way'' (Bischof and Del Giudice, 2013).

Evidences that intermolecular interactions do not occur as individual-independent events in living organisms (Bertolaso et al., 2014) but as a part of a collective array of interconnected events (Bischof and Del Giudice, 2013) pose an interesting challenge from a scientific point of view and epistemologically as well. On one hand, regulation among different functional levels of the biological organization has to be explained, and, on the other hand, we need to understand how such levels are conceptualized and which kind of mechanisms are at work in such dynamics. At the crossroad of these two issues, there is the common question regarding the emergence of collective dynamics.

In the paper by Bischof and Del Giudice (2013), Del Giudice revised the paradigm of modern molecular biology from the perspective of what he called ''biocommunication'' through a scheme based on quantum field theory ''where molecules are able to perform in phase-correlated unison among them and with a self-produced electromagnetic field''. Plankar et al. (2012) developed a holistic view on cancer that from the scheme mentioned above is shown to be a system disease (see also Fath et al., 2001; Saetzler et al., 2011; Soto and Sonnenschein, 2012) in which energetic issues must be taken into consideration as well. In this way, he aimed to show how different biological aspects of cancer might be causally connected. The global and unspecific progressive disorganization at a variety of organizational levels is revealed by the loss of tissue organization and intercellular signaling, aberrant epigenetic regulation and gene expression profiles, disregulated metabolic pathways, instability of the genome, increased informational and thermodynamic entropy, and impairment of oxidative energy flow. Again, the concept of long-range dynamic order provides a synthetic theoretical framework for

Address correspondence to Simonetta Filippi, Nonlinear Physics and Mathematical Modeling Laboratory, University Campus Bio-Medico, Via A. del Portillo 21, I-00128 Rome, Italy. E-mail: s.filippi@unicampus.it

Alessandro Loppini

DOI: 10.3109/15368378.2015.1036069

different aspects of carcinogenesis from both biological and physical perspectives. Such an order is epitomized by coherent molecular dynamics. Although the nature of such a self-reinforcing interplay between energy and information remains to be elucidated, ''increased entropy is an immediate consequence of impaired coherence, and a subsequent decline of energy dissipation may exert an imbalance in metabolic and gene regulatory networks, disrupting normal flow of energy and information that percolates from one organizational level to the other and manifests as different biological aspects of cancer'' (Plankar et al., 2012).

In this paper, we use another case study to show the fecundity of Del Giudice approach and the terms of discussion of such biological dynamics. Examples are taken from the electrophysiology of the pancreas. Our aim is to spell out some consequences of the Del Giudice view and approach in the study of biological systems bringing into a unitary picture the functional and structural dimension of long-range dynamics. This poses the basis for the discussion in epistemological terms regarding the limits of genetic deterministic approaches or regarding how the concept of biological information should be revised when accounting for intra organismic dynamics and regulation.

Coherence and emergent behavior in a pancreatic beta cells model

While in the past the typical systems investigated by Physics have been characterized by a relatively small level of complexity in comparison to a living being, nowadays this branch of Science is oriented in investigating such a more structurally complex systems by using the same methods which in the past allowed scientists to obtain, for instance, a successful theory of condensed matter both at classical and quantum levels. On these lines, in the context of Computational Endocrinology, Portuesi et al. (2013) performed several numerical simulations on a stochastic model for a cluster of pancreatic beta-cells, following Sherman et al. (1991) basic formulation based on animal data.

Islets of Langerhans in the pancreas are ellipsoidal clusters of excitable cells, which regulate blood glucose homeostasis. Within these structures, beta cells regulate glycemic levels by releasing insulin. In rodents, such cells appear to be centrally clustered and are coupled through specific proteins (connexins) that form gap junctions. In response to specific glucose variations in the extracellular space, these cells dynamically change their membrane potential and their intracellular calcium concentration and release insulin. In order to model such a complex dynamics at a basic level, one can adopt a Hodgkin–Huxley type model, namely an extended version of the stochastic multi-cell model (Sherman et al., 1991) and study bursting activity of beta cells cubic clusters of variable size for different glycemic levels. Without presenting here all the technical details (which can be found in Loppini et al. 2014), we only mention that numerical integration of the model non-linear ordinary differential equations shows that for intact clusters (Figure 1), at physiological glucose concentrations, a coherent electrical activity is generated, leading to a synchronized free intracellular calcium concentration dynamics. Experimentally, the oscillations in such a calcium concentration are well known to be linked to insulin pulsations. On the contrary, (i) a drastic lowering of glucose, (ii) a stochastic activity suppression towards a deterministic regime, and/or (iii) a destruction on immune attack of several cells in the cluster lead to a coherence loss and to a severe insulin production weakening and final interruption. These findings are interesting from a fundamental point of view for two main reasons, i.e., (i) it seems that the stochastic activity in biological systems plays a fundamental role in producing emergent behaviors and (ii) a cell's efficient communication with other similar cells appears to be a key ingredient for robustness in view of efficient functional properties. Inspired by the strong formal links existing between stochastic and quantum physics, these ideas have been further investigated (Loppini et al., 2014), creating a link between a surprising self-similarity in the spectral analysis of the electrical patterns observed in the ''in silico'' system (Figure 2) and the coherent states formalism. According to recent results in quantum field theory (Vitiello, 2012, 2014), showing indeed the isomorphism between scale free self-similar structures and deformed coherent states, the self-similarity found in the spectral analysis signals the coherent dynamics of the cells in the cluster. Cellular coherence is also confirmed by additional studies (Cherubini et al., 2015) on interacting beta cells subclusters showing that there exists a ''functional coordination geography'' in this peculiar system which goes well beyond the simple spatial pattern of cellular communication.

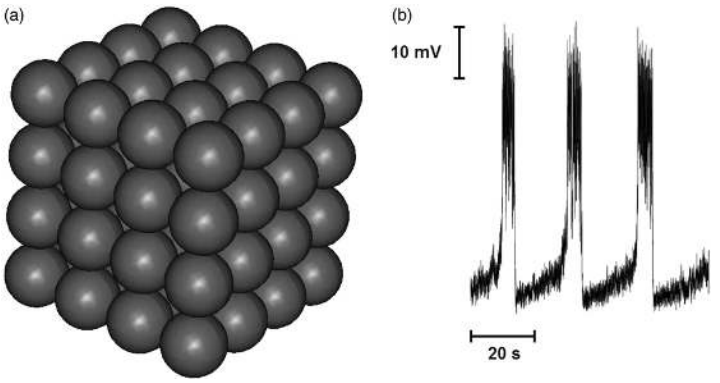

Figure 1. (a) Pancreatic cluster adopted in the simulations made of beta cells interacting via a Von Neumann neighborhood. (b) Typical action potential pattern of a beta cell in a synchronized scenario. The stochastic nature of the signal is evident.

Alessandro Loppini

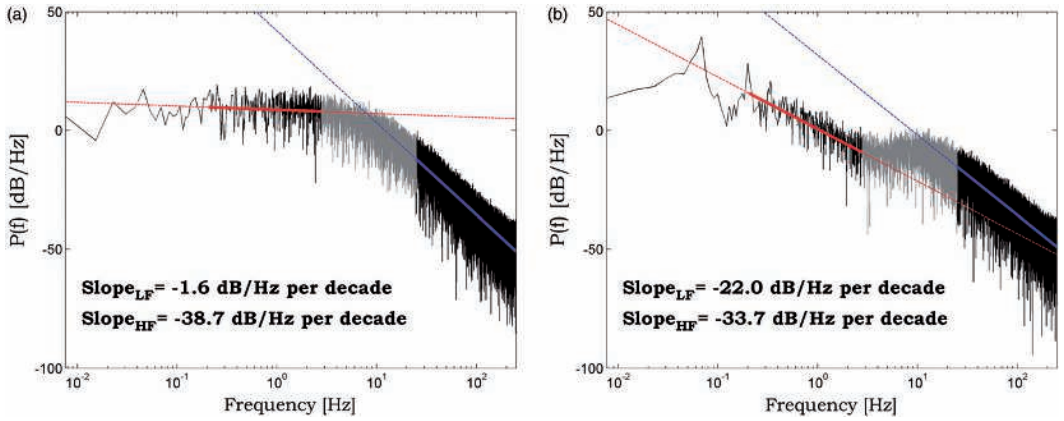

Figure 2. Log -log power density spectra of membrane potential signals of (a) a single cell cluster and (b) a representative cell in a $10 \times 10 \times 10$ cell cluster, both stimulated by a postprandial glucose concentration ([G] = 9.5 mM). The slopes at low (SLF) and high frequencies (SHF) are obtained by linear fitting highligthed by dashed lines. Specifically continuous line segments identify the power density spectrum points used for fitting data. The transition region between the two linear zones is shown in gray. The increase of the cluster population enhances the scale free self-similar behavior of the representative cell at low frequencies (the SLF increases) signaling many-body (many-cell) collective coherent effect.

Concluding remarks

The emergent behavior of synchronized beta cells just described offers an interesting case study to see Del Giudice's point of view on biological systems at work. The organizing principles of such systems are based on local communication effects modulated by intrinsically stochastic dynamics and by microscopic coherent state domains. The outcome is a long-range coherent behavior of the entire biological system. Linking these communication effects with the functional and structural components of such a biological system highlights the interesting relation between the system classical macroscopic properties and the coherent dynamics of its constituents: the system functional robustness finds its root in the microscopic coherent dynamics.

Declaration of interest

C. C., S. F., A. G., and A. L. acknowledge the International Center for Relativistic Astrophysics Network, ICRANet, and the GNFM-INdAM; G. V. and A. C. acknowledge INFN for support.

References

Bertolaso, M., Giuliani, A., Filippi, S. (2014). The mesoscopic level and its epistemological relevance in systems biology. In: Valente, A. X. C. N., Sarkar, A., Gao, Y. *Recent Advances in Systems Biology Research*. Commack, NY: Nova Science Publishers, Inc. pp. 19–36.

Bischof, M., Del Giudice, E. (2013). Communication and the emergence of collective behavior in living organisms: A quantum approach. *Mol Biol Int*. [Epub ahead of print] doi 10.1155/2013/987549.

Cherubini, C., Filippi, S., Gizzi, A., Loppini, A. (2015). The role of topology in beta-cells complex functional networks. *Phys. Rev. E*. [submitted].

Fath, B. D., Patten, B. C., Choi, J. S. (2001). Complementarity of ecological goal functions. *J. Theor. Biol.* 208:493–506.

Loppini, A., Capolupo, A., Cherubini, C., et al. (2014). On the coherent behavior of pancreatic beta cell clusters. *Phys. Lett. A* 378:3210–3217.

Plankar, M., Del Giudice, E., Tedeschi, A., Jerman, I. (2012). The role of coherence in a systems view of cancer development. *Theor. Biol. Forum* 105:15–46.

Portuesi, R., Cherubini, C., Gizzi, A., et al. (2013). A stochastic mathematical model to study the autoimmune progression towards type 1 diabetes. *Diabetes Metab. Res. Rev.* 29:194–203.

Saetzler, K., Sonnenschein, C., Soto, A. (2011). Systems biology beyond networks: Generating order from disorder through self-organization. *Semin. Cancer Biol.* 21:165–174.

Sherman, A., Rinzel, J. (1991). Model for synchronization of pancreatic beta-cells by gap junction coupling. *Biophys. J.* 59:547–559.

Soto, A. M., Sonnenschein, C. (2012). Is systems biology a promising approach to resolve controversies in cancer research? *Cancer Cell Int.* 12:1–5.

Vitiello, G. (2012). Fractals, coherent states and self-similarity induced noncommutative geometry. *Phys. Lett. A* 376:2527–2532.

Vitiello, G. (2014). On the isomorphism between dissipative systems, fractal self-similarity and electrodynamics. Toward an integrated vision of nature. *Systems* 2:203–216.

Alessandro Loppini

Am J Physiol Gastrointest Liver Physiol 307: G77–G88, 2014.
First published May 15, 2014; doi:10.1152/ajpgi.00385.2013.

Experimental evidence and mathematical modeling of thermal effects on human colonic smooth muscle contractility

A. Altomare,[1] A. Gizzi,[2] M. P. L. Guarino,[1] A. Loppini,[2] S. Cocca,[1] M. Dipaola,[2,4] R. Alloni,[3] M. Cicala,[1] and S. Filippi[2,5]

[1]*Gastroenterology Unit, University Campus Bio-Medico of Rome, Rome, Italy;* [2]*Nonlinear Physics and Mathematical Modeling Laboratory, University Campus Bio-Medico of Rome, Rome, Italy; and* [3]*Surgery Unit, University Campus Bio-Medico of Rome, Rome, Italy;* [4]*Politecnico di Milano, Milano, Italy; and* [5]*International Center for Relativistic Astrophysics, Pescara, Italy*

Submitted 13 November 2013; accepted in final form 2 May 2014

Altomare A, Gizzi A, Guarino MPL, Loppini A, Cocca S, Dipaola M, Alloni R, Cicala M, Filippi S. Experimental evidence and mathematical modeling of thermal effects on human colonic smooth muscle contractility. *Am J Physiol Gastrointest Liver Physiol* 307: G77–G88, 2014. First published May 15, 2014; doi:10.1152/ajpgi.00385.2013.—It has been shown, in animal models, that gastrointestinal tract (GIT) motility is influenced by temperature; nevertheless, the basic mechanism governing thermal GIT smooth muscle responses has not been fully investigated. Studies based on physiologically tuned mathematical models have predicted that thermal inhomogeneity may induce an electrochemical destabilization of peristaltic activity. In the present study, the effect of thermal cooling on human colonic muscle strip (HCMS) contractility was studied. HCMSs were obtained from disease-free margins of resected segments for cancer. After removal of the mucosa and serosa layers, strips were mounted in separate chambers. After 30 min, spontaneous contractions developed, which were measured using force displacement transducers. Temperature was changed every hour (37, 34, and 31°C). The effect of cooling was analyzed on mean contractile activity, oscillation amplitude, frequency, and contraction to ACh (10^{-5} M). At 37°C, HCMSs developed a stable phasic contraction (~0.02 Hz) with a significant ACh-elicited mean contractile response (31% and 22% compared with baseline in the circular and longitudinal axis, respectively). At a lower bath temperature, higher mean contractile amplitude was observed, and it increased in the presence of ACh (78% and 43% higher than the basal tone in the circular and longitudinal axis, respectively, at 31°C). A simplified thermochemomechanical model was tuned on experimental data characterizing the stress state coupling the intracellular Ca^{2+} concentration to tissue temperature. In conclusion, acute thermal cooling affects colonic muscular function. Further studies are needed to establish the exact mechanisms involved to better understand clinical consequences of hypothermia on intestinal contractile activity.

human colonic smooth muscle strips; thermal cooling; postoperative ileus; thermochemomechanical coupling; mathematical model

IT IS WELL KNOWN that temperature can influence the contractile activity of smooth muscle, acting at different levels (33, 47). Gastrointestinal tract (GIT) motility in animal models seems to be influenced by temperature: cooling of isolated rat GIT smooth muscle preparations rapidly induced a tonic contractile response inversely proportional to the temperature (46).

During major abdominal surgery, both deep anesthesia and operating theatre low temperature can significantly alter the thermal state of the tissue for a long period, probably playing a role in the pathogenesis of postoperative ileus (POI) (15, 32, 40, 70). POI is a multifactorial disease (4, 61), being the result of many interacting factors such as surgical trauma, local inflammatory reactions to intestinal manipulation, overactivation of the sympathetic nervous system due to several autonomic, hormonal, and behavioral responses to stressful regional stimuli, and low temperature (11, 22, 32, 41, 57). More recently, it has been shown that tissue damage and inflammatory cytokine release into the circulation are important factors determining the severity of POI, which most likely can contribute to the impaired motility of the nonmanipulated intestine (69). Less investigated is the role that temperature variations during surgery determine POI in humans.

Such a cooling-induced contraction appears not to be linked to a neural process, involving receptor activation and the release of neurotransmitters or mediators, but a myogenic response (47). Nevertheless, the basic mechanism governing thermal GIT smooth muscle responses has not been fully investigated in experimental measurements in in vivo and in vitro models. Studies based on physiologically tuned mathematical models have predicted that thermal cooling may induce an electrochemical destabilization of peristaltic activity (29).

The objective of the present study was to assess the effect of thermal cooling on human colonic smooth muscle strip (HCMS) contractility and to analyze the different responses of both circular and longitudinal smooth muscles (1). We statistically quantified basal tone, contraction frequency, and amplitude variations. Moreover, we proposed a thermochemomechanical model for intestine smooth muscle contraction reproducing the experimental recorded thermal effects by extending the mechanochemical formulation proposed by Stålhand et al. (64).

MATERIALS AND METHODS

Tissue specimens. Muscle specimens were obtained from the healthy margins of colonic resections from 10 patients with adenocarcinoma of the colon (6 men and 4 women, age range: 53–72 yr) treated at the Campus Bio-Medico University of Rome between September 2012 and May 2013. None of the patients had a history of colonic motility or a neuromuscular or collagen disorder; specimens found with diverticula were excluded. Hemicolectomy was performed in all patients, and a specimen from the resected colon was obtained at a distance from the area involved by the carcinoma.

Specimens were immediately taken to the laboratory in oxygenated, chilled Krebs solution containing (in mM) 116.6 NaCl, 21.9 $NaHCO_3$, 1.2 KH_2PO_4, 5.4 dextrose, 1.2 $MgCl_2$, 3.4 KCl, and 2.5 $CaCl_2$. The experimental protocols were approved by the Ethics Committee of Campus Bio-Medico University of Rome, and written informed consent was obtained from all individuals before surgery.

Address for reprint requests and other correspondence: M. Cicala, Gastroenterology Unit, Univ. Campus Bio-Medico of Rome, Via Alvaro del Portillo 200, Rome 00128, Italy (e-mail: m.cicala@unicampus.it).

Alessandro Loppini

Experimental setup. After removal of the mucosa and submucosa layers, colonic smooth muscle was cut into small strips (10 mm long by 2 mm wide, weight: 0.7 ± 0.3 g) by sharp dissection, identifying the circular and longitudinal orientation according to the position of the taenia coli. Strips were mounted in separate 10-ml muscle chambers as previously described (6). Strips were initially stretched to 20 g of load to bring them near conditions of optimum force development and equilibrated for an additional 30 min after continuous perfusion with oxygenated Krebs solution. The solution was equilibrated with a gas mixture containing 95% O_2 and 5% CO_2 at pH 7.4 and 37 ± 0.5°C (hereafter all temperature values are meant to present an accuracy of ±0.5°C). During the perfusion period, spontaneous phasic contractions developed gradually and stabilized after 30 min of equilibration. Isometric contractions were measured using force displacement transducers connected with a computer using MacLab system (Oxford, UK). The four obtained strips were then gradually exposed to thermal cooling (from 37 to 34 to 31 and back to 37°C, in the reverse order), with each temperature variation lasting for at least 1 h (the average time for strips stabilization). One colonic longitudinal muscle strip and one circular muscle strip were stimulated with a maximally effective dose of ACh (25 μl of 10^{-5} M ACh) to analyze ACh-induced contraction variations during thermal cooling. Temperature values were established on the basis of intraoperative colonic temperature measurements during surgery. A preliminary histopathological evaluation of the dissected mucosa and submucosa was also conducted. To perform histopathological evaluation after the thermal cooling protocol, smooth muscle strips were fixed in buffered formalin for 12 h and embedded in paraffin with a melting point of 55–57°C. Three- to four-micrometer sections were cut and stained with hematoxylin-eosin stain for morphological analysis.

Statistical methods. Calculated force amplitude and frequencies within the defined range of interest for each experiment were analyzed as both time variations and averages. Fast Fourier transform (FFT) analysis was also applied for a fine identification of the main contraction frequencies that varied due to both temperature and ACh effects. A Wilcoxon signed-rank test for paired observations (hereafter termed Wilcoxon test) was used to test the significance of the measurement variations between 31 and 37°C on the same tissue ($P < 0.05$). This choice was motivated by non-normal data distributions and by the low number of samples considering matched-paired observations, which makes the median more informative than the mean. Significant differences were therefore studied in terms of the medians of the groups. The following two different data normalization procedures were also implemented on mean values of the exerted force to gain a fine characterization of the statistical significance of the analysis: *1*) specimen normalization according to the force exerted by the strip at 31°C without ACh (*Norm 1*) and *2*) percent normalization according to the absolute minimum and maximum force exerted by the strip (*Norm 2*). A further level of analysis was also introduced considering paired measurements on the same strip. Principal component analysis (PCA) was finally performed to highlight segregation patterns and to identify data correlations. Means were calculated; means ± SE are reported unless means ± SD are specified.

Thermochemomechanical contraction model. Electrochemical destabilizations of myogenic activity due to thermal inhomogeneities have been recently considered as a possible cofactor for the pathogenesis of POI through a physiologically based mathematical model (29). Accordingly, similar investigations have been performed applying the same reasoning to different tissues, thus building predictive mathematical models on experimental evidence (8, 9, 25). In this context, inhomogeneity and anisotropy are well known to induce complex electrical spiraling behaviors in many biological contexts, such as the heart (26) and brain (17, 42), affecting the action potential propagation velocity as well as the entire electrophysiological dynamics (7). Dysrhythmias, in particular, have been theoretical predicted and experimentally recorded in the stomach and intestine (2, 29, 36, 50, 65) by making similar observations to what is known in brain and heart tissues (18, 28, 55). It is well known that the contractile rhythm of intestinal smooth muscle is due to the pivotal role of interstitial cells of Cajal (ICCs), which form a network of cells between the circular and longitudinal muscle layers making contact with surrounding smooth muscle cells and acting as a pacemaker of spontaneous motility in the gut (33). Advanced experimental tools have been developed in this direction (24, 48, 49, 52), leading to a fine characterization of electrical propagating fronts. Noninvasive measurements are currently being investigated to extend the diagnostic analysis to a wider clinical audience (13, 62).

From a biomechanical point of view, characterizing the complete response of soft biological media is still an open problem, although there have been recent technological improvements (58, 59, 66), and these tools are fundamental for the tissue specimen tests performed in the present work (5). The theoretical formulation proposed here is based on a continuum thermodynamical framework for smooth muscle cell contraction (44, 63) and was applied to HCMS modeling. Such an approach has received growing attention due to its general statements and applicability in a wide range of smooth muscle tissue models (61, 64). Explicit derivation and details of model equations are given in the APPENDIX.

Smooth muscle cells contract thanks to a complex chain of mechanical, electrochemical, and metabolic stimuli (34). The electrochemical states involve *1*) depolarization of the cell membrane, *2*) binding of Ca^{2+} to calmodulin, *3*) phosphorylation of myosin chains, and *4*) actin-myosin cross-bridge activation. The last phase is thought to be a continuous cycling with repetitive attaching of phosphorylated myosin to actin heads, thus generating a force-related power stroke. The active force and contraction, thus, are the result of the combined emerging effects of the ensemble of cross-bridge cycles. Moreover, as for all the excitable and deformable media of the human body, mechanical stimuli induce an important impact on the force generation (31, 56, 71). In particular, cell stretching can increase the phosphorylation rate and alter the tissue sensitivity to Ca^{2+} concentration.

In this work, we introduce a simplified thermodynamic relationship able to modify the ionic variables dynamics according to the thermal bath considered. In particular, a linear coupling between temperature and intracellular Ca^{2+} concentration was established as a first approximation. Such a procedure allowed us to set a complete feedback between Ca^{2+} dynamics and mechanical variables via stretch and, at the same time, the coupling between temperature gradients and stress variations via Ca^{2+}. In detail, the intracellular Ca^{2+} concentration ($[Ca^{2+}]_i$) is no longer assumed constant but is linearly linked to the thermal bath temperature (T) according to the following equation:

$$[Ca^{2+}]_i(T) = [Ca^{2+}]_{i0} + \alpha(T - T_0) \quad (1)$$

where $[Ca^{2+}]_{io}$ is a reference initial $[Ca^{2+}]_i$ typical of normal tissue at 37°C, T_0 is the reference tissue temperature, and α is a slope parameter. The simplified proposed relation states that the intracellular Ca^{2+}, ruling the activation of the contraction process, varies according to the thermal state reached by the tissue, thus inducing different stretch and stress levels in HCMSs for different thermal baths.

The linear formulation adopted was based on the experimental protocol implemented (see MATERIALS AND METHODS), where the stepwise variation of the thermal bath was interpolated after both increasing or decreasing law. Below, we show the agreement between this simplified modeling approach with the experimental evidence.

RESULTS

Statistical trend analysis. Our data set was composed of a total of 253 samples obtained from 40 strips of human colon, with 165 samples analyzed without ACh and 88 samples in the presence of Ach. Due to the high variability of the observed

Alessandro Loppini

frequencies, we used 120 samples for the evaluation of the average oscillation frequency in longitudinal-oriented HCMSs and 107 samples in circular-oriented HCMSs. A preliminary histological evaluation showed no necrotic signs or significant inflammatory infiltrates in the specimens examined.

Missing values were selected if the calculated period was >360 s. The smallest data set at 39°C confirmed the observations done for the other three temperatures and is shown in the figures as well.

Figure 1 shows a comparison of averaged normalized mean values in *Norm I* and oscillation amplitude and frequency of

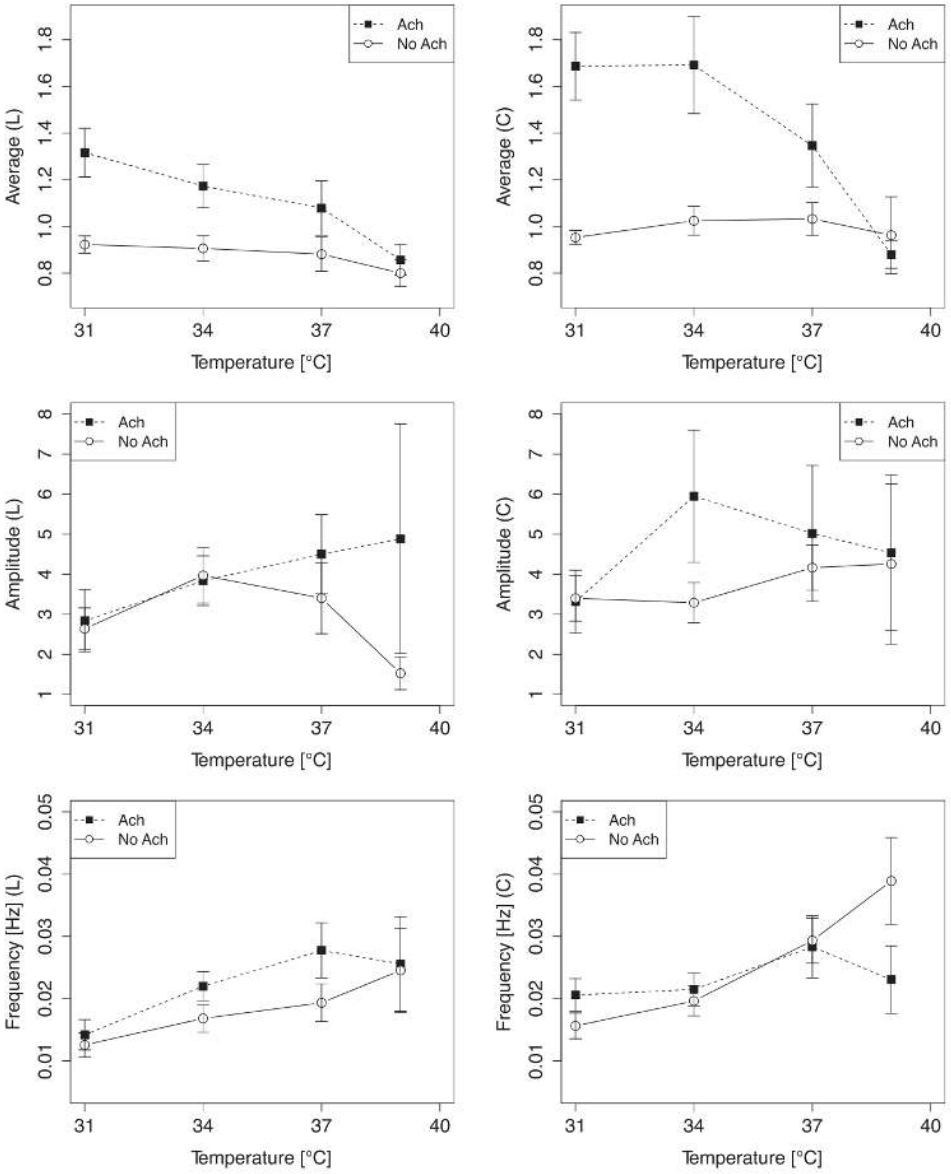

Fig. 1. Longitudinal (L)- and circular (C)-oriented human colonic muscle strip (HCMS) trend analysis with respect to temperature (T) variations for average values of mean force, oscillation amplitude, and frequencies. Specimen normalization according to the force exerted by the strip at 31°C without ACh (*Norm I*) was adopted.

Alessandro Loppini

the force exerted with respect to temperature variations in the presence and absence of ACh and distinguishing between longitudinal- and circular-oriented HCMSs. As shown in Fig. 1*A*, a decrease of the temperature resulted in a clear increment of the mean value for the two strip orientations, which was more significant in the presence of ACh than in the absence of the cholinergic stimulus. In fact, at 37°C, HCMSs developed a stable phasic contraction with a visible ACh-elicited contractile response, 31% and 22% higher than the baseline in the circular and longitudinal axis, respectively. At 31°C, the absolute highest difference was observed with the ACh-elicited response equal to 78% and 43% compared with baseline in the circular and longitudinal axis, respectively. The Wilcoxon test between these two temperatures revealed $P < 0.05$ for the total data set (a complete list of statistical test results is shown in Table 1).

Thermal bath cooling also induced an observable decrease in the oscillation amplitude, as expected, with the exception of the longitudinal-oriented strips, as shown in Fig. 1*B*. In particular, the Wilcoxon test between 31 and 37°C for the oscillation amplitude resulted in significant differences considering all data ($P < 0.005$) and longitudinal-oriented strips ($P < 0.05$) in the presence of the ACh-elicited response. More pronounced global variation due to temperature setup is shown in Fig. 1*C* in terms of oscillation frequency. In this case, when the temperature was decreased, a decrement of the frequency (equivalently an increment of the period) was observed for both strip orientations. These differences (between 31 and 37°C) were statistically significant for the ACh-elicited response and for the basal tone considering all data ($P < 0.05$ and $P < 0.005$, respectively). A significant difference was also obtained for the basal tone frequency considering the circular-oriented strips ($P < 0.05$).

Table 1. *Wilcoxon signed-rank test for paired measurements on the same tissue*

	Temperature			
P Value	31°C	37°C	Direction	ACh
		Average		
0.0063*	16	16	T	Yes
0.1713	36	36	T	No
0.0391*	8	8	L	Yes
0.0987	18	18	L	No
0.1094	8	8	C	Yes
0.8650	18	18	C	No
		Amplitude		
0.0042†	16	16	T	Yes
0.0321*	36	36	T	No
0.1953	8	8	L	Yes
0.1540	18	18	L	No
0.0156*	8	8	C	Yes
0.1084	18	18	C	No
		Frequency		
0.0438*	16	16	T	Yes
0.0013†	27	27	T	No
0.0781	8	8	L	Yes
0.1294	12	12	L	No
0.4469	8	8	C	Yes
0.0067*	15	15	C	No

*$P < 0.05$; †$P < 0.005$. Mean force, oscillation amplitude, and period were tested for two different temperatures (31 and 37°C) reporting the numerosity of the data set analyzed. The test was performed on the total data set (T) and distinguishing between longitudinal (L)- and circular (C)-oriented data in the presence (yes) and absence (no) of ACh.

Figure 2 shows the comparison of median averaged normalized mean values in *Norm I* and oscillation amplitude and frequency of the force exerted with respect to temperature variations in the presence and absence of ACh for the full data set. The boxplot representation was adopted to show data distributions at each temperature and was motivated by the fact that the median gains more robustness with respect to the mean in the presence of outliers. Moreover, this representation was in line with the statistical test adopted characterizing the differences in the medians of two groups of paired observations. In this case as well, the partial observations done for the longitudinal- and circular-oriented strips were confirmed for the overall data set.

In summary, when the temperature was decreased, a reduction of the baseline, oscillation amplitude, and frequency was observed, whereas an increase of the ACh-elicited contractile response was registered.

Two-dimensional PCA scores and loading plots on the first two principal components are shown in Fig. 3. The information recovered was equal to the 60% of the total information gained from the data set. Temperature was positively correlated with oscillation amplitude and negatively correlated with normalized means and periods. The negative correlation with the mean was probably due to the dominating trend of the ACh-elicited response, in which the tone mean value decreased for temperature increments. The solid and open circles in Fig. 3 further distinguish between the different point distributions for ACh-free and ACh-stimulated HCMSs, highlighting that the differences were focused within period-mean directions.

Representative examples. Figure 4 shows two representative sequences of the adopted experimental protocol. In particular, the *top* traces in Fig. 4 show the force variation with respect to the sole temperature, whereas the *bottom* traces in Fig. 4 show the same variation comparing the coupled effects of ACh and temperature.

These trends were in agreement with the statistical analysis previously discussed. Figure 5 shows two representative examples of different active contraction at 34°C together with their corresponding FFT spectra. In Fig. 5*A*, the clear frequency peak was centered at 0.038 Hz (period: 26.4 s), highlighting a very active phase with an amplitude of ~4 g, whereas in Fig. 5*B*, a wide range of the spectrum was invaded (period: 15.5–82.0 s) with a corresponding small oscillation amplitude of the recorded pattern at ~1.2 g. These examples highlight the strong variability of the frequency response recorded in the HCMS specimen data set.

Interestingly, in a limited number of cases, we observed peculiar patterns similar to those known for other biological systems, i.e., cardiac electrical arrhythmias (28) and pancreatic β-cell electrical activity (53). Figure 6, *left*, shows the high variability of the phasic contractions in terms of amplitude, frequency, and waveform at three different temperatures. Figure 6, *right*, shows alternating patterns and burst-like behaviors varying between long and short oscillating phases. These observations unveil how critical our understanding of the overall complex dynamics of the intestine tissue is still.

Mathematical modeling. The thermochemomechanical model presented in above was able to reproduce the experimental

Alessandro Loppini

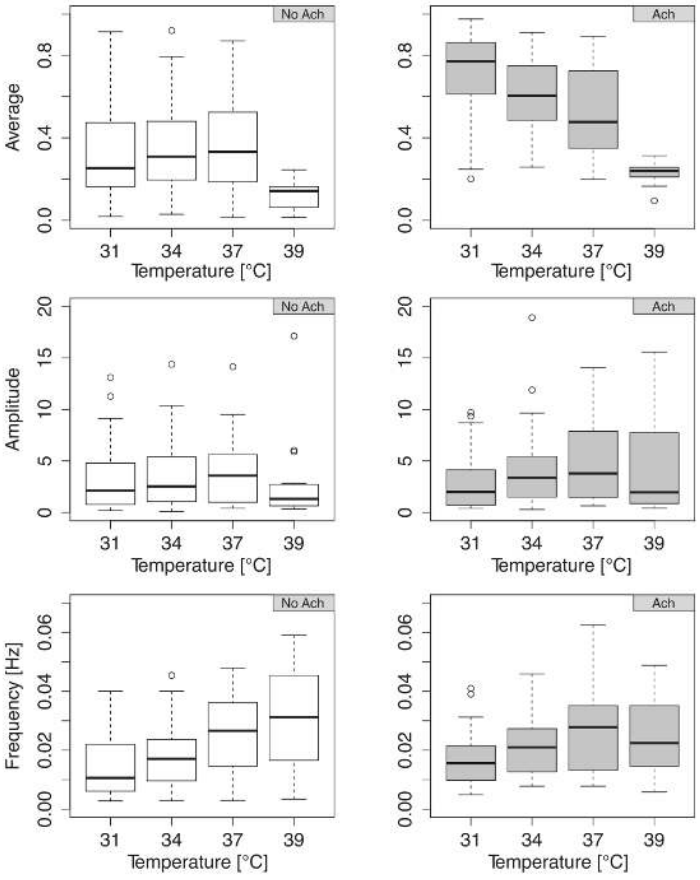

Fig. 2. HCMS boxplot analysis with respect to temperature for mean force, oscillation amplitude, and frequency values obtained from the complete data set. *Left*: no ACh; *right*: presence of ACh. Percent normalization according to the absolute minimum and maximum force exerted by the strip (*Norm 2*) was adopted for the average plots.

observed phenomena in terms of mean stress state varying with temperature. Figure 4*C* shows the time variation of mean stress by applying the same experimental thermal protocol in the model (31-34-37-34-31°C) compared with the basal tone recorded for representative tissue preparations. In particular, the model was able to catch the increasing of the tone as temperature lowered with a short accommodation time. Such a fast dynamic stabilization of mean stress allowed an optimal tuning of the model onto the desirable stress state. This feature underlines the wide range of applicability of the model toward different thermal protocols inducing different tissue stress regimes. Moreover, nonlinear Ca^{2+}-temperature coupling would result in similar stress-temperature dynamic analysis for the mean stress state.

Finally, Fig. 7 shows the stress-strain response for five different Ca^{2+} concentrations fine tuned on different thermal baths. The resulting nonlinear relations changed according to *Eq. 1* and highlight the physical hyperelastic nature of the model, which is typical of fiber reinforced biological media. The normalized stress at zero strain (stretch = 1) increased nonlinearly with the Ca^{2+} concentration, reaching a saturation level for Ca^{2+} concentration of ≈11 μM; when the stretch was increased into the tissue, the resulting normalized stresses similarly tended to the maximum allowable value but followed very different patterns. These features are very important for modeling applications, with more complex Ca^{2+} dynamics coupling slow and fast oscillations of the voltage membrane as well.

DISCUSSION

Data emerging from the present study show that lowering of temperature induced a significant stepwise increase of the tonic contractile response in human colonic smooth muscle, which was more significant in the presence of ACh than in the absence of the cholinergic stimulus. Moreover, cooling significantly decreased the frequency and amplitude of rhythmic contractions, which was more evident in circular than in longitudinal muscle layers. When temperature was restored up to 37°C, the tone, amplitude, and frequency were rapidly restored, suggesting that a morphological alteration during the cooling period does not occur, as reported in another similar

Alessandro Loppini

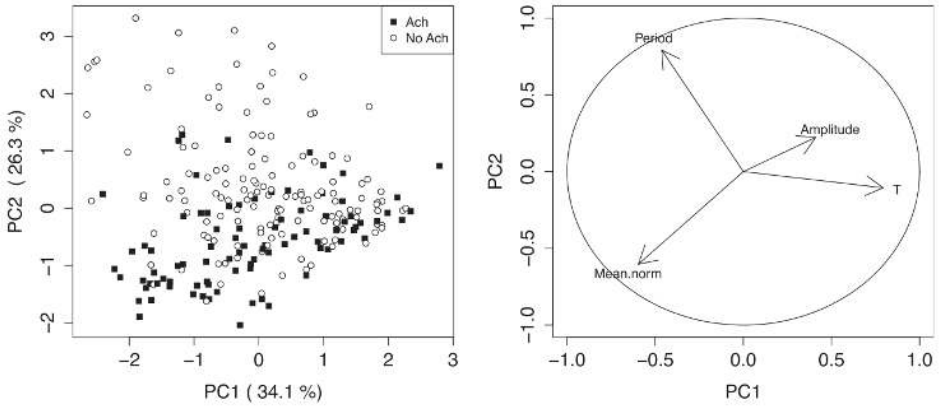

Fig. 3. Principal component analysis of the two mose significant components (PC1 and PC2) recovering 60% of the total information available from the full data set. *Norm 2* was adopted in this case.

experimental setup (37). This evidence was confirmed by the histological evaluation, in which no necrotic signs or significant inflammatory infiltrates were detected in the specimens examined.

Our results are in agreement with previous findings in which Mustafa et al. (47) reported that cooling of intestinal smooth muscle results in an increased force of contraction, with a significant reduction of the frequency and amplitude of the spontaneous activity. The authors (47) tested, in an animal model, a large scale of temperature (from 37 to 5°C) and showed a rapid and reproducible stepwise increase in the level of tone that was inversely proportional to the temperature. In the present study, temperature values were established on the basis of intraoperative colonic temperature measurements during surgery that ranged between 31 and 37°C and were in line with the animal model evidence. Moreover, Mustafa et al. studied the effect of cooling in various segments of the intestinal tract and showed the same response in the esophagus, stomach, duodenum, jejunum, and colon.

As stated above, in animal models, the contractile responses to cooling were not influenced by pretreatment with either muscarinic and histamine H_1 antagonists or neural blockers (capsaicin and tetrodotoxin), suggesting that it is likely not mediated by a neurogenic response but by a myogenic mechanism (47). The same authors demonstrated that cooling affected Ca^{2+} homeostasis by interfering with processes of translocation of extracellular Ca^{2+}. For this reason, the mathematical model formulated here takes into account the linear relationship between Ca^{2+} concentration and temperature. It is known that temperature affects both ionic conductances and rate constants modulating action potential propagation. We hypothesized that temperature could influence the chemomechanical response of intestinal muscle. Confirming this theory, animal studies and clinical trials have demonstrated that the duration of POI is significantly decreased in patients undergoing laparoscopic instead of open procedures for colon surgery, in which the abdominal organs are more exposed to manipulation and intraoperative thermal cooling (12, 35, 62). On the other hand, recent studies have shown that there are not significant clinical differences in POI outcomes using warmed humidified laparoscopic gas versus dry cold gas during laparoscopic colectomy and appendectomy (60, 75), hypothesizing that thermal changes after main abdominal surgeries may be transitory and that they don't permanently damage the tissue for longer periods.

In summary, these findings may provide several different applications considering the complex electrical activity of the gastrointestinal system (16). First, the experimental setup used in this investigation can be adopted to study the pharmacological effects of single or multiple drugs at both experimental and modeling levels to identify possible therapeutic approaches for POI, in particular exploring the role of ICCs. As mentioned above, increasing evidence confirmed the main role of ICCs as the pacemaker of spontaneous motility in the gut (38, 68). In a recent study (33) performed on an animal model, the authors examined the effects of temperature and metabolic inhibitors on the generation of pacemaker potentials recorded from ICCs in situ in the mouse small intestine. They showed that altering temperature over the range of 26–40°C influenced the frequency, half-width, and maximal change in voltage over time of pacemaker potentials without affecting the resting membrane potential and amplitude, showing that ICCs in situ have different temperature sensitivities.

Moreover, engineering and clinical applications rely on the experimental validation of new endoscopic robotic devices as well (21). It has been demonstrated that these devices can affect the local temperature of internal colon layers, thus leading to unexpected and undesirable effects similar to POI drawbacks. On this line, in particular, hyperelastic-based models are being studied for applications in medical robotics (20, 30), taking into account the internal irregularities of intestinal villi (3), intestinal edema (74), and viscoelasticity (10, 67). The effect of temperature may play an interesting role in most of these open problems. At the same time, investigating the role of intraoperative thermal cooling on intestinal motor function could also be explored to prevent POI modulating the operating theatre room temperature during surgery.

Limitations and future perspectives. Limitations to the present study can be identified at both the experimental and modeling levels. From the experimental point of view. a better

Alessandro Loppini

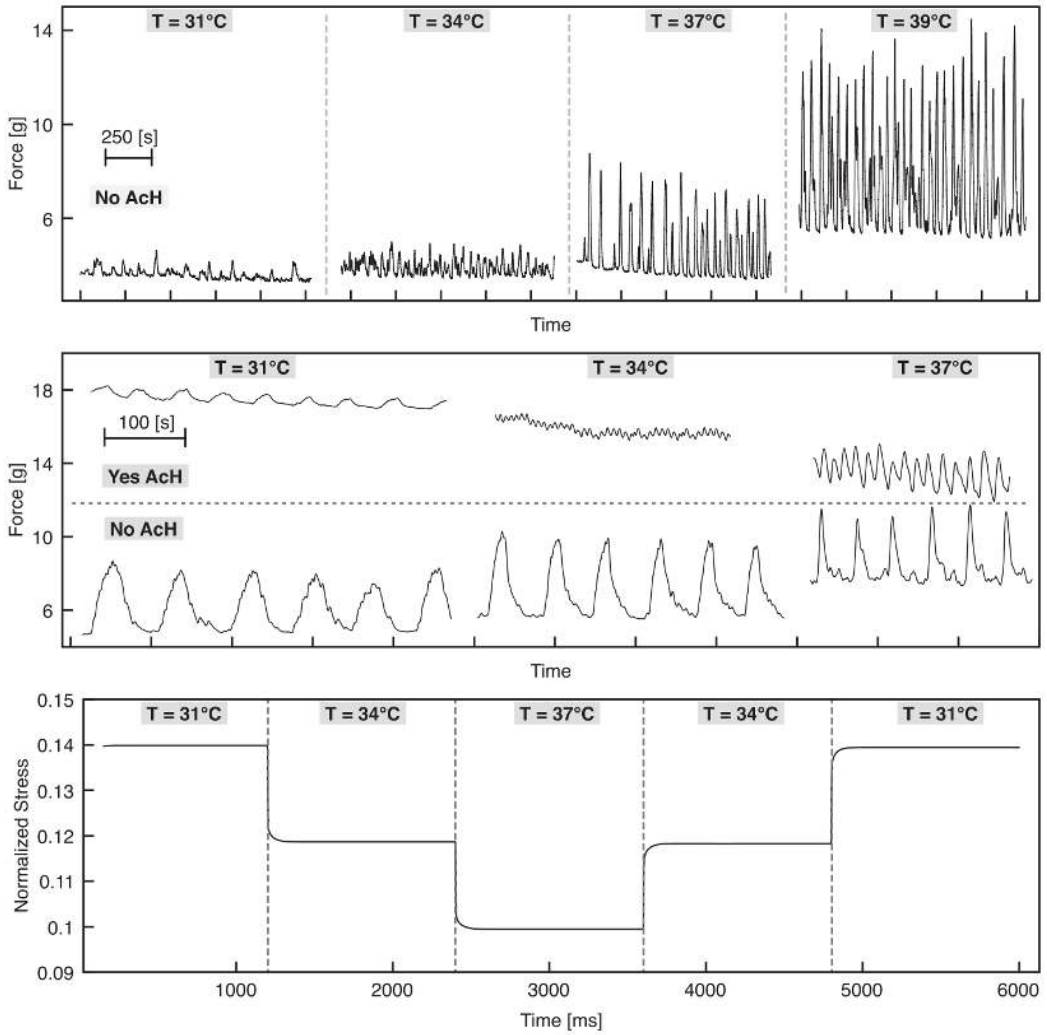

Fig. 4. Representative examples of recorded signal variations with respect to the sole temperature (*A*) and comparing the coupled effects of ACh and temperature (*B*). Statistics were confirmed. *C*: normalized stress values from model simulations following the experimental thermal protocol. Average mean values agreed qualitatively.

characterization of the recorded signal would be of great interest to explore the colonic contractile response upon a wider thermal range and different external stimuli could be applied, such as drugs or inhibitors of neural mechanisms (27). Particularly, external electrical stimulations could also be studied, as stretch-induced contractions, blocking the neural activity to better identify the role of ICCs in modulating the contractile response to cooling. Moreover, in vitro tissue studies have demonstrated that some inflammatory mediators, especially prostaglandins, can modulate the frequency of contractions in the stomach (50, 73); for this reason, use of selective inhibitors would help to better explore the mechanism responsible for the cooling contractile response of smooth muscle tissue. An extended data set for a wider range of thermal conditions would also help to unveil the contractile response of longitudinal- and circular-oriented human colonic strips. Other cumulative and coupled factors could also be studied, such as stretch-induced contractions of external electrical stimulations (19, 54).

From a modeling point of view, a forthcoming work in this direction will deal with realistic intestinal geometries with space-dependent dynamics of slow wave propagation and entrainment on the line of previous theoretical and experimental works (14, 39, 45, 72). More complex Ca^{2+} dynamics will be

Alessandro Loppini

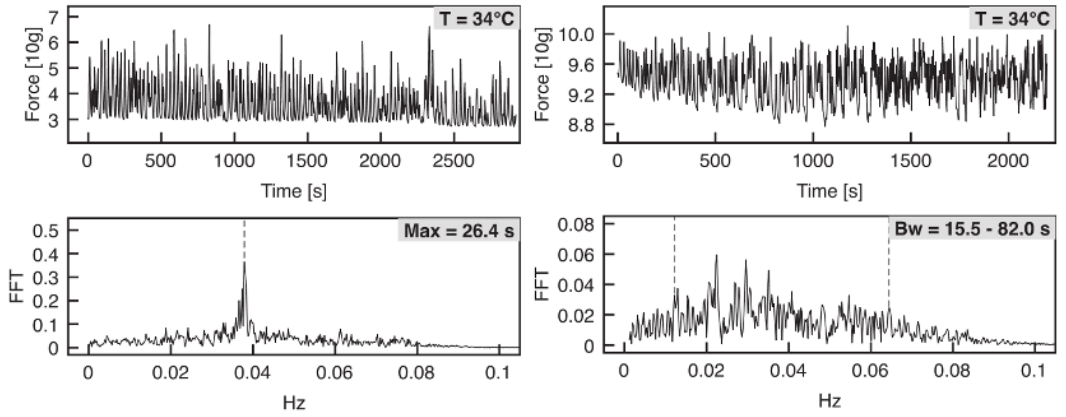

Fig. 5. Representative examples of the recorded force signal at 34°C showing the corresponding fast Fourier transform (FFT) response. *Left*: peak frequency corresponding with a period of 26.4 s. *Right*: distributed spectrum over a wide range of frequencies corresponding with a period bandwidth (Bw) of 15.5–82.0 s.

considered in the nonlinear coupling, with both mechanical quantities and temperature gradients. An extra level of coupling will consider the electrical activity of the tissue in conjunction with thermal and metabolic feedbacks. In particular, thermal heterogeneities will be introduced, analyzing the resulting stress and deformation state. Fiber reinforcement and dispersion will be considered as well to better match the high degree of anisotropy of the intestinal wall based on micro-

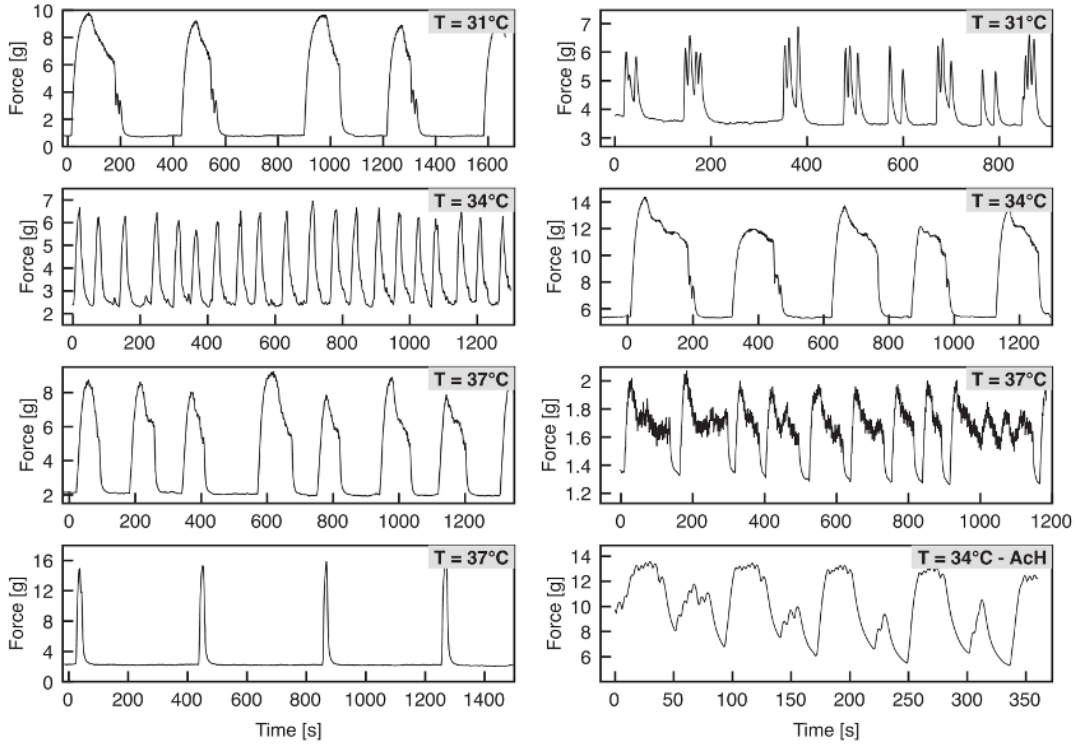

Fig. 6. Representative examples of the recorded force signal showing the variability of the contraction at three different temperatures (i.e., 31, 34, and 37°C; *A*) and alternans and burst-like patterns (*B*).

Alessandro Loppini

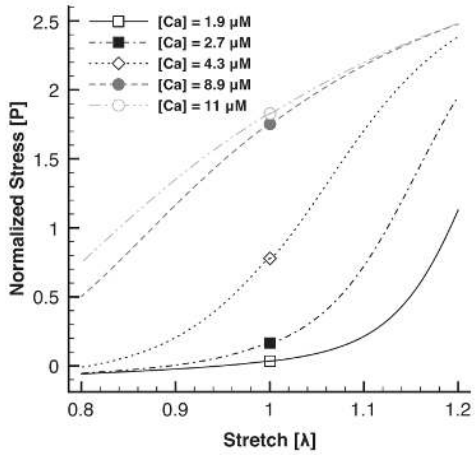

Fig. 7. Stress-strain relationships obtained from the numeric solution of the mathematical model discussed in MATERIALS AND METHODS. Different Ca^{2+} concentrations are shown, highlighting the highly nonlinear response of the model corresponding to different thermal setups according to *Eq. 1*.

scopic Ca^{2+} dynamics (43, 51, 70). A direct extension of such an approach should consist in analyzing thermoionic feedback on realistic reconstructed domains.

APPENDIX

A continuum thermodynamical framework was adopted here based on the additive decomposition of the deformation gradient (a filament translation and a stretch of myosin heads) (19, 44). Balance laws for the mechanical and electrochemical relationships were justified via the virtual power principle (23). Constitutive equations were derived by applying the dissipation inequality for a nonlinear hyperelastic material model, and the chemical state of myosin was modeled as a first-order kinetic (18, 43, 45). The coupling between the different models was also justified, and the effect of temperature was introduced.

Chemical model. The chemical state was based on Hai and Murphy (31) smooth muscle cell myosin phosphorylation and stress development, modeling a so-called latch state allowing for a basal tone level. It consists of four variables (n_1, n_2, n_3, and n_4) representing the different functional states of the smooth muscle thus connected via seven kinetic constants (with rates k_1–k_7). The resulting coupled system of first-order ordinary differential equations can be described as follows:

$$\dot{n_1} = \eta_1 k_1 n_1 + \eta_2 k_2 n_2 + \eta_4 k_7 n_4 \quad (2)$$

$$\dot{n_2} = \eta_1 k_1 n_1 + \eta_2 (k_2 + k_3) n_2 + \eta_4 k_4 n_4 \quad (3)$$

$$\dot{n_3} = \eta_2 k_3 n_2 + \eta_3 (k_4 + k_5) n_3 + \eta_4 k_6 n_4 \quad (4)$$

$$\dot{n_4} = \eta_3 k_5 n_3 - \eta_4 (k_6 + k_7) n_4 \quad (5)$$

where $\Sigma_{i=1}^{4} n_i = 1$, $\eta_i = A_i(\lambda - 1.12) + 1$, for $i = 1 \ldots 4$, varies according to tissue deformation [stretch (λ)], where η is a positive material fitting parameter and A_i is a chemical state parameter. These equations thus represent the direct effect of the mechanical deformation (stretch) onto the chemical variables of the Hai and Murphy model. In particular, the rate variables vary according to the strain level induced into the tissue. Ca^{2+} concentration and deformation feedbacks were introduced through the following equations:

$$k_1 = k_6 = \frac{\beta^4}{\beta^4 + \beta_0^4}, \quad \beta_0 = C_0 + \frac{C_1}{\lambda}, \quad \beta = Ca^{2+} \quad (6)$$

where β is the current configuration, β_0 is a reference configuration, and C_0 and C_1 are chemical state paramters. Model parameters are shown in Table 2.

Table 2. *Parameters and physical dimensions of the mathematical model*

Parameter	Description	Value	Units	Reference(s)
α	Slope of the Ca^{2+}-temperature function	0.033	μM/°C	
λ	Experimental stretch conditions	1.12		45
λ_{opt}	Optimal stretch	1.40		53
ξ	Bandwidth of the effective area function	0.707		
A_1	Chemical state parameter	2.069		45
A_2	Chemical state parameter	−3.289		45
A_3	Chemical state parameter	−1.744		45
A_4	Chemical state parameter	0.989		45
C_0	Chemical state parameter	−13.723		45
C_1	Chemical state parameter	19.807		45
$[Ca^{2+}]_{io}$	Reference intracellular Ca^{2+} concentration	2.1–1.9	μM	
E_1	Stiffness of the PSP cross-bridge	12.5	μN/μm	51
E_2	Stiffness of the attached cross-bridge	8.8	μN/μm	51
f_1	Friction of the PSP cross-bridge	1.3	μN·μs·μm^{-1}	51
f_2	Friction of the attached cross-bridge	85.5	μN·μs·μm^{-1}	51
k_1	PSP rate			45
k_2	DPSP rate	0.5	s^{-1}	52
k_3	PSP myosin attachment rate	0.4	s^{-1}	52
k_4	DPSP myosin attachment rate	0.1	s^{-1}	52
k_5	DPSP rate	0.5	s^{-1}	52
k_6	PSP rate			45
k_7	Detachment rate of the attached state	0.01	s^{-1}	52
q_1	Fitting parameter	3		52
q_2	Fitting parameter	0.1		52
T_0	Reference tissue temperature	31–37	°C	
v	Cycling velocity of the cross-bridge	5	μm/μs	51

PSP, phosphorylated; DPSP, dephosphorylated.

Alessandro Loppini

Thermodynamic model. Considering smooth muscle as composed of two parallel sections, a spring and a contractile element, we set β_0 and β where the total length was measured. To reach such a state, an intermediate noncompatible configuration (β_a) was passed through, in which the contractile element was separately activated to a length (λ_a) and the cross-bridge elasticity then acted via an additional stretch (λ_c). Such a structure formalized in the following multiplicative decomposition relation:

$$\lambda = \lambda_c \lambda_a \tag{7}$$

Upon these assumptions, we can defined the total Helmholtz strain-energy function associated with passive and active phases of the myocyte contraction as follows: $\Psi = \Psi(\lambda, \lambda_c, n_i, \beta, T)$. We thus considered the superposition of free energies in isothermal conditions as follows:

$$\psi = \psi_1(\lambda) + \mathcal{M}(\lambda_a)\psi_2(\lambda_c, n_i) + \psi_3(n_i) + \psi_4(\beta) \tag{8}$$

which was explicitly defined by applying the extended balance principle of mechanics (51). In particular, $\mathcal{M}(\lambda_a)$ represents the effective area overlap between the active filaments for generating the contractile force. Such an approach allowed us to define, in general terms, the evolutionary laws of λ_a, n_i, β, and T, thus allowing us to measure the stress (P) for a given stretch λ as follows:

$$P = \frac{\partial \psi}{\partial \lambda}, B = \frac{\partial \psi}{\partial \beta}, \eta = -\frac{\partial \psi}{\partial T}, P_a = \frac{\partial \psi}{\partial \lambda_a} + C\dot{\lambda}_a, \sum_{i=1}^{4} a_{ij}\dot{n}_j = -\frac{\partial \psi}{\partial n_j} + r \tag{9}$$

where B is the force work conjugate with beta, P_a is the active stress contribution with $C = (f_1 n_3 + f_2 n_4)\mathcal{M}(\lambda_a)$, where f_1 is the friction of the phosphorylated cross-bridge and f_2 is the friction of the attached cross, a_{ij} is $[a_{ij} = a_{ij}(\lambda_a, \lambda_c, \beta)]$, and r is a time multiplier constrained by *Eq. 2*.

Specific forms of the following potential functions were selected according to Refs. 44 and 67:

$$\psi_1 = \frac{q_1}{q_2}\left[e^{q_2(\lambda-1)} - 1 - q_2(\lambda - 1)\right] \tag{10}$$

$$\psi_2 = \frac{1}{2}(n_3 E_1 + n_4 E_2)(\lambda_c - 1)^2 \tag{11}$$

$$\psi_3 = \sum_{i=1}^{3} \psi_{3,i}(n_i) \tag{12}$$

$$\psi_4 = \frac{1}{2}\beta^2 \tag{13}$$

where q_1 and q_2 are fitting parameter, E_1 is the stiffness of the phosphorylated cross-bridge, E_2 is the stiffness of the attached cross-bridge. We can thus recover the active stress definition as $P_a = -f_1 n_3 \nu \mathcal{M}(\lambda_a)$ (where ν is the cycling velocity of the cross-bridge) and $[Ca^{2+}]_i$ as $B = \beta$.

Finally, total stress can be described as follows:

$$P = \frac{\partial \psi_i}{\partial \lambda} + \frac{\mathcal{M}(\lambda_a)}{\partial \lambda_a}\frac{\partial \psi_2}{\partial \lambda} \tag{14}$$

and active contraction evolution can be described as follows:

$$C\dot{\lambda}_a = P_a - \frac{\partial \mathcal{M}(\lambda_a)}{\partial \lambda_a}\psi_2 + \frac{\lambda_c}{\lambda_a}\mathcal{M}(\lambda_a)\frac{\partial \psi_2}{\partial \lambda_c} \tag{15}$$

In case HCMS fiber orientations is considered, the Helmholtz free energy would modify its functional dependence with respect to the principal directions of activations. In particular, the introduction of fiber-based invariants would be necessary (see Ref. 32a).

ACKNOWLEDGMENTS

The authors thank the Pathological Anatomy Laboratory at the University Campus Bio-Medico of Rome for support with the histological analysis.

GRANTS

The International Center for Relativistic Astrophysics Network partially supported this work.

DISCLOSURES

No conflicts of interest, financial or otherwise, are declared by the author(s).

AUTHOR CONTRIBUTIONS

A.A., A.G., M.P.L.G., R.A., M.C., and S.F. conception and design of research; A.A., S.C., M.D., and R.A. performed experiments; A.A., A.G., A.L., S.C., and M.D. analyzed data; A.A., A.G., M.P.L.G., S.C., M.D., M.C., and S.F. interpreted results of experiments; A.A., A.G., M.P.L.G., A.L., S.C., M.C., and S.F. drafted manuscript; A.A., A.G., M.P.L.G., R.A., M.C., and S.F. edited and revised manuscript; A.A., A.G., M.P.L.G., A.L., S.C., M.D., R.A., M.C., and S.F. approved final version of manuscript; A.G., A.L., and M.D. prepared figures.

REFERENCES

1. **Altomare A, Guarino MP, Gizzi A, Cocca S, Cherubini C, Alloni R, Filippi S, Cicala M.** Mo1157 human colonic smooth muscle contractility following acute thermal cooling. *Gastroenterology* 142, Suppl 1: S608–S609, 2012.
2. **Angeli TR, O'Grady G, Du P, Paskaranandavadivel N, Pullan AJ, Bissett IP, Cheng LK.** Circumferential and functional re-entry of in vivo slow-wave activity in the porcine small intestine. *Neurogastroenterol Motil* 25: e304–e314, 2013.
3. **Balbi V, Ciarletta P.** Morpho-elasticity of intestinal villi. *J R Soc Interface* 10: 20130109, 2013.
4. **Bauer AJ, Boeckxstaens GE.** Mechanisms of postoperative ileus. *Neurogastroenterol Motil* 16: 54–60, 2004.
5. **Bellini C, Glass P, Sitti M, Di Martino ES.** Biaxial mechanical modeling of the small intestine. *J Mech Behav Biomed Mat* 4: 1727–1740, 2011.
6. **Biancani P, Walsh JH, Behar J.** Vasoactive intestinal polypeptide. A neurotransmitter for lower esophageal sphincter relaxation. *J Clin Invest* 73: 963–967, 1984.
7. **Bini D, Cherubini C, Filippi S, Gizzi A, Ricci PE.** On spiral waves arising in natural systems. *Commun Comput Phys* 8: 610, 2010.
8. **Bini D, Cherubini C, Filippi S.** Heat transfer in FitzHugh-Nagumo models. *Phys Rev E* 74: 041905, 2006.
9. **Bini D, Cherubini C, Filippi S.** On vortices heating biological excitable media. *Chaos* 42: 2057–2066, 2009.
10. **Bini D, Cherubini C, Filippi S.** Viscoelastic FitzHugh-Nagumo models. *Phys Rev E* 72: 041929, 2005.
11. **Boeckxstaens GE, de Jonge WJ.** Neuroimmune mechanisms in postoperative ileus. *Gut* 58: 1300–1311, 2009.
12. **Bohm B, Milsom JW, Fazio VW.** Postoperative intestinal motility following conventional and laparoscopic intestinal surgery. *Arch Surg* 130: 415–419, 1995.
13. **Bradshaw LA, Irimia A, Sims JA, Gallucci MR, Palmer RL, Richards WO.** Biomagnetic characterization of spatiotemporal parameters of the gastric slow wave. *Neurogastroenterol Motil* 18: 619–631, 2006.
14. **Buist ML, Corrias A, Poh YP.** A model of slow wave propagation and entrainment along the stomach. *Ann Biomed Eng* 38: 3022–3030, 2010.
15. **Cannon WB, Murphy FT.** The movement of the stomach and intestines in some surgical conditions. *Ann Surg* 43: 512–536, 1906.
16. **Cheng LK, O'Grady G, Du P, Egbuji JU, Windsor JA, Pullan AJ.** Gastrointestinal system. *Wiley Interdiscip Rev Syst Biol Med* 2: 65–79, 2010.
17. **Cherubini C, Filippi S, Gizzi A.** *Diffusion Processes in Human Brain Using COMSOL Multiphysics.* Milano, Italy: Proceedings of the COMSOL Users Conference, 2006.
18. **Cherubini C, Filippi S, Gizzi A.** Electroelastic unpinning of rotating vortices in biological excitable media. *Phys Rev E* 85: 031915, 2012.
19. **Cherubini C, Filippi S, Nardinocchi P, Teresi L.** An electromechanical model of cardiac tissue: constitutive issues and electrophysiological effects. *Prog Biophys Mol Biol* 97: 562–573, 2008.
20. **Ciarletta P, Dario P, Tendick F,** .Hyperelastic model of anisotropic fiber reinforcements within intestinal walls for applications in medical robotics. *Int J Robot Res* 28: 1279–1288, 2009.

Alessandro Loppini

21. **Dario P, Ciarletta P, Menciassi A, Micera S.** Modeling and experimental validation of the locomotion of endoscopic robots in the colon. *Int J Robot Res* 23: 549–556, 2004.
22. **Delaney CP.** Clinical perspective on postoperative ileus and the effect of opiates. *Neurogastroenterol Motil* 16, Suppl 2: P61, 2004.
23. **Di Carlo A, Quiligotti S.** Growth and balance. *Mech Res Comm* 29: 449–456, 2002.
24. **Du P, O'Grady G, Egbuji JU, Lammers WJ, Budgett D, Nielsen P, Windsor JA, Pullan AJ, Cheng LK.** High-resolution mapping of in vivo gastrointestinal slow wave activity using exible printed circuit board electrodes: methodology and validation. *Ann Biomed Eng* 37: 839–846, 2009.
25. **Fenton FH, Gizzi A, Cherubini C, Pomella N, Filippi S.** Role of temperature on nonlinear cardiac dynamics. *Phys Rev E* 87: 042717, 2013.
26. **Fischer G, Tilg B, Modre R, Huiskamp GJ, Fetzer J, Rucker W, Wach P.** A bidomain model based BEM-FEM coupling formulation for anisotropic cardiac tissue. *Ann Biomed Eng* 28: 1229–1243, 2000.
27. **Gizzi A, Bernaschi M, Bini D, Cherubini C, Filippi S, Melchionna S, Succi S.** Three-band decomposition analysis of wall shear stress in pulsatile ows. *Phys Rev E* 83: 031902, 2011.
28. **Gizzi A, Cherry EM, Gilmour RF Jr, Luther S, Filippi S, Fenton FH.** Effects of pacing site and stimulation history on alternans dynamics and the development of complex spatiotemporal patterns in cardiac tissue. *Front Physiol* 4: 71, 2013.
29. **Gizzi A, Cherubini C, Migliori S, Alloni R, Portuesi R, Filippi S.** On the electrical intestine turbulence induced by temperature changes. *Phys Biol* 7: 16011, 2010.
30. **Gizzi A, Cherubini C, Pomella N, Persichetti P, Vasta M, Filippi S.** Computational modeling and stress analysis of columellar biomechanics. *J Mech Behav Biomed Mat* 15: 46–58, 2012.
31. **Hai CM, Murphy RA.** Cross-bridge phosphorylation and regulation of latch state in smooth muscle. *J Appl Physiol* 254: C99–C106, 1988.
32. **Holte K, Kehlet H.** Postoperative ileus: a preventable event. *Br J Surg* 87: 1480–1493, 2000.

32a. **Holzapfel GA.** *Nonlinear Solid Mechanics: A Continuum Approach for Engineering*. Chichester, UK: Wiley, 2006.

33. **Kito Y, Suzuki H.** Effects of temperature on pacemaker potentials in the mouse small intestine. *Pflügers Arch* 454: 263–275, 2007.
34. **Kito Y.** The functional role of intramuscular interstitial cells of Cajal in the stomach. *J Smooth Muscle Res* 47: 47–53, 2011.
35. **García-Valdecasas JC, Piqué JM, Delgado S, Campo E, Bordas JM, Taurá P, Grande L, Fuster J, Pacheco JLe, .**Short-term outcome analysis of randomized study comparing laparoscopic versus open colectomy for colon cancer. *Surg Endosc* 9: 1101–1105, 1995.
36. **Lammers WJ.** Arrhythmias in the gut. *Neurogastroenterol Motil* 25: 353–357, 2013.
37. **Langer GA, Brady AJ.** The effects of temperature upon contraction and ionic exchange in rabbit ventricular myocardium. Relation to control the active state. *J Gen Physiol* 52: 682–713, 1968.
38. **Lees-Green R, Gibbons SJ, Farrugia G, Sneyd J, Cheng LK.** Computational modeling of anoctamin 1 calcium-activated chloride channels as pacemaker channels in interstitial cells of Cajal. *Am J Physiol Gastrointest Liver Physiol* 306: G711–G727, 2014.
39. **Lin AS, Buist ML, Smith NP, Pullan AJ.** Modelling slow wave activity in the small intestine. *J Theor Biol* 242: 356–362, 2006.
40. **Livingston EH, Passaro EP Jr.** Postoperative ileus. *Dig Dis Sci* 35: 121–132, 1990.
41. **Luckey A, Livingston E, Taché Y.** Mechanisms and treatment of postoperative ileus. *Arch Surg* 138: 206–214, 2003.
42. **Murray JD.** *Mathematical Biology II: Spatial Models and Biomedical Applications*. Berlin: Springer, 2001.
43. **Murtada SC, Arner A, Holzapfel GA.** Experiments and mechanochemical modeling of smooth muscle contraction: significance of filament overlap. *J Theor Biol* 297: 176–186, 2012.
44. **Murtada SI, Kroon M, Holzapfel GA.** A calcium-driven mechanochemical model for prediction of force generation in smooth muscle. *Biomech Model Mechanobiol* 9: 749–762, 2010.
45. **Murtada SI, Kroon M, Holzapfel GA.** Modeling the dispersion effects of contractile fibers in smooth muscles. *J Mech Phys Sol* 58: 165–182, 2010.
46. **Mustafa SM, Thulesius O.** Cooling-induced bladder contraction, studies on isolated detrusor muscle preparations in the rat. *Urology* 53: 653–657, 1999.
47. **Mustafa SM, Thulesius O.** Cooling-induced gastrointestinal smooth muscle contractions in the rat. *Fundam Clin Pharmacol* 15: 349–354, 2001.
48. **O'Grady G, Angeli TR, Du P, Lahr C, Lammers WJ, Windsor JA, Abell TL, Farrugia G, Pullan AJ, Cheng LK.** Abnormal initiation and conduction of slow-wave activity in gastroparesis, defined by high-resolution electrical mapping. *Gastroenterology* 143: 589–598, 2012.
49. **O'Grady G, Du P, Cheng LK, Egbuji JU, Lammers WJ, Windsor JA, Pullan AJ.** Origin and propagation of human gastric slow-wave activity defined by high-resolution mapping. *Am J Physiol Gastrointest Liver Physiol* 299: G585–G592, 2010.
50. **O'Grady G, Du P, Paskaranandavadivel N, Angeli TR, Lammers WJ, Asirvatham SJ, Windsor JA, Farrugia G, Pullan AJ, Cheng LK.** Rapid high-amplitude circumferential slow wave propagation during normal gastric pacemaking and dysrhythmias. *Neurogastroenterol Motil* 24: e299–e312, 2012.
51. **Pandolfi A, Vasta M.** Fiber distributed hyperelastic modeling of biological tissues. *Mech Mat* 44: 151–162, 2012.
52. **Paskaranandavadivel N, Gao J, Du P, O'Grady G, Cheng LK.** Automated classification and identification of slow wave propagation patterns in gastric dysrhythmia. *Ann Biomed Eng* 42: 177–192, 2014.
53. **Portuesi R, Cherubini C, Gizzi A, Buzzetti R, Pozzilli P, Filippi S.** A stochastic mathematical model to study the autoimmune progression towards type 1 diabetes. *Diabetes Metab Res Rev* 29: 194–203, 2013.
54. **Pullan A, Cheng L, Yassi R, Buist M.** Modelling gastrointestinal bioelectric activity. *Prog Biophys Mol Biol* 85: 523–550, 2004.
55. **Pumir A, Sinha S, Sridhar S, Argentina M, Hörning M, Filippi S, Cherubini C, Luther S, Krinsky V.** Wave-train-induced termination of weakly anchored vortices in excitable media. *Phys Rev E* 81: 010901, 2010.
56. **Rachev A, Hayashi K.** Theoretical study of the effects of vascular smooth muscle contraction on strain and stress distributions in arteries. *Ann Biomed Eng* 27: 459–468, 1999.
57. **Rychter J, Clavé P.** Intestinal inflammation in postoperative ileus: pathogenesis and therapeutic targets. *Gut* 62: 1534–1535, 2013.
58. **Sacks MS, Sun W.** Multiaxial mechanical behavior of biological materials. *Annu Rev Biomed Eng* 5: 251–284, 2003.
59. **Sacks MS.** Biaxial mechanical evaluation of planar biological materials. *J Elasticity* 61: 199–246, 2000.
60. **Sammour T, Kahokehr A, Hayes J, Hulme-Moir M, Hill AG.** Warming and humidification of insufflation carbon dioxide in laparoscopic colonic surgery: a double-blinded randomized controlled trial. *Ann Surg* 251: 1024–1033, 2010.
61. **Sayani FA, Keenan CM, Van Sickle MD, Amundson KR, Parr EJ, Mathison RD, MacNaughton WK, Braun JE, Sharkey KA.** The expression and role of Fas ligand in intestinal inflammation. *Neurogastroenterol Motil* 16: 61–74, 2004.
62. **Senagore AJ, Luchtefeld MA, Mackeigan JM, Mazier WP.** Open colectomy versus laparoscopic colectomy: are there differences? *Am Surg* 59: 549–553, 1993.
63. **Somarajan S, Muszynski ND, Obioha C, Richards WO, Bradshaw LA.** Biomagnetic and bioelectric detection of gastric slow wave activity in normal human subjects–a correlation study. *Physiol Meas* 33: 1171–1179, 2012.
64. **Stålhand J, Klarbring A, Holzapfel GA.** A mechanochemical 3D continuum model for smooth muscle contraction under finite strains. *J Theor Biol* 268: 120–130, 2011.
65. **Stålhand J, Klarbring A, Holzapfel GA.** Smooth muscle contraction: mechanochemical formulation for homogeneous finite strains. *Prog Biophys Mol Biol* 96: 465–481, 2008.
66. **Story SK, Chamberlain RS.** A comprehensive review of evidence-based strategies to prevent and treat postoperative ileus. *Dig Surg* 26: 265–275, 2009.
67. **Sun W, Sacks MS, Scott MJ.** Effects of boundary conditions on the estimation of the planar biaxial mechanical properties of soft tissues. *J Biomech Eng* 127: 709–715, 2005.
68. **Takaki M.** Gut pacemaker cells: the interstitial cells of Cajal (ICC). *J Smooth Muscle Res* 39: 137–161, 2003.
69. **van Bree SH, Cailotto C, Di Giovangiulio M, Jansen E, van der Vliet J, Costes L, Depoortere I, Gomez-Pinilla PJ, Matteoli G, Boeckxstaens GE.** Systemic inflammation with enhanced brain activation contributes to more severe delay in postoperative ileus. *Neurogastroenterol Motil* 25: e540–e549, 2013.

Alessandro Loppini

70. **Vasta M, Pandolfi A, Gizzi A.** A fiber distributed model of biological tissues. *Procedia IUTAM* 6: 79–86, 2013.
71. **Wilson JP.** Postoperative motility of the large intestine in man. *Gut* 16: 689–692, 1975.
72. **Wu CC, Lin YM, Gao J, Winston JH, Cheng LK, Shi XZ.** Are interstitial cells of Cajal involved in mechanical stress-induced gene expression and impairment of smooth muscle contractility in bowel obstruction? *PLOS ONE* 8: e76222, 2013.
73. **Xue S, Valdez DT, Tremblay L, Collman PI, Diamant NE.** Electrical slow wave activity of the cat stomach: its frequency gradient and the effect of indomethacin. *Neurogastroenterol Motil* 7: 157–167, 1995.
74. **Young J, Riviére B, Cox CS Jr, Uray K.** A mathematical model of intestinal oedema formation. *Math Med Biol* 31: 1–15, 2014.
75. **Yu TC, Hamill JK, Liley A, Hill AG.** Warm, humidified carbon dioxide gas insufflation for laparoscopic appendicectomy in children: a double-blinded randomized controlled trial. *Ann Surg* 257: 44–53, 2013.

Alessandro Loppini

Spatio-Temporal Correlation of Paced Cardiac Tissue

Simonetta Filippi*, Christian Cherubini, Alessio Gizzi, Alessandro Loppini, and Flavio H. Fenton

***Abstract*—Complex spatiotemporal alternans patterns of action potential duration have been recently observed in large mammalian hearts. Multiple routes between the occurrence of high-order rhythms (discordant alternans) and their transition to chaos (ventricular fibrillation) have also been reported. In this work we extend the analysis of voltage optical mapped signals from right canine ventricles during rhythmic and arrhythmic regimes. We evaluate the correlation length between pairs of points of large spatial domains to extract the typical length scale of the system in different regimes. Critical scale length transitions are discussed with respect to regular pacing frequencies and onset of fibrillation.**

I. INTRODUCTION

Biological excitable systems show many different rhythms. How these are generated, coupled and affected by external and internal dynamics is of interest both from the experimental and theoretical points of view [1], [2]. The heart is not an exception, showing several spatiotemporal complex dynamics from the microscopic cellular level up to the macroscopic tissue scale [3], [4].

Cardiac arrhythmias, and fibrillation in particular, are well known to be supported by increased dispersion of repolarization, inducing high variations in the refractory period and in the conduction velocity [5]. Moreover, experimental and theoretical evidences have recently linked the spatiotemporal dispersion of the action potential duration (APD) to oscillations of the T wave in the electrocardiogram signal, highlighting the clinical importance of these quantities in risk stratification for arrhythmic sudden cardiac death [6], [7], [8], [9]. Dispersion of APD and period-doubling bifurcations are usually recorded via fast periodic stimulations of ventricular tissues, resulting in long-short alternations of APD [10], [11]. Discordant alternans dynamics in space are supported by large gradients of repolarization and can eventually induce conduction blocks with the subsequent initiation of tachycardia and fibrillation [12].

Quantitative indicators for spatial order have been proposed within the context of ventricular fibrillation [13], [14], [15]. However, since most of the studies addressing cardiac alternans have been conducted in small ventricular tissues or monolayers, our understanding of these complex spatiotemporal dynamics present still several unknowns.

In the present study, we characterize the transition from normal rhythm to concordant/discordant alternans to sustained fibrillation in terms of spatiotemporal correlation length measures. The main goal is to investigate the transition from regular to chaotic regimes in spatially extended optical mapped canine ventricular preparations. Possible regularities within chaotic systems are discussed adopting different correlation functions in search of universal behaviors [16].

Research partially supported by the International Center for Relativistic Astrophysics Network (ICRANet) and by Gruppo Nazionale per la Fisica Matematica (GNFM, INdAM).

C. C., S. F., A. G., A. L. are with the University Campus Bio-Medico of Rome, Italy (*corresponding author e-mail: s.filippi@gmail.com).

F. H. F. is with the School of Physics, Georgia Institute of Technology, USA (e-mail: flavio.fenton@physics.gatech.edu).

II. METHODS

Fluorescence action potential (AP) optical mapping experimental procedures were approved by the Institutional Animal Care and Use Committee of the Center for Animal Resources and Education at Cornell University (tissue preparation has been previously described [11], [17]).

In order to characterize the response of cardiac preparations at different pacing frequencies a two-point spatiotemporal correlation measure for increasing distances was computed. Specifically, we evaluated the Pearson product-moment correlation index [18], R, between different voltage time series extracted from selected points at distance $\vec{r}$:

$$R(\vec{r}) = \frac{\mathrm{cov}(V_A, V_B)}{\sigma_A \sigma_B} = \frac{\langle (V_A - \langle V_A \rangle)(V_B - \langle V_B \rangle) \rangle}{\sigma_A \sigma_B}, \quad (1)$$

where $V_A = V(\vec{x}, t)$, $V_B = V(\vec{x} + \vec{r}, t)$. The correlation index at distance $\vec{r}$ was then averaged in the spatial domain. Information about the correlation length are extracted from the exponential decay of the correlation index (linear range in the semi-log plot) at increasing distances between selected points, i.e.:

$$R(\vec{r}) \propto \exp\left(-\frac{\|\vec{r}\|}{L_0}\right), \quad (2)$$

where L_0 represents the sought correlation length.

III. RESULTS

Correlation length values, L_0, decrease reducing the pacing period from $550\,ms$ (normal rhythm) to $100\,ms$ (fibrillation inducing frequency). Variability within ventricular preparations was observed but a net reduction of the correlation length dispersion was obtained at shorter pacing periods highlighting a significant exponential decay. A long-range interaction of the plane wave is characteristic of longer CLs on the other hand. Interestingly, during sustained fibrillation the correlation length falls down to an average value of about $1.0\,cm$ in agreement with [14], [19]. Moreover, the fact that no more than three spirals are contemporary present within the mapped ventricle corroborates the obtained L_0 during fibrillation regimes. Figure 1 shows a representative example of the Pearson correlation function analysis and relative exponential decay region performed during endocardial sustained fibrillation.

978-1-4799-3969-5/14/$31.00

Alessandro Loppini

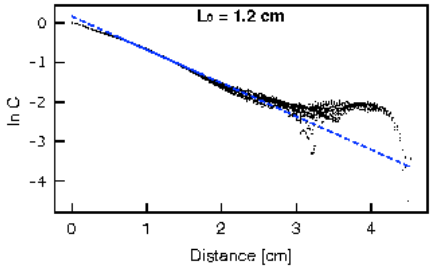

Fig. 1: Pearson index analysis (points distribution, C_{ij}) and correlation length slope, L_0, (blue line) for a representative example during sustained ventricular fibrillation.

IV. DISCUSSION & FUTURE PERSPECTIVES

The correlation length is a well known statistical indicator of spatial organization of physical processes [20], [21]. Higher values of correlation length are associated with larger structures and, apparently, more organized behavior. Smaller values are usually associated with local coherent states. However, the interpretation of spatial correlation is not restricted to a certain physical system nor linked to a particular mechanism (i.e. spiral waves) [14], [16], [22]. Several studies proposed such a tool to analyze cardiac fibrillation [3], [23]. The chaotic nature of electrochemical waves in the heart and the quantification of the degree of spatial organization during ventricular fibrillation, in fact, are fundamental for understanding and developing useful models finding effective clinical treatments.

Adopting a similar reasoning we characterize the spatial scales of correlations during the transition from normal rhythm, passing through a period doubling bifurcation ending with sustained ventricular fibrillation upon the stimulation frequency as control parameter. Critical values of pacing periods and correlation length were identified i) at the onset of discordant alternans, CL $=\sim 200\,ms$ with $L_0 \sim 10\,cm$, and ii) at the onset of fibrillation, CL $< 100\,ms$ with $L_0 < 3\,cm$. In future studies, we aim at performing correlation length analyses in biventricular preparations characterizing the double voltage-calcium signals. Numerical simulations will be also performed [24], [25] testing realistic three-dimensional geometries introducing tissue heterogeneity, anisotropy and stochasticity [26].

REFERENCES

[1] A. T. Winfree, *When Time Breaks Down: The Three-Dimensional Dynamics of Electrochemical Waves and Cardiac Arrhythmias*, Princeton University Press, 1987.

[2] L. Glass, and M. C. Mackey, *From clocks to chaos: The rhythms of life*. Princeton University Press, 1988.

[3] M. R. Guevara, L. Glass, and A. Shrier, "Phase locking, period-doubling bifurcations, and irregular dynamics in periodically stimulated cardiac cells," *Science*, vol. 214, pp. 1350–1353, December 1981.

[4] R. Perez, and L. Glass, "Bistability, period doubling bifurcations and chaos in a periodically forced oscillator," *Physics Letters A*, vol. 90, pp. 441–443, September 1982.

[5] J. Han, and G. K. Moe, "Nonuniform recovery of excitability in ventricular muscle," *Circulation Research*, vol. 14, pp. 44–60, January 1964.

[6] J. M. Pastore, S. D. Girouard, K. R. Laurita, F. G. Akar, and D. S. Rosenbaum, "Mechanism linking T-wave alternans to the genesis of cardiac fibrillation," *Circulation*, vol. 99, pp. 1385–1394, March 1999.

[7] Z. Qu, A. Garfinkel, P. S. Chen, and J. N. Weiss, "Mechanisms of discordant alternans and induction of reentry in simulated cardiac tissue," *Circulation*, vol. 102, pp. 1664–1670, October 2000.

[8] R. L. Verrier, T. Klingenheben, M. Malik, N. El-Sherif, D. V. Exner, S. H. Hohnloser, T. Ikeda, J. P. Martinez, S. M. Narayan, T. Nieminen, and D. S. Rosenbaum, "Microvolt T-wave alternans: physiological basis, methods of measurement, and clinical utility–consensus guideline by international society for holter and Noninvasive Electrocardiology," *Journal of the American College of Cardiology*, vol. 58, pp. 1309–1324, September 2011.

[9] A. Burykin, M. D. Costa, L. Citi, and A. L. Goldberger, "Dynamical density delay maps: simple, new method for visualising the behaviour of complex systems," *BMC Medical Informatics and Decision Making*, vol. 14, pp. 6, January 2014.

[10] B. G. Mitrea, M. Wellner, and A. M. Pertsov, "Monitoring intramyocardial reentry using alternating transillumination," *Engineering in Medicine and Biology Society, 2009. EMBC 2009. Annual International Conference of the IEEE*, pp. 4194–4197, 2009.

[11] A. Gizzi, E. M. Cherry, R. F. Gilmour, Jr, S. Luther, S. Filippi, and F. H. Fenton, "Effects of pacing site and stimulation history on alternans dynamics and the development of complex spatiotemporal patterns in cardiac tissue," *Frontiers in Physiology*, vol. 4, pp. 71, April 2013.

[12] J. J. Fox, M. L. Riccio, F. Hua, E. Bodenschatz, and R. F. Gilmour, Jr., "Spatiotemporal transition to conduction block in canine ventricle," *Circulation Research*, vol. 90, pp. 289–296, February 2002.

[13] D. A. Egolf, and H. S. Greenside, "Relation between fractal dimension and spatial correlation length for extensive chaos," *Nature*, vol. 369, pp. 129–131, 1994.

[14] P. V. Bayly, E. E. Johnson, P. D. Wolf, H. S. Greenside, W. M. Smith, and R. E. Ideker, "A quantitative measurement of spatial order in ventricular fibrillation," *Journal of Cardiovascular Electrophysiology*, vol. 4, pp. 533–546, 1993.

[15] M. Yashima, Y. H. Kim, S. Armin, T. J. Wu, Y. Miyauchi, W. J. Mandel, P. S. Chen, and H. S. Karagueuzian, "On the mechanism of the probabilistic nature of ventricular defibrillation threshold," *American Journal of Physiology and Heart and Circulation Physiology*, vol. 284, pp. H249–255, September 2002.

[16] Frisch U., "Turbulence: the Legacy of A. N. Kolmogorov", Cambridge University Press (1995).

[17] S. Luther, F. H. Fenton, B. G. Kornreich, A. Squires, P. Bittihn, D. Hornung, M. Zabel, J. Flanders, A. Gladuli, L. Campoy, E. M. Cherry, G. Luther, G. Hasenfuss, V. I. Krinsky, A. Pumir, R. F. Gilmour, and E. Bodenschatz, "Low-energy control of electrical turbulence in the heart," *Nature*, vol. 475, pp. 235–239, July 2011.

[18] J. L. Rodgers, and W. A. Nicewander, "Thirteen Ways to Look at the Correlation Coefficient," *The American Statistician*, vol. 42, pp. 59–66, February 1988.

[19] R. S. Damle, N. M. Kanaan, N. S. Robinson, Y. Ge, J. J. Goldberger, and A. H. Kadish, "Spatial and temporal linking of epicardial activation patterns during ventricular fibrillation in dogs: evidence for underlying spatial organization," *Circulation*, vol. 86, pp. 1547–1558, 1992.

[20] J. L. Lumley, "Stochastic tools in turbulence," Academic Press, New York, 1970.

[21] D. Palumbo, "Determining correlation and coherence lengths in turbulent boundary layer flight data," *Journal of Sound and Vibration*, vol. 331, pp. 3721–3737, July 2012.

[22] D. A. Egolf, I. V. Melnikov, W. Pesch, and R. E. Ecke, "Mechanisms of extensive spatiotemporal chaos in Rayleigh–Bénard convection," *Nature*, vol. 404, pp. 733–736, April 2000.

[23] A. L. Goldberger, V. Bhargava, B. J. West, and A. J. Mandell, "Some observations on the question: Is ventricular fibrillation chaos?," *Physica D*, vol. 19, pp. 282–289, 1986.

[24] F. H. Fenton, A. Gizzi, C. Cherubini, N. Pomella, and S. Filippi, "Role of temperature on nonlinear cardiac dynamics," *Physical Review E*, vol. 87, pp. 042717, 2013.

[25] S. Filippi, A. Gizzi, C. Cherubini, S. Luther, and F. H. Fenton, "Mechanistic insights into hypothermic ventricular fibrillation: the role of temperature and tissue size," *Europace*, vol. 16, pp. 424–434, 2014.

[26] A. Gizzi, M. Vasta, and A. Pandolfi, "Modeling collagen recruitment in hyperelastic bio-material models with statistical distribution of the fiber orientation," *International Journal of Engineering Science*, vol. 78, pp. 48–60, March 2014.

Alessandro Loppini

Bibliography

[1] Albert Baert. *Radiology of the Pancreas*. Springer Berlin Heidelberg, Berlin, Heidelberg, 1994. ISBN 978-3-642-97489-2.

[2] G. C. Balboni. *Anatomia umana*. Edi. Ermes, Milano, 2000. ISBN 88-7051-075-1.

[3] http://www.kumc.edu/instruction/medicine/anatomy/histoweb/endo/endo.htm.

[4] Xiaojun Wang, Ryosuke Misawa, Mark C Zielinski, Peter Cowen, Junghyo Jo, Vipul Periwal, Camillo Ricordi, Aisha Khan, Joel Szust, Junhui Shen, et al. Regional differences in islet distribution in the human pancreas–preferential beta-cell loss in the head region in patients with type 2 diabetes. *PLoS One*, 8(6), 2013.

[5] Donald J Steiner, Abraham Kim, Kevin Miller, and Manami Hara. Pancreatic islet plasticity: interspecies comparison of islet architecture and composition. *Islets*, 2 (3):135–145, 2010.

[6] Elisabeth R Trimble, Philippe A Halban, Claes B Wollheim, and AE Renold. Functional differences between rat islets of ventral and dorsal pancreatic origin. *Journal of Clinical Investigation*, 69(2):405, 1982.

[7] William Montague. *Diabetes and the endocrine pancreas : a biochemical approach*. Croom Helm, London, 1983. ISBN 978-0-85664-888-5.

[8] Md. Shahidul Islam. *The islets of Langerhans*. Springer, Dordrecht London, 2010. ISBN 978-90-481-3270-6.

[9] Nils Wierup, Frank Sundler, and R Scott Heller. The islet ghrelin cell. *Journal of molecular endocrinology*, 52(1):R35–R49, 2014.

[10] Diabetes Mellitus. Diagnosis and classification of diabetes mellitus. *Diabetes care*, 28:S37, 2005.

[11] Sarah Wild, Gojka Roglic, Anders Green, Richard Sicree, and Hilary King. Global prevalence of diabetes estimates for the year 2000 and projections for 2030. *Diabetes care*, 27(5):1047–1053, 2004.

Alessandro Loppini

[12] World Health Organization et al. Global health estimates: Deaths by cause, age, sex and country, 2000-2012. *Geneva, WHO*, 2014.

[13] *Global status report on noncommunicable diseases 2014*. World Health Organization, Geneva, Switzerland, 2014. ISBN 978-92-4-156485-4.

[14] *Diabetes Atlas - 7th Edition*. International Diabetes Federation, 2015. Available at http://www.diabetesatlas.org/component/attachments/?task=download&id=116.

[15] Jin-Xiong She. Susceptibility to type i diabetes: Hla-dq and dr revisited. *Immunology today*, 17(7):323–329, 1996.

[16] Marc Y Donath, Joachim Størling, Kathrin Maedler, and Thomas Mandrup-Poulsen. Inflammatory mediators and islet β-cell failure: a link between type 1 and type 2 diabetes. *Journal of molecular medicine*, 81(8):455–470, 2003.

[17] Houria Ounissi-Benkalha and Constantin Polychronakos. The molecular genetics of type 1 diabetes: new genes and emerging mechanisms. *Trends in molecular medicine*, 14(6):268–275, 2008.

[18] ST Bennett, AM Lucassenz, SCL Gough, EE Powell, DE Undlien, LE Pritchardl, ME Merriman, Y Kawaguchi, MJ Dronsfield, F Pociots, et al. Susceptibility to human type 1 diabetes at iddm2 is determined by tandem repeat variation at the insulin gene minisatellite locus. *Nature genetics*, 9:284, 1995.

[19] Lorenza Nisticò, Raffaella Buzzetti, Lynn E Pritchard, Bart Van der Auwera, Claudio Giovannini, Emanuele Bosi, Maria Teresa Martinez Larrad, Manuel Serrano Rios, CC Chow, Clive S Cockram, et al. The ctla-4 gene region of chromosome 2q33 is linked to, and associated with, type 1 diabetes. *Human molecular genetics*, 5(7):1075–1080, 1996.

[20] Miriam Cnop, Nils Welsh, Jean-Christophe Jonas, Anne Jörns, Sigurd Lenzen, and Decio L Eizirik. Mechanisms of pancreatic β-cell death in type 1 and type 2 diabetes many differences, few similarities. *Diabetes*, 54(suppl 2):S97–S107, 2005.

[21] Michael Stumvoll, Barry J Goldstein, and Timon W van Haeften. Type 2 diabetes: principles of pathogenesis and therapy. *The Lancet*, 365(9467):1333–1346, 2005.

[22] Ali H Mokdad, Barbara A Bowman, Earl S Ford, Frank Vinicor, James S Marks, and Jeffrey P Koplan. The continuing epidemics of obesity and diabetes in the united states. *Jama*, 286(10):1195–1200, 2001.

[23] James Keener. *Mathematical physiology*. Springer, New York, 1998. ISBN 0-387-98381-3.

Alessandro Loppini

[24] Christof Koch. *Biophysics of computation information processing in single neurons*. Oxford University Press, New York, 1999. ISBN 0-19-510491-9.

[25] Christopher Fall. *Computational cell biology*. Springer, New York, 2002. ISBN 978-0-387-95369-4.

[26] Alan L Hodgkin and Andrew F Huxley. A quantitative description of membrane current and its application to conduction and excitation in nerve. *The Journal of physiology*, 117(4):500–544, 1952.

[27] Daniel Gillespie. *Markov processes : an introduction for physical scientists*. Academic Press, Boston, 1992. ISBN 978-0-12-283955-9.

[28] Frances M Ashcroft and Patrik Rorsman. Electrophysiology of the pancreatic β-cell. *Progress in biophysics and molecular biology*, 54(2):87–143, 1989.

[29] E Bittar. *The biology of the pancreatic β-cell*. JAI Press, Stamford, Conn, 1999. ISBN 0-7623-0547-9.

[30] Md. Shahidul Islam. *The islets of Langerhans*. Springer, Dordrecht London, 2010. ISBN 978-90-481-3270-6.

[31] Illani Atwater, Christine M Dawson, B Ribalet, and E Rojas. Potassium permeability activated by intracellular calcium ion concentration in the pancreatic beta-cell. *The Journal of physiology*, 288(1):575–588, 1979.

[32] Teresa Ree Chay and Joel Keizer. Minimal model for membrane oscillations in the pancreatic beta-cell. *Biophysical journal*, 42(2):181, 1983.

[33] Arthur Sherman, John Rinzel, and Joel Keizer. Emergence of organized bursting in clusters of pancreatic beta-cells by channel sharing. *Biophysical journal*, 54(3): 411, 1988.

[34] Sven O Göpel, Takahiro Kanno, Sebastian Barg, Lena Eliasson, Juris Galvanovskis, Erik Renström, and Patrik Rorsman. Activation of ca2+-dependent k+ channels contributes to rhythmic firing of action potentials in mouse pancreatic β cells. *The Journal of general physiology*, 114(6):759–770, 1999.

[35] PB Goforth, R Bertram, FA Khan, M Zhang, A Sherman, and LS Satin. Calcium-activated k+ channels of mouse β-cells are controlled by both store and cytoplasmic ca2+ experimental and theoretical studies. *The Journal of general physiology*, 120(3):307–322, 2002.

Alessandro Loppini

[36] Leonid E Fridlyand, N Tamarina, and Louis H Philipson. Bursting and calcium oscillations in pancreatic β-cells: specific pacemakers for specific mechanisms. *American Journal of Physiology-Endocrinology and Metabolism*, 299(4): E517–E532, 2010.

[37] Philippe Detimary, Patrick Gilon, and J Henquin. Interplay between cytoplasmic ca2+ and the atp/adp ratio: a feedback control mechanism in mouse pancreatic islets. *Biochem. J*, 333:269–274, 1998.

[38] Jean-François Rolland, Jean-Claude Henquin, and Patrick Gilon. Feedback control of the atp-sensitive k+ current by cytosolic ca2+ contributes to oscillations of the membrane potential in pancreatic β-cells. *Diabetes*, 51(2):376–384, 2002.

[39] Gerhard Magnus and Joel Keizer. Model of β-cell mitochondrial calcium handling and electrical activity. i. cytoplasmic variables. *American Journal of Physiology-Cell Physiology*, 274(4):C1158–C1173, 1998.

[40] Keith Tornheim. Are metabolic oscillations responsible for normal oscillatory insulin secretion? *Diabetes*, 46(9):1375–1380, 1997.

[41] Richard Bertram, Leslie S Satin, Morten Gram Pedersen, Dan S Luciani, and Arthur Sherman. Interaction of glycolysis and mitochondrial respiration in metabolic oscillations of pancreatic islets. *Biophysical journal*, 92(5):1544–1555, 2007.

[42] Richard Bertram, Arthur Sherman, and Leslie S Satin. Metabolic and electrical oscillations: partners in controlling pulsatile insulin secretion. *American Journal of Physiology-Endocrinology And Metabolism*, 293(4):E890–E900, 2007.

[43] Leonid E Fridlyand, Natalia Tamarina, and Louis H Philipson. Modeling of ca2+ flux in pancreatic β-cells: role of the plasma membrane and intracellular stores. *American Journal of Physiology-Endocrinology and Metabolism*, 285(1): E138–E154, 2003.

[44] Hiroshi Kitasato, Rihei Kai, Wei-Guang Ding, and Mariko Omatsu-Kanbe. The intrinsic rhythmicity of spike-burst generation in pancreatic beta-cells and intercellular interaction within an islet. *The Japanese journal of physiology*, 46(5): 363–373, 1996.

[45] Yoshihisa Miwa and Yusuke Imai. Simulation of spike-burst generation and ca2+ oscillation in pancreatic beta-cells. *The Japanese journal of physiology*, 49(4): 353–364, 1999.

Alessandro Loppini

[46] Abdelilah Arredouani, Jean-Claude Henquin, and Patrick Gilon. Contribution of the endoplasmic reticulum to the glucose-induced [ca2+]c response in mouse pancreatic islets. *American Journal of Physiology-Endocrinology and Metabolism*, 282(5):E982–E991, 2002.

[47] Guy A Rutter. Nutrient–secretion coupling in the pancreatic islet β-cell: recent advances. *Molecular aspects of medicine*, 22(6):247–284, 2001.

[48] Teresa Ree Chay. Effects of extracellular calcium on electrical bursting and intracellular and luminal calcium oscillations in insulin secreting pancreatic beta-cells. *Biophysical journal*, 73(3):1673, 1997.

[49] Jennings F Worley, Margaret S McIntyre, Benjamin Spencer, Robert J Mertz, Michael W Roe, and Iain D Dukes. Endoplasmic reticulum calcium store regulates membrane potential in mouse islet beta-cells. *Journal of Biological Chemistry*, 269 (20):14359–14362, 1994.

[50] Melanie C Beauvois, Charafa Merezak, Jean-Christophe Jonas, Magalie A Ravier, Jean-Claude Henquin, and Patrick Gilon. Glucose-induced mixed [ca2+]c oscillations in mouse β-cells are controlled by the membrane potential and the serca3 ca2+-atpase of the endoplasmic reticulum. *American Journal of Physiology-Cell Physiology*, 290(6):C1503–C1511, 2006.

[51] Rosa M Santos, Luis M Rosario, Angel Nadal, Javier Garcia-Sancho, Bernat Soria, and Miguel Valdeolmillos. Widespread synchronous [ca2+]i oscillations due to bursting electrical activity in single pancreatic islets. *Pflügers Archiv*, 418(4): 417–422, 1991.

[52] Peter Bergsten, Eva Grapengiesser, Erik Gylfe, Anders Tengholm, and B Hellman. Synchronous oscillations of cytoplasmic ca2+ and insulin release in glucose-stimulated pancreatic islets. *Journal of Biological Chemistry*, 269(12):8749–8753, 1994.

[53] Francoise C Jonkers, Jean-Christophe Jonas, Patrick Gilon, and Jean-Claude Henquin. Influence of cell number on the characteristics and synchrony of ca2+ oscillations in clusters of mouse pancreatic islet cells. *The Journal of physiology*, 520 (3):839–849, 1999.

[54] Jonathan V Rocheleau, Glenn M Walker, W Steven Head, Owen P McGuinness, and David W Piston. Microfluidic glucose stimulation reveals limited coordination of intracellular ca2+ activity oscillations in pancreatic islets. *Proceedings of the National Academy of Sciences of the United States of America*, 101(35):12899–12903, 2004.

Alessandro Loppini

[55] DR Matthews, BA Naylor, RG Jones, GM Ward, and RC Turner. Pulsatile insulin has greater hypoglycemic effect than continuous delivery. *Diabetes*, 32(7):617–621, 1983.

[56] G Paolisso, S Sgambato, R Torella, M Varricchio, André Scheen, F D'onofrio, and PJ Lefebvre. Pulsatile insulin delivery is more efficient than continuous infusion in modulating islet cell function in normal subjects and patients with type 1 diabetes. *The Journal of Clinical Endocrinology & Metabolism*, 66(6):1220–1226, 1988.

[57] Cynthia L Stokes and John Rinzel. Diffusion of extracellular k+ can synchronize bursting oscillations in a model islet of langerhans. *Biophysical journal*, 65(2):597, 1993.

[58] Magalie A Ravier, Martin Güldenagel, Anne Charollais, Asllan Gjinovci, Dorothée Caille, Goran Söhl, Claes B Wollheim, Klaus Willecke, Jean-Claude Henquin, and Paolo Meda. Loss of connexin36 channels alters β-cell coupling, islet synchronization of glucose-induced ca2+ and insulin oscillations, and basal insulin release. *Diabetes*, 54(6):1798–1807, 2005.

[59] Andrew L Harris. Emerging issues of connexin channels: biophysics fills the gap. *Quarterly reviews of biophysics*, 34(03):325–472, 2001.

[60] A Harris and D Locke. Connexin biology: the role of gap junction in disease. *The Humana, Totowa, NJ, USA*, 2008.

[61] Goran Söhl and Klaus Willecke. Gap junctions and the connexin protein family. *Cardiovascular research*, 62(2):228–232, 2004.

[62] Carville G Bevans and Andrew L Harris. Direct high affinity modulation of connexin channel activity by cyclic nucleotides. *Journal of Biological Chemistry*, 274 (6):3720–3725, 1999.

[63] Gary S Goldberg, Paul D Lampe, and Bruce J Nicholson. Selective transfer of endogenous metabolites through gap junctions composed of different connexins. *Nature Cell Biology*, 1(7):457–459, 1999.

[64] Gary S Goldberg, Alonso P Moreno, and Paul D Lampe. Gap junctions between cells expressing connexin 43 or 32 show inverse permselectivity to adenosine and atp. *Journal of Biological Chemistry*, 277(39):36725–36730, 2002.

[65] S Bavamian, P Klee, A Britan, C Populaire, D Caille, J Cancela, A Charollais, and P Meda. Islet-cell-to-cell communication as basis for normal insulin secretion. *Diabetes, Obesity and Metabolism*, 9(s2):118–132, 2007.

Alessandro Loppini

[66] Romain Hamelin, Florent Allagnat, Jacques-Antoine Haefliger, and Paolo Meda. Connexins, diabetes and the metabolic syndrome. *Current Protein and Peptide Science*, 10(1):18–29, 2009.

[67] Domenico Bosco, Jacques-Antoine Haefliger, and Paolo Meda. Connexins: key mediators of endocrine function. *Physiological reviews*, 91(4):1393–1445, 2011.

[68] Martha Perez-Armendariz, Christine Roy, David C Spray, and MV Bennett. Biophysical properties of gap junctions between freshly dispersed pairs of mouse pancreatic beta cells. *Biophysical journal*, 59(1):76, 1991.

[69] A Rafacho, LP Roma, SR Taboga, AC Boschero, and JR Bosqueiro. Dexamethasone-induced insulin resistance is associated with increased connexin 36 mrna and protein expression in pancreatic rat islets. *Canadian journal of physiology and pharmacology*, 85(5):536–545, 2007.

[70] Paolo Meda, Alain Perrelet, and Lelio Orci. Increase of gap junctions between pancreatic b-cells during stimulation of insulin secretion. *The Journal of cell biology*, 82(2):441–448, 1979.

[71] Florent Allagnat, David Martin, Daniele F Condorelli, Gérard Waeber, and Jacques-Antoine Haefliger. Glucose represses connexin36 in insulin-secreting cells. *Journal of cell science*, 118(22):5335–5344, 2005.

[72] Florent Allagnat, Florian Alonso, David Martin, Amar Abderrahmani, Gérard Waeber, and Jacques-Antoine Haefliger. Icer-1γ overexpression drives palmitate-mediated connexin36 down-regulation in insulin-secreting cells. *Journal of Biological Chemistry*, 283(9):5226–5234, 2008.

[73] Stephanie Urschel, Thorsten Höher, Timm Schubert, Cantas Alev, Goran Söhl, Philipp Wörsdörfer, Takayuki Asahara, Rolf Dermietzel, Reto Weiler, and Klaus Willecke. Protein kinase a-mediated phosphorylation of connexin36 in mouse retina results in decreased gap junctional communication between aii amacrine cells. *Journal of biological chemistry*, 281(44):33163–33171, 2006.

[74] Linda S Musil and Daniel A Goodenough. Biochemical analysis of connexin43 intracellular transport, phosphorylation, and assembly into gap junctional plaques. *The Journal of cell biology*, 115(5):1357–1374, 1991.

[75] Paul D Lampe. Analyzing phorbol ester effects on gap junctional communication: a dramatic inhibition of assembly. *The Journal of Cell Biology*, 127(6):1895–1905, 1994.

Alessandro Loppini

[76] Maribel Elvira, JA Diez, Kevin K Wang, and Antonio Villalobo. Phosphorylation of connexin-32 by protein kinase c prevents its proteolysis by mu-calpain and m-calpain. *Journal of Biological Chemistry*, 268(19):14294–14300, 1993.

[77] Denis Salomon and Paolo Meda. Heterogeneity and contact-dependent regulation of hormone secretion by individual b cells. *Experimental cell research*, 162(2): 507–520, 1986.

[78] Domenico Bosco, Lelio Orci, and Paolo Meda. Homologous but not heterologous contact increases the insulin secretion of individual pancreatic b-cells. *Experimental cell research*, 184(1):72–80, 1989.

[79] P Meda, D Bosco, M Chanson, E Giordano, L Vallar, C Wollheim, and L Orci. Rapid and reversible secretion changes during uncoupling of rat insulin-producing cells. *Journal of Clinical Investigation*, 86(3):759, 1990.

[80] Françoise C Jonkers and Jean-Claude Henquin. Measurements of cytoplasmic ca2+ in islet cell clusters show that glucose rapidly recruits β-cells and gradually increases the individual cell response. *Diabetes*, 50(3):540–550, 2001.

[81] IJ Stamper, Elais Jackson, and Xujing Wang. Phase transitions in pancreatic islet cellular networks and implications for type-1 diabetes. *Physical Review E*, 89(1): 012719, 2014.

[82] Thomas H. Hraha, Matthew J. Westacott, Marina Pozzoli, Aleena M. Notary, P. Mason McClatchey, and Richard K. P. Benninger. Phase transitions in the multi-cellular regulatory behavior of pancreatic islet excitability. *PLoS Comput Biol*, 10(9):e1003819, 2014.

[83] Linda M Nguyen, Marina Pozzoli, Thomas H Hraha, and Richard KP Benninger. Decreasing cx36 gap junction coupling compensates for overactive katp channels to restore insulin secretion and prevent hyperglycemia in a mouse model of neonatal diabetes. *Diabetes*, 63(5):1685–1697, 2014.

[84] Jacques Philippe, Emanuele Giordano, Asllan Gjinovci, and Paolo Meda. Cyclic adenosine monophosphate prevents the glucocorticoid-mediated inhibition of insulin gene expression in rodent islet cells. *Journal of Clinical Investigation*, 90(6): 2228, 1992.

[85] N Belluardo, A Trovato-Salinaro, G Mudo, YL Hurd, and DF Condorelli. Structure, chromosomal localization, and brain expression of human cx36 gene. *Journal of neuroscience research*, 57(5):740–752, 1999.

Alessandro Loppini

[86] Yohan Bossé, Jean-Pierre Després, Yvon C Chagnon, Treva Rice, DC Rao, Claude Bouchard, Louis Pérusse, and Marie-Claude Vohl. Quantitative trait locus on 15q for a metabolic syndrome variable derived from factor analysis. *Obesity*, 15(3): 544–550, 2007.

[87] Yasumichi Mori, Shuichi Otabe, Christian Dina, Kazuki Yasuda, Céline Populaire, Cécile Lecoeur, Vincent Vatin, Emmanuelle Durand, Kazuo Hara, Terumasa Okada, et al. Genome-wide search for type 2 diabetes in japanese affected sib-pairs confirms susceptibility genes on 3q, 15q, and 20q and identifies two new candidate loci on 7p and 11p. *Diabetes*, 51(4):1247–1255, 2002.

[88] Jacques-Antoine Haefliger, David Martin, Dimitri Favre, Yannick Petremand, Lucia Mazzolai, Amar Abderrahmani, Paolo Meda, Gérard Waeber, and Florent Allagnat. Reduction of connexin36 content by icer-1 contributes to insulin-secreting cells apoptosis induced by oxidized ldl particles. *PloS one*, 8(1):e55198, 2013.

[89] Paolo Meda, P Halban, Alain Perrelet, AE Renold, and Lelio Orci. Gap junction development is correlated with insulin content in the pancreatic b cell. *Science*, 209(4460):1026–1028, 1980.

[90] F Allagnat, P Klee, M Peyrou, D Martin, A Charollais, D Caille, J-A Haefliger, and P Meda. The gap junctional protein connexin36 (cx36) protects pancreatic beta cells against cytotoxic attacks: a possible role in cytokine-mediated beta cell death. In *Diabetologia*, volume 50, pages S45–S45. SPRINGER 233 SPRING STREET, NEW YORK, NY 10013 USA, 2007.

[91] Philippe Klee, Florent Allagnat, Helena Pontes, Manon Cederroth, Anne Charollais, Dorothée Caille, Aurore Britan, Jacques-Antoine Haefliger, and Paolo Meda. Connexins protect mouse pancreatic β cells against apoptosis. *The Journal of clinical investigation*, 121(12):4870, 2011.

[92] Florent Allagnat, Philippe Klee, Alessandra K Cardozo, P Meda, and JA Haefliger. Connexin36 contributes to ins-1e cells survival through modulation of cytokine-induced oxidative stress, er stress and ampk activity. *Cell Death & Differentiation*, 20(12):1742–1752, 2013.

[93] P Rorsman and G Trube. Calcium and delayed potassium currents in mouse pancreatic beta-cells under voltage-clamp conditions. *The Journal of Physiology*, 374(1):531–550, 1986.

[94] Arthur Sherman and John Rinzel. Model for synchronization of pancreatic beta-cells by gap junction coupling. *Biophysical journal*, 59(3):547, 1991.

Alessandro Loppini

[95] Paul Smolen, John Rinzel, and Arthur Sherman. Why pancreatic islets burst but single beta cells do not. the heterogeneity hypothesis. *Biophysical journal*, 64(6): 1668, 1993.

[96] Junghyo Jo, Hyuk Kang, Moo Young Choi, and Duk-Su Koh. How noise and coupling induce bursting action potentials in pancreatic β-cells. *Biophysical journal*, 89(3):1534–1542, 2005.

[97] Morten Gram Pedersen. A comment on noise enhanced bursting in pancreatic β-cells. *Journal of theoretical biology*, 235(1):1–3, 2005.

[98] Arthur Sherman. Anti-phase, asymmetric and aperiodic oscillations in excitable cells—i. coupled bursters. *Bulletin of mathematical biology*, 56(5):811–835, 1994.

[99] Gerda De Vries, Arthur Sherman, and Hsiu-Rong Zhu. Diffusively coupled bursters: effects of cell heterogeneity. *Bulletin of mathematical biology*, 60(6): 1167–1200, 1998.

[100] Richard KP Benninger, Min Zhang, W Steven Head, Leslie S Satin, and David W Piston. Gap junction coupling and calcium waves in the pancreatic islet. *Biophysical journal*, 95(11):5048–5061, 2008.

[101] R Portuesi, C Cherubini, A Gizzi, R Buzzetti, P Pozzilli, and S Filippi. A stochastic mathematical model to study the autoimmune progression towards type 1 diabetes. *Diabetes/metabolism research and reviews*, 29(3):194–203, 2013.

[102] HP Meissner and H Schmelz. Membrane potential of beta-cells in pancreatic islets. *Pflügers Archiv*, 351(3):195–206, 1974.

[103] Stephan Speier, Asllan Gjinovci, Anne Charollais, Paolo Meda, and Marjan Rupnik. Cx36-mediated coupling reduces β-cell heterogeneity, confines the stimulating glucose concentration range, and affects insulin release kinetics. *Diabetes*, 56(4): 1078–1086, 2007.

[104] Alessandro Loppini, Antonio Capolupo, Christian Cherubini, Alessio Gizzi, Marta Bertolaso, Simonetta Filippi, and Giuseppe Vitiello. On the coherent behavior of pancreatic beta cell clusters. *Physics Letters A*, 378(44):3210–3217, 2014.

[105] Marta Bertolaso, Antonio Capolupo, Christian Cherubini, Simonetta Filippi, Alessio Gizzi, Alessandro Loppini, and Giuseppe Vitiello. The role of coherence in emergent behavior of biological systems. *Electromagnetic biology and medicine*, 34(2):138–140, 2015.

[106] Heinz-Otto Peitgen, Hartmut Jürgens, and Dietmar Saupe. *Chaos and fractals: new frontiers of science*. Springer Science & Business Media, 2006.

Alessandro Loppini

[107] Horace P Yuen. Two-photon coherent states of the radiation field. *Physical Review A*, 13(6):2226, 1976.

[108] Giuseppe Vitiello. Fractals, coherent states and self-similarity induced noncommutative geometry. *Physics Letters A*, 376(37):2527–2532, 2012.

[109] Giuseppe Vitiello. On the isomorphism between dissipative systems, fractal self-similarity and electrodynamics. toward an integrated vision of nature. *Systems*, 2 (2):203–216, 2014.

[110] Askold Perelomov. *Generalized coherent states and their applications*. Springer Science & Business Media, 2012.

[111] E Celeghini, S Demartino, S Desiena, Mario Rasetti, and G Vitiello. Quantum groups, coherent states, squeezing and lattice quantum mechanics. *Annals of Physics*, 241(1):50–67, 1995.

[112] Andraž Stožer, Marko Gosak, Jurij Dolenšek, Matjaž Perc, Marko Marhl, Marjan Slak Rupnik, and Dean Korošak. Functional connectivity in islets of langerhans from mouse pancreas tissue slices. *PLoS Comput Biol*, 9(2):e1002923, 2013.

[113] Giuseppe Vitiello. Fractals and the fock-bargmann representation of coherent states. In *Quantum Interaction*, pages 6–16. Springer, 2009.

[114] Giuseppe Vitiello. Coherent states, fractals and brain waves. *New Mathematics and Natural Computation*, 5(01):245–264, 2009.

[115] Francesco Guerra. Introduction to nelson stochastic mechanics as a model for quantum mechanics. In *The Foundations of Quantum Mechanics—Historical Analysis and Open Questions*, pages 339–355. Springer, 1995.

[116] Ken Kiyono, Zbigniew R Struzik, and Yoshiharu Yamamoto. Criticality and phase transition in stock-price fluctuations. *Physical review letters*, 96(6):068701, 2006.

[117] Debashish Chowdhury, Ludger Santen, and Andreas Schadschneider. Statistical physics of vehicular traffic and some related systems. *Physics Reports*, 329(4): 199–329, 2000.

[118] Giovani L Vasconcelos. First-order phase transition in a model for earthquakes. *Physical review letters*, 76(25):4865, 1996.

[119] Yamir Moreno, Romualdo Pastor-Satorras, and Alessandro Vespignani. Epidemic outbreaks in complex heterogeneous networks. *The European Physical Journal B-Condensed Matter and Complex Systems*, 26(4):521–529, 2002.

Alessandro Loppini

[120] Valentino Braitenberg and Almut Schüz. *Cortex: statistics and geometry of neuronal connectivity*. Springer Science & Business Media, 2013.

[121] Klaus Linkenkaer-Hansen, Vadim V Nikouline, J Matias Palva, and Risto J Ilmoniemi. Long-range temporal correlations and scaling behavior in human brain oscillations. *The Journal of neuroscience*, 21(4):1370–1377, 2001.

[122] Rudolph C Hwa and Thomas C Ferree. Scaling properties of fluctuations in the human electroencephalogram. *Physical Review E*, 66(2):021901, 2002.

[123] Walter J Freeman. A field-theoretic approach to understanding scale-free neocortical dynamics. *Biological cybernetics*, 92(6):350–359, 2005.

[124] Dietmar Plenz and Tara C Thiagarajan. The organizing principles of neuronal avalanches: cell assemblies in the cortex? *Trends in neurosciences*, 30(3):101–110, 2007.

[125] Christian Cherubini, Simonetta Filippi, Alessio Gizzi, and Alessandro Loppini. Role of topology in complex functional networks of beta cells. *Physical Review E*, 92(4):042702, 2015.

[126] Over Cabrera, Dora M Berman, Norma S Kenyon, Camillo Ricordi, Per-Olof Berggren, and Alejandro Caicedo. The unique cytoarchitecture of human pancreatic islets has implications for islet cell function. *Proceedings of the National Academy of Sciences of the United States of America*, 103(7):2334–2339, 2006.

[127] Catherine Bernard-Kargar and Alain Ktorza. Endocrine pancreas plasticity under physiological and pathological conditions. *Diabetes*, 50(suppl 1):S30, 2001.

[128] Sebastian Rieck and Klaus H Kaestner. Expansion of β-cell mass in response to pregnancy. *Trends in Endocrinology & Metabolism*, 21(3):151–158, 2010.

[129] Erwin Ilegems, Andrea Dicker, Stephan Speier, Aarti Sharma, Alan Bahow, Patrick Karlsson Edlund, Ingo B Leibiger, and Per-Olof Berggren. Reporter islets in the eye reveal the plasticity of the endocrine pancreas. *Proceedings of the National Academy of Sciences*, 110(51):20581–20586, 2013.

[130] Marcela Brissova, Michael J Fowler, Wendell E Nicholson, Anita Chu, Boaz Hirshberg, David M Harlan, and Alvin C Powers. Assessment of human pancreatic islet architecture and composition by laser scanning confocal microscopy. *Journal of Histochemistry & Cytochemistry*, 53(9):1087–1097, 2005.

[131] Alejandro Caicedo. Paracrine and autocrine interactions in the human islet: more than meets the eye. In *Seminars in cell & developmental biology*, volume 24, pages 11–21. Elsevier, 2013.

Alessandro Loppini

[132] Robin L Michaels and Judson D Sheridan. Islets of langerhans: dye coupling among immunocytochemically distinct cell types. *Science*, 214(4522):801–803, 1981.

[133] P Meda, RM Santos, and I Atwater. Direct identification of electrophysiologically monitored cells within intact mouse islets of langerhans. *Diabetes*, 35(2):232–236, 1986.

[134] Quan Zhang, Juris Galvanovskis, Fernando Abdulkader, Christopher J Partridge, Sven O Göpel, Lena Eliasson, and Patrik Rorsman. Cell coupling in mouse pancreatic β-cells measured in intact islets of langerhans. *Philosophical Transactions of the Royal Society of London A: Mathematical, Physical and Engineering Sciences*, 366(1880):3503–3523, 2008.

[135] Aparna Nittala, Soumitra Ghosh, and Xujing Wang. Investigating the role of islet cytoarchitecture in its oscillation using a new beta-cell cluster model. *PLoS One*, 2(10):e983, 2007.

[136] M Sahini and M Sahimi. *Applications of percolation theory*. CRC Press, 1994.

[137] Véronique Serre-Beinier, Domenico Bosco, Laurence Zulianello, Anne Charollais, Dorothée Caille, Eric Charpantier, Benoit R Gauthier, Giuseppe R Diaferia, Ben N Giepmans, Roberto Lupi, et al. Cx36 makes channels coupling human pancreatic β-cells, and correlates with insulin expression. *Human molecular genetics*, 18(3): 428–439, 2009.

[138] Martijn P Van Den Heuvel and Hilleke E Hulshoff Pol. Exploring the brain network: a review on resting-state fmri functional connectivity. *European Neuropsychopharmacology*, 20(8):519–534, 2010.

[139] Willem de Haan, Yolande AL Pijnenburg, Rob LM Strijers, Yolande van der Made, Wiesje M van der Flier, Philip Scheltens, and Cornelis J Stam. Functional neural network analysis in frontotemporal dementia and alzheimer's disease using eeg and graph theory. *BMC neuroscience*, 10(1):101, 2009.

[140] Cornelius J Stam. Functional connectivity patterns of human magnetoencephalographic recordings: a 'small-world'network? *Neuroscience letters*, 355(1):25–28, 2004.

[141] Rene Markovič, Andraž Stožer, Marko Gosak, Jurij Dolenšek, Marko Marhl, and Marjan Slak Rupnik. Progressive glucose stimulation of islet beta cells reveals a transition from segregated to integrated modular functional connectivity patterns. *Scientific reports*, 5, 2015.

Alessandro Loppini

[142] Alain Barrat, Marc Barthelemy, and Alessandro Vespignani. *Dynamical processes on complex networks*. Cambridge University Press, 2008.

[143] Stefano Boccaletti, Vito Latora, Yamir Moreno, Martin Chavez, and D-U Hwang. Complex networks: Structure and dynamics. *Physics reports*, 424(4):175–308, 2006.

[144] Patrick Gilon, Ruth M Shepherd, and Jean-Claude Henquin. Oscillations of secretion driven by oscillations of cytoplasmic ca2+ as evidences in single pancreatic islets. *Journal of Biological Chemistry*, 268(30):22265–22268, 1993.

[145] Albert-Laszlo Barabasi and Zoltan N Oltvai. Network biology: understanding the cell's functional organization. *Nature reviews genetics*, 5(2):101–113, 2004.

[146] Marten Scheffer, Stephen R Carpenter, Timothy M Lenton, Jordi Bascompte, William Brock, Vasilis Dakos, Johan Van De Koppel, Ingrid A Van De Leemput, Simon A Levin, Egbert H Van Nes, et al. Anticipating critical transitions. *science*, 338(6105):344–348, 2012.

[147] Jennie C Brand-Miller, Karola Stockmann, Fiona Atkinson, Peter Petocz, and Gareth Denyer. Glycemic index, postprandial glycemia, and the shape of the curve in healthy subjects: analysis of a database of more than 1000 foods. *The American journal of clinical nutrition*, 89(1):97–105, 2009.

[148] Bryan W Wolf, Phillip M Humphrey, Craig W Hadley, Kati S Maharry, Keith A Garleb, and Jeffrey L Firkins. Supplemental fructose attenuates postprandial glycemia in zucker fatty fa/fa rats. *The Journal of nutrition*, 132(6):1219–1223, 2002.

[149] Yuriy Yu Tarasevich and Steven C van der Marck. An investigation of site-bond percolation on many lattices. *International Journal of Modern Physics C*, 10(07): 1193–1204, 1999.

[150] Hawoong Jeong, Bálint Tombor, Réka Albert, Zoltan N Oltvai, and A-L Barabási. The large-scale organization of metabolic networks. *Nature*, 407(6804):651–654, 2000.

[151] Nabil Guelzim, Samuele Bottani, Paul Bourgine, and François Képès. Topological and causal structure of the yeast transcriptional regulatory network. *Nature genetics*, 31(1):60–63, 2002.

[152] Victor M Eguiluz, Dante R Chialvo, Guillermo A Cecchi, Marwan Baliki, and A Vania Apkarian. Scale-free brain functional networks. *Physical review letters*, 94(1):018102, 2005.

Alessandro Loppini

[153] Guillaume Marrelec, Alexandre Krainik, Hugues Duffau, Mélanie Pélégrini-Issac, Stéphane Lehéricy, Julien Doyon, and Habib Benali. Partial correlation for functional brain interactivity investigation in functional mri. *Neuroimage*, 32(1):228–237, 2006.

[154] Alberto De La Fuente, Nan Bing, Ina Hoeschele, and Pedro Mendes. Discovery of meaningful associations in genomic data using partial correlation coefficients. *Bioinformatics*, 20(18):3565–3574, 2004.

[155] Weijie Lin, Yafeng Wang, Heping Ying, Ying-Cheng Lai, and Xingang Wang. Consistency between functional and structural networks of coupled nonlinear oscillators. *Physical Review E*, 92(1):012912, 2015.

[156] Moitrayee Bhattacharyya, Soma Ghosh, and Saraswathi Vishveshwara. Protein structure and function: Looking through the network of side-chain interactions. *Current Protein and Peptide Science*, 17(1):4–25, 2016.

[157] Havva Kohestani and Alessandro Giuliani. Organization principles of biological networks: An explorative study. *Biosystems*, 141:31–39, 2016.

[158] Patrik Rorsman and Matthias Braun. Regulation of insulin secretion in human pancreatic islets. *Annual review of physiology*, 75:155–179, 2013.

[159] Stanley Misler, David W Barnett, Kevin D Gillis, and David M Pressel. Electrophysiology of stimulus-secretion coupling in human β-cells. *Diabetes*, 41(10): 1221–1228, 1992.

[160] Matthias Braun, Reshma Ramracheya, Martin Bengtsson, Quan Zhang, Jovita Karanauskaite, Chris Partridge, Paul R Johnson, and Patrik Rorsman. Voltage-gated ion channels in human pancreatic β-cells: electrophysiological characterization and role in insulin secretion. *Diabetes*, 57(6):1618–1628, 2008.

[161] Morten Gram Pedersen. A biophysical model of electrical activity in human β-cells. *Biophysical journal*, 99(10):3200–3207, 2010.

[162] Michela Riz, Matthias Braun, and Morten Gram Pedersen. Mathematical modeling of heterogeneous electrophysiological responses in human β-cells. *PLoS computational biology*, 10(1):e1003389, 2014.

[163] Jia Li, HY Shuai, Erik Gylfe, and Anders Tengholm. Oscillations of sub-membrane atp in glucose-stimulated beta cells depend on negative feedback from ca2+. *Diabetologia*, 56(7):1577–1586, 2013.

Alessandro Loppini

[164] Anne Wojtusciszyn, M Armanet, Philippe Morel, Thierry Berney, and Domenico Bosco. Insulin secretion from human beta cells is heterogeneous and dependent on cell-to-cell contacts. *Diabetologia*, 51(10):1843–1852, 2008.

[165] Ivan Quesada, Mariana G Todorova, Paloma Alonso-Magdalena, Marta Beltrá, Everardo M Carneiro, Franz Martin, Angel Nadal, and Bernat Soria. Glucose induces opposite intracellular ca2+ concentration oscillatory patterns in identified α-and β-cells within intact human islets of langerhans. *Diabetes*, 55(9):2463–2469, 2006.

[166] Robert A Ritzel, Juris J Meier, Chia-Yu Lin, Johannes D Veldhuis, and Peter C Butler. Human islet amyloid polypeptide oligomers disrupt cell coupling, induce apoptosis, and impair insulin secretion in isolated human islets. *Diabetes*, 56(1): 65–71, 2007.

[167] Susanne G Straub, RF James, Mark J Dunne, and GW Sharp. Glucose activates both k (atp) channel-dependent and k (atp) channel-independent signaling pathways in human islets. *Diabetes*, 47(5):758–763, 1998.

[168] Pål O Westermark and Anders Lansner. A model of phosphofructokinase and glycolytic oscillations in the pancreatic β-cell. *Biophysical journal*, 85(1):126–139, 2003.

[169] David A Jacobson, Felipe Mendez, Michael Thompson, Jacqueline Torres, Olivia Cochet, and Louis H Philipson. Calcium-activated and voltage-gated potassium channels of the pancreatic islet impart distinct and complementary roles during secretagogue induced electrical responses. *The Journal of physiology*, 588(18): 3525–3537, 2010.

[170] James Maylie, Chris T Bond, Paco S Herson, Wei-Sheng Lee, and John P Adelman. Small conductance ca2+-activated k+ channels and calmodulin. *The Journal of physiology*, 554(2):255–261, 2004.

[171] Barbara Rosati, Piero Marchetti, Olivia Crociani, Marzia Lecchi, Roberto Lupi, Annarosa Arcangeli, Massimo Olivotto, and Enzo Wanke. Glucose-and arginine-induced insulin secretion by human pancreatic β-cells: the role of herg k+ channels in firing and release. *The FASEB Journal*, 14(15):2601–2610, 2000.

[172] Roland Schönherr, Barbara Rosati, Solveig Hehl, Valesvara G Rao, Annarosa Arcangeli, Massimo Olivotto, Stefan H Heinemann, and Enzo Wanke. Functional role of the slow activation property of erg k+ channels. *European Journal of Neuroscience*, 11(3):753–760, 1999.

Alessandro Loppini

[173] Liangyi Chen, Duk-Su Koh, and Bertil Hille. Dynamics of calcium clearance in mouse pancreatic β-cells. *Diabetes*, 52(7):1723–1731, 2003.

[174] Yi-der Chen, Shaokun Wang, and Arthur Sherman. Identifying the targets of the amplifying pathway for insulin secretion in pancreatic β-cells by kinetic modeling of granule exocytosis. *Biophysical journal*, 95(5):2226–2241, 2008.

[175] Alessandro Loppini, Matthias Braun, Simonetta Filippi, and Morten Gram Pedersen. Mathematical modeling of gap junction coupling and electrical activity in human β-cells. *Physical Biology*, 12(6):066002, 2015.

[176] Etelvina Andreu, Bernat Soria, and Juan V Sanchez-Andres. Oscillation of gap junction electrical coupling in the mouse pancreatic islets of langerhans. *The Journal of physiology*, 498(3):753–761, 1997.

[177] Krasimira Tsaneva-Atanasova, Charles L Zimliki, Richard Bertram, and Arthur Sherman. Diffusion of calcium and metabolites in pancreatic islets: killing oscillations with a pitchfork. *Biophysical journal*, 90(10):3434–3446, 2006.

[178] Elli Kohen, Cahide Kohen, Bo Thorell, Daniel H Mintz, and Alexander Rabinovitch. Intercellular communication in pancreatic islet monolayer cultures: a microfluorometric study. *Science*, 204(4395):862–865, 1979.

[179] Paolo Meda, Alain Perrelet, and Lelio Orci. Increase of gap junctions between pancreatic b-cells during stimulation of insulin secretion. *The Journal of cell biology*, 82(2):441–448, 1979.

[180] Guy A Rutter and David J Hodson. Minireview: intraislet regulation of insulin secretion in humans. *Molecular Endocrinology*, 27(12):1984–1995, 2013.

[181] Robert A Ritzel, Johannes D Veldhuis, and Peter C Butler. Glucose stimulates pulsatile insulin secretion from human pancreatic islets by increasing secretory burst mass: dose-response relationships. *The Journal of Clinical Endocrinology & Metabolism*, 88(2):742–747, 2003.

[182] D Mears, NF Sheppard Jr, I Atwater, and E Rojas. Magnitude and modulation of pancreatic β-cell gap junction electrical conductance in situ. *The Journal of membrane biology*, 146(2):163–176, 1995.

Alessandro Loppini